Alma Mater Studiorum – Università di Bologna

DOTTORATO DI RICERCA IN

CHIMICA

Ciclo XXXI

Settore Concorsuale: 03/B1

Settore Scientifico Disciplinare: CHIM/03

Photoactive coordination compounds based on Cu(I) and Ir(III)

Presentata da Enrico Leoni

Coordinatore del Dottorato
Prof. Aldo Roda

Supervisore
Prof. Giacomo Bergamini

Cosupervisore
Dott. Nicola Armaroli

Cosupervisore
Prof.ssa Paola Ceroni

Esame finale anno 2019

"*Se si escludono istanti prodigiosi e singoli che il destino ci può donare, l'amare il proprio lavoro (che purtroppo è privilegio di pochi) costituisce la migliore approssimazione concreta alla felicità sulla terra. Ma questa è una verità che non molti conoscono.*"

Primo Levi

Abstract

Among photoactive coordination compounds, transition-metal complexes with d^6 and d^{10} electronic configuration are of particular interest for light emitting devices (OLEDs, LECs). As d^{10} emitters, copper(I) complexes attracted research interest due to the abundance of the metal, its relatively low cost and, at the same time, the remarkable photoluminescence quantum yield. Iridium(III) complexes (d^6 configuration), on the other hand, show tunable luminescence across the whole visible region and high stability.
The first part of my PhD work was devoted to the study of copper(I) heteroleptic complexes with general formula $[Cu(NN)(PP)]^+$, where NN = 1,10-phenanthroline or a related derivative and PP = bisphosphine, *i.e.*, a bidentate phosphine ligand. In particular, I focussed on their photophysics, electrochemistry and coordination structure, also with the support of DFT calculations. The research was targeted at answering the following three questions. How the structure of the ligands does affect the electronic properties of a given complex? Which ligand design does prevent the distortion in the excited state? How can the stability in solution be increased, while preserving good luminescence?
A library of more than thirty $[Cu(NN)(PP)]^+$ complexes has been investigated, evidencing the effects of such chelators on the electronic and structural properties. It was found that the size of the PP bite angle has a key role in preventing the dynamic ligand exchange in solution, but also in controlling the HOMO-LUMO gap and, accordingly, in enhancing the luminescence. High PLQY has been achieved combining large diphosphines with 2,9-substituted phenanthrolines (PLQY ≥ 70 % for **19** and **25** in PMMA). Notably, the use of macrocyclic-phenanthroline ligands has proved to be a good solution to answer the three challenges. The pseudo-rotaxane **31** was tested as emissive material in OLEDs and affords bright green devices with higher luminance and greater stability compared to **17**, which lacks the macrocyclic ring. This highlights the importance of structural factors in the stability of electroluminescent devices based on Cu(I) materials.
The second part of this thesis focusses on the study of $[Ir(C\hat{}N)_2(A\hat{}A)]^n$ compounds (where C^N are cyclometalated ligands, A^A an ancillary ligand and n = -1, 0). Two unconventional classes of luminescent Ir(III) complexes have been photophysically and electrochemically characterized, one with negative net charge and the other with an unusual ancillary azaborine ligand.

The chelating effect of the two ancillary ligands is promoted by an optimized structure and geometry. The anionic complexes **32-34** exhibit remarkable PLQY (up to 95 % in PMMA) with red, green, and blue emission, along with reversible oxidation and reduction processes, which make them interesting candidates as active materials for light emitting electrochemical cells. In thin films, the photoluminescence quantum yield decreases substantially, but stable electroluminescence was observed for devices made with complex **33**, highlighting the stability of the anionic compounds.
The theoretical and photophysical study of the azaborine compound (**Hpbzn**) evidenced properties comparable to its C=C analogue, confirming the planarity and the aromaticity of such ligand. **Hpbzn** and its complexes show higher HOMO-LUMO energy gap relative to the isoelectronic **Hnpy** compounds. Pristine **Hpbzn** exhibits good photophysical properties, which are even enhanced in the protonated form, obtained upon stoichiometric addition of acid. Complexes **35-37** exhibit good luminescence, but in solution are not sufficiently stable to be tested in electroluminescent devices.

Contents

1 Introduction

1.1 Luminescent Metal Complexes

A coordination complex consists of a central atom or ion, which is usually a metal, and a surrounding of bound molecules or atoms, called ligands and typically constituted by nonmetal elements [1].
The coordination bond that connects the metal ion and the ligands can result from different interactions. The most common Lewis acid-base reaction, where the ligand is the Lewis base and the metal is the acid, prompt two type of interactions, function of orbital used for the bond creation. If (i) a lone-pair of the ligand is used, a σ-coordination bond is obtained (*e.g.*, $[Fe(H_2O)_6]^{2+}$), otherwise, (ii) an unsaturated π bond can be the electron source to create a π-coordinated complex (*e.g.*, metallocene or metallacyclopropane). Moreover, (iii) a third metal-carbon σ-coordination bond can be formed through a cyclometalation reaction (*e.g.*, $Ir(ppy)_3$, with ppy = 2-phenylpyridine), in the presence of a negatively charged ligand (Figure 1.1).
Coordination compounds include molecules that are fundamental for life such as chlorophyll, hemoglobin, vitamin B_{12} and many metalloenzymes. Their role is also essential in chemical catalysis, luminescent devices, dyes and pigments, while their formation is the main step in many hydrometallurgical and purification processes.
Probably one of the earliest known metal complexes was based on the alizarin dye chelator combined with calcium or aluminum metal ions. This compound shows a bright color that varies with the metal ion. The extraction process from the madder to obtain the ligand dates back to ancient India, Egypt and Persia times.

The first observation of a completely inorganic complex was reported by the German alchemist Andreas Libavius, who in 1597 described the blue color assumed by the brass when exposed to lime water containing ammonium chloride. The deep blue $[Cu(NH_3)_4]^{2+}$ was the reaction product.
$KFe[Fe(CN)_6]$ is another dye used as pigment by artists since the 18th century, while one of the first examples of metal complexes used in a chemical process is the $K_2[PtCl_6]$, an intermediate compound in Pt refining.
The foundations of modern theory of coordination chemistry were laid by the chemist

Alfred Werner. He explained the correlation between the number of coordinated ligands, the metal itself and its oxidation state. Finally he determined the complex spatial configuration as a function of the number of ligands. In 1913 he was awarded the Nobel Prize in Chemistry, "in recognition of his work on the linkage of atoms in molecules by which he has thrown new light on earlier investigations and opened up new fields of research especially in inorganic chemistry".
Early photophysical and photochemical studies on metal complexes were essentially restricted to ligand photoexchange upon excitation of metal centered states (see Paragraph 1.1.1) and primarily involved the Cr(III) ion [2]. One of the major advancements in the field occurred in 1971, thanks to the discovery of the metal-to-ligand charge transfer excited states of Ruthenium(II) complexes [3]. The gold era of luminescent transition-metal complexes was opened by Adamson and coworkers, who first discussed the photophysical properties of what became the most extensively investigated metal complex, namely $[Ru(bpy)_3]^{2+}$ (with bpy = 2,2′-bipyridine) [4]. Another fundamental contribution was given by Meyer and coworkers. They demonstrated the validity of the energy gap law for the MLCT state, reporting an increase of the non-radiative constant with the reduction of the emission energy [5].
With the knowledge accumulated on Ru(II) coordination compounds, the interest for other d^6 systems, like Os(II) [6], Ir(III) [7] and Re(I) [8], quickly increased. Systematic studies on the photophysics of $Ir(ppy)_3$, were firstly reported in the mid 1980s by Watts et al. [7], while the introduction of an ancillary ligand to replace one of the ppy ligands brought about luminescence color tuning, increasing stability and electrochemical reversibility. Eventually, the use of Ir(III) complexes in OLEDs, due to their outstandingly tunable luminescence, became widespread [9].
Besides metal ions with d^6 electronic configuration, platinum(II) (d^8) cyclometallated compounds also showed interesting emission properties, with a peculiar square planar coordination geometry [10]. Another ion displaying MLCT electronic states is the d^{10} Cu(I). McMillin et al. firstly reported the luminescence properties of these promising coordination structures: $[Cu(NN)_2]^+$ and $[Cu(NN)(PP)]^+$ (with NN = diimide and PP = diphosphine) [11, 12]. The popularity acquired by copper(I) complexes is due to low cost of the metal as well as ease of preparation and photoluminescence.
In the frame of this research domain, I investigated luminescence, electrochemical and structural properties of two classes of transition-metal coordination compounds with d^6 and d^{10} electronic configuration, namely Ir(III) and Cu(I), with the aim of identifying

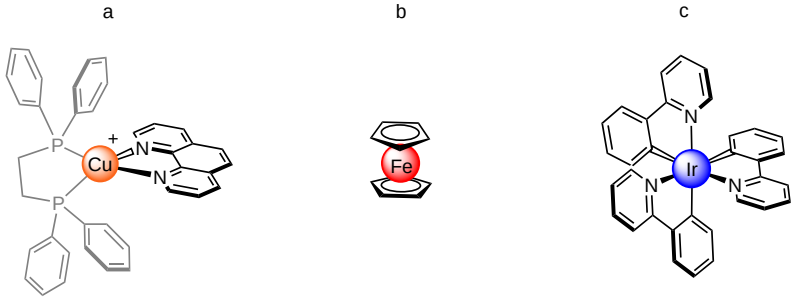

Figure 1.1. Example of coordination metal complexes. (a) Copper(I) complex showing σ-coordination bonds, (b) Ferrocene π-coordination metallocene and (c) *fac*-$Ir(ppy)_3$ cyclometallated complex.

good candidates for electroluminescent devices.

1.1.1 Electronic states

The electronic transitions in metal complexes typically results from the contributions of different parts of the compound. For the sake of simplicity, the most common electronic transitions are described by indicating the molecular orbitals (MOs) concerned with the specific electronic motion.
Luminescence predominantly arises from frontier molecular orbitals (FMOs). This definition includes the highest occupied and the lowest unoccupied MOs (HOMO and LUMO respectively). They are located on the π and π^* orbitals of the ligands, d and d^* orbitals on the metal core. Four main transitions can be highlighted. As depicted in Figure 1.2 (a, b), the electron may be promoted from a π to a π^* orbital of the same chelator, thus affording a ligand centered (LC) transition. In coordination complexes, the transition of an electron from a ligand to another one may also be observed; accordingly, the process is named ligand-to-ligand charge transfer (LLCT).
A metal centered (MC) transition can occur when an electron moves from a d orbital to an unoccupied orbital of the metal element – usually again a d^* orbital. This transition does not occur in the closed-shell Cu(I) complexes, while it is observed for Ir(III) and Pt(II) compounds. The MC transition is usually not emissive and, if not the lowest, it is often close in energy to the lowest excited state and, in some cases, may be thermally populated at room temperature. The non radiative deactivation through this state is observed in complexes emitting at high energy (i.e., blue emitters), when the HOMO-LUMO gap gets close in energy to the MC level (10^3-10^4 cm^{-1} between the two transitions). Furthermore, the MC transitions may induce variations in the coordination sphere, leading to ligand detachment and decomposition of the complex.
A metal-to-ligand charge transfer (MLCT) transition corresponds to the promotion of an electron from the metal center to one of the ligands. The MLCT transition is by far the most important for electroluminescent devices based on metal complexes, since it is typically the most favored radiative path. The MLCT excited states, in the presence of a strong spin orbit coupling (SOC), are usually characterized by lifetimes in the microsecond time range (in absence of oxygen) and may exhibit high photoluminescence quantum yields (PLQY).
It must be pointed out that so far, the electron-electron (Coulomb and exchange) interactions have been neglected for the sake of simplicity. By taking them into account, each transition splits into two sublevels corresponding to the spin configuration adopted by the state, i.e., a singlet or a triplet (Figure 1.2, c). The splitting depends on the exchange interaction and so varies with the spatial overlap of the two orbitals involved in the transition. The lower the overlap – *i.e.*, the higher the charge transfer character – the smaller is the energy gap. As an example, MLCT transitions involve two distinct parts of the compound as donor and acceptor orbitals (*e.g.*, d of the metal ion and π^* of a ligand), while in a LC transition both the orbitals (*i.e.*, π and π^* on a ligand) belong to the same part of the complex. As a consequence, a lower energy singlet-triplet splitting is observed in the former case.
The metal core may affect the excited state also in a different manner, *i.e.*, due to the presence of a heavy element, when an increase of the SOC is observed. This interaction

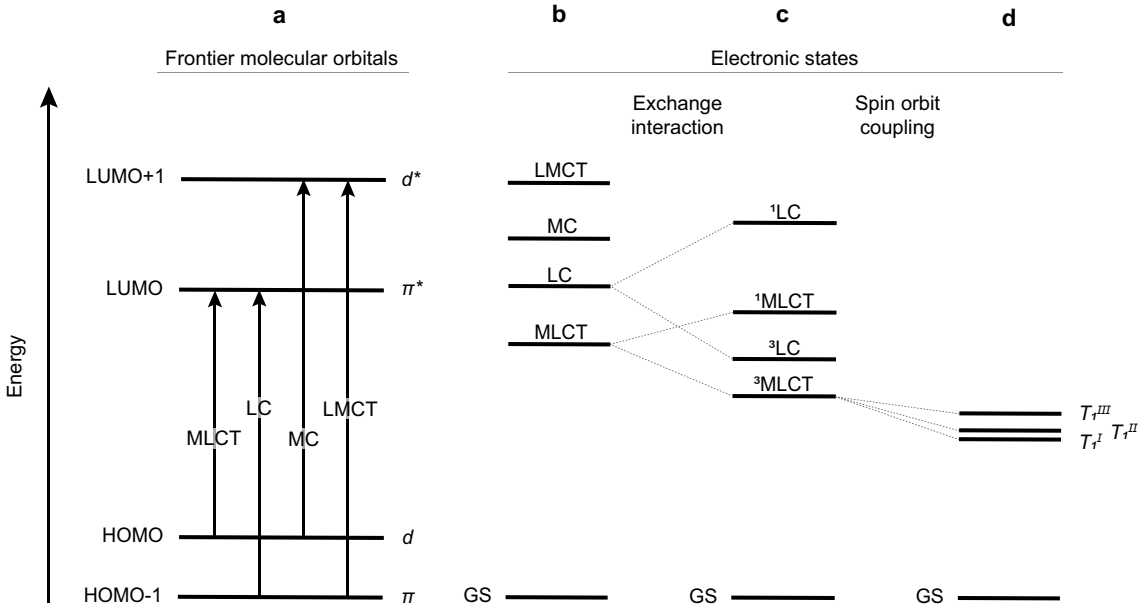

Figure 1.2. Scheme of FMOs (a) and of electron transitions (b), including exchange interaction (c) and spin orbit coupling (d) effects.

induces a partial mixing of the singlet and triplet character, thus making allowed otherwise forbidden transitions. As a consequence, the $S_1 \longrightarrow T_1$ intersystem crossing (ISC) rate (Figure 2.4 b, c) is enhanced. Depending on the specific atomic weight, the ISC can be tuned from femtoseconds (as for Ir(III)) to picoseconds (in the case of Cu(I)) but – compared to the nanosecond time range of a prompt fluorescence – the ISC remains the kinetically most favored transition from the S_1 state for most of the complexes. Likewise, the SOC enables a high constant rate for the $T_1 \longrightarrow S_0$ conversion. Therefore, in the presence of strong coupling and according to the energy gap law, the lowest triplet has a relatively short lifetime (microseconds) and a high luminescence quantum yield. It is important to point out that the mixed character added by the SOC to the degenerated states is not uniform and a different triplets stabilization can be observed (Figure 1.2, d). Usually, the energy splitting among the triplets increases as the metal ion moves down along a given group of the periodic table. As an example, a tiny energy gap of a few cm^{-1} has been reported for $3d^{10}$ Cu(I) compounds, while in the case of the $5d^6$ Ir(III) ion, this separation can be one order of magnitude higher [13].

1.1.2 Iridium(III): low spin d^6 complexes

A typical Ir(III) metal complex adopts an octahedral coordination geometry with a total charge that depends on the type of coordination bond with the ligands. Cationic, neutral and rarely anionic complexes have been reported.
Earlier studies on the homoleptic $[Ir(bpy)_3]^{3+}$ system showed the possibility to protonate the pyridine nitrogens and prompt a cyclometallating reaction, upon flipping of the pyridine ring [14, 15]. The tendency to cyclometallation has been then exploited to obtain a large number of Ir(III) complexes. Nowadays, the preparation of heteroleptic complexes, equipped with two equivalent chelators (*e.g.*, ppy, bpy) and a so called "ancillary" ligand, has become the most utilized strategy to control the charge and the electronic properties

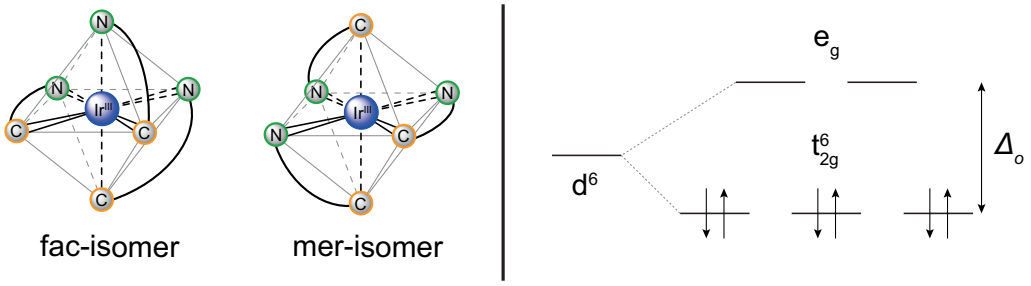

Figure 1.3. Isomers of the tris-cyclometallated Ir(ppy)$_3$ (left) and low spin d^6 electronic configuration in octahedral ligand field.

of the complex.

The presence of two different types of bonds – σ-cyclometallating Ir–C and σ-coordinating Ir–N ones – enables the formation of different isomers [16]. The labilization of the bond in trans position with respect to a cyclometallated carbon drives the preferential location of a pyridinic nitrogen in such position. The neutral homoleptic Ir(ppy)$_3$ complex can exemplify this behavior. It exhibits two isomers, the *facial* (*fac*-) displays all the cyclometallating carbons on the same triangular face of the octahedron and is thermodynamically more stable, while the *meridional* (*mer*-) contains two cyclometallating carbons in trans position (Figure 1.3).

The relative amount of the two isomers can be controlled by the preparative conditions. The easier synthetic route for preparing [Ir(C^N)$_2$(A^A)]^n (with C^N as a cyclometallating ligand and A^A as any possible bidentate ancillary ligand), starts from the dinuclear μ-dichloro-bridged Ir(III) dimer ([Ir(C^N)$_2$Cl]$_2$). The solution with this reagent is treated with an excess of the desired A^A ligand, in a simple one-step reaction. The key tool to isolate each isomer is the temperature applied during the addition and reflux steps. Performing the reaction with a temperature below 150 °C *mer*-Ir(ppy)$_3$ is preferentially obtained, while the more stable *fac*-Ir(ppy)$_3$ is isolated at higher temperature (>180 °C) [17]. The photo and thermal conversion into the most stable *fac*- isomer is observed for the *mer*-Ir(ppy)$_3$ complex [14].

From the ligand field theory, it is known that d orbitals of any transition metal complex are systematically subject to a destabilization and a splitting in two groups, depending on their spatial orientation of the chelators and the coordination number. In a octahedral ligand field, the e_g orbitals (d_{z^2} and $d_{x^2-y^2}$), pointing directly to the ligand, are subject to electrostatic repulsion and are destabilized. On the contrary, a stabilization occur for the non-bonding t_{2g} orbitals (d_{xy}, d_{yz} and d_{xz}) pointing between the ligands.

The splitting energy Δ_o is essentially a function of (i) the oxidation number of the metal ion (the lower the oxidation, the lower the Δ_o), (ii) the group number of the metal (the lower the group, the lower the Δ_o) and (iii) the ligand field (defined by the spectrochemical series) [18]. In Ir(III) complexes (5th group) the high charge and the strong field character of the cyclometallating ligands maximize the splitting and a low spin $t_{2g}^6 e_g^0$ electronic configuration is obtained. Due to the closed shell $5d^6$ configuration, the ground state of Ir(III) complexes is a singlet. Light absorption prompts the population of spin allowed excited states of various nature: ligand centered (^{1}LC), metal-centered (^{1}MC), metal-to-ligand charge transfer (^{1}MLCT), and, possibly, ligand-to-ligand charge transfer (^{1}LLCT) states (Figure 1.2).

The heavy metal ion induces large SOC, hence the lowest triplets are efficiently popu-

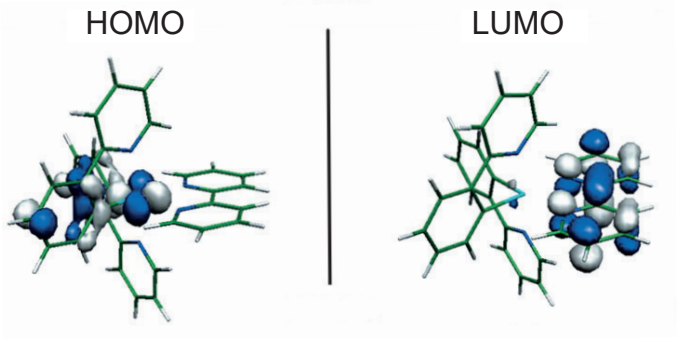

Figure 1.4. Density contours of FMOs calculated for $[Ir(ppy)_2(bpy)]^+$. Image for reference [19].

lated by quick ISC (see Paragraph 1.1.1). Accordingly, light emission is always related to a triplet state [20]. Unlike other transition-metal complexes, the character of the triplet state is strongly affected by the type of ligands and their substituents, and the emission may involve LC or CT states. Non-radiative ^{3}MC states are usually higher in energy and less thermally accessible, compared to Ru(II) analogues.
Based on what described above, remarkable luminescent properties and high stability of iridium organometallic compounds are expected, but the key feature of these compounds is the luminescence tunability across the whole visible region [14, 21–23]. An effective solution to shift the emission band is the judicious selection and functionalization of the ligands, which enable tuning of the HOMO and LUMO energy levels.
As an example, the FMOs of the $[Ir(ppy)_2(bpy)]^+$ are reported in Figure 1.4. The character of the HOMO arises from the contribution of the two cyclometallated phenyls and the non-bonding d_{xy} orbitals of the Ir(III) core. The LUMO, on the contrary, is located on the π^* orbital of the ancillary bpy ligand, with a minor contribution of the $d_{x^2-y^2}$ anti-bonding orbital of the metal ion. As a consequence, the expected character for the lowest emitting triplet should be a mixing of the ^{3}LLCT and ^{3}MLCT transitions.
Well established strategies to increase the HOMO-LUMO energy gap (*i.e.*, obtaining a blue shift) are based on: (i) the decoration of the cyclometallating ligands with electron withdrawing groups to stabilize the HOMO, (ii) the enhancement of the ligand field to increase the Δ_o and (iii) destabilize the LUMO on the ancillary ligand by increasing electron-donor character of this chelator. On the other hand, the last two strategies could also lead to an increase of the LC character of the triplet transition. In fact, by destabilizing the LUMO on the ancillary ligand, the two empty molecular orbitals on the cyclometallated ppy may become the lowest-lying ones (i.e. the LUMO).
Similarly, a reduction in the HOMO-LUMO gap and the consequent red-shift of the emission is observed if (i) the electronic conjugation is extended on the cyclometallating ligands or (ii) on the ancillary ligand and (iii) integrating soft atoms (*i.e.*, N, S) in the cyclometallated aromatic ring.
All these features have been practically applied in many fields, making available a large number of stable charged and neutral Ir(III) complexes. It must be highlighted that, despite the availability of a wide range of red and green emitters, blue luminescent Ir(III) coordination compounds still lack stability and this remain a critical issue for practical applications.
Over the last years, the complexes of this metal ion have been integrated both in organic light emitting diodes (OLEDs) [23, 24] and light-emitting electrochemical cells (LECs)

[25]. Recently, the LEC architecture has evolved to a point that the device instability is almost solved, maintaining strong luminance and a short switch-on-time [26].

1.1.3 Copper(I): a shining d^{10} metal ion

Copper(I) complexes proved to be interesting alternatives to traditional photoactive transition-metal complexes based on more precious ions such as Ru(II), Pt(II), Ag(I) and Ir(III). Cu(I) complexes have attracted research interest due to the abundance of the metal, its relatively low cost and, at the same time, the interesting photophysical properties. As a d^{10} emitter, it has a closed shell electronic configuration that prevents the population of non-radiative MC states at low energy (see Paragraph 1.1.1).
Copper(I) complexes equipped with a suitable ligand environment may exhibit long-lived excited states and strong luminescence, which makes them increasingly important for electroluminescent devices [19, 27], photoredox catalysis [28, 29], solar-to-fuels conversion [30–33] and sensing [34, 35].
A great deal of work has been devoted to the study of homoleptic $[Cu(NN)_2]^+$ complexes (where NN denotes diimmine ligands, typically substituted 1,10-phenanthrolines) [11, 36]. In most cases, these compounds, despite a wide absorption band in the visible spectral region, are weak emitters both in solution and in the solid state, due to extensive excited state structural rearrangements [37] that can be traced by ultrafast absorption [38, 39] and X-ray spectroscopy [40–42]. Upon light irradiation, the ground state quasi tetrahedral geometry undergoes flattening distortions that promote non-radiative deactivations (see Paragraph 2.0.3). When phenanthroline ligands are equipped with multiple bulky substituents (as a matter of fact, very limited cases) strong luminescence may be detected also for $[Cu(NN)_2]^+$ compounds [43–45].
Seminal work by McMillin and coworkers demonstrated that heteroleptic complexes of general formula $[Cu(NN)P_2]^+$ (where P is a phosphine ligand such PPh_3) can also show luminescence, but they proved relatively unstable [12, 46]. A few years after this discovery, Nishikawa and coworkers rationalized the observed luminescence as a thermally activated delayed fluorescence (TADF) process (see Paragraph 2.0.5) [47].
Eventually, substantial progress was achieved when, the McMillin's group showed that chelating phosphine ligands such as POP (bis[2-(diphenylphosphino)phenyl] ether, also referred ad dpePhos), may afford $[Cu(NN)(PP)]^+$ complexes (with PP as a diphosphine ligand) with good stability and photo-luminescence quantum yields (PLQYs) above 15 % [48, 49], *i.e.*, at least two orders of magnitude higher than typical $[Cu(NN)_2]^+$ counterparts [37]. This finding prompted extensive research on $[Cu(NN)(PP)]^+$ compounds, in an effort to understand their complex behavior and establish rational criteria for the design of copper-based materials exhibiting good chemical stability, high PLQY, long-lived and strongly reductant excited states [13, 50–63].
The vast majority of luminescent Cu(I)-based complexes reported to date are cationic with tetrahedral structure, but the coordination environments explored have grown large. Recently, bright emission from tricoordinated [64, 65] and even biscoordinated [66] Cu(I) complexes, often displaying N-heterocyclic carbene ligands, has been reported. Some neutral Cu(I) compounds have been also prepared [58, 67–69], including cyclometalated systems [70], but commonly their stability remains an issue. On the other hand, coordination polymers in which Cu(I) centers are connected to halogen ions (typically

I^-) in combination with heteroaromatic (N– or P–) ligands have been extensively investigated and may exhibit very strong emission [71, 72]. Other types of Cu(I)-based networks with intense luminescence have also been studied [73]. Very recently, all such aspects of Cu(I) complexes have been comprehensively reviewed [74].
Generally, Cu(I) coordination polymer can be handled just in solid, moreover, also Cu(I) complexes may suffer limited thermal and photochemical stability, particularly in solution. In liquid media, heteroleptic Copper(I) systems may also easily undergo ligand exchange reactions affording the two homoleptic species (see Paragraph 2.0.4) [75].
Their several relevant properties like high PLQYs, microseconds lifetimes, singlet-harvesting via TADF [76] and the substantial lack of self-quenching in solid, prompted the use of these compounds in electroluminescent devices, as described in the next Section (1.2) [63].

1.2 Electroluminescence

Electroluminescence (EL), namely electrogenerated luminescence, relies on the generation of an emissive excited state through the application of an electrical field to a solid material. Such mechanism changes with the type of device considered, but is generally based on a simple structure where two electrodes inject electrons and holes into a layer (or a series of stacked layers), that contains the active material (*e.g.*, the latter can be an organic molecule, a metal complex, quantum dots, nanoparticles, or conjugated polymers). The charge recombination generates the excited states on the EL material and, eventually, light emission is observed.
Various types of EL devices have been proposed, the two related to this PhD work are described below. OLEDs are made by a series of solid layers between the electrodes, thoroughly juxtaposed to favor the injection and mobility of electrons on the cathodic side and of holes on the anodic side, favoring the electron-hole pair formation (exciton) in the active layer with the EL material.
On the contrary, LECs are based on a simplified structure, made of a single layer containing the ions to transport the charges and the EL compound. The EL generation is again based on the coupling of electrons and holes on the same molecule (or complex), followed by radiative deactivation of the excited state.
The research in this field started over 60 years ago, when EL was demonstrated for the first time for an organic molecule, an amine-anthracene derivative. This discovery was made by Bernanose and coworkers in 1953 [77, 78]. The first experiment was based on the use of alternating current, while Pope at al. in 1963 exploited a high voltage direct current EL device, again based on a similar anthracene crystal [79]. A major breakthrough was made by reducing the thickness of the emitting layer down to a few hundred of nanometers. This allowed a remarkable reduction of the operating voltage [80].
In 1987, Tang and Van Skyle described the first OLED requiring only 10 V and two layers to transport hole and electrons. This simple geometry was based on the successful approach of reducing the recombination area to the interface and resulted in an external quantum efficiency (EQE) of ≈ 1 % [81].
In 1995, Pei and coworkers further moved towards simplification, proposing an original approach to the device structure. Their LEC was made of a single layer containing a blend of the luminescent material characterized by an electrochemical stable redox process, an inorganic salt used as stabilizer and a charge transporter (*i.e.*, ionic conductive polymer) to increase the conductivity [82].
Soon after, a Ru(II) emitting complex was reported as active material in a LEC in 1996 [83], whereas the most promising devices are now based on Ir(III) complexes [22, 26, 84].

1.2.1 OLED: working principle and device structure

As demonstrated by Tang and VanSkyle, an OLED can contain even only one layer (the emissive material itself) [81], but in such a simple device the internal quantum efficiency is negatively impacted. Here we consider a three-layers device since closer to the most common manufactured devices (Figure 1.5).
The electrical potential is applied to the device through the two electrodes. The cathode is

usually made with a low work-function metal, such as aluminum or magnesium, while a thin transparent metal oxide – indium tin oxide, ITO – that can transmit the light generated by the device, constitutes the anode. The electrodes are interfaced with two layers (one on each side) that promote charge injection and mobility. Their thickness must be tailored so as the negative and positive charges combine in the central active material. Moreover, the type of material used to dope these layers is judiciously selected to get the same number of holes and electrons injected. In the presence of an even number of opposite charges (represented by the charge balance γ), the internal quantum efficiency (η_{int}) is enhanced as shown by equation 1.1.

$$\eta_{int} = \beta * \phi_{em} * \gamma \tag{1.1}$$

Where ϕ_{em} indicates the photoluminescence quantum yield (PLQY) of the emitting molecule, while β, the spin statistic factor, is related to the fraction of collected excitons, as reported below. The external quantum efficiency η_{ext} (EQE) is strictly related to the η_{int} by equation 1.2.

$$\eta_{ext} = \eta_{int} * \mathrm{X}_{out} \tag{1.2}$$

Where X_{out} corresponds to the outcoupling efficiency, *i.e.*, the percentage of the generated light that is able to get out of the device.
The two main losses for η_{ext} are the high refractive index of the various organic layers, and the formation of surface plasmons on the electrode due to dipoles of the emitting molecule and the metal cathode. The easiest solution to the latter problem is the increase of the thickness of the layer that separates the cathode and the central part of the device, so as to reduce the coupling.
The most important part of the device is the active layer with the EL material, which must support the recombination of the charges to get the exciton. The injected electrons and hole move through various layers to the opposite sides driven by the electric potential. When the positive and negative charges are close enough to each other (few hundreds of Å, depending on the material), they start to be attracted. Another crucial point for the the recombination process is the spin multiplicity of the electron and hole. The spin of these subatomic particles is 1/2, thus the total spin angular momentum of the pair ranges from $S = 0$, a singlet with spin multiplicity $M = 1$ ($M = 2S + 1$), and $S = 1$, a triplet with $M = 3$. At this stage, the states are assumed to be degenerate, which makes equally probable the formation of such excitons; consequently, the statistic ratio of the triplet/singlet is 3:1.
As the charges get closer, the electron and the hole wave function start to overlap, undergoing exchange interaction. Accordingly, the singlet and the triplet are no longer degenerate. Whenever opposite charges converge on the same molecule, an excited state is formed.
It must be highlighted that the spin multiplicity of an excited-state is coherent with the spin multiplicity of the exciton that generates it. The system then deactivates to the lowest singlet or triplet configuration.
In order to maximize the η_{int}, the EL material must be able to produce an excited state which emits from any of the parent states (triplet or singlet). For this reason, triplet emitters (phosphors) or TADF materials are preferred, due to their capability of converging

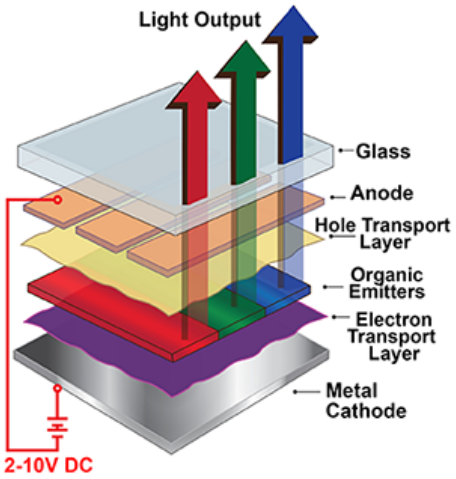

Figure 1.5. Schematic representation of a three-layer OLED device. Digital image from www.newhavendisplay.com

towards both triplet and singlet excitons and generate a "useful" excited state.

As a general rule, the majority of organic molecules do not present an efficient ISC (millisecond to second time range) [85–87], because the transition $T_1 \longrightarrow S_0$ is strongly forbidden. The fluorescence process relies only on the transition $S_1 \longrightarrow S_0$ (decay in nanoseconds) and, assuming the PLQY = 1, just one exciton out of four (the singlet) can be usefully collected, while triplets do not contribute to the emission process. Therefore, if the $\gamma = 1$ and the β factor of eq. 1.1 has a value of 0.25, a maximum internal quantum efficiency $\eta_{int} = 0.25$ is obtained.

Transition-metal complexes, on the contrary, due to non negligible SOC, exhibit a competitive ISC process and can emit from the triplet state. It is therefore evident that all the excitons are efficiently collected. In fact, if PLQY is assumed to be one [88–90], $\gamma = 1$, $\eta_{int} = 1$ is obtained. This mechanism of collection of all the excitons to the lowest triplet state is named *triplet harvesting effect*. The most promising compounds belonging to this category are Ir(III) and Pt(II) complexes [88–90].

A class of emitters of high relevance for OLEDs are TADF systems. These materials are characterized by a low $\Delta E(S_1 - T_1)$ energy gap and, as reported in Paragraph 2.0.5, the energy proximity between these two states enable the $T_1 \longrightarrow S_1$ reverse ISC upon thermal activation (Figure 2.4). In this way, at room temperature, the long-lived triplet acts as a thermal activated reservoir of the singlet state. The radiative decay is reduced by the short singlet-state lifetime, from which the light emission is observed. The advantages of this *singlet harvesting effect*, is the reduction of detrimental processes observed in the triplet emitters, such as triplet-triplet quenching and, in general, efficiency roll-off. Furthermore, a TADF material does not need to contain an expensive high SOC transition-metal, since the radiative transition $S_1 \longrightarrow S_0$ is spin allowed. Some Cu(I) and Ag(I) complexes are the most efficient transition-metal TADF complexes, along with some organic molecules [91–95].

1.2.2 LEC: working principle and device structure

Pei et al. in 1995 presented the proof-of-concept of a new type of electroluminescent device [82], a light emitting electrochemical cell (LEC). The LEC achieved some goals

that were pursued by researchers for years: (i) air stability, (ii) capability to work with any metal work-function, (iii) extreme simplicity of the structure, (iv) easy and cheap processability by printing techniques [19, 96].
The first LEC was based on a salt, a conductive and luminescent polymer mixed in a single active layer placed between the electrodes. One year later, Maness and coworkers proposed an alternative approach based on an electropolymerized material containing a metal complex (poly-$[Ru(vbpy)_3][PF_6]$, with vbpy = 4-vinyl-4‘-methyl-2,2‘-bipyridine) [83]. In this device the components were further reduced simply to the fixed-site redox polymer and its counterion.
Two different operational mechanisms were proposed for early devices, the electrodynamic (ED) elaborated by deMello [97–99] and the electrochemical doping (ECD) models reported by Pei and coworkers [82, 100, 101]. In 2010, Ginger et al. demonstrated that these mechanisms were two regimes of the same electrical behavior, thus both correct [102].
Upon the application of a voltage greater that the emitter band gap, electrons and holes are injected into the active layer. As a consequence, an electrochemical doping of the material close to the anode and the cathode is observed, through the formation of the reduced and oxidized species of the luminescent material. The highly conductive doped regions (Figure 1.6 (b)) formed in the proximity of the electrodes are separated by a central insulating region, in which the electronic potential drops. This condition defines the ECD model.
Over time, the doped regions grow at the expenses of the insulating layer and the EL is accordingly reduced: in the presence of electrochemical doping the luminescence is quenched. At switch-on, the light emission is usually observed in close proximity of the electrodes, while the number of oxidized/reduced species close to the injection zone increase over time, hence the luminescent layer is shifted deeper inside the device.
In the situation of poor injection of charge from the electrode-solution interface, a ED model is applied. The electric potential is constant inside the device, but a significant drop is observed in the double layers in close contact with the electrodes, which are formed upon bias application (Figure 1.6 (a)).
For proper operation, a 1:1 balance between the opposite charges and similar mobility

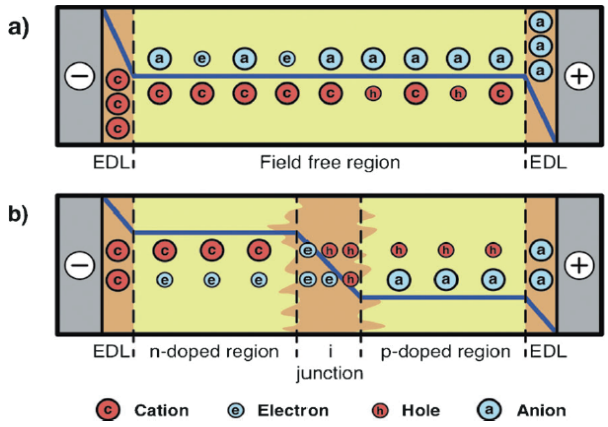

Figure 1.6. Schematic illustration of potential profile as well as electronic and ionic charge distribution in a LEC device. a) ED and b) ECD models. Image from reference [19].

are necessary. The continuous luminescence reduction observed, due to the shrinking of the undoped region, can be reversed by switching off the device for several minutes. When the absorption features of the oxidized/reduced species match the emission bands, detrimental self-absorption phenomena may arise upon increase of the doped region.
Intrinsically-ionic luminescent complexes are the best choice in LEC devices, since (i) they are easy to solubilize in polar or ionic liquids [19], (ii) eliminate the need of electrolytes, in addition (iii) are typically triplet emitters (Paragraph 1.1.1) thus the probability of exciton collection is enhanced. Indeed Ir(III) complexes are good candidates for LECs, due to their high stability in solution, reversible redox processes, possibility to tune the emission by ligand design, luminescence decays in the microsecond time range and generally high PLQY.

2 Copper(I) photoactive complexes

The work presented in this Chapter was done in collaboration with Jean-François Nierengarten (University of Strasbourg), Jean-Pierre Sauvage (University of Strasbourg), and Béatrice Delavaux-Nicot (University of Toulouse).
J.F. Nierengarten provided the complexes, planning the synthetic procedure and performing it in collaboration with his coworkers, J.P. Sauvage firstly designed and reported macrocyclic systems applied to coordination compounds and inspired the pseudorotaxane series, B. Delavaux-Nicot performed all the electrochemical experiments. Their crucial contribution to this work is gratefully acknowledged.

2.0.1 Why Copper(I) complexes?

Owing to a peculiar combination of electronic and structural features (*e.g.*, flexible geometric structure, chromophoric character, luminescence, electrochemical behavior), Cu(I) complexes have attracted wide interest in several areas such as supramolecular chemistry [103], molecular machines [104], catalysis [28], ultrafast spectroscopy [105], solar energy conversion [106], optoelectronics [33, 107], and luminescence [13].
In the latter area, the main goal is finding brightly emitting materials based on an abundant element as alternatives to standard triplet emitters, which typically contain expensive platinum group elements [108–111]. Compared to the noble metals, Cu(I) systems may exhibit TADF [76]. This means that the lowest lying triplet emitting level can get very close in energy ($\approx$300–1300 cm^{-1}) to the upper lying singlet [13], which can be spontaneously populated at ambient temperature via reverse intersystem crossing. Accordingly, emission comes from the singlet level (*singlet harvesting*) but its intrinsic lifetime is prolonged via the thermal equilibration with the longer-lived triplet (see Paragraph 2.0.5). The overall result is that (i) both singlet and triplet excitons can be harvested and (ii) the excited-state lifetime of the luminescent species can occur in the range of 1–20 µs at room temperature [13]. These features are particularly relevant for electroluminescent devices (*e.g.*, OLEDs) because the efficiency of electricity-to-light conversion are optimized and, on the other hand, saturation effects or undesired photochemical processes are significantly disfavored, due to the relatively short lifetime.
Compounds exhibiting good photoluminescence primarily include $[Cu(NN)_2]^+$ (where NN is a diimine ligand such as 1,10-phenanthroline [44], 2,2′-bipyridine [112], or 4,5-diazafluorene [60]), $[Cu(NN)(PP)]^+$ (where PP is a diphosphine ligand [48, 53]), $[Cu(PP)_2]^+$ [113, 114] and other tetracoordinated systems [115].
In many cases, the luminescence properties of Cu(I) compounds are only investigated in the solid state because solution instability compromises the reproducibility of experimental measurements. Complexation/decomplexation equilibria have been investigated in tetrahedral systems, which can be partially controlled by a thorough selection of ligands that can minimize steric congestion (see Paragraph 2.0.4) [75]. Further instability can occur due to the strong reducing character of Cu(I) complexes in the excited state [37] which, on the other hand, can be fruitfully exploited in photoredox catalysis [28] or photocatalytic water reduction [116].

2.0.2 Purpose of the research activity

As part of this research, we became interested in exploiting luminescent $[Cu(NN)(PP)]^+$ complexes in lighting systems, in particular OLED devices (see Paragraph 1.2.1). The comprehensive understanding of how structural parameters affect the electronic properties, together with the creation of a wide library of compounds, with the determination of their luminescence as a function of the ligands is the main goal of this work.
A systematic photophysical investigation of a large number of $[Cu(NN)(PP)]^+$complexes, of which 31 have been here reported, has been performed both in solution, solid state and polymeric media, also carefully evaluating their stability in solution. The temperature effect on the luminescence has been assessed for all the samples and some selected cases have been studied at variable temperature to prove the occurrence of TADF (see Paragraph 2.0.5). The results have been correlated with electrochemical properties, while

theoretical calculation, validated by single crystal structure if available, were used to rationalize the coordination geometry of fundamental and excited-states, but also to describe the electronic character of the latter.
The results have been organized in three series of complexes, grouped as a function of the studied properties. In the **Section 2.1** it has been assessed the effect of the diphosphine ligand on the structure and the luminescence, using highly stable complexes. The poor emission performance observed for this series in solution is due to the type of diimine used that cannot effectively prevent photoinduced distortions, which favor the non-radiative deactivation of the excited state. In the second part (**Section 2.2**), we combined various diphosphines, with functionalized phenantrolines, with the aim to maximize PLQY and tune the luminescence wavelength, trying to maintain high stability in solution. This series was designed to increase the radiative constant by minimizing the structural distortion in the excited-state. Finally, in **Section 2.3**, an idea to solve the ligand scrambling equilibrium in solution is reported. The strategy entails in the use of a macrocyclic diimide as NN ligand in $[Cu(NN)(PP)]^+$. This derivatized phenanthroline allows, at the same time, to keep high the PLQY (avoiding excited-state distortion) and to shift the ligand scrumbling equilibria towards the heteroleptic complex, enhancing the stability. The good results concerning TADF and luminescence prompted us to test the best performer, as proof of concept, in an OLED device. The device incorporating our Cu(I) complex outperformed the luminescence efficiency of a reference established material.

2.0.3 Photoinduced distortion

In the neutral state Copper has twenty nine electrons ($[Ar]4s^1 3d^{10}$), eleven in the outer sphere and a completely filled set of $3d$ orbitals. Copper(I) ion, losing the $4s$ electron, preserve the closes shell $3d^{10}$ electronic configuration and adopts a preferential pseudo-tetrahedral D_{2d} coordination geometry [33, 117, 118]. As highlighted in Paragraph 1.1.1, the fully occupied d shell prevents $d \longrightarrow d^*$ low energy transition and the consequent kinetically favored non-radiative deactivation path.
On the other hand, Copper(II) has a d^9 electronic configuration and undergoes a Jahn-Teller distortion (JTD) that breaks the coordination symmetry and adopts a distorted octahedral configuration with elongated axial distances [118, 119].

Assuming a simplified geometry for a Cu(I) complex, four coordinating atoms would be positioned at the edge of the tetrahedron. Upon light excitation, a Frank-Condon (FC) ^{1}MLCT state, possessing the same ground-state geometry, is generated. The photon absorption transiently generates a Cu(II) ion, upon promotion of one electron from the metal core to the π^* orbital of one ligand:

$$[Cu^{I}(L)_4]^+ \longrightarrow [Cu^{II}(L)^-(L)_3]^+$$

The FC ^{1}MLCT state is then subject to an internal conversion, a reorganization of the $^1S_1$ coordination geometry to that adopted by the Cu^{II} ion. Based on the binding position occupied by the coordinating atoms and assuming no steric influence played by the ligands, the pseudo-JTD (PJTD) leads to a square planar configuration (Figure 2.1), *i.e.*, the closest one to the distorted octahedron usually adopted by Cu^{II}.
The photoinduced flattened state ($^1MLCT_{flat}$) is energetically stabilized compared to FC

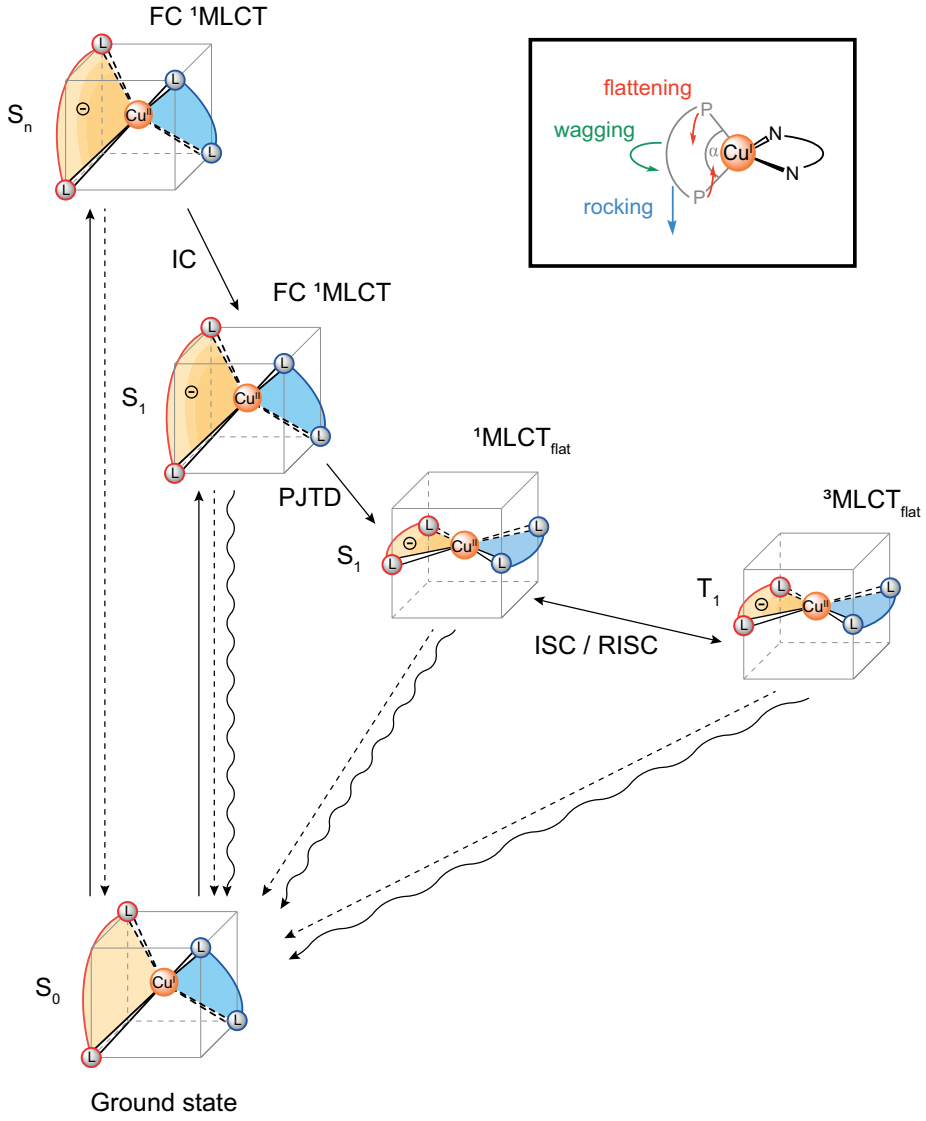

Figure 2.1. Geometrical rearrangements of a Cu(I) tetracoordinated complex upon photoexcitation. Vertical full lines: photon absorption; dashed lines: non-radiative deactivation process; waved line: photon emission (fluorescence/phosphorescence). Inset: typical deformations observed for the pseudo-tetrahedral $[Cu(NN)(PP)]^+$ complex and diphosphine bite angle (α).

state, thereby the non-radiative deactivation constant increases exponentially, according to the energy gap law [120]. Moreover, the intersystem crossing (ISC) process, due to the reduced spin orbit coupling (SOC) between $^1MLCT_{flat}$ and $^3MLCT_{flat}$, is significantly slowed down and the triplet formation can be considered negligible [121].
The pseudo-JT distortion, due to the capability of Cu^{II} to accept ligands also in the axial sites, enables a nucleophilic attack by a coordinating solvent molecule to the flattened compound in solution, which further promotes non-radiative relaxation [37, 113].
The combination of these processes: (i) pseudo-JT distortion that brings the formation of a flattened compound and (ii) exciplex formation with solvent molecule, strongly affect the PLQY of the material.
A possible solution to minimize the detrimental distortion process induced by the Cu(II)

transiently formed, is a judicious choice of the ligands. Due to the flexible tetrahedral geometry, weak interactions and steric factors may strongly affect the geometry and crystal structure [59]. Accordingly, the ligands play a crucial role in dictating geometric distortions both in the ground and in the excited state [33, 43].
Historically, many works on the design of novel chelators have been reported. The first remarkable increase in the luminescence properties of Cu(I) coordination compounds was observed by McMillin and coworkers, with the exchange of a NN ligand in $[Cu(NN)_2]^+$ with a diphosphine [48, 49]. This simple strategy enhanced the PLQY of one order of magnitude with respect to the homoleptic complexes. The same group, in 2002, highlighted another dramatic change in the PLQY by acting on the NN ligand. The introduction of alkyl functionality in 2,9 positions of the phenanthroline in $[Cu(\mathbf{phen})(POP)]^+$ brought PLQY to a level comparable with Ir(III) complexes. The new sterically demanding ligand, due to the presence of the substituents in position close to the metal centre, proved to be an efficient solution to limit excited-state flattening, increasing by almost two orders of magnitude the emission efficiency and the luminescence lifetime with respect to complexes with pristine phenantrholine (see Paragraph 2.0.3) [48].
The optimized design of the ligands, is the key point of the Copper(I) photoactive complexes part of this thesis. In Section 2.1, the structure and the electronic properties of a series of Cu(I) complexes, are analiyzed as a function of diphosphines of different size, in Section 2.2 the focus is shifted to the effect of mono- and symmetric functionalization of the phenantrholine in 2,9-positions, with particular attention on luminescence properties. Finally, the complexes discussed in Section (2.3) are based on the most promising ligands identified in the two previous parts.

2.0.4 Ligand dynamic equilibrium in solution

The stability in solution is the key for the large majority of the potential applications of Cu(I) complexes. For example, it is of crucial importance the possibility to dissolve this type of compounds in solution for the preparation of an optoelectronic device, because they are charged and it is usually impossible to deposit them by sublimation. Unfortunately, one of the main issues characterizing heteroleptic Cu(I) complexes is a fast ligand exchange in solution, which may affect also thermodynamically stable $[Cu(NN)(PP)]^+$ complexes. This kinetically controlled reaction implies the formation of the homoleptic $[Cu(NN)_2]^+$ and $[Cu(PP)_2]^+$ complexes starting from the heteroleptic one (Figure 2.2). The equilibrium is observed in solution as soon as the complex is dissolved, even in non-coordinating solvent such as CH_2Cl_2, while polar coordinating media may amplify this effect [122].
The speciation among $[Cu(NN)(PP)]^+$, $[Cu(NN)_2]^+$ and $[Cu(PP)_2]^+$ is governed by the ratio of their relative stability, since all the binding sites present on the Cu(I) core are saturated by these ligands. The 2,9-substituted-1,10-phenanthroline, with large and flat substituents, may form particularly stable $[Cu(NN)_2]^+$ complexes ($log\beta$ = 10-12) [123, 124], thus, when these diimine ligands are used in heteroleptic complexes, the equilibrium is pushed towards the homoleptic species. On the other hand, phenanthrolines that do not have substituents close to the copper core produce significantly less stable $[Cu(NN)_2]^+$ systems, hence the formation of homoleptic complexes may be disfavored with respect the heteroleptic form.

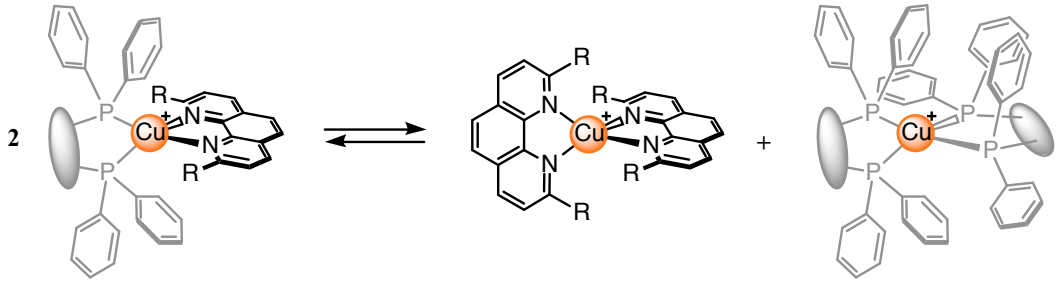

Figure 2.2. Dynamic equilibrium evidenced in solution between the heteroleptic complexes and their homoleptic species. R = any substituent bulkyer than −H. Courtesy from [75]

The *negative steric effect* above reported competes with a *positive steric effect* observed when the ligands are too bulky to form the $[Cu(XX)_2]^+$ systems (with XX = NN or PP ligands). This effect was firstly proposed by Schmittel et al. in 1997 [125], when they took advantage of large groups in 2,9-substituted-1,10-phenanthroline (*e.g.*, mesityl groups) to sterically obstruct the formation of the homoleptic complex, and obtain the heretoleptic complex quantitatively in presence of an unhindered counterpart. Bulky and rigid PP ligands can act in a similar manner, effectively reducing the stability of the related $[Cu(PP)_2]^+$ complex, thus partially hindering this equilibrium reaction.
In order to evaluate the capability to form homoleptic complexes, it is of common use to classify the diphosphine as a function of the the so called bite angle, *i.e.*, the angle described by the two phosphorus with the metal core (α, Figure 2.1, inset). As a general rule, low bite angle PP ligands ($\alpha < 110°$) can be easily accommodated also in a homomoleptic $[Cu(PP)_2]^+$ complex, while in the case of diphosphine with large bite angle ($110° > \alpha > 130°$), the homoleptic PP complex is substantially destabilized, as demonstrated by the crystal structure of $[Cu(POP)_2]^+$ [126]. In this case the Cu(I) cation is too small to be fully coordinated by the two POPs, thus one of the two diphosphines acts as a monodentate ligand, and the complex has a distorted trigonal geometry.
Also other approaches have been used to increase the stability in solution. A smart solution consist in joining the imine and the phosphine functional group together in an NP ligand. The $[Cu(NP)_2]^+$ motif shows promising properties (*e.g.*, high PLQY and long lifetimes), but this particular class of complexes is outside of the scope of this thesis [127–129].
Another strategy, applicable to classical $[Cu(NN)(PP)]^+$, exploits *topological constraints* [130–133] to form a stable heteroleptic complex also in presence of NN and PP ligands, both of large size. This idea was firstly reported in 1983 by Sauvage and coworkers who prepared a Cu(I) complex containing two different phenanthrolines. The goal was the use of a macrocyclic phenanthroline to avoid the formation of the homoleptic species: pairing of two of these macrocycles in the same Cu(I) metal core is topologically impossible and "frustrated" dicoordinated $[Cu(\mathbf{phen})]^+$ is intrinsically unstable in solution, thus the system rearranges towards a tetracoordinated configuration. Furthermore, following the same maximum site occupancy rule, also the formation of the second competing species, *i.e.*, the homoleptic complex based on the other ligand, is prevented [103]. Accordingly, the preferential configuration is the mixed ligand coordination compound (Figure 2.3). The *topological constraint* in Cu(I) complexes was then applied in many rotaxanes, catenanes, molecular machines, and it prompted the beginning of mechanically interlocked molecules [134, 135].

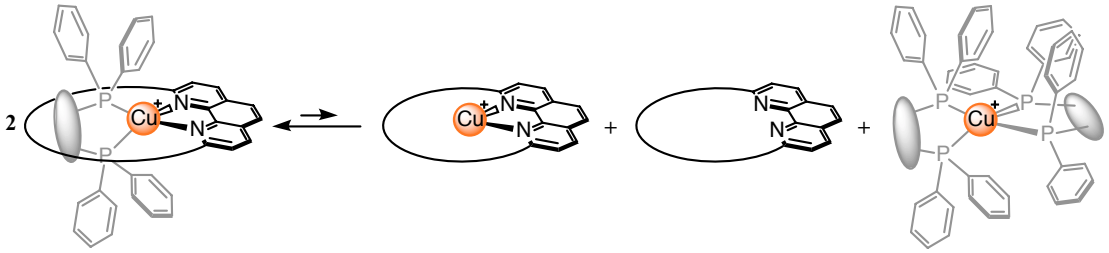

Figure 2.3. Dynamic equilibrium evidenced in solution between $[Cu(NN)(PP)]^+$ and its corresponding homoleptic complexes, in the presence of a macrocyclic ligand. Adapted from [75].

The series of Cu(I) complexes reported in Section 2.3, incorporate different macrocyclic ligands and has been designed to exploit the *topological constraint* and increase the stability of these heteroleptic coordination systems.

2.0.5 Temperature dependent emission

In pure fluorescent emitters (*i.e.*, most organic luminophores), the spin multiplicity is preserved, the luminescence is due to the $S_1 \longrightarrow S_0$ radiative deactivation (Figure 2.4, a). On the other hand, common luminescent coordination compounds, such as Ir(III) or Ru(II) complexes, emit from the triplet excited state. The phosphorescence mostly arises from the population of the lowest $^3T_1$ by the conversion of higher lying singlets, because the formation of triplet by direct light absorption is spin forbidden. The $S_1 \longrightarrow T_1$ ISC process is kinetically competitive only in the presence of a significant SOC (see Paragraph 1.1.1) induced by the metal atom [55, 136–139]. By partially mixing the character of singlet and triplet state, the SOC increases the radiative constant of the already forbidden deactivation from the triplet state (Figure 2.4, b) and splits the triplets by contributing differently in the spin mixing.

First row transition metals possess a less effective SOC, therefore they tipically show much longer triplet lifetimes. The longer lifetime, in presence of a reduced $\Delta E(S_1 - T_1)$ separation ($< 3000\ cm^{-1}$; Figure 2.4, c), may turn the triplet in a reservoir for the thermal repopulation of the S_1 state at room temperature. Accordingly, emission comes, to a major extent, from the singlet level (*singlet harvesting*) but its intrinsic lifetime is prolonged via the thermal equilibration with the longer-lived triplet. According to the Boltzmann distribution, depending on the energy difference between the two states, both the singlet and the triplet can contribute to the deactivation process. It is obvious that, the closer the triplet states to the singlet, the higher is the reverse-ISC and consequently the TADF efficiency.

With the assumption of degenerate triplets and a fast equilibration among the states – in Cu(I) complexes the energy splitting among the triplets is a few cm^{-1} – it is possible to express the dependence of the luminescence decay on the temperature with the following equation:

$$\tau_{exp} = \frac{3 + e^{-\frac{\Delta E_{(S_1-T_1)}}{k_b T}}}{\frac{3}{\tau_{(T_1)}} + \frac{1}{\tau_{(S_1)}} e^{-\frac{\Delta E_{(S_1-T_1)}}{k_b T}}} \tag{2.1}$$

Where τ_{exp} represents the measured excited-state lifetime (see Appendix A for details),

$\Delta E_{(S_1-T_1)}$ is the energy separation between the lowest excited singlet and triplet states of the copper complexes, $\tau_{(S_1)}$ and $\tau_{(T_1)}$ are the related excited-state lifetimes, T is the temperature, and k_b is the Boltzmann constant.
By applying equation 2.1 to fit the decays, the deactivation rate constant of the involved states and their energy separation can be determined. The experimental procedure is based on the fact that, in the presence of TADF, the emission is temperature dependent: as the temperature is enhanced, the excited-state lifetimes decrease and the emission bands are blue-shifted.
The TADF mechanism has been studied as part of the PhD activity, for it's key role in singlet harvesting electroluminescent devices (*e.g.*, OLEDs), as described in Paragraph 1.2.1. The key point of TADF materials in electricity-to-light conversion devices is the capability of collecting all the excitons formed by charge injection (singlet and triplets), hence OLEDs with almost 100 % internal quantum efficiency can be obtained [65, 140].
Cu(I) complexes have been demonstrated to be low cost and efficient TADF materials, with a singlet-triplet energy difference in the range of 300-1300 cm^{-1} and an excited-state lifetime of the luminescent species of ≈ 1-20 µs at room temperature [13, 63].
We observed TADF in different types of complexes (*i.e.*, dinuclear, mononuclear and pseudorotaxanes), in various media, as PMMA matrix, pure powders (Section 2.1) and CH_2Cl_2 solution. While the first two matrices afforded comparable results, in the latter, luminescence and decays are strongly affected by the solid-liquid phase variation, so that the rigidochromic effects prevail on the temperature dependent emission (Figure 2.46).

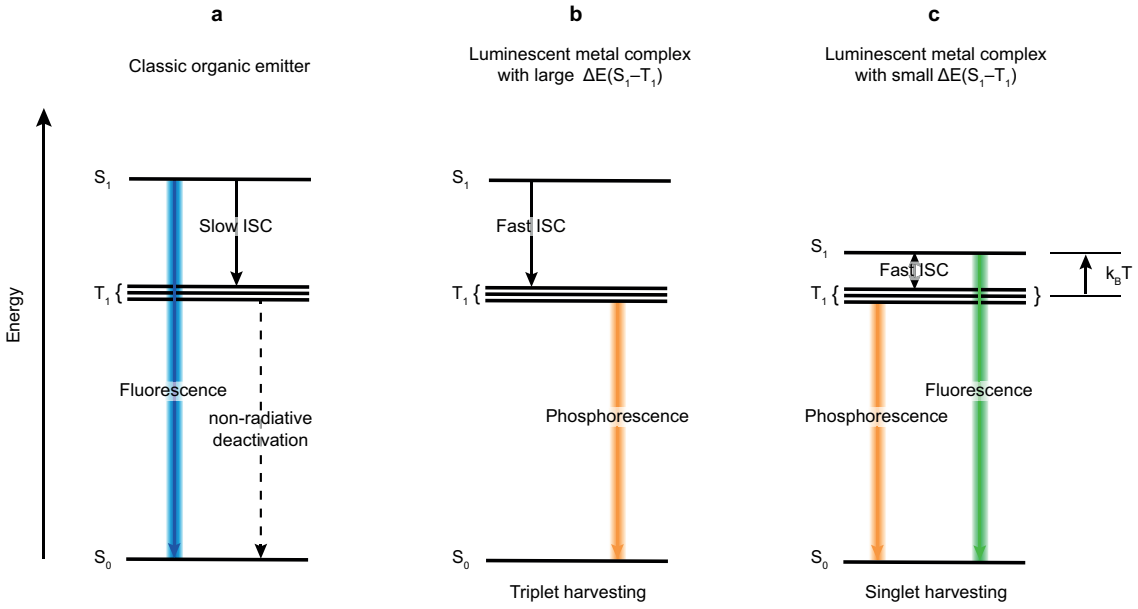

Figure 2.4. Schematic representation of luminescence process. (a) Pure fluorescent emitter, in which triplet state non-radiative deactivation prevails. (b) Phosphorescent emitter (*e.g.*, organic molecule, metal complex) with large $\Delta E(S_1 - T_1)$ energy difference. The fast ISC promote the S_1 to T_1 transition, thus all the excited states may be converted in triplets. (c) Thermally activated delayed fluorescence (TADF) emitter. The $\Delta E(S_1 - T_1)$ separation is small, hence at room temperature the k_BT is sufficient to repopulate S_1 from T_1, through a reverse ISC. At low temperature, with reduced k_BT contribution, the phosphorescence is observed. All the excited states are collected to the triplets also in the case of TADF emitter since the fast $S_1 \longrightarrow T_1$ ISC process.

2.1 The limits of the [Cu(NN)(PP)]$^+$ complexes: pristine phenanthroline

This Section focusses on which are the main limits of Copper(I) heteroleptic complexes with phenanthroline derivatives and diphosphine ligands, as far as luminescence is concerned. To start with, we analyzed the effects played by the crystal structure and the type of diphosphine ligand on the ground and lowest electronic excited state.
In a previous paper, we carried out a systematic investigation of the thirty heteroleptic Cu(I) complexes which, in principle, are obtainable from the combination of five NN and six PP ligands [75]. By means of ^{1}H and ^{31}P NMR spectroscopy, we demonstrated that, whatever the diphosphine moiety, highly stable heteroleptic [Cu(NN)(PP)]$^+$ complexes are obtained only from 2,9-unsubstituted-1,10-phenantholines [75]. When substituents at the 2,9 positions of the NN ligands provide limited steric hindrance – *e.g.*, 2,9-dimethyl-1,10-phenanthroline (**dmp**), and 2,9-diphenethyl-1,10-phenanthroline (**dpep**) – the related complexes are stable in the solid state, but a dynamic ligand exchange is systematically observed in solution, with the homoleptic/heteroleptic ratio highly dependent on the diphosphine ligand. The outcome of the ligand exchange reactions is mainly influenced by the relative thermodynamic stability of the different possible complexes [75]. Passing to bulky substituents on the "sentinel" 2,9-NN positions (*e.g.*, 2,9-diphenyl-1,10-phenanthroline, **dpp**) only homoleptic [Cu(NN)$_2$]$^+$ and [Cu(PP)$_2$]$^+$ complexes are obtained, whatever the diphosphine ligand [75].
With the aim of excluding the detrimental dynamic ligand exchange and deal with complexes exhibiting the highest possible stability in solution, we chose pristine 1,10-phenanthroline (**phen**) and 4,7-diphenyl-1,10-phenanthroline (**Bphen**) as NN ligands.

2.1.1 The series of complexes considered

To correlate the structure with the electronic properties, ten [Cu(NN)(PP)]$^+$ are studied. The two NN ligands selected (**phen** and **Bphen**) have been combined with five diphosphines which differ for the number of carbon atoms connecting the two P atoms, bis(diphenylphosphino)methane (dppm), 1,2-bis(diphenylphosphino)ethane (dppe), 1,3-bis(diphenylphosphino)propane (dppp), 1,2-bis(diphenylphosphino)benzene (dppb), and bis[(2-diphenylphosphino)phenyl]ether (POP or dpePhos), as depicted in Figure 2.5.
The small PP bite angle of dppm (72°) enables only the formation of binuclear complexes (*i.e.*, each ligand connecting two copper ions) whereas the other diphosphine analogues (natural PP bite angle in the range 85–102°) yield mononuclear complexes [74].
A detailed study of the photophysical and electrochemical properties, with the fundamental support of theoretical calculations and X-ray diffraction (XRD) is carried out. The results and discussion given in this section are essentially following the ones given in [141].

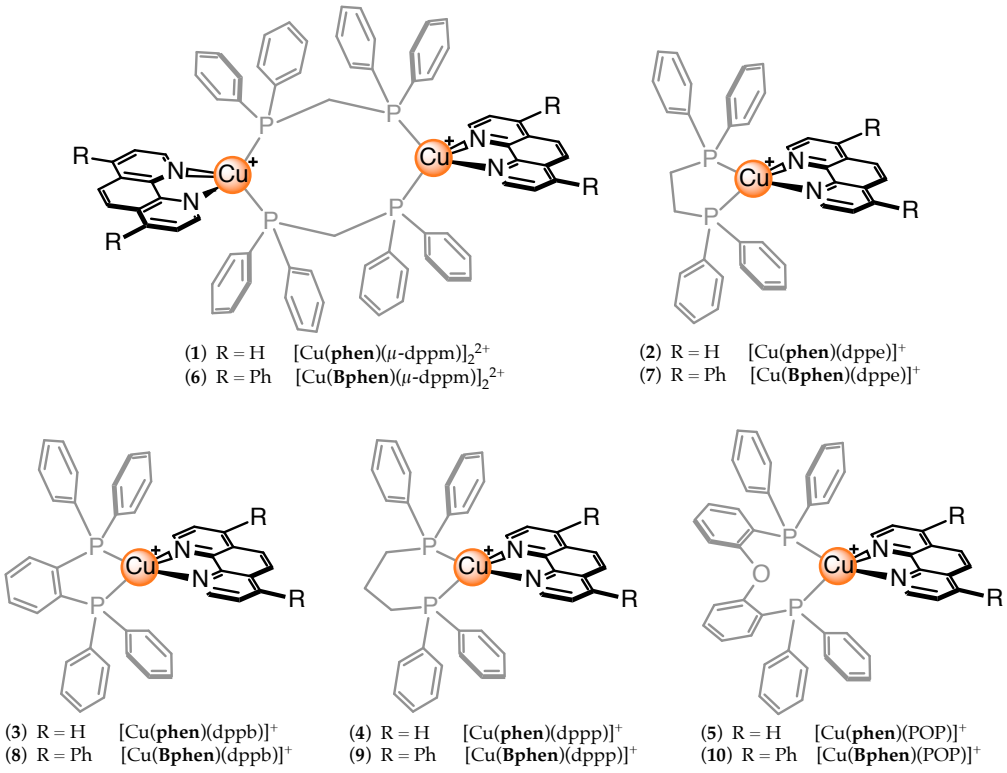

Figure 2.5. Heteroleptic $[Cu(NN)(PP)]^+$ complexes **1-10** as $[BF_4]^-$ salt.

2.1.2 Ground-state structural analysis

The purpose of this Section is not just expanding the database of photoactive Cu(I) complexes available in the literature, but also providing a more comprehensive rationale of the structural, electronic, and luminescence properties of two selected classes of $[Cu(NN)(PP)]^+$ systems, in order to consolidate the general understanding of the electronic properties of this important class of coordination compounds.

To the best of our knowledge, the emission properties of at least six compounds out of the ten systematically investigated here have been discussed, at least in part, earlier, namely, $[Cu(\mathbf{phen})(\mu\text{-dppm})]_2^{2+}$ [142–144], $[Cu(\mathbf{phen})(dppe)]^+$ [145, 146], $[Cu(\mathbf{phen})(dppb)]^+$ [25, 147], $[Cu(\mathbf{phen})(POP)]^+$ [25, 48–50, 52, 59], $[Cu(\mathbf{Bphen})(dppb)]^+$ [148], $[Cu(\mathbf{Bphen})(POP)]^+$ [50, 149–151].

The analysis of the ground-state geometry of $[Cu(NN)(PP)]^+$ complexes is somewhat challenging because, as already evidenced by Kubiček and coworkers [59], different crystal structures may be found in the literature for the same compound. This suggests that the molecular structures of Cu(I) complexes are strongly influenced by several factors (*e.g.*, counterions, solvent used for crystallization, intramolecular and intermolecular π-interactions, etc.), and many virtually isoenergetic minima can be found by slightly changing the crystallization conditions.

This unconventional behavior prompted us to investigate the five $[Cu(\mathbf{phen})(PP)]^+$ complexes (*i.e.*, with bare phenanthroline ligand) by Density Functional Theory (DFT) calculations at the M06 level of theory [153, 154] (see the Appendix A for details). The PBE0 functional was also tested with the same aforementioned basis set, but the optimized geometries were unsatisfactory, when compared to the experimental X-ray structures. In fact, copper(I) complexes usually adopt very flexible coordination geometries since

the metal center has a d^{10} electronic configuration with no net ligand-field stabilization energy due to d–d orbital splitting. Therefore, steric factors, noncovalent interactions, and also crystal packing strongly dictate the structure of this class of complexes. This is the reason why the M06 functional, characterized by higher accuracy for interactions dominated by medium-range correlation energy (*e.g.*, van der Waals attractions and aromatic π-stacking) can provide more reliable results than PBE0 in describing the ground state structure of d^{10} Cu(I) complexes [153, 155–157].
In the top part of Figure 2.6 is reported a comparison between different X-ray structures found in the literature for [Cu(**phen**)(dppb)]$^+$ (a, a') and [Cu(**phen**)(POP)]$^+$ (b, b'), as representative examples of the investigated series [25, 48, 49, 75]. In the bottom of the two panels of Figure 2.6 are reported the same comparison, but adding the DFT calculated geometries to the corresponding X-ray structures indicated above. By determining the root-mean-square deviation (RMSD) of all atomic positions, it is possible to estimate the quality of the theoretically evaluated geometries calculated by the M06 or PBE0 functionals. In fact, the RMSD between the M06 calculated structures and the X-ray geometries is comparable to that between the X-ray structures of identical compounds from different crystals (≈0.5 Å for both dppb- and POP-based complexes). Larger deviations are observed when the PBE0 structures are compared to the experimental ones (RMSD ≈0.8 Å). All these structural discrepancies are attributable to different π-stacking interactions or to different ways of modeling them. In the case of [Cu(**phen**)(dppe)]$^+$, where no intramolecular π-interactions are observed, the RMSD between the X-ray, the PBE0- and M06-calculated ones is only 0.53 Å in all the cases (Figure 2.7).

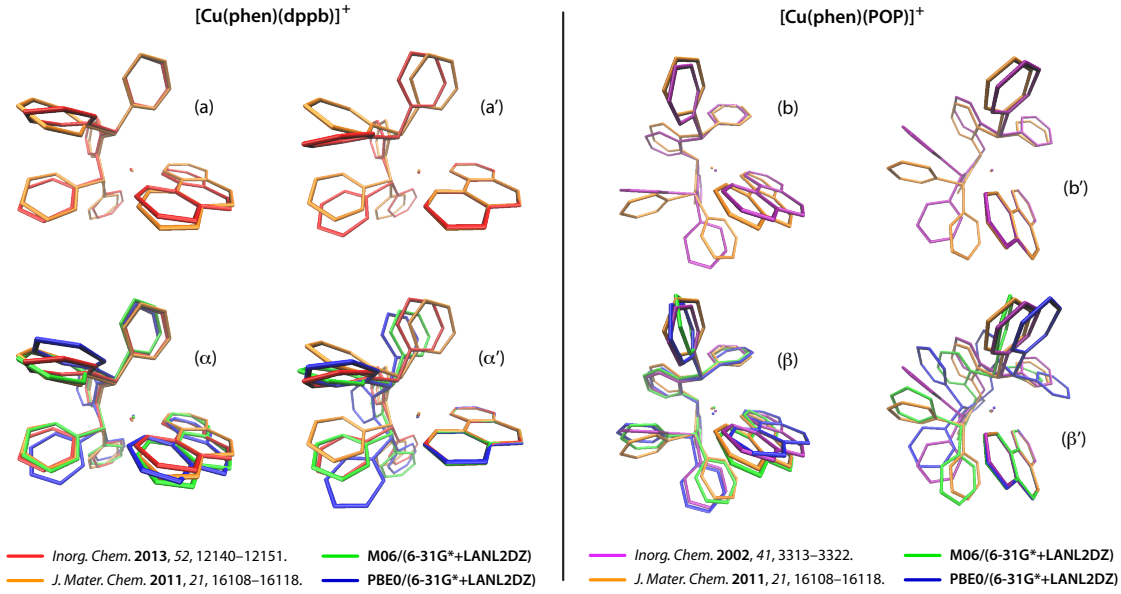

Figure 2.6. Latin letters: superimposition of different X-ray crystal structures of [Cu(**phen**)(dppb)]$^+$ (a, a') and [Cu(**phen**)(POP)]$^+$ (b, b'). Greek letters: comparison between experimental and theoretically calculated structures. All structures are superimposed by minimizing the RMSD of all atomic positions (a, α and b, β) or by maximizing the superposition of the phenanthroline ligands alone (a', α' and b', β'), which enables a more refined comparison between the molecular structures. All RMSD calculations, optimizations and visualizations were performed by VMD 1.9.1 [152]. Hydrogen atoms are excluded from the statistic and omitted in the figure.

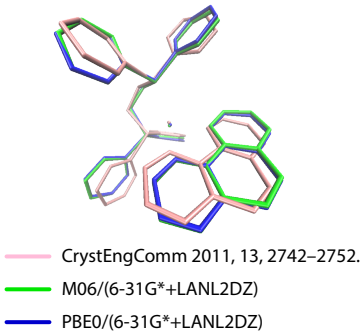

Figure 2.7. Superimposition of different experimental and theoretical structures of [Cu(**phen**)(dppe)]$^+$. All structures are superimposed by minimizing the RMSD of all atomic positions, except hydrogen atoms. All RMSD calculations, optimizations and visualizations were performed by VMD 1.9.1 [152].

Herein, the M06 functional is adopted to theoretically investigate both the structural and electronic properties of [Cu(**phen**)(PP)]$^+$ compounds. We limit such investigations only to this series because, for the [Cu(**Bphen**)(PP)]$^+$ family, intermolecular π-interactions of the phenyl groups in the 4,7-positions of the phenanthroline ligand are so extensive that calculations on a single Cu(I)-complex unit could not adequately model the actual properties of such compounds, particularly in the solid state.
The chelating PP ligands investigated in this work are characterized by a relatively wide range of P–Cu–P bite angles, from 87° to up to 135°, observed for the dinuclear complexes with the dppm ligand. In an effort to assess the effect of this parameter on the bond lengths and angles involving the metal center (and hence on the overall structure), we have theoretically investigated the two simplest possible [Cu(NN)(PP)]$^+$ analogues of the investigated complexes, namely, [Cu(**phen**)$(PX_3)_2$]$^+$, where X = H or CH_3. The data reported in Figure 2.8 are obtained by gradually changing the PP bite angle of the [Cu(**phen**)$(PX_3)_2$]$^+$ model complexes and by performing a geometry optimization of the other structural parameters (keeping the P–Cu–P bite angle frozen and imposing a C_2v point group).
Such a simple model reproduces well the trends of the corresponding structural parameters experimentally measured by X-ray diffraction analysis on a collection of around twenty [Cu(NN)(PP)]$^+$ complexes available in literature (Figure 2.8 and Table 2.1). It should be emphasized that the unrealistic behavior theoretically predicted for the Cu–P bond length at low P–Cu–P angles in the model compounds (*i.e.*, a spurious elongation of the Cu–P distance) is basically due to the steric hindrance between the phosphine ligands that cannot be mitigated due to the overall C_{2v}-symmetry constraint of the complexes (Figure 2.8). On the contrary, in real complexes, different substituents on the phosphorus atoms and additional degrees of freedom of the ligands (*e.g.*, rocking, wagging) allow an almost constant Cu–P length of 2.25 ± 0.02 Å to be preserved, regardless of the PP bite angle, as it also happens for the model compounds, but only at larger P–Cu–P angles (Figure 2.8 and Table 2.1).
On the contrary, the model compounds very well reproduce the trend of the Cu–N bonds as a function of the P–Cu–P bite angles. In fact, when the P–Cu–P angle increases, the Cu–N bond length also increases (Table 2.1 and Figure 2.8). Moreover, almost a perfect match is observed when comparing the experimental phenanthroline bite angles

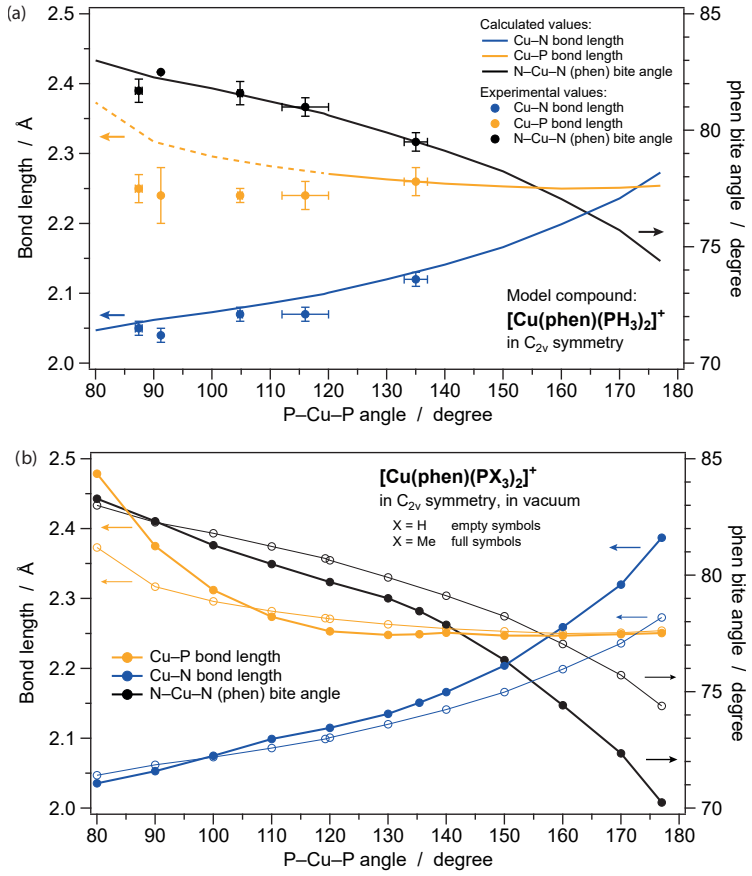

Figure 2.8. (a) Key structural parameters of the model compounds [Cu(**phen**)(PP)]$^+$ in C_{2v} symmetry (full lines); data refer to a relaxed scan of the P–Cu–P angle at the M06 level of theory, in vacuum (see Figure (b)). Experimental data are taken from X-ray structure reported in Table 2.1 (circles with relative errors). (b) Key structural parameters of the model compounds [Cu(**phen**)(PX_3)$_2$]$^+$ (where X = H or CH_3). Data refer to relaxed scans of the P–Cu–P bite angles within a C_{2v}-symmetry constraint. Calculations are performed at the M06/6-31G(d) and LANL2DZ(Cu) level of theory, in vacuum. It should be emphasized that, due to the steric hindrance of the phosphine ligands within the imposed C_{2v} symmetry, a spurious elongation of the Cu–P bonds is observed at small P–Cu–P angles; accordingly, the phenomenon is more pronounced for the bulkier PMe_3 ligand, respect to the smaller PH_3 ones.

and theoretically predicted one of the model complexes (Figure 2.8). Notably, such N–Cu–N angle can be expressed as a function of the above-mentioned Cu–N bond length, assuming that the phenanthroline ligand is rigid (Figure 2.9, inset); consequently, as the P–Cu–P angle increases, a reduction in the **phen** bite angle is observed. Taken in concert, the above findings unambiguously show the central role played by the P–Cu–P bite angle in dictating the overall structure of [Cu(NN)(PP)]$^+$ complexes.

DFT methods were also used to calculate the minimum-energy geometries of all the complexes belonging to the [Cu(**phen**)(PP)]$^+$ series; the structures were fully optimized in vacuum without any symmetry constraint. A direct comparison between experimentally available key structural parameters for these complexes (data obtained from Table 2.2) and those theoretically computed at the M06 level of theory is reported in Table 2.1. A very good agreement is observed as far as the Cu–N and Cu–P bond lengths are concerned, and even the bite angles of the phenanthroline and diphosphine ligands are

Table 2.1. Key structural parameters of the complexes belonging to the [Cu(**phen**)(PP)]$^+$ series (where PP = dppb, dppe, POP and μ-dppm). Data are taken from X-ray crystal structures reported in literature and available through the Cambridge Crystallographic Data Center (CCDC).[a]

Type of PP ligand	Cu–N (Å)	Cu–P (Å)	N–Cu–N (°)	P–Cu–P (°)	phen–PCuP dihedral angle (°)	CCDC
dppb	2.040 – 2.049	2.238 – 2.249	81.92	88.11	85.58	953017
	2.038 – 2.053	2.240 – 2.257	81.99	87.14	87.37	802648
	2.059 – 2.063	2.260 – 2.280	81.06	86.96	87.84	826035
	2.05 ± 0.01	**2.25 ± 0.02**	**81.7 ± 0.5**	**87.4 ± 0.6**	**87 ± 1**	
dppe	2.041 – 2.042	2.239 – 2.245	82.46	91.57	82.76	796689
	2.04 ± 0.01	**2.24 ± 0.04**	**82.5**	**91.6**	**83**	
dppp	2.058 – 2.077	2.230 – 2.245	81.50	104.56	81.59	844532[b]
	2.046 – 2.073	2.234 – 2.236	81.91	104.68	79.18	”
	2.060 – 2.066	2.228 – 2.244	81.88	105.08	80.75	899896[b]
	2.057 – 2.086	2.232 – 2.239	81.27	104.77	77.74	”
	2.07 ± 0.01	**2.24 ± 0.01**	**81.6 ± 0.5**	**104.8 ± 0.4**	**80 ± 3**	
POP[c]	2.063 – 2.071	2.231 – 2.261	80.83	110.81	87.66	177684
	2.063 – 2.070	2.206 – 2.283	81.02	119.18	89.09	802647
	2.073 – 2.079	2.235 – 2.271	80.89	113.52	87.80	224679
	2.054 – 2.079	2.195 – 2.270	81.59	117.50	88.63	1498327[b]
	2.055 – 2.109	2.195 – 2.270	80.85	117.50	89.52	”
	2.07 ± 0.01	**2.24 ± 0.02**	**81.0 ± 0.4**	**116 ± 4**	**88 ± 1**	
μ-dppm	2.114 – 2.136	2.235 – 2.286	79.80	134.34	84.89	1188267
	2.111 – 2.124	2.231 – 2.269	79.21	133.33	83.95	296675
	2.100 – 2.134	2.246 – 2.279	79.41	135.58	81.55	198781
	2.109 – 2.116	2.236 – 2.272	79.40	135.19	85.25	1028806
	2.12 ± 0.01	**2.26 ± 0.02**	**79.5 ± 0.4**	**134 ± 2**	**84 ± 3**	

[a] In bold are reported the mean values of the structural parameters taken from the different available conformer. [b] Complex is co-crystallized in two different structure. [c] Cu–O has a non-bonding average distance of 3.14 ± 0.07 Å (respectively 3.205, 3.085, 3.025 and 3.182 Å for the co-crystal).

reproduced with great accuracy by the DFT optimization (Table 2.2). Also the interplanar angle between the phenanthroline and the plane defined by the P–Cu–P coordinates is in excellent agreement with the experimental one, since it is always within the interval defined by different conformers (with the only exception of [Cu(**phen**)(dppe)]$^+$ (Figure 2.7) tiveness of the adopted theoretical model.

2.1.3 Ground-state electronic properties

With the help of the same model complexes mentioned above, we also tried to rationalize the ground-state electronic properties of the investigated [Cu(**phen**)(PP)]$^+$ series. In Figure 2.10 (a) the energy diagram of the frontier molecular orbitals of the [Cu(**phen**)(PMe_3)$_2$]$^+$ model complex are reported, again as a function of the P–Cu–P

Table 2.2. Key structural parameters of the fully-optimized complexes belonging to the [Cu(**phen**)(PP)]$^+$ series (where PP = dppb, dppe, POP and μ-dppm). All the geometry optimizations were performed at the M06 level of theory in vacuum (see Appendix A for further details). For the sake of comparison, the mean values of the same structural parameters taken from X-ray experimental data are reported in bold (from Table 2.1).

	Cu–N	Cu–P	N–Cu–N	P–Cu–P	phen–PCuP
Type of PP ligand	bond length (Å)		angle (°)		dihedral angle (°)
dppb	**2.05 ± 0.01**	**2.25 ± 0.02**	**81.7 ± 0.5**	**87.4 ± 0.6**	**87 ± 1**
	2.072 – 2.087	2.271 – 2.284	81.0	86.9	85.5
dppe	**2.04 ± 0.01**	**2.24 ± 0.04**	**82.5**	**91.2**	**83**
	2.059 – 2.093	2.265 – 2.283	81.2	91.6	72.8
dppp	**2.07 ± 0.01**	**2.24 ± 0.01**	**81.6 ± 0.5**	**104.8 ± 0.4**	**80 ± 3**
	2.078 – 2.103	2.238 – 2.273	80.6	101.8	85.1
POP	**2.07 ± 0.01**	**2.24 ± 0.02**	**81.0 ± 0.4**	**116 ± 4**	**88 ± 1**
	2.101 – 2.108	2.243 – 2.318	80.1	116.2	89.2
μ-dppm	**2.12 ± 0.01**	**2.26 ± 0.02**	**79.5 ± 0.4**	**134 ± 2**	**84 ± 3**
	2.141 – 2.157	2.255 – 2.286	78.5	137.7	85.9

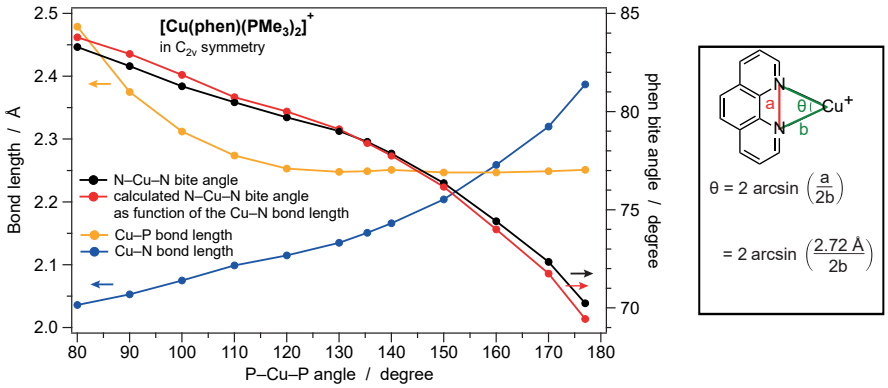

Figure 2.9. Calculated N–Cu–N bite angles (red line and dots) as function of the Cu–N bond length (assumed constant the distance between nitrogens – 2.72 Å – upon variation of the P–Cu–P angle); predicted data are compared to the real ones obtained by DFT calculations (black line and dots). Inset: Trigonometric derivation of the mathematical function relating the phenanthroline N–Cu–N bite angle to the corresponding Cu–N bond length.

angle. At low P–Cu–P angle (*i.e.*, < 135°) the HOMO is a b_1 orbital strongly characterized by a σ^* bond between the d_{xz} orbital of the copper center and the lone-pair orbitals on the phosphine ligands. Such molecular orbital is more and more stabilized as the P–Cu–P angle increases. As a consequence, when P–Cu–P angles are larger than 135°, an orbital flipping occurs and the HOMO becomes an a_1 orbital, which on the contrary is destabilized by an increase in the P–Cu–P angle. Such an orbital is essentially characterized by a nonbonding interaction between the copper $d_{x^2-y^2}$ orbital and the lone-pair orbitals on the phosphine ligands (Figure 2.10 (a)). On the contrary, the variation of

the P–Cu–P angle has virtually no effects on the nature and energy of the LUMO and LUMO+1, since they are both localized on the π^* orbitals of the phenanthroline ligand. As a consequence, mainly due to HOMO stabilization, the HOMO–LUMO energy gap is expected to increase by increasing the P–Cu–P angle up to an angle of 135–140°, when it reaches a maximum value (*i.e.*, ≈ 4.32 eV, see Figure 2.10 (a)). Then, due to orbital flipping, the HOMO-LUMO energy gap inverts its trend and slightly decreases, if the P–Cu–P angle is further increased beyond 140° (Figure 2.10 (a)).

The scenario depicted by the simple model described above is anyhow extremely effective in explaining what is observed in the real case for the [Cu(**phen**)(PP)]$^+$ series. In fact, as shown in Figure 2.10 (b), the same findings already discussed for the model [Cu(**phen**)(PMe_3)$_2$]$^+$ series are also qualitatively observed in real complexes. Actually, in the case of the [Cu(**phen**)(PP)]$^+$ series, there is no complex displaying a PP bite angle well beyond the critical value of 135°. Notably, however, the dinuclear complex [Cu(**phen**)(μ-dppm)]$_2^{2+}$ (with an experimental PP bite angle of 134° and a theoretically predicted one of 138°, Table 2.2) already undergoes the orbital flipping described in Figure 2.10. In fact, while all the other complexes of the series exhibit a b_1-type HOMO, in the case of [Cu(**phen**)(μ-dppm)]$_2^{2+}$ such orbital is the HOMO–1 and the HOMO has the same topology of the a_1 orbital of the [Cu(**phen**)(PMe_3)$_2$]$^+$ model compound (compare Figure 2.10 (a) and (b)). This orbital flipping explains the different absorption profile of [Cu(**phen**)(μ-dppm)]$_2^{2+}$, with respect to the other complexes of the series (see below). In line with our model, also HOMO stabilization is observed upon increasing the PP bite angles within the phen series, as predicted for P–Cu–P angles within the range of 80–140° (compare again Figure 2.10 (a) and (b)). In fact, the [Cu(**phen**)(PP)]$^+$ complexes

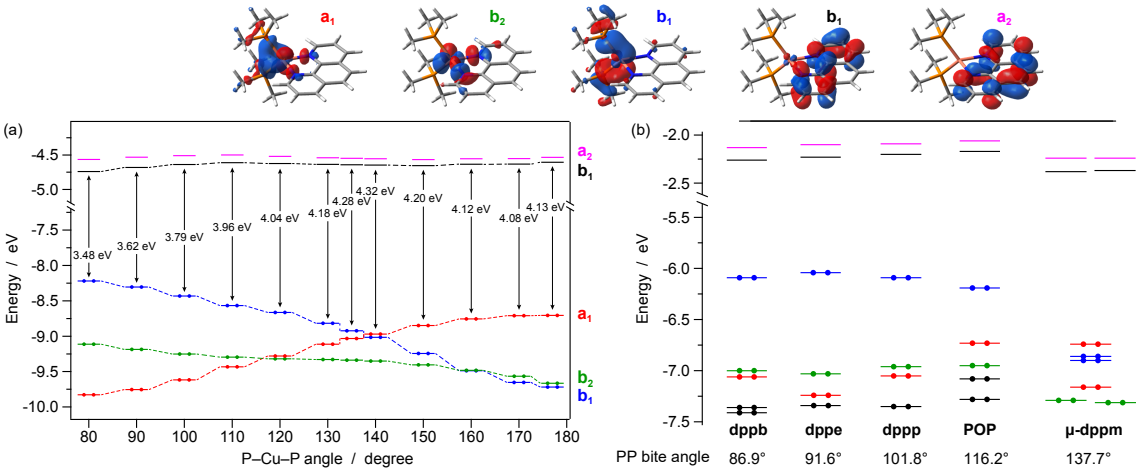

Figure 2.10. (a) Energy diagram showing the frontier Kohn-Sham molecular orbitals of the model compound [Cu(**phen**)(PMe_3)$_2$]$^+$ in vacuum (C_{2v} symmetry). Data refer to relaxed scans of the P–Cu–P angle. For each type of orbital reported in the graph, the associated symmetry and the corresponding isosurface is also displayed (isovalue = 0.04 $e^{1/2}$ $bohr^{-3/2}$). (b) Energy diagram showing the frontier Kohn-Sham molecular orbitals of the five complexes belonging to the [Cu(**phen**)(PP)]$^+$ series. Data refer to PCM-M06 single-point calculations in CH_2Cl_2, using molecular geometry previously optimized in vacuum (see the Appendix A for details). Each frontier molecular orbital belonging to the real [Cu(**phen**)(PP)]$^+$complexes has been associated to the ones already described for the model compound [Cu(**phen**)(PMe_3)$_2$]$^+$ in C_{2v} symmetry (according to its nature and topology).

having smaller PP bite angles (*i.e.*, those with PP = dppb, dppe and dppp) display higher lying HOMOs, while such an orbital is more stabilized in $[Cu(\mathbf{phen})(POP)]^+$ and even more in $[Cu(\mathbf{phen})(\mu\text{-dppm})]_2^{2+}$ (PP bite angles of 116° and 138°, respectively). As a result, as the PP bite angle of the $[Cu(\mathbf{phen})(PP)]^+$ series increases, an increase in the HOMO–LUMO energy gap is also observed, according to the predictions and in very good agreement with electrochemical data.

2.1.4 Electrochemical properties

The electrochemical properties of the ten Cu(I) complexes were investigated in CH_2Cl_2 at 298 K by both cyclic voltammetry (CV) and Osteryoung square wave voltammetry (OSWV).[1] Experimental data are reported in Table 2.3 and Figure 2.11.
All the complexes exhibit an oxidation process centered on the Cu(I) metal ion, which is always irreversible, except in complexes displaying small P–Cu–P angles (*i.e.*, $[Cu(\mathbf{phen})(dppb)]^+$, $[Cu(\mathbf{phen})(dppp)]^+$ and $[Cu(\mathbf{Bphen})(dppb)]^+$), which show a quasi-reversible oxidation already at a scan rate of 0.1 V s^{-1}. Such a one-electron process is only lightly affected by the type of diamine ligand (**phen** or **Bphen**). The highest potentials are observed for POP and dppm compounds, indicating stronger structural rigidity.

The first reduction event is centered on the **phen**/**Bphen** ligands, and it is generally irreversible at a low scan rate. However, when the scan rate increases, especially in the

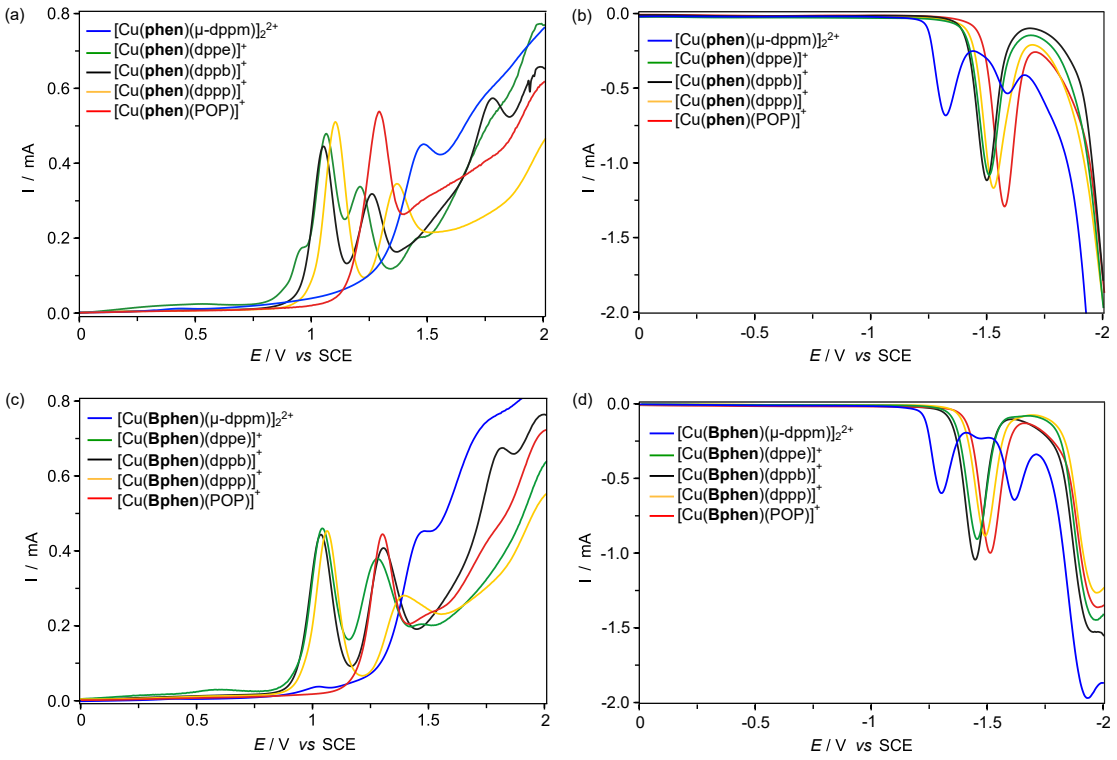

Figure 2.11. OSWVs of $[Cu(\mathbf{phen})(PP)]^+$ (anodic (a) and cathodic (b) scans) and of $[Cu(\mathbf{Bphen})(PP)]^+$ (anodic (c) and cathodic (d) scans) on a Pt electrode in CH_2Cl_2 + 0.1 M $[n\text{Bu}_4\text{N}][BF_4]$ at room temperature (OSWVs: frequency 20 Hz, amplitude 20 mV, step 5 mV).

[1] Electrochemistry has been performed by Béatrice Delavaux-Nicot's group, Laboratoire de Chimie de Coordination du CNRS in Toulouse, France.

Table 2.3. Selected electrochemical data and DFT energies of the FMOs for the [Cu(**phen**)(PP)]$^+$ and [Cu(**Bphen**)(PP)]$^+$ series in CH_2Cl_2.

	Electrochemical data[a] (V)			DFT calculated energies[b] (eV)		
	E_{Ox}	E_{Red}	ΔE_{Redox}	E_{HOMO}	E_{LUMO}	ΔE_{DFT}
[Cu(**phen**)(dppb)]$^+$	+1.05[c]	−1.50	2.55	−6.09	−2.26	3.83
[Cu(**phen**)(dppe)]$^+$	+1.04[d]	−1.53	2.57	−6.04	−2.23	3.81
[Cu(**phen**)(dppp)]$^+$	+1.07[c]	−1.57	2.64	−6.09	−2.20	3.89
[Cu(**phen**)(POP)]$^+$	+1.29	−1.58[e]	2.87	−6.19	−2.17	4.02
[Cu(**phen**)(μ-dppm)]$_2^{2+}$	+1.44	−1.35	2.79	−6.74	−2.38	4.36
[Cu(**Bphen**)(dppb)]$^+$	+1.03[c]	−1.46	2.49	-	-	-
[Cu(**Bphen**)(dppe)]$^+$	+1.03[d]	−1.46	2.49	-	-	-
[Cu(**Bphen**)(dppp)]$^+$	+1.06	−1.49	2.55	-	-	-
[Cu(**Bphen**)(POP)]$^+$	+1.28	−1.53	2.81	-	-	-
[Cu(**Bphen**)(μ-dppm)]$_2^{2+}$	+1.44[f]	−1.31	2.75	-	-	-

[a] Data refer to OSWV or CV experiments; ferrocene is used as internal reference (Fc^+/Fc = 0.55 ± 0.01 V vs. SCE). E_{Ox} is the first oxidation potential, E_{Red} is the first reduction potential, in V vs. SCE. The electrochemical energy gap ΔE_{Redox} is obtained from: $\Delta E_{Redox} = E_{Ox} - E_{Red}$. The HOMO and the LUMO energy levels can be calculated in eV using the following equations: $E_{LUMO} = -(E_{Red} + 4.8)$, $E_{HOMO} = -(E_{Ox} + 4.8)$. [b] Data refer to calculation performed in CH_2Cl_2 using a fully optimized structure in vacuum (see Appendix A), with the theoretical energy gap: $\Delta E_{DFT} = E_{LUMO} - E_{HOMO}$. DFT energies determined only for [Cu(**phen**)(PP)]$^+$ series. [c] Quasi-reversible process at 0.1 V s^{-1}.
[d] Shoulder at +0.93 V and peak at +1.44 V appear and increase during the experiment.
[e] Quasi-reversible at 1 V s^{-1}. [f] Minor peak at +1.01 V attributed to the formation of some traces of [Cu(**Bphen**)]$^+$, as already observed in similar cases (see [63]).

case of **phen** compounds, it can become quasi-reversible. The extension of the electronic conjugation in the **Bphen** is reflected in a decrease of the reduction potential (40–70 mV with respect to the **phen** analogues, Table 2.3).
Oxidation and reduction potentials show a good correlation with the energy of the frontier molecular orbitals, with the HOMO–LUMO energy gap being systematically higher than the ΔE_{Redox} of 1.2 ± 0.1 eV for all the reported complexes (Table 2.3). Only in the case of the binuclear compound [Cu(**phen**)(μ-dppm)]$_2^{2+}$ an overstabilization of the HOMO is observed, if compared to electrochemical data; however, the overall trend is respected.

2.1.5 Absorption spectra and vertical excitations

The absorption spectra of [Cu(**phen**)(PP)]$^+$ and Cu(**Bphen**)(PP)]$^+$ series at 298 K are depicted in Figure 2.12. Some of these compounds have been already reported in the literature (see Paragraph 2.1.2), and our results essentially confirm the previous experimental findings. Upon dissolution in air-equilibrated CH_2Cl_2, spectral shapes and intensities do not vary significantly after over 10 days in the dark at 298 K, confirming the expected stability in the absence of 2,9 substituents on the phenanthroline ligands (Figure 2.13) [75]. In the UV region, LC features of both the NN and PP ligands are predominant, while the bands observed in the visible spectral domain down to about 500 nm are attributed

to MLCT transitions involving the metal cation and the phenanthroline moieties [48, 49, 63, 74].
Interestingly, molar absorption coefficients of MLCT bands (λ > 350 nm) are generally higher for the **Bphen** complexes compared to the **phen** analogues. This enhancement is the highest for the dinuclear complex equipped with the dppm ligands.

In both series, the spectra of the POP complexes are remarkably blue-shifted compared to the three mononuclear analogues, confirming a trend observed earlier for other [Cu(NN)(PP)]$^+$ systems, which typically show blue shift as a function of the bulkiness of the ligands [74]. It must be also emphasized that the compounds with blue-shifted features (POP and dppm ligands) have the highest oxidation potentials, indicating a more rigid structure that disfavors flattening upon Cu(II) formation in the excited state [37]. Notably, the energy of the MLCT bands well correlates with the bite angle of the diphosphine ligands: as the PP bite angle increases, the energy of the MLCT absorption maximum increases (Figure 2.14). Time-dependent-DFT (TD-DFT) calculations, carried out on the fully optimized ground-state geometries of these complexes, further confirm the picture described above. In fact, a linear correlation is also observed by plotting the energy associated with the first singlet vertical excitation and the PP bite angle calculated by ground-state optimization (Figure 2.14, black dots and line). Such results are in line

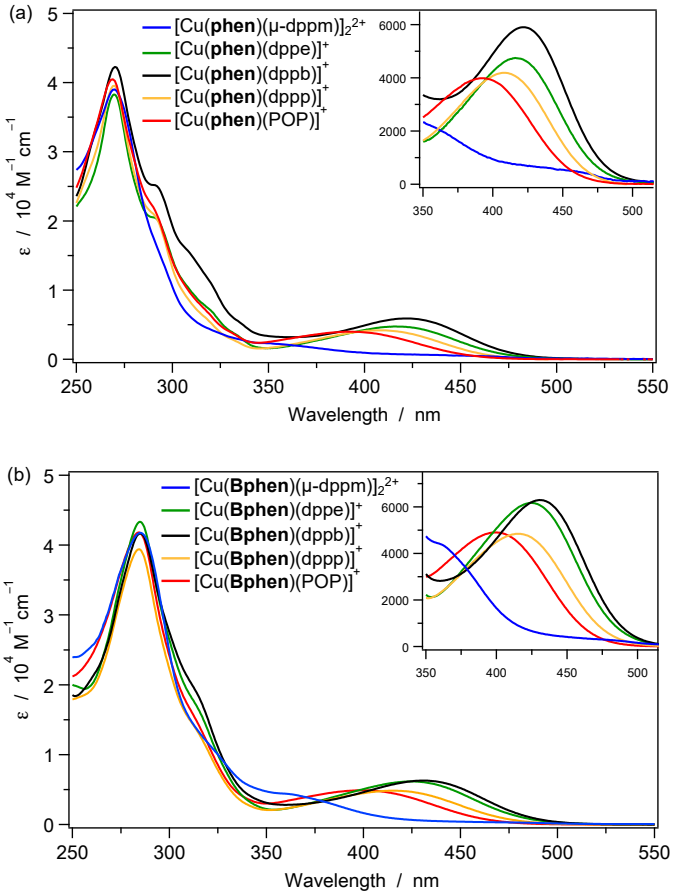

Figure 2.12. Absorption spectra of the ten [Cu(NN)(PP)]$^+$ complexes in CH_2Cl_2 solution at 298 K; (a) **phen** series, (b) **Bphen** series. For the sake of comparison, the molar absorption coefficients of the dinuclear complexes with PP = dppm is divided by two.

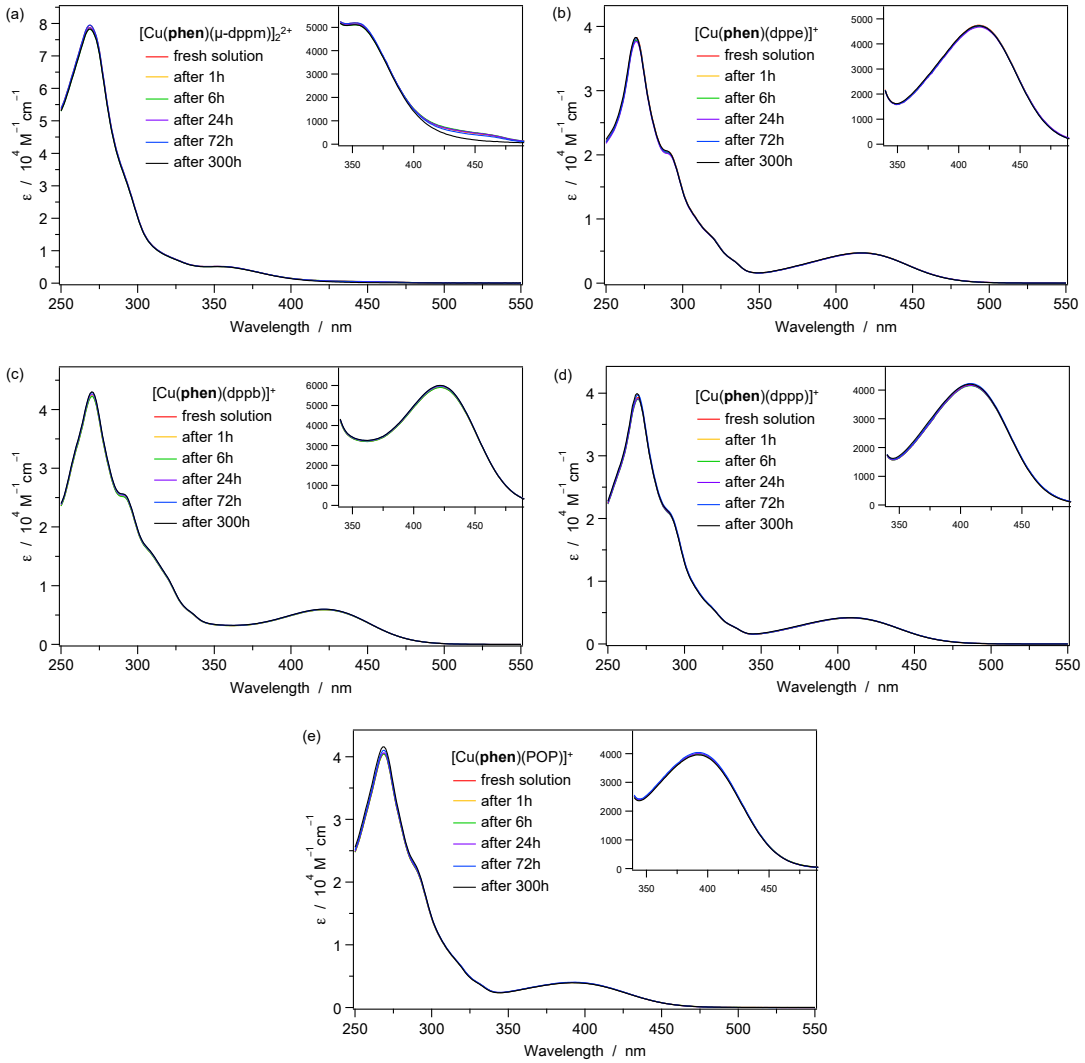

Figure 2.13. Absorption spectra of (a) [Cu(**phen**)(μ-dppm)]$_2$$^{2+}$, (b) [Cu(**phen**)(dppe)]$^+$, (c) [Cu(**phen**)(dppb)]$^+$, (d) [Cu(**phen**)(dppp)]$^+$, (e) [Cu(**phen**)(POP)]$^+$ in CH_2Cl_2 at 298 K taken at several time intervals after sample solubilization.

with the predicted increase in the HOMO–LUMO gap upon increasing the PP bite angle within this series of complexes (Table 2.3); a phenomenon that is mainly due to HOMO stabilization (Figure 2.14).

With the aim of more deeply rationalizing the ground-state absorption properties of these complexes and to further confirm the correlation observed above (Figure 2.14), we theoretically investigated the model complex [Cu(**phen**)(PMe_3)$_2$]$^+$ by TD-DFT calculations, to evaluate the lowest-lying singlet electronic transitions. The results are reported in Figure 2.15 for the lowest six excited states, which are named according to their symmetry and represented in terms of monoelectronic excitations, as in Figure 2.10.
In the [Cu(**phen**)(PMe_3)$_2$]$^+$ model compound, at low P–Cu–P angles (*i.e.*, < 130°), the lowest energy transition corresponds to a $b_1 \longrightarrow b_1$ mono-excitation, leading to the population of an A_1 excited state. Such a state is MLCT in nature and is mainly responsible of the unstructured absorption band experimentally observed in the [Cu(**phen**)(PP)]$^+$ series at around 350–500 nm (Figure 2.12 (a)).

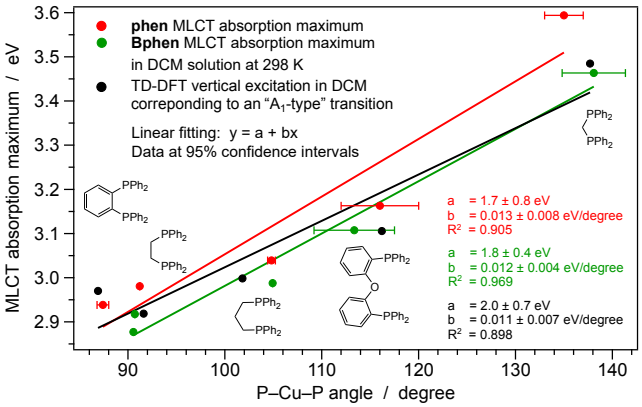

Figure 2.14. Linear correlation between the energy of the [Cu(**phen**)(PP)]$^+$ (red line) and [Cu(**Bphen**)(PP)]$^+$ (green line) MLCT absorption maximum and the PP bite angle of the chelating diphosphine ligand (data obtained from absorption spectra in CH_2Cl_2 and from X-ray crystal structures, respectively). Black line: Same correlation using theoretical data (*i.e.*, "A1-type" vertical excitation vs. PP bite angle calculated from the ground-state optimized geometry).

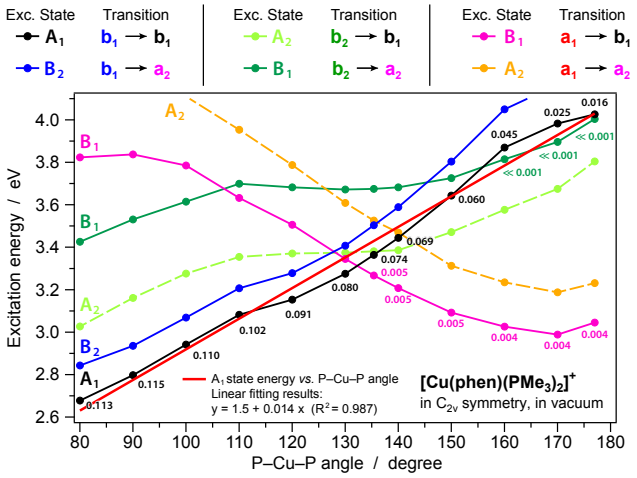

Figure 2.15. Lowest vertical excitations calculated for the model compound [Cu(**phen**)$(PMe_3)_2$]$^+$ in vacuum (C_{2v} symmetry), at different P–Cu–P angles. For each vertical excitation, the corresponding couple of orbitals involved in the transition is reported in the legend (top, according to the nomenclature used in Figure 2.10). Oscillator strength values are reported as small numbers inside the graph; transition to A_2 excited states are symmetry forbidden (dashed). The most intense transition is to the lowest A_1 excited state and its transition energy increases linearly with an increase in the P–Cu–P angles (see linear fitting – red line).

Following the theoretical evidences proposed by the [Cu(**phen**)$(PMe_3)_2$]$^+$ model, it should be emphasized that: (i) the energy of the excitation to the lowest A_1 excited state increases linearly with the P–Cu–P angle (see linear fitting in Figure 2.15); and (ii) the oscillator strength associated to such transition becomes weaker and weaker by increasing the P–Cu–P angle (Figure 2.15). Both these findings are in line with experimental data of the [Cu(**phen**)(PP)]$^+$ series. In fact, a decrease in both the wavelength maximum and in the molar absorptivity of the lowest MLCT band is observed upon increasing the PP bite angle along the series (Figure 2.12, (a) - inset). Another important point that is well described by the relatively simple model herein adopted regards the excited-state

scenario at high P–Cu–P angles (*i.e.*, > 130°). At such large P–Cu–P angles, the transition to the A_1 excited state is so destabilized that the excitation to B_1 ($a_1 \longrightarrow b_1$ transition) becomes the lowest in energy (Figure 2.15). This theoretical finding is able to justify the presence of a minor absorption tail at longer wavelength ($\lambda > 400$ nm) next to the main MLCT band ($\lambda \approx 345$ nm) of the experimental spectrum of the binuclear complex $[Cu(\mathbf{phen})(\mu\text{-dppm})]_2^{2+}$(Figure 2.12 (a)).

2.1.6 Luminescence properties

The ten $[Cu(\mathbf{phen})(PP)]^+$ and $Cu(\mathbf{Bphen})(PP)]^+$ complexes were investigated as powders, in CH_2Cl_2 (298 and 77 K) and Poly(methyl methacrylate) (PMMA) matrix (sample 1 wt%). The emission properties of some of these compounds have been already discussed, and our results confirm previous experimental findings [25, 48–50, 52, 59, 148–151], excluding those which misinterpreted the second harmonic of the excitation light as the emission of the complex [142, 148].
All key data are gathered in Tables 2.4 (solution and 77 K) and 2.5 (solid state). In CH_2Cl_2 solution, (faint) luminescence is observable only for the dinuclear complexes with dppm and the bulky POP chelator. PLQYs are of the order of 10^{-3}–10^{-4}. For all the other compounds, no luminescence is detected in room temperature solution. This result is in line with what was reported elsewhere for some of these compounds and is typical for homoleptic and heteroleptic Cu(I) compounds lacking substituents in the 2,9 phenanthroline positions [37, 48].
NN ligands of this type are the least effective in preventing the photoinduced distortion of these Cu(I) tetrahedral complexes to square planar excited-state geometries, which favor nonradiative deactivations [36]. This phenomenon is extensively described in the literature and is virtually prevented in a rigid matrix at 77 K, where all of the compounds exhibit emission bands with maxima in the range of 560–650 nm and associated lifetimes of ≈ 140–200 µs (Table 2.4 and Figure 2.16). Such bands are unstructured, which indicates a MLCT character; the observed blue-shift compared to 298 K (dppm and POP ligands) shows a limited geometric relaxation of the excited state [63]. **Bphen** compounds tend to be red-shifted and longer-lived compared to **phen** analogues. A detailed temperature dependent study is discussed below.
Luminescence spectra were recorded in PMMA matrix for all of the compounds (Figure 2.17 (b)). The PLQYs are below 5 % (and as low as 0.2 %) for the dppe, dppb, and dppp based Cu(I) complexes, regardless of the NN chelator; the dppm and POP systems show stronger emission, with PLQY in the range of 11–15 %. PLQYs are typically stronger in powders, *i.e.*, in the range of 35–45 % for the dppm (dinuclear) and POP systems (Table 2.5 and Figure 2.17 (a)).
We wish to emphasize that the emission intensity and the band position of powder samples can be substantially affected by the way the sample is selected or treated (*e.g.*, grinding) [56], as shown in Figure 2.18; therefore these measurements require particular care when comparisons among different compounds are made and rationalizations are attempted. This observation underpins the relevance of intermolecular interactions in the solid state, also affecting the excited state properties. It is also in line with the occurrence of non-negligible differences found in the X-ray crystal structures of the same compounds, which was already highlighted above.
The PLQY values along the two series appear to be scattered. The diagram in Figure

2.19 shows no linear correlations of emission energy (and PLQY) with the PP bite angle, differently from that observed for the absorption data (Figure 2.14, data from the $[Cu(\mathbf{phen})(PP)]^+$ series in PMMA 1 wt% matrix, Table 2.19).

However, there is a consistent trend between emission energies and PLQYs: red-shifting of the emission bands implies lower quantum yields. This phenomenon can hardly be attributed only to the energy gap law [120, 160, 161], because variations of PLQY are very large (0.2–45.3 %, data from Table 2.6 for both **phen** and **Bphen** series) while spectral shifts are rather limited (530–620 nm, *i.e.*, 2.34–2.00 eV). On the contrary, it can be supposed that excited-state relaxation processes are mainly responsible for these trends [36, 59].

Table 2.4. Photophysical data in CH_2Cl_2 at 298 K and in frozen solution at 77 K.

	CH_2Cl_2 at 298 K					CH_2Cl_2 at 77 K	
	λ_{MLCT} (nm)	ϵ_{MLCT} ($M^{-1}\,cm^{-1}$)	λ_{em} (nm)	ϕ_{em} [a] (%)	τ [b] (ns)	λ_{em} (nm)	τ_{av} [c] (µs)
$[Cu(\mathbf{phen})(dppb)]^+$	422	5910	–[d]			615	191
$[Cu(\mathbf{phen})(dppe)]^+$	416	4750	–[d]			652	161
$[Cu(\mathbf{phen})(dppp)]^+$	408	4190	–[d]			622	159
$[Cu(\mathbf{phen})(POP)]^+$	392	3990	690	0.10	200	587	132
$[Cu(\mathbf{phen})(\mu\text{-dppm})]_2^{2+}$	$345^{sh}/450^{sh}$	2340 / 550	653	0.06	184	560	147
$[Cu(\mathbf{Bphen})(dppb)]^+$	431	6300	–[d]			640	199
$[Cu(\mathbf{Bphen})(dppe)]^+$	425	6180	–[d]			650	161
$[Cu(\mathbf{Bphen})(dppp)]^+$	415	4850	–[d]			643	183
$[Cu(\mathbf{Bphen})(POP)]^+$	399	4910	640	0.13	203	610	145
$[Cu(\mathbf{phen})(\mu\text{-dppm})]_2^{2+}$	$360^{sh}/475^{sh}$	8820 / 610	653	0.04	–[e]	585	160

[a] Measured with respect to $[Ru(bpy)_3]^{2+}$ as standard (ϕ_{em} = 0.028)[158]; λ_{em} = 380 nm.
[b] λ_{exc} = 373 nm. [c] λ_{exc} = 370 nm; emission lifetime reported as average of biexponential decay.
[d] Luminescence not detectable.
[e] Faint luminescence prevents the determination of the emission lifetime. [sh] Shoulder.

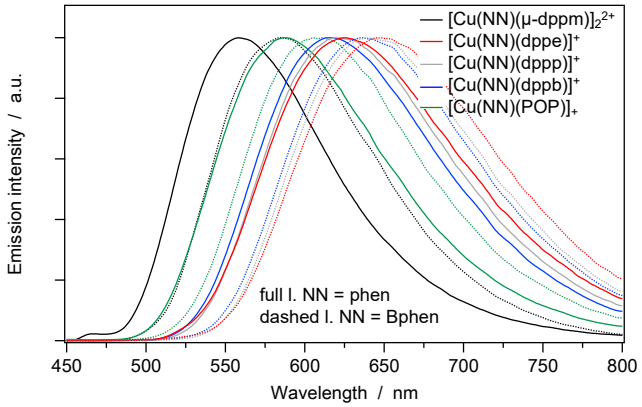

Figure 2.16. Luminescence spectra at 77 K in CH_2Cl_2 rigid matrix; λ_{exc} = 380 nm. Full lines: **phen**; dashed lines: **Bphen**.

Table 2.5. Photophysical data of the complexes in PMMA (1 wt%) and as powders at 298 K.

	PMMA (1 wt%)			powders		
	λ_{em} (nm)	ϕ_{em} [a] (%)	τ (µs)	λ_{em} (nm)	ϕ_{em} [a] (%)	τ (µs)
[Cu(**phen**)(dppb)]$^+$	588	2.4	6.77[b]	583	24.1	9.95
[Cu(**phen**)(dppe)]$^+$	612	0.2	2.87[b]	600	5.1	4.30
[Cu(**phen**)(dppp)]$^+$	598	1.4	7.75[b]	590	8.1	7.27
[Cu(**phen**)(POP)]$^+$	565	11.3	14.08	566	36.6	12.75
[Cu(**phen**)(µ-dppm)]$_2^{2+}$	550	15.4	17.88	533	45.3	33.76
[Cu(**Bphen**)(dppb)]$^+$	598	4.5	9.66	600	20.8	8.65
[Cu(**Bphen**)(dppe)]$^+$	618	0.5	6.27[b]	598	1.2	0.52
[Cu(**Bphen**)(dppp)]$^+$	603	2.6	13.34[b]	600	21.5	14.38
[Cu(**Bphen**)(POP)]$^+$	577	15.0	17.72	581	35.3	11.72
[Cu(**Bphen**)(µ-dppm)]$_2^{2+}$	560	14.9	26.21	575	4.0	6.58[c]

[a] Determined using an integrating sphere [159], λ_{exc} = 380 nm.
[b] Luminescence lifetime reported as average of biexponential decay, λ_{exc} = 370 nm.
[c] Best fit with biexponential equation results in τ_1 = 2.76 µs (32 %) and τ_2 = 9.12 µs.

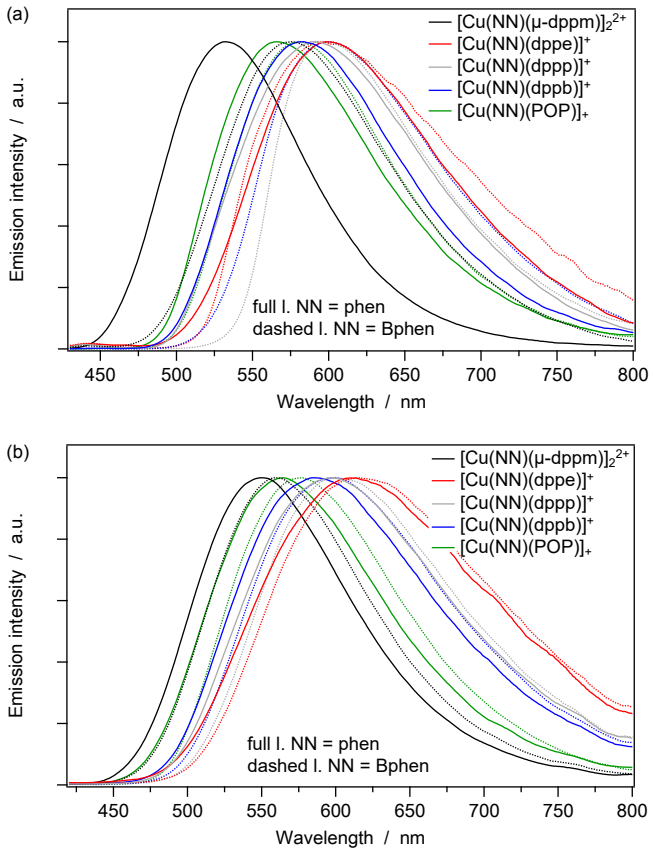

Figure 2.17. Normalized emission spectra of [Cu(**phen**)(PP)]$^+$and [Cu(**Bphen**)(PP)]$^+$ (a) as powders at 298 K in quartz tubes, and (b) in PMMA 1 wt%, at room temperature; λ_{exc} = 380 nm. Full lines: **phen**; dashed lines: **Bphen**

It is well-known that Cu(I) complexes, upon excitation to their lowest-energy triplet state of MLCT nature, undergoes flattening distortion [36, 162]. The degree of such excited-state geometry relaxation strongly depends on the bulkiness and/or rigidity of both the ligands and the overall complex [59].
In order to assess the nature and the geometry of the excited state, all the complexes belonging to the [Cu(**phen**)(PP)]$^+$ series have been fully optimized in their lowest triplet state (T_1) by a spin-unrestricted DFT approach. It should be strongly emphasized that, as it occurs for the ground state, also the potential energy surface of T_1 presents several minima, which are nearly isoenergetic even though they can display rather different structures. As an example, in Figure 2.20 (b) are depicted some selected T_1 minimum conformations adopted by [Cu(**phen**)(dppp)]$^+$, which are all nearly isoenergetic (*i.e.*, ΔE < 0.005 eV) despite their rather different geometries. The most stable T_1 conformers generally adopt the most flattened geometry, which tends to assume a pseudo square-planar coordination around the metal center (*e.g.*, in the case of [Cu(**phen**)(dppe)]$^+$, an almost ideal square-planar complex is obtained, Figure 2.20 (c)).
Key structural parameters of the most stable T_1 flattened conformers are reported in Table 2.7. Compared to the ground-state, a Cu-–N bond shortening is observed in the triplet excited state of all [Cu(**phen**)(PP)]$^+$ complexes, as expected for an MLCT state

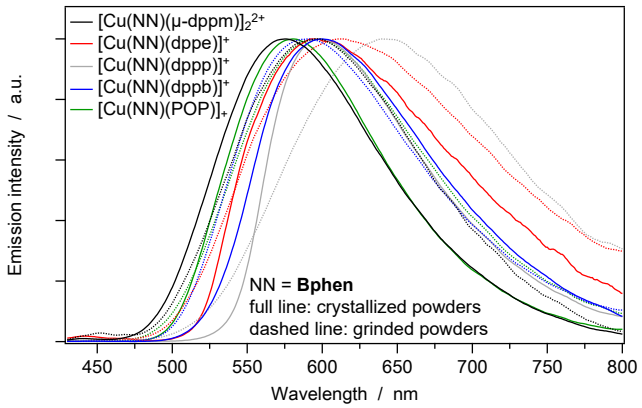

Figure 2.18. Luminescence spectra of [Cu(**Bphen**)(PP)]$^+$ series, comparison between as crystallized powders samples (full lines) and ground powder samples (dashed lines); λ_{exc} = 380 nm.

Table 2.6. Excited-state properties and key structural parameters for the [Cu(**phen**)(PP)]$^+$ series.

Type of PP ligand	Flattening distortion between S_0 and T_1[a] (°)	ϕ_{em} in PMMA at 298 K (%)	Number of intramolecular π-interaction in the ground state
dppb	51.4	2.4	1
dppe	69.6	0.2	0
dppp	46.8	1.4	0
POP	27.2	11.3	2
dppm	−4.1	15.4	4

[a] This angle is determined as the difference between the S_0 and T_1 dihedral angles defined by the phenanthroline and the P–Cu–P planes.

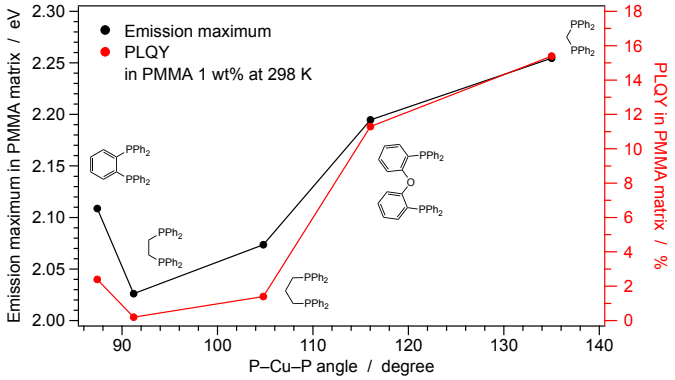

Figure 2.19. Emission data for the [Cu(**phen**)(PP)]$^+$series in PMMA matrix at 298 K. No correlation can be observed between these emission parameters and the diphosphine bite angle. On the contrary, the emission maxima (black dots) and the PLQYs (red dots) appear to follow a similar trend and to correlate well.

characterized by a $Cu^I \longrightarrow$ phen transition [59]. As a consequence, the N–Cu–N angles vary from the typical 80 ± 1° of the ground state to an average value of 84 ± 1° in the lowest ^{3}MLCT state. As far as the diphosphine ligand is concerned, upon T_1 relaxation, an elongation of the Cu–P distance is observed for all the complexes, and a correlated decrease of the PP bite angle is registered with respect to S_0.
On the contrary, the degree of flattening distortions shows a much larger variability, which depends not only from one complex to another (*i.e.*, depending on the type of diphosphine used), but also on the different conformations that an identical complex can adopt on the T_1 potential energy surface. In order to quantitatively evaluate the excited-state flattening distortions, we calculated the difference between the S_0 and T_1 dihedral angles defined by the phenanthroline and the P–Cu–P planes, respectively (Table 2.7). Such variation is very pronounced for the less bulky diphosphine ligands (*i.e.*, dppe, dppp and dppb), while it is reduced for the larger POP ligand, and almost negligible for the very rigid binuclear complex $[Cu(\textbf{phen})(\mu\text{-dppm})]_2^{2+}$ (Table 2.7).
These structural theoretical data are compared to the photophysical experimental ones of the [Cu(**phen**)(PP)]$^+$ series; the comparison is not extended to the **Bphen** series because intermolecular interactions involving the outbound phenyl groups could strongly bias comparisons with DFT data. The key results are reported in Table 2.6, where a very interesting trend can be found: the lower the excited-state flattening, the higher the PLQY.
Since flattening distortions in the excited state are mainly due to the structural flexibility of the overall complex, it can be safely assumed that PLQYs are related (i) to the rigidity and/or bulkiness of the diphosphine ligand itself [59]; and (ii) to phenomena that are able to "lock" the complex geometry, *i.e.*, inter- and intramolecular π-stacking interactions.
By comparing the X-ray structures of the [Cu(**phen**)(PP)]$^+$ series and their PLQYs in PMMA matrix (*i.e.*, a solid-state sample in which the emitters are very diluted in the inert polymeric matrix, so that any intermolecular interaction can be reasonably neglected), we discovered a nice, yet simple, qualitative correlation: the higher the number of intermolecular π-interactions, the larger the PLQY (Table 2.6). These interactions exert a "locking" effect on a given complex, which is crucial to maximize the luminescence output because excited state distortions are minimized. Such a qualitative approach is

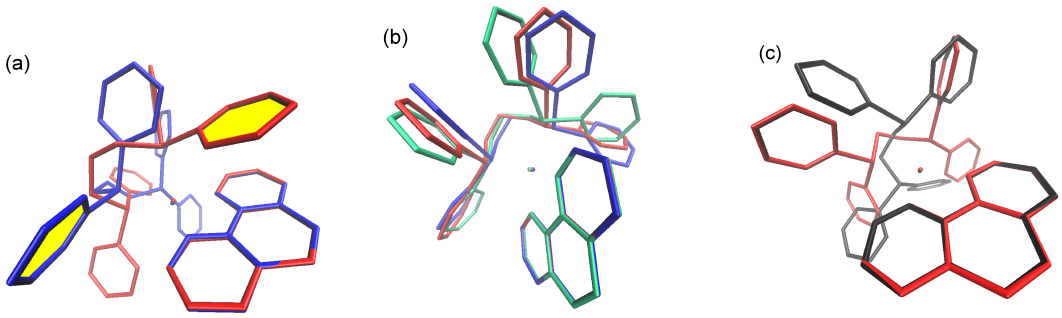

Figure 2.20. (a) Superimposition of the rocked (red) and flattened (blue) T_1 minimum conformers for the [Cu(**phen**)(dppp)]$^+$ complex, calculated at the M06 level of theory in vacuum. The phenyl moiety responsible for the interligand π-interaction leading to rocking is highlighted in yellow. (b) Superimposition of some selected T_1 minimum conformers of the [Cu(**phen**)(dppp)]$^+$ complex in its lowest triplet state (T_1), calculated at the M06 level of theory in vacuum. All T_1 conformers are virtually degenerate (*i.e.*, the energy difference between the highest- and lowest-energy conformer is less than 0.005 eV). The adiabatic energy difference between S_0 and T_1 is 2.17 eV (*i.e.*, 570 nm). (c) Superimposition of the ground-state geometry (black) of the [Cu(**phen**)(dppe)]$^+$ complex and the one of its most stable T_1 conformer (red), which displays an almost ideal square-planar coordination around the copper ion. Both geometries are fully optimized at the M06 level of theory in vacuum (see Appendix A for further details). The adiabatic energy difference between S_0 and T_1 is 1.93 eV (*i.e.*, 640 nm). All the structures are superimposed by minimizing the RMSD of all the atoms of the phenanthroline ligand with VMD 1.9.1 [152]; hydrogen atoms are excluded from the statistic and omitted in the figure.

able to qualitatively estimate the PLQY of a specific copper(I) complex, based solely on its ground-state structural parameters.

Even though it is widely assumed that flattening is the main, if not the sole, mechanism responsible for the excited-state geometry relaxation in copper(I) complexes [36], it should be stressed that these molecules can undergo other types of excited-state distortion in order to relax their lowest ^{3}MLCT state T_1. One of these modes is rocking. In the present study, we found "rocked" minima on the T_1 potential energy surfaces of both [Cu(**phen**)(dppe)]$^+$ and [Cu(**phen**)(dppp)]$^+$. Such complexes are equipped with diphosphine ligands which are particularly flexible due to their aliphatic bridges. As a consequence, upon excitation, these complexes can undergo the formation of energetically favorable interligand π-interactions between the phenanthroline ligand and one of the phenyl substituents on the diphosphine, that can only be achieved by rocking distortions in the T_1 excited state (Figure 2.20 (a)).

Notably, in the case of [Cu(**phen**)(dppp)]$^+$, both the rocked and the flattened T_1 conformers are virtually isoenergetic (*i.e.*, $\Delta E \approx 0.001$ eV), so that rocking seems to be as effective as the well-known flattening mode to stabilize the energy of the T_1 state (Figure 2.20 (a)).

On the contrary, in the case of the diphosphine ligands equipped with a more rigid bridge, the identification of rocked minima was not successful; all the attempted optimizations, starting from "rocked" guess, ended up into the well-known flattened T_1 minima.

Table 2.7. Key structural parameters of the fully-optimized complexes belonging to the [Cu(**phen**)(PP)]$^+$series (where PP = dppb, dppe, POP and μ-dppm). Data refer to both the ground state (S_0) and the lowest triplet excited state in its most stable flattened conformation (T_1). All the geometry optimizations were performed at the M06 level of theory in vacuum (see Appendix A for further details).

Type of PP ligand		Cu–N bond length (Å)	Cu–P bond length (Å)	N–Cu–N angle (°)	P–Cu–P angle (°)	phen–PCuP dihedral angle (°)	Flattening distortion between S_0 and T_1 (°)
dppb	S_0	2.072 – 2.087	2.271 – 2.284	81.0	86.9	85.5	51.4
	T_1[a]	1.977	2.333	84.3	84.0	34.1	
dppe	S_0	2.059 – 2.093	2.265 – 2.283	81.2	91.6	72.8	69.6
	T_1	1.983 – 1.988	2.353 – 2.359	83.6	84.2	3.2	
dppp	S_0	2.078 – 2.103	2.238 – 2.273	80.6	101.8	85.1	46.8
	T_1	1.972 – 1.986	2.335 – 2.370	83.9	91.1	38.3	
POP	S_0	2.101 – 2.108	2.243 – 2.318	80.1	116.2	89.2	27.2
	T_1	1.959 – 1.980	2.326 – 2.365	84.7	103.8	62.0	
μ-dppm	S_0	2.141 – 2.157	2.255 – 2.286	78.5	137.7	85.9	
	T_1[b]	1.958 – 2.096	2.313 – 2.322	84.9	151.2	90.0	−4.1
		(2.173 – 2.169)	(2.275 – 2.292)	(77.8)	(144.9)	(88.5)	(−2.6)

[a] The T_1 minimum-energy geometry turns out to display C_2 symmetry. [b] The T_1 minimum-energy geometry does not display the C_i symmetry as S_0 minimum; consequently, the two Cu nuclei are no longer equivalent. The excited triplet is localized on one copper center only (data reported in the first row), while the other one almost retains the ground-state geometry (data in brackets).

2.1.7 Temperature-dependent luminescence studies

Three complexes have been studied in detail regarding the temperature dependence of their luminescence and of their excited state lifetimes in the interval 78–358 K (both as ground powders and in diluted PMMA matrix). We have turned our attention to the **phen** series, in which intermolecular interactions are minimized. Our selection includes [Cu(**phen**)(μ-dppm)]$_2^{2+}$ – binuclear complex and stronger emitter – as well as [Cu(**phen**)(POP)]$^+$ and [Cu(**phen**)(dppe)]$^+$, as the strongest and weakest emitters of the mononuclear compounds.

In Figure 2.21 (a-c) are collected the emission spectra of the three selected complexes (as ground powders) at different temperatures. For all the samples, a blue shift of the emission bands is detected when increasing the temperature, as typically found for emitters displaying TADF (see Paragraph 2.0.5) [13, 76]. The same phenomenon is also observed when these complexes are dissolved in a PMMA matrix (Figure 2.21 (d-f)), although in some cases the sample preparation leads to a partial dissociation of the complexes and to a minor phosphorescence emission from the phenanthroline free-ligand, visible at a lower wavelength.

To confirm the TADF hypothesis, we also investigated the variation in the excited-state lifetimes of the three complexes as a function of temperature. These data are gathered in Figure 2.22 (c-e) for the ground powders and in Figure 2.22 (a-b) for the samples dissolved in PMMA matrix. The marked shortening of the excited-state lifetimes at higher temperatures (observed in both media) underpins the shifting from a pure triplet emission to TADF [63]. On the basis of these observations, we have fitted the excited-state lifetimes as a function of temperature using equation 2.1 [158]. The results of the fitting procedure are summarized in Table 2.8, while the quality of the fitting itself can be visually assessed from Figure 2.22 (a-e).

The energy gap between the lowest singlet and triplet excited states (*i.e.*, $\Delta E_{(S1-T1)}$ in Table 2.8) is around 0.10 ± 0.02 eV for all the complexes, regardless the type of solid-state sample under investigation. These results are in line with those reported in the literature for similar heteroleptic cationic copper(I) complexes based on chelating bisimine and diphosphine ligands [13, 63, 76].

Table 2.8. Energy splitting $\Delta E_{(S_1-T_1)}$ between the lowest singlet and triplet excited states and related lifetimes in solid state.[a]

	$\Delta E_{(S_1-T_1)}$ (eV)	$\tau_{(S_1)}$ (ns)	$\tau_{(T_1)}$ (μs)	χ^2
[Cu(**phen**)(dppe)]$^+$	0.082 ± 0.004 [b]	158 ± 35 [b]	94 ± 2 [b]	3.557 [b]
[Cu(**phen**)(POP)]$^+$	0.094 ± 0.003	164 ± 27	139 ± 1	4.729
	0.115 ± 0.004	111 ± 21	179 ± 2	2.085
[Cu(**phen**)(μ-dppm)]$_2^{2+}$	0.113 ± 0.004	194 ± 36	130 ± 1	1.351
	0.114 ± 0.004	139 ± 29	123 ± 1	2.149

[a] Data are calculated according to equation 2.1 and given at the 95 % confidence interval. Double entries for each complex refer to solid-state samples as ground powders (top) or dissolved in PMMA matrix (bottom). [b] Not available data due to biexponential decays.

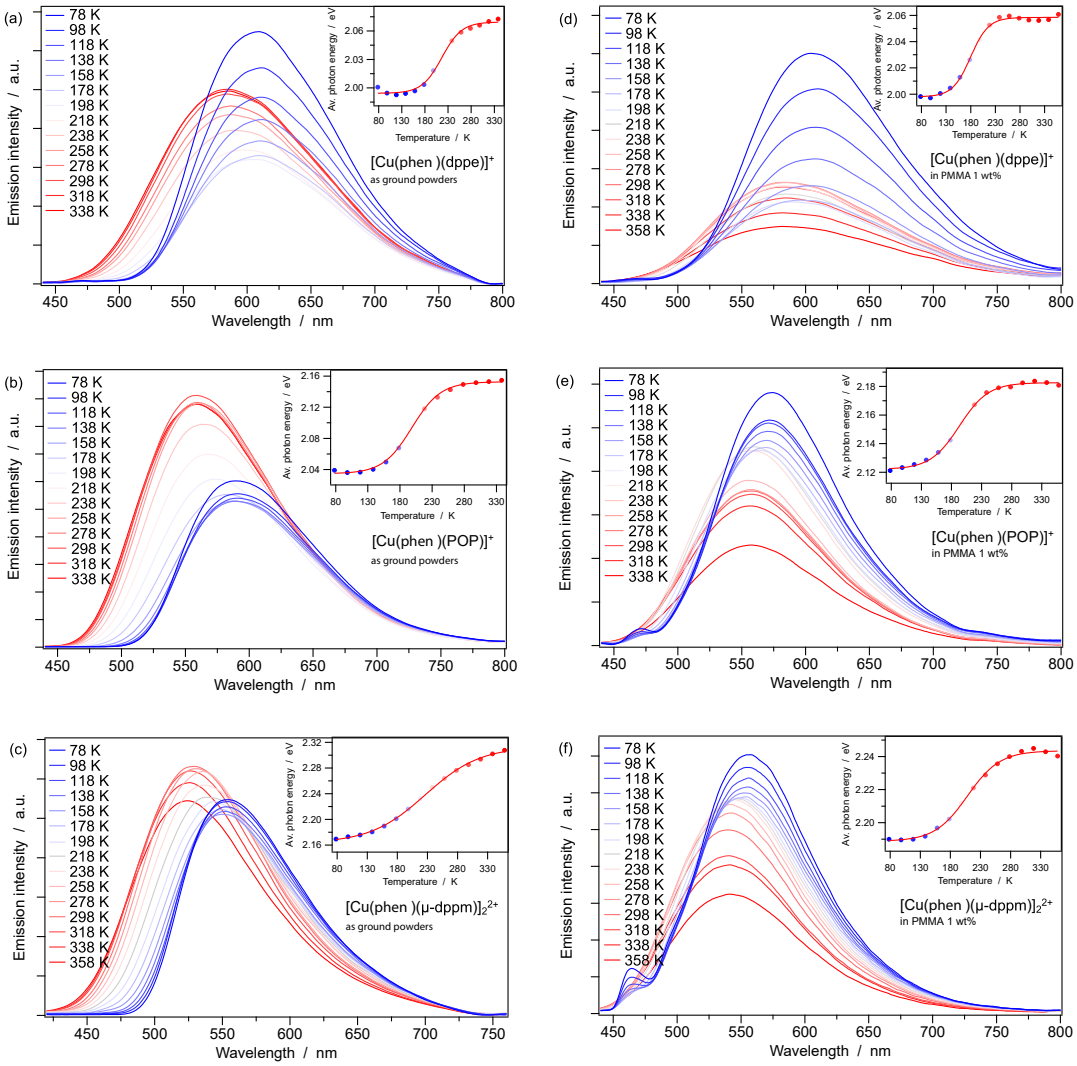

Figure 2.21. Luminescence spectra of three selected $[Cu(\mathbf{phen})(PP)]^+$ complexes as ground powders (a-c) or in PMMA matrix (d-f), in the temperature range 78–338 K. Inset: variation of the average photon energy as function of the temperature and data fitting with a sigmoid function to estimate the $\Delta E_{(S_1-T_1)}$; λ_{exc} = 380 nm. (a) $[Cu(\mathbf{phen})(dppe)]^+$ as pure powder, estimated $\Delta E_{(S_1-T_1)}$ of 0.075 ± 0.009 eV; (b) $[Cu(\mathbf{phen})(POP)]^+$ as pure powder, estimated $\Delta E_{(S_1-T_1)}$ of 0.118 ± 0.009 eV; (c) $[Cu(\mathbf{phen})(\mu\text{-dppm})]_2{}^{2+}$ as pure powder, estimated $\Delta E_{(S_1-T_1)}$ of 0.15 ± 0.01 eV; (d) $[Cu(\mathbf{phen})(dppe)]^+$ in PMMA matrix, estimated $\Delta E_{(S_1-T_1)}$ of 0.060 ± 0.005 eV; (e) $[Cu(\mathbf{phen})(POP)]^+$ in PMMA matrix, estimated $\Delta E_{(S_1-T_1)}$ of 0.061 ± 0.004 eV; (f) $[Cu(\mathbf{phen})(\mu\text{-dppm})]_2{}^{2+}$ in PMMA matrix, estimated $\Delta E_{(S_1-T_1)}$ of 0.055 ± 0.005 eV.

IIn the case of the ground-powder samples, all three complexes display monoexponential decays at all temperatures, confirming a fast equilibration between the emitting states of singlet and triplet spin multiplicity. However, it should be emphasized that the simple two-state approach (*i.e.*, S_1 and T_1) adopted by equation 2.1 to model TADF phenomenon is probably oversimplified to take into account potentially important intermolecular interactions between the complexes in the powders; accordingly, in some cases, the χ^2 of the fitting reaches values well above 2 (Table 2.8). This is particularly evident in the

case of [Cu(**phen**)(dppe)]$^+$ and [Cu(**phen**)(POP)]$^+$ complexes, which display strong intermolecular interactions, as corroborated by their crystal packing obtained by X-ray diffraction [25, 49, 50, 59, 145]. On the other hand, for the more rigid and "caged" binuclear complex [Cu(**phen**)(μ-dppm)]$_2^{2+}$, equation 2.1 nicely fits the experimental results ($\chi^2 \approx 1$, Table 2.8), proving that, in this case, a simple two-state model is perfectly suitable to take into account TADF.
On the contrary, the use of PMMA matrix at 1 wt% doping concentration affords more uniform, transparent and reproducible samples, where emission properties do not strongly depend on minimal variation of sample preparation as it happens for powders (see above). Moreover, since the complexes are very diluted in the inert polymeric matrix,

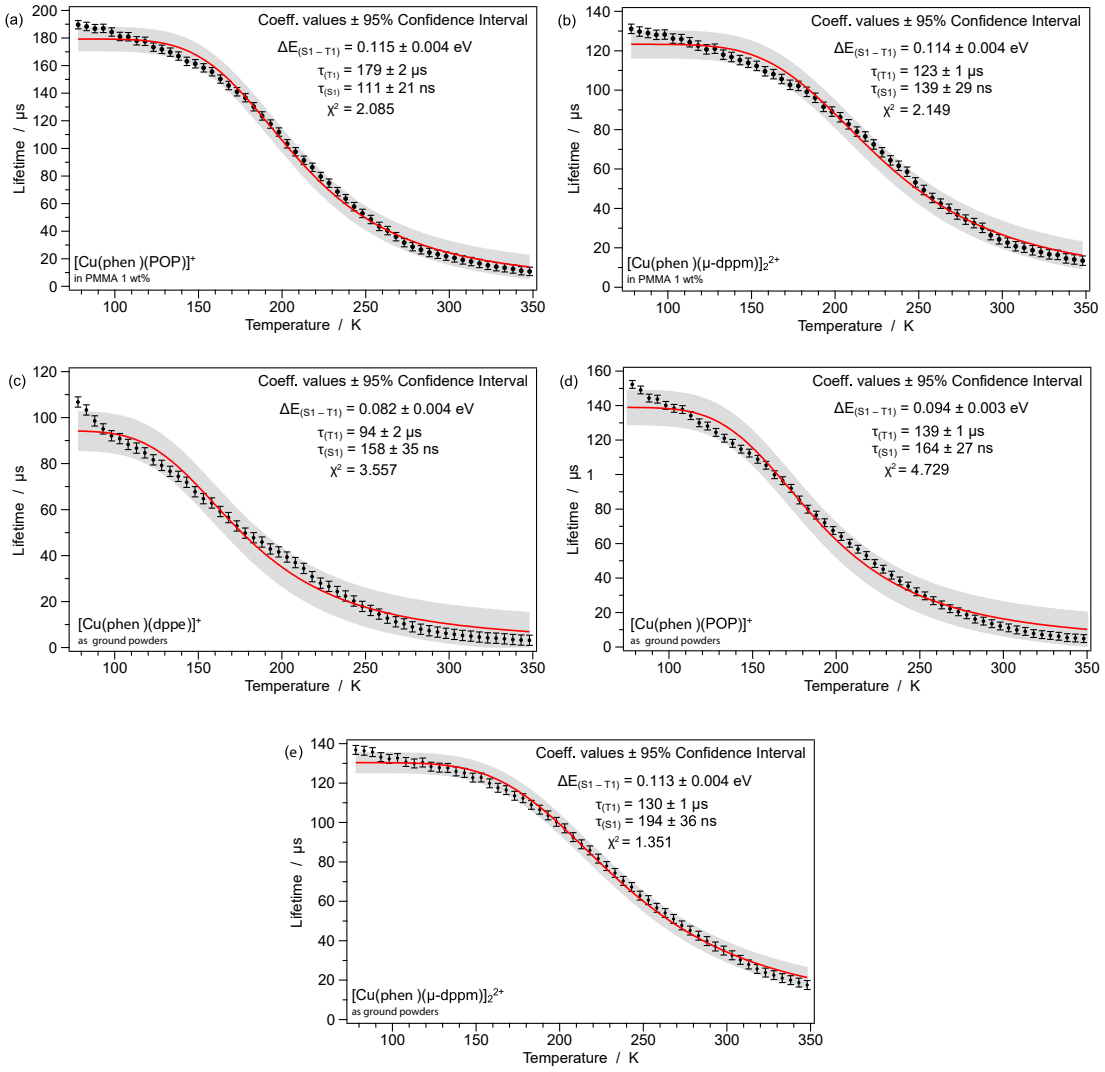

Figure 2.22. Temperature-dependent excited-state lifetimes (τ) three selected [Cu(**phen**)(PP)]$^+$ complexes in PMMA matrix (a-b) or as ground powders (c-e), recorded in the range of 78–348 K; λ_{exc} = 380 nm. The red line fitting the experimental points is calculated according to using eq 2.1; the gray region is the prediction interval at 95 % confidence; the fitting parameters reported in the graph are the same as in Table 2.8. (a) [Cu(**phen**)(POP)]$^+$ in PMMA matrix; (b) [Cu(**phen**)(μ-dppm)]$_2^{2+}$ in PMMA matrix; (c) [Cu(**phen**)(dppe)]$^+$ as pure powder; (d) [Cu(**phen**)(POP)]$^+$ as pure powder; (e) [Cu(**phen**)(μ-dppm)]$_2^{2+}$ as pure powder.

intermolecular interactions can be safely ruled out. As a consequence, the adopted model is overall more reliable in fitting the experimental data (*i.e.*, $\chi^2 \approx 2$ in all investigated samples, see Table 2.8). Anyway, no dramatic differences are observed compared to powder data, especially in the case of the more rigid and "caged" $[Cu(\mathbf{phen})(\mu\text{-dppm})]_2^{2+}$ dinuclear complex.

2.1.8 Conclusion

By selecting two phenanthroline ligands without substituents in the 2,9 positions (**phen**, **Bphen**), we have systematically investigated the electronic and structural properties of ten highly stable and luminescent $[Cu(NN)(PP)]^+$ complexes, where PP indicates five different chelating diphosphine ligands.he elaboration of a large number of photophysical, electrochemical, and structural data, with the crucial support of DFT modeling, highlighted clear interconnections among the key properties. Theoretical tools and models to investigate $[Cu(NN)(PP)]^+$ systems were successfully tested, demonstrating the central role played by the P–Cu–P bite angle and intramolecular π-stacking interactions in dictating light absorption and emission feature.
The main findings are (i) dependence of the ground-state geometry on the crystallization conditions, with the same complex often yielding different crystal structures; (ii) simple model compounds with imposed C_{2v} symmetry ($[Cu(\mathbf{phen})(PX_3)_2]^+$; X = H or CH_3) are capable of modeling structural parameters as a function of the P–Cu–P bite angle, which plays a key role in dictating the overall structure of $[Cu(NN)(PP)]^+$ complexes; (iii) as the P–Cu–P angle increases, the energy of the metal-to-ligand charge transfer absorption bands linearly increases; (iv) the former correlation does not hold for emission spectra, which are red-shifted for the weaker luminophores; (v) the larger the number of intramolecular π-interactions within the complex in the ground state, the higher the luminescence quantum yield, underpinning a geometry locking effect that limits the structural flattening of the excited state.
These results provide a deeper insight on the correlation between structural and electronic properties in $[Cu(NN)(PP)]^+$ complexes, opening the route to the optimization-by-design of a class of compounds of increasing relevance in the areas of photochemistry, catalysis and materials science.

2.2 Enhancing the luminescence with the *steric effect*: phenanthroline functionalization

The experiments reported in Section 2.1 already pointed out the importance of the structural and geometrical features of the PP ligand (*i.e.*, rigidity, PP bite angle and use of diphosphine instead of a monodentate phosphine [48]) in reducing non-radiative deactivation of the excited state, but also the need of tailoring the structure of the ligands to disfavor undesired photoinduced distortions that affect Cu(I) coordination compounds in solution.
In literature several examples highlights the importance of adapting the NN ligand, by inserting the substituents in the right position, in order to tailor the performance for the desired application. For example, 4,7 and 3,8 functionalization are not effectively preventing distortion in the excited state, nor significantly increase the luminescence properties [37]. However, if such "back" substituted phenanthroline bears moieties also in the 2,9 positions, a cooperative effect in terms of steric locking of the tetrahedral geometry is observed also in the excited state, yielding an increase of the luminescence lifetimes in solution [43, 74, 163].
The **phen** functionalization has been widely reported, but usually not assessed in a systematic fashion. Therefore, despite a large number of papers published on the subject, it is still hard to find a rational strategy to design ligands for $[Cu(NN)(PP)]^+$ complexes, which are targeted to a particular application (*e.g.*, as lighting materials, photosensitizers or photoredox catalysts). To overcome the trial and error approach, in this Section it is reported a small library of luminescent Cu(I) complexes where the functionalization of the phenanthroline ligands has been correlated with the photophysical properties and the stability of the complexes.
A series of thirty $[Cu(NN)(PP)]^+$complexes (Figure 2.23) has been synthesized, the stability in solution of these compounds has been then determined by ^1H and ^{13}C NMR spectrocopy.[2]
The complexes that do not rapidly convert into the related homoleptic ones when dissolved in solution (green smiles), have been further investigated to obtain a picture of the ground and excited-state electronic properties, as a function of the substituent on the **phen** ligand and the bite angle imposed by the diphosphine. As depicted in Figure 2.23 (red smiles), when diphosphines with a small bite angle (dppb, dppe and dppp) are coupled with phenanthrolines bearing at least one large group in ortho- position to the pyridine nitrogens, the Cu(I) complex is substantially unstable. The formation of the homoleptic complexes is kinetically favored, thus it is not possible to isolate of the related $[Cu(NN)(PP)]^+$ complex for further experiments.

2.2.1 The series of complexes considered

This series of heteroleptic Cu(I) complexes is constituted by a combination of six different **phen** ligands bearing one or two substituents in the 2,9 position(s), namely -methyl, -isopropyl, -*tert*-butyl or -phenyl groups, with five diphosphines: dppe, dppb, dppp, POP

[2]Synthesis and NMR mesurements have been performed by the group of Jean-François Nierengarten, CNRS, Strasbourg, France.

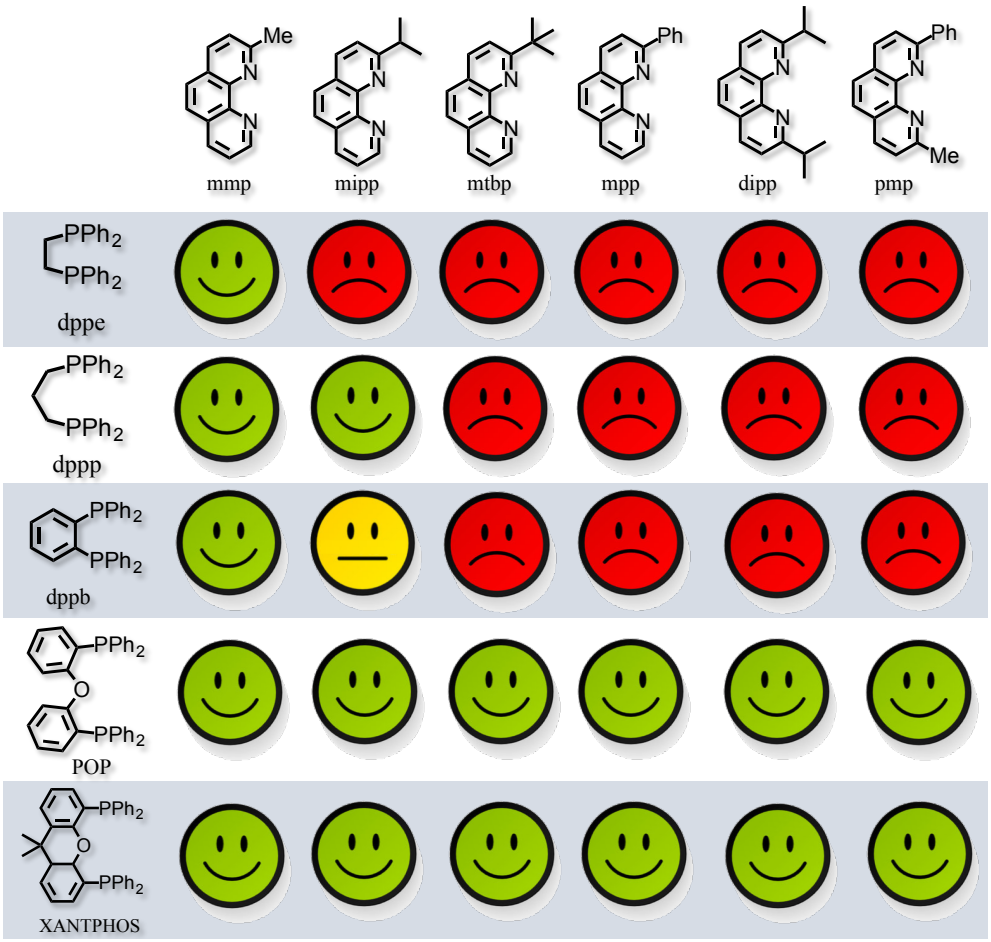

Figure 2.23. Series of heteroleptic $[Cu(NN)(PP)]^+$ synthesized. The green smile refers to compounds stable in solution, the yellow smile indicates samples stable in solid state and the red one stems for samples obtained as a mixture of homoleptics and heteroleptic complexes.

and 4,5-bis(diphenylphosphino)-9,9-dimethylxanthene (XANTPHOS). The PP ligands, as in Section 2.1, differ by the number of carbon atoms connecting the two phosphorous and therefore by the rigidity of this bridge. The series, made of seventeen $[Cu(NN)(PP)]^+$ complexes plus $[Cu(\mathbf{dmp})(POP)]^+$ and $[Cu(\mathbf{phen})(POP)]^+$, taken as references, is depicted in Figure 2.24.

A comprehensive study of structural and photophysical properties of the series, both in solid and solution, has been carried out. The effect of the mono- and di-functionalization in 2,9 positions of the phenanthroline and the distortions caused to the Cu(I) pseudo-tetrahedral structure has been also assessed. The effect of bulky **phen** substituents has been carefully evaluated in order to determine which is the appropriate size for this group to prevent excited-state distortion, preserving the stability in solution.

For the sake of clarity, the complexes of this series will be divided in four groups, (i) one describing the PP bite angle effect, (ii) the second assessing the effect of the size of mono-substitution of the **phen**, (iii) the third related to the symmectric functionalization of the same diimine ligand, and (iv) the last group concerned with the extension of the aromaticity of the **phen**.

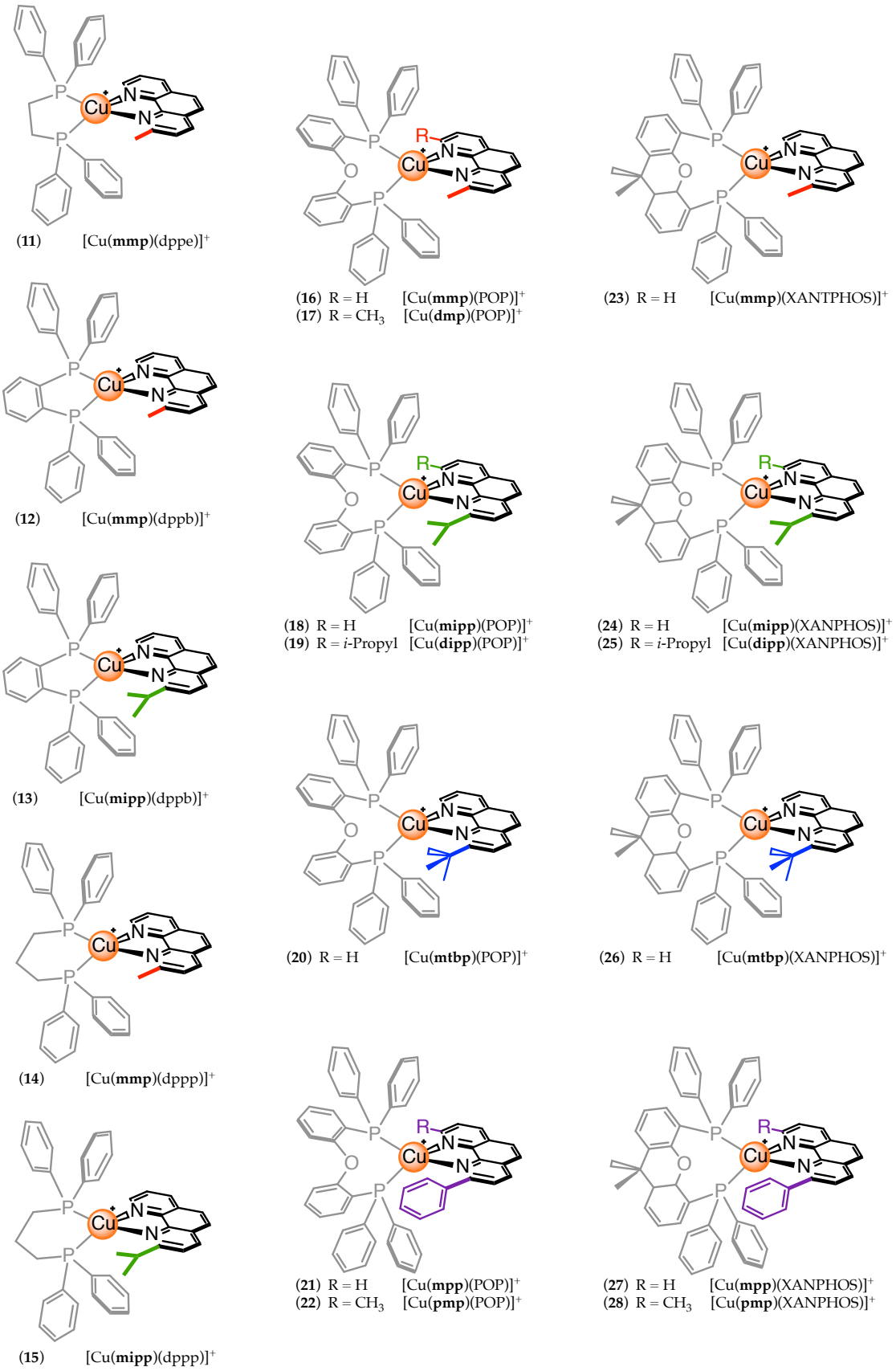

Figure 2.24. Heteroleptic $[Cu(NN)(PP)]^+$ complexes **11**–**28** as $[BF_4]^-$ salt.

2.2.2 X-ray single crystal structures

It is interesting to compare simmetrically functionalized diimines in XANTPHOS complexes (with **dmp** or **dipp**), to assess the effect of the size of the substituents in the 2,9 positions on the single crystal structure [164]. Both structures adopt a similar rocked coordination geometry (≈ 25°), due to the π-interaction between one phenyl on XANTPHOS and the NN ligand. In the case of the **dmp** complex, it also forms an intermolecular π-interaction, through an inversion center between the two diimine ligands. On the other hand, the intermolecular coordination structure of [Cu(**dipp**)(XANTPHOS)]$^+$ is dominated by a π-stacking between two phenyls of the PP ligand belonging to two different complexes, and involves also the xanthene moiety with an edge-to-face π-interaction. The sizable changes observed in the coordination environment, in addition to the different moieties in 2,9-position of the NN ligand, hardly affect the pseudo-tetrahedral geometry of the complexes, as depicted in Figure 2.25 (a). Both the compounds are characterized by the same PP bite angle (118.4°) and also the Cu–N and Cu–P bond lengths are virtually identical (Table 2.9). Since geometrical parameters are unchanged, it is expected that any locking effect played by the bulkier symmetric substituents on the phenanthroline, would be apparent in the excited state. This will be evaluated by examining the radiative and non radiative deactivation paths, which highlight the presence of quenching phenomena affecting the emitting state [37].

The POP ligand, as shown in Figure 2.25 (b), is more flexible, hence the introduction of 2,9-moieties on the NN ligand changes significantly the coordination structure of the complex. With a more accurate comparison of the key structural parameters (Tables 2.1 and 2.9), it is clear that the strongest variation is related to the rocking angle of the POP

Table 2.9. Selected interatomic distance and angles of [Cu(**dmp**)(XANTPHOS)]$^+$, [Cu(**dipp**)(XANTPHOS)]$^+$ [164] and [Cu(**dmp**)(POP)]$^+$ [48] complexes, as obtained from X-ray single crystal structure. Data are taken from X-ray crystal structures reported in literature and available through the Cambridge Crystallographic Data Center (CCDC).[a]

	Cu–N	Cu–P	N–Cu–N	P–Cu–P	phen–PCuP	
NN ligand	bond length[b] (Å)		angle (°)		dihedral angle (°)	CCDC
dmp[c]	2.094 – 2.123	2.257 – 2.304	79.30	118.38	80.78	829668
	2.11 ± 0.02	**2.28 ± 0.03**	**79.3**	**118.4**	**80.8**	
dipp[c]	2.122 – 2.123	2.255 – 2.294	80.08	118.42	84.28	829667
	2.123 ± 0.001	**2.27 ± 0.03**	**80.1**	**118.4**	**84.3**	
dmp[d]	2.084 – 2.104	2.269 – 2.273	80.88	116.44	79.13	177685
	2.076 – 2.099	2.228 – 2.284	81.39	117.03	88.77	224966[e]
	2.100 – 2.110	2.265 – 2.269	80.26	116.52	83.39	”
	2.071 – 2.094	2.260 – 2.262	81.06	115.98	78.93	1498328
	2.09 ± 0.01	**2.27 ± 0.02**	**80.9 ± 0.5**	**116.5 ± 0.4**	**83 ± 5**	

[a] In bold are reported the mean values of the structural parameters taken from the different available conformers. [b] Cu–O has a non-bonding distance > 3.15 Å.

[c] [Cu(NN)(XANTPHOS)]$^+$ complexes. [d] [Cu(**dmp**)(POP)]$^+$complex.

[e] Complex is co-crystallized in two different structures.

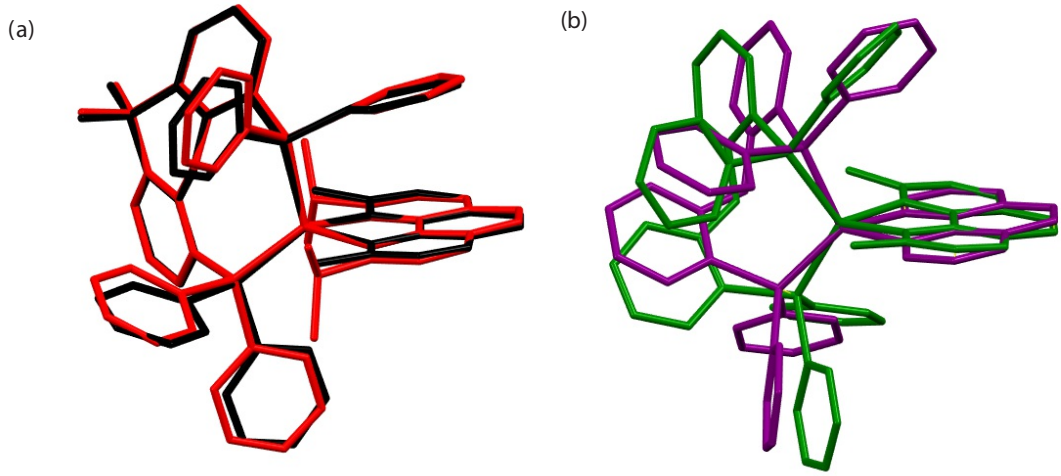

Figure 2.25. Superimposition of X-ray single crystal structure of (a) [Cu(**dmp**)(XANTPHOS)]$^+$ (black) and [Cu(**dipp**)(XANTPHOS)]$^+$ (red) and (b) [Cu(**dmp**)(POP)]$^+$ (green) and [Cu(**phen**)(POP)]$^+$ (purple) (b) complexes [53, 164]. Superimposition and visualizations were performed by Mercury CSD 3.10 [165]. H atoms and counterions are omitted.

ligand and its bonding distance – which is increased by the introduction of **dmp** – while the other parameters are kept substantially unchanged.
Generally speaking, the interatomic distances and bonds of XANTPHOS-bearing complexes are similar to the POP ones, despite the different rigidity of the two PP ligands. This suggests that these key structural parameters are mainly dictated by the P–Cu–P bite angle, which is almost identical in POP and XANTPHOS. The observed increase of the Cu–N bond length for the complexes reported in this Section with respect to [Cu(**phen**)(POP)]$^+$ (Table 2.1, Cu–N_{phen} = 2.07 ± 0.01 Å; Cu–N_{dmp} > 2.09 Å) is essentially a consequence of the repulsion effect caused by the introduction of the 2,9-groups on the NN ligand (-methyl or -isopropyl), which increase the steric crowding around the copper core. The same Cu–N bond elongation is observed in [Cu(**dmp**)(POP)]$^+$, as reported in Table 2.9.
Independently from the PP ligand (POP or XANTPHOS), the diphosphinic oxygen has been determined to have a non-coordinating distance greater than 3.15 Å from the Cu(I). On the contrary, the methyl hydrogens in **dmp** and on the isopropyl tertiary carbon of **dipp**, are close to the metal core (< 2.85 Å), which may cause a weak interaction categorized as Cu···H–C anagostic bond [166]. Further experiments (*i.e.*, neutron diffraction spectroscopy) are necessary to corroborate this hypothesis, but the absence of specific C–H bond elongation or angle distortions, suggests that the metal-hydrogen "close contact" is simply a steric consequence related to the molecular structure.

2.2.3 Electrochemical properties

The electrochemical properties were determined by CVs and OSWVs and are reported in Table 2.10 and Figure 2.26.[3] The measurements were made at room temperature, on

[3]Electrochemical experiments were performed by Béatrice Delavaux-Nicot and coworkers, Laboratoire de Chimie de Coordination du CNRS in Toulouse, France.

a 10^{-3} M CH_2Cl_2 solution of the complexes. The tetra-n-butylammonium tetrafluoroborate ([nBu$_4$N][BF$_4$]) was added as electrolyte (0.1 M), and ferrocene (Fc) was used as internal reference (Fc^+/Fc observed at 0.55 ± 0.01 V vs. SCE). The cell was made of a SCE reference electrode, a Pt wire as the working electrode and Pt mesh as counterelectrode (see Appendix A).
All the complexes exhibit a quasi-reversible first reduction process, centered on the diimine moiety. Similarly, the oxidation process attributed to the Cu(II)/Cu(I) redox couple is quasi-reversible for all the compounds except those bearing the smaller-bite-angle diphosphine (dppb and dppe) or the bulkier group on the **phen** (-*tert*-butyl). It must be emphasized that in some CV experiments, especially for complexes with the bulkier diimines (**mtbp**, **dipp**, **mpp** and **pmp**) a weak reduction at lower energy is observed after the first oxidation. This process is attributed to the reduction of the homoleptic $[Cu(NN)_2]^+$ complex, whose formation was promoted by *negative steric effect* caused by the crowded structure and the intrinsic instability of the heteroleptic complexes in the oxidized form. A strong instability of $[Cu(NN)(PP)]^+$ complexes has been reported when 2,9-diphenyl-1,10-phenanthroline (**dpp**) is used as NN ligand and combined with any diphosphine. This is due to the remarkable thermodynamic stability of $[Cu(\mathbf{dpp})_2]^+$ homoleptic complex [75, 124]. On the contrary, mono-phenyl **mpp** and the asymmetrically functionalized **pmp** (2-methyl-9-phenyl-1,10-phenanthroline) afford slightly less stable $[Cu(NN)_2]^+$ complexes, thus their heteroleptic form is relatively stable.
The effect of the bite angle was studied on two groups of complexes containing **mmp** or **mipp** as NN ligands. Increasing the P–Cu–P bite angle, the reduction potential was unaffected, while the oxidation process occurred at higher energy, indicating an enhanced protection exerted by the diphosphine on the metal core. The stability was increased in the same way: dppb and dppe complexes can more easily form homoleptic complexes, while the systems equipped with dppp, POP and XANTPHOS are remarkably stable. The general trend observed with the increase of the PP bite angle, is due to a stabilization of the HOMO orbital and the consequent increase of the ΔE_{Redox}, in line with results highlighted in Paragraph 2.1.4.

Notably, the variation of the size of the substituent on the **phen** moiety, slightly affects the one-electron transfer process centered on this ligand (20–30 mV passing from the -methyl to the -*tert*-butyl). Such an electronic effect is more evident comparing the difference of the E_{Red} between pristine phenanthroline and **mmp** (60 mV). It seems reasonable that the introduction of an alkyl substituent strongly impacts the capacity of the NN ligand to accept an electron, increasing the LUMO energy, while the variation of this alkyl functionality has just a minor impact.
Moreover, the increase of the steric hindrance caused by the 2-substituent evidenced two other effects: (i) the increase of the rigidity of the complexes, causing a shift of the oxidation potential to higher energy [36, 37, 167, 168] and (ii) the destabilization of the coordination compounds, due to the irreversible oxidation, as described above.
Passing from one to two alkyl groups on the NN ligand, a steep rise in the ΔE_{Redox} is observed (120–150 mV). The potential increase is due to both the stabilization of the HOMO (as a consequence of the caging effect played by the **dmp** or **dipp** on the Cu(I)) and the destabilization of the LUMO (due to slight electron releasing character of alkyl groups that reduce the capacity to host a negative charge of the diimide). It is evident the cooperative effect played by the addition of these moieties on the electronic properties of the **phen** ligand (E_{Red}), with an increase of the reduction potential of 60–70 mV by

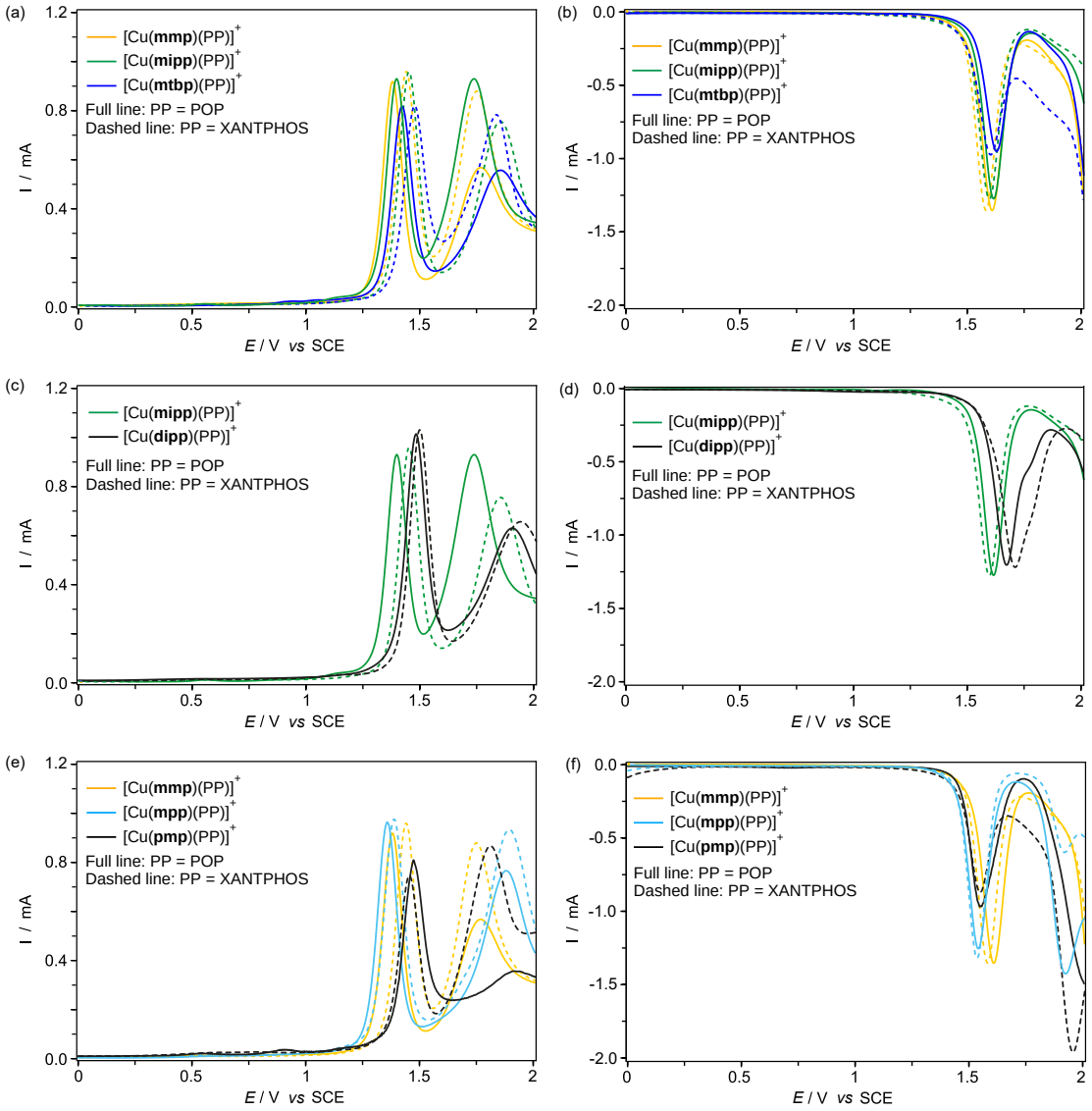

Figure 2.26. OSWVs scans: size effect of the substituent (anodic (a) and cathodic (b) scans), effect of symmetrical functionalization (anodic (c) and cathodic (d) scans) and effect of increased electronic conjugation (anodic (e) and cathodic (f) scans), on a Pt electrode in CH_2Cl_2 + 0.1 M [nBu$_4$N][BF$_4$] at room temperature (OSWVs: frequency 20 Hz, amplitude 20 mV, step 5 mV).

adding the first moiety and then a further enhancement of 40 mV with the insertion of the second substituent.

Finally, the oxidation and the reduction processes become easier by expanding the conjugation via the substitution of the -methyl group on NN with a -phenyl, as observed also in the case of the **Bphen** ligand (Table 2.3). On the contrary, when the NN ligand is functionalized with both these moieties in an asymmetric fashion (2,9-position), a cooperative effect is observed and the anodic one-electron-transfer process becomes rather difficult. The extended conjugation favors the electronic delocalization, keeping the reduction process at lower potential for the substituted-**phen**.

Table 2.10. Electrochemical data determined by OSWVs and CVs at room temperature, in CH_2Cl_2 solution. Ferrocene has been used as internal reference. Potential values in Volts vs. SCE (Fc^+/Fc is observed at 0.55 ± 0.01 V vs SCE).

	E_{Ox1} (V)	E_{Red}[a] (V)	ΔE_{Redox} (V)
[Cu(**mmp**)(dppb)]$^+$	+1.19	−1.56	2.75
[Cu(**mmp**)(dppe)]$^+$	+1.17	−1.56	2.73
[Cu(**mmp**)(dppp)]$^+$	+1.21[b]	−1.58	2.79
[Cu(**mmp**)(POP)]$^+$	+1.37[b]	−1.62	2.99
[Cu(**mmp**)(XANTPHOS)]$^+$	+1.44[b]	−1.58	3.02
[Cu(**mipp**)(dppb)]$^+$	+1.19[b]	−1.57	2.77
[Cu(**mipp**)(dppp)]$^+$	+1.22[b]	−1.60	2.82
[Cu(**mipp**)(POP)]$^+$	+1.38[b]	−1.63	3.01
[Cu(**mipp**)(XANTPHOS)]$^+$	+1.45[b]	−1.60	3.05
[Cu(**mtbp**)(POP)]$^+$	+1.41[b]	−1.64	3.05
[Cu(**mtbp**)(XANTPHOS)]$^+$	+1.47	−1.61	3.08
[Cu(**dmp**)(POP)]$^+$	+1.45[b]	−1.66	3.11
[Cu(**dipp**)(POP)]$^+$	+1.49[a]	−1.67	3.16
[Cu(**bipp**)(XANTPHOS)]$^+$	+1.50[b,c]	−1.70	3.20
[Cu(**mpp**)(POP)]$^+$	+1.35[b]	−1.55	2.90
[Cu(**mpp**)(XANTPHOS)]$^+$	+1.39[b,c]	−1.53	2.92
[Cu(**pmp**)(POP)]$^+$	+1.48[d,e]	−1.55	3.03
[Cu(**pmp**)(XANTPHOS)]$^+$	+1.46[b,d]	−1.54	3.00
[Cu(**phen**)(POP)]$^+$	+1.31	−1.56	2.87

[a] Quasi-reversible process in CV around 5 V s^{-1}. [b] Quasi-reversible process in CV at 0.2 V s^{-1}. [c] Anticipated by a very weak signal at 0.75 V.
[d] Anticipated by a very weak signal at 0.95 V.
[e] Quasi-reversible process in CV around 10 V s^{-1}.

2.2.4 Ground-state electronic properties and stability in solution

The complexes reported in this Section are stable in solid and can be stored for years. In solution – under argon and protected from ambient light – they can be safely handled for several days without noticing degradation. We checked the stability of the complexes bearing the bulkier group on the phenanthroline, which are potentially the most problematic. The spectra depicted in Figure 2.27 were recorded right upon dissolution in CH_2Cl_2 and after 24 h. The experiments, performed keeping the solution aerated and exposed to light to foster degradation, evidenced that the XANTPHOS complexes are perfectly stable for the time considered by the experiment, while the POP complexes show degradation under light in the same time range.

As reported in Paragraph 2.0.4, the degradation might be a consequence of the relative stability of the homoleptic complexes. Both POP and XANTPHOS can bis-coordinate Cu(I), but homoleptic POP complexes are in principle less stable, given its capability to chelate the metal only in a tridentate fashion [126], while XANTPHOS can only form

a pseudo-tetrahedral Cu(I) homoleptic complex [114]. On the other hand, we observed a higher stability of $[Cu(NN)(XANTPHOS)]^+$ with respect to the POP complex, thus $[Cu(XANTPHOS)_2]^+$ seems less kinetically favored. This unexpected behavior is most probably related to the wider volume occupied by the POP, due to the flexible ether connection with respect to the xanthene one. In the presence of a bulky diimine, the greater space requirements promote a *negative steric effect*, thus an easier ligand detachment.
The ground state electronic absorption spectra reported in Figure 2.28–2.31 show the typical features of $[Cu(NN)(PP)]^+$ complexes. In the visible region are observed MLCT bands (with maximum in the 380–420 nm range) that involves the promotion of one electron from the Cu(I) core to the π^* electron of the phenanthroline ligand ($\varepsilon \approx$ 2-6 $\times 10^3$ $M^{-1}\,cm^{-1}$) [48–50, 53, 54, 57, 169]. Moreover, in the UV region, a stronger band is observed ($\varepsilon \approx$ 4-5 $\times 10^4$ $M^{-1}\,cm^{-1}$). It is located in the 270–300 nm range, corresponding to the $\pi \longrightarrow \pi^*$ LC transitions of both the NN and PP ligands [126, 170]. The energy of these transitions has been systematically compared with the electrochemical data (Table 2.10), and the results are in excellent agreement.

Examining the electronic properties of the ground-state as a function of the diphosphines bite angle can provide fruitful hints, as discussed in Section 2.1. The absorption spectra of the first group of compounds is reported with respect the increase of this key parameter: dppb < dppe < dppp < POP and XANTPHOS, with the last showing an average P–Cu–P angle of ≈ 118° [164], approximately equal to the POP one (116 ± 4°).
Comparing the complexes by the variation of this parameter, we observed that the energy of the MLCT absorption maximum essentially follows the same behaviour reported in Paragraph 2.1.3 both in presence of **mmp** (complexes **12**, **11**, **14**, **16** and **22**) and **mipp** (complexes **13**, **15**, **18** and **24**). Increasing the PP bite angle we observed: (i) the shift of the MLCT band to higher energy, (ii) the reduction of the MLCT absorption intensity (ε), moreover, (iii) the LC transition is kept at the same energy, while (iv) the LC oscillator strength seems not correlated to the P–Cu–P bite angle (Figures 2.12 and 2.28).
When a moiety is added in 2-position, the MLCT absorption band is similarly affected. With an increase of the size of the substituent on the **phen**, keeping constant the diphosphine ligand, a bathochromic shift and a reduction of the oscillator strength is observed (Figure 2.29). The electrochemistry observations (Table 2.10) suggest an increase of both

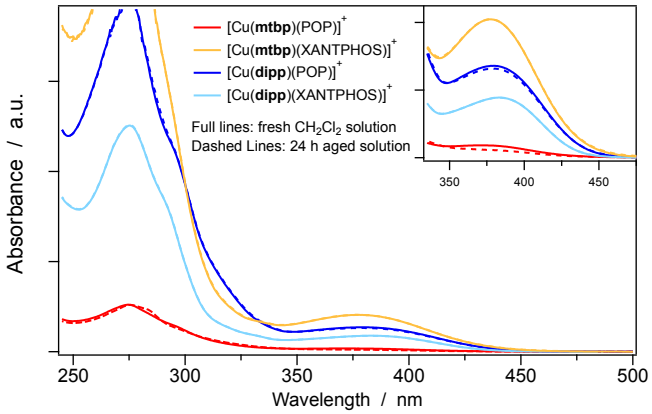

Figure 2.27. Absorption spectra of freshly prepared CH_2Cl_2 solution (full line) and after 24 hours (dashed line), of the four most sterically hindered complexes of the series (**19**, **20**, **25** and **26**).

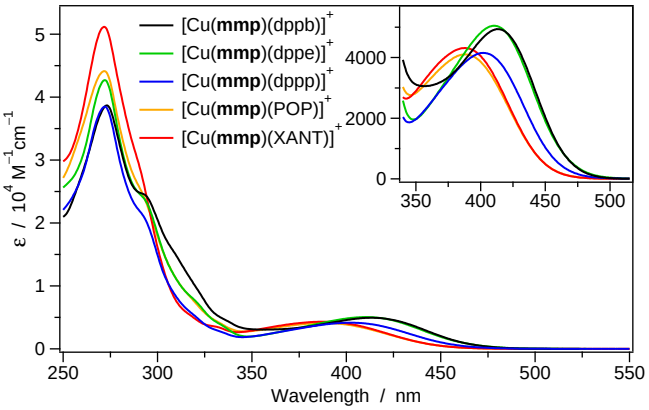

Figure 2.28. Absorption spectra in CH_2Cl_2, effect of the bite angle (dppb < dppe < dppp < POP and XANTPHOS). XANT = XANTPHOS

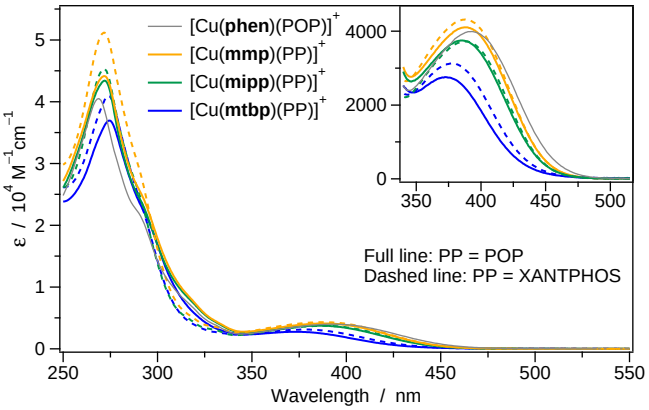

Figure 2.29. Absorption spectra in CH_2Cl_2, effect of the size of the **phen** 2-substituent (**phen** < **mmp** < **mipp** < **mtbp**).

the oxidation potential of the Cu(I) (HOMO) and the reduction potential of the substituted **phen** (LUMO), when the size of the substituent is increased. We argue that the stabilization the HOMO is somehow promoted by a moiety-induced cage effect, while a concomitant slight destabilization of the LUMO, located on the diimine, is due to the electron-donating character of the same moiety in the 2-position.
At the same time, changing the group from the -methyl to the -*tert*-butyl, an hypsochromic shift of the LC band is observed, again along with a reduction of the molar extinction coefficient. As a reference, the spectrum of [Cu(**phen**)(POP)]$^+$ is depicted in Figure 2.29 (gray line). The trend is essentially respected, since this bare **phen** complex shows the highest energy LC transition, but also the lowest energy MLCT band.
By putting substituents in both the 2 and 9 positions, the impact on the electronic properties is the same as that seen above, when only one position is occupied (Figure 2.30).
The last group of spectra (Figure 2.31) show the effect of the increased conjugation on the NN ligand, by attaching a -phenyl in the position 2. The HOMO and the LUMO are both stabilized (Table 2.10) and both the LC and MLCT transitions are shifted to the red.

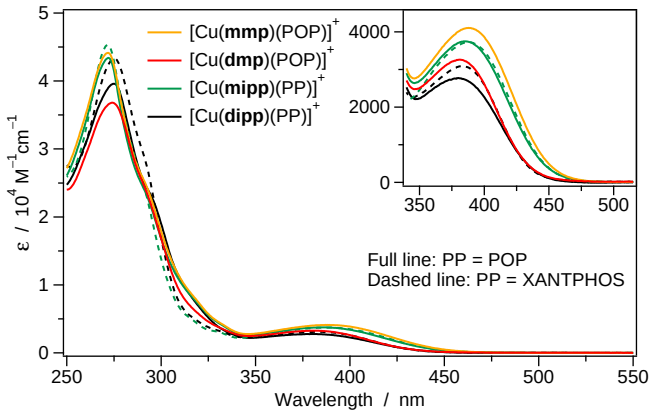

Figure 2.30. Absorption spectra in CH_2Cl_2, effect of the symmetric functionalization of the **phen**.

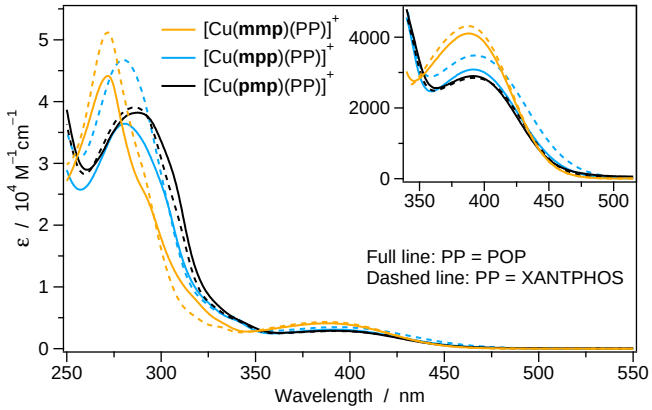

Figure 2.31. Absorption spectra in CH_2Cl_2, effect of the asymmetric functionalization and the increase of the conjugation system on the **phen**.

2.2.5 Luminescence properties

The photophysical measurements done on the Cu(I) complexes reported in Section 2.1 highlighted the importance of a rigid coordination environment to limit the non-radiative deactivation of the excited state, with particular attention to liquid media. The **phen** and **Bphen** ligands were not capable to prevent the excited-state flattening in solution, hence the luminescence was very weak. The study of such series, provide key clues to properly design $[Cu(NN)(PP)]^+$ complexes [141].
The electrochemical data confirmed that the introduction of one or two substituents on the NN ligand enhances, among other parameters, the oxidation potential of the Cu(I) metal ion. This finding underpins the caging effect promoted by a more rigid ligand, which efficiently protects the copper(I) from the oxidation. The effective shielding of the metal core, by increasing the overall rigidity of the complexes, is also the key to get higher PLQYs and longer excited state lifetimes. The luminescence properties (emission profiles and excited-state lifetimes) of the eighteen complexes have been studied in deaerated CH_2Cl_2 solution at room temperature and at 77 K, to assess the effect of a rigid matrix in diluted condition. The results are summarized in Table 2.11 and in Figure 2.32. The conditions similar to those found in a device (*e.g.*, OLED, LEC, solar concentrator) have been simulated with solid-state experiments, preparing sample in PMMA matrix

Table 2.11. Photophysical data in CH_2Cl_2 at 298 K and in frozen solution at 77 K.

	CH_2Cl_2 at 298 K						CH_2Cl_2 at 77 K	
	λ_{MLCT} (nm)	ϵ_{MLCT} ($M^{-1}\,cm^{-1}$)	λ_{em} (nm)	ϕ_{em} [a] (%)	τ_1 [b] (µs)	τ_2 [b] (µs)	λ_{em} (nm)	τ_{av} [c] (µs)
[Cu(**mmp**)(dppb)]$^+$	413	4940	625	0.13	1.60	-	600	438[e]
[Cu(**mmp**)(dppe)]$^+$	411	5050	660	0.06	1.49	-	603	365[e]
[Cu(**mmp**)(dppp)]$^+$	402	4150	630	0.19	4.37	-	600	339
[Cu(**mmp**)(POP)]$^+$	389	4020	618	3.6	2.47[d]	11.6	578	196
[Cu(**mmp**)(XANT)]$^+$	388	4320	604	5.5	4.07[d]	8.26	568	194
[Cu(**mipp**)(dppb)]$^+$	402	3747	670	0.14	0.33	7.38[d]	597	343
[Cu(**mipp**)(dppp)]$^+$	410	4540	680	0.07	0.52[d]	3.75	585	292[e]
[Cu(**mipp**)(POP)]$^+$	385	3750	617	4.0	2.42[d]	14.3	570	177
[Cu(**mipp**)(XANT)]$^+$	388	3720	598	9.4	6.20	-	550	209
[Cu(**mtbp**)(POP)]$^+$	373	2760	647	1.8	0.42	-	570	199
[Cu(**mtbp**)(XANT)]$^+$	377	3130	623	1.3	0.83	-	557	102[e]
[Cu(**dmp**)(POP)]$^+$	381	3260	565	23.9	11.5	-	518	211
[Cu(**dipp**)(POP)]$^+$	380	2770	548	51.9	17.5	-	548	302
[Cu(**bipp**)(XANT)]$^+$	382	3090	540	40.4	17.1	-	515	277
[Cu(**mpp**)(POP)]$^+$	392	3090	645	1.5	0.47[d]	2.49	582	258[e]
[Cu(**mpp**)(XANT)]$^+$	392	3480	640	1.8	2.06	-	588	188[e]
[Cu(**pmp**)(POP)]$^+$	392	2900	579	24.3	13.9	-	549	348[e]
[Cu(**pmp**)(XANT)]$^+$	391	2850	562	26.1	20.0	-	545	601[e]
[Cu(**phen**)(POP)]$^+$	392	3990	690	0.10	0.20	-	587	132

[a] Measured with respect to Quinine Sulphate as standard (1 N H_2SO_4 solution; ϕ_{em} = 0.546) [171]; λ_{exc} = 360 nm. [b] λ_{exc} = 370 nm. [c] λ_{exc} = 370 nm. [d] predominant decay obtained from the biexponential fitting. [e] Decay reported as τ_{av}. XANT = XANTPHOS

(1 wt%) and as pure neat films. The experimental details are reported in Appendix A.
In aerated solution, as commonly observed for [Cu(NN)(PP)]$^+$, the emissions are strongly quenched by oxygen, producing $^1O_2$, thus the the PLQYs are very low and excited-state lifetimes usually below 1 µs. On the contrary, all of the compounds are luminescent in deaerated CH_2Cl_2 solution at room temperature. The POP and XANTPHOX complexes show intense emission (PLQY ≈ 1–50 %), while the compounds bearing the dppb, dppe or dppp are characterized by faint photoluninescence, in line with the series reported in the previous Section 2.1 (PLQY < 0.2 %), independently from the NN ligand used. Such behavior confirms the fundamental role played by the bulky diphosphine, in preventing photoinduced distortion [48, 141].
The emission bands are unstructured with lifetimes in the microsecond time range. Due to the not negligible dipole moment of the transition, the energy of the band is significantly affected by the media, thus emissions at 77 K are rigidochromically shifted to higher energy. The above observations perfectly reflect the MLCT character of the transition, characteristic of [Cu(NN)(PP)]$^+$complexes [37].

By modifying the size of the moiety on the mono-functionalized NN ligand, we ob-

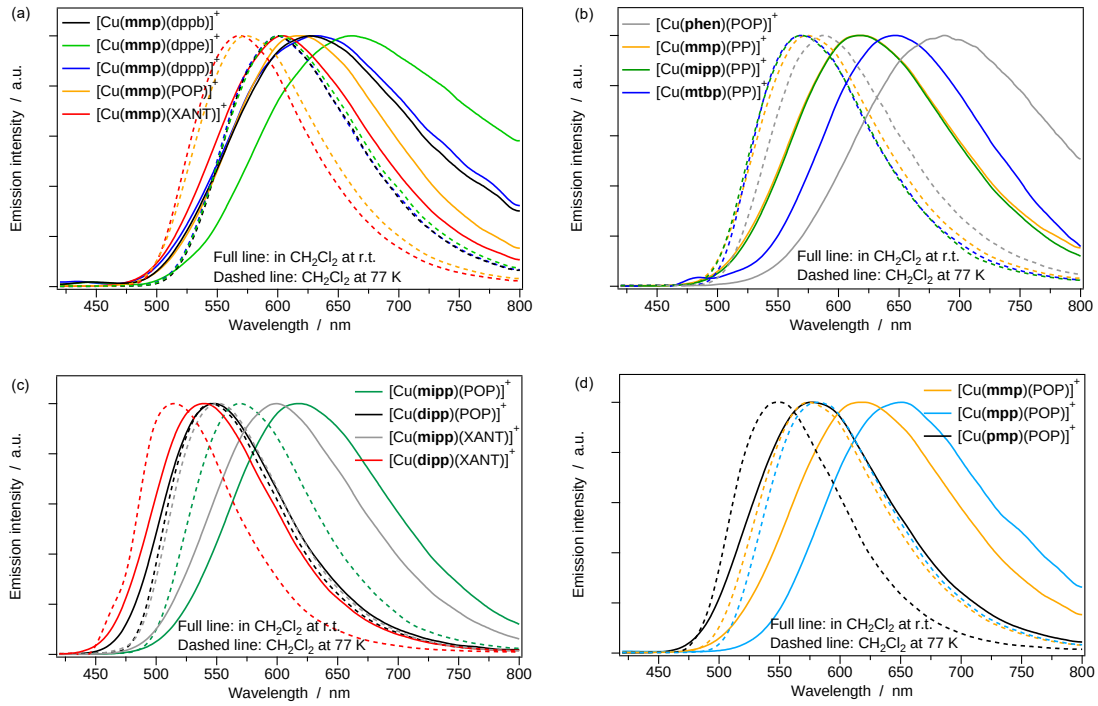

Figure 2.32. Normalized emission spectra in CH_2Cl_2 at room temperature (full lines) and at 77 K (dashed lines), (a) bite angle effect, (b) effect of the size of one single substituent on the **phen**, (c) effect of the symmetrical functionalization and (d) effect of the increase of the electronic conjugation; λ_{exc} = 360 nm.

served that (i) passing from bare **phen**, to **mmp** and **mipp** the PLQY is increased and (ii) the emission band position is unaffected (from -methyl to -isopropyl), but (iii) if a -*tert*-butyl is applied to the diimine (**mtbp**) the PLQY is reduced (respect **mmp** and **mipp**) and, as well, (iv) the energy of the emission band. Moreover, such sterically hindered complexes show also stronger bathochromic shift when the temperature is reduced to 77 K; similar observations have been reported for highly distorted excited-state geometries [141].

Equipping the **phen** ligands with two substituents in positions facing the Cu(I) core (**dmp** and **dipp**), proved to be one of the most efficient strategies to effectively enhance PLQY in DCM (ϕ_{em} = 52 % for [Cu(**dipp**)(POP)]$^+$ and ϕ_{em} = 40 % for [Cu(**bipp**)(XANTPHOS)]$^+$), but also to shift the emission to the blue (≈ 0.19–0.25 eV). Interestingly, symmetrically functionalized complexes are also less affected by the rigidochromic effect at low temperature, confirming the locking of the coordination structure.

A well-known method to red-shift the emission wavelength consists in the stabilization of the LUMO. Among other methods, such effect can be obtained by increasing the conjugation on the moiety involved in the transition. By enhancing the electronic delocalization on the **phen**, with the addition of a -phenyl group, we observed a red-shifting of 0.08–0.12 eV of the emission band, with respect the **mmp** complex (Figure 2.32 (d)). The bulky **mpp** ligand, in the presence of a large PP ligand, like POP and XANTPHOS, most probably induces a strong distortion of the coordination geometry. This affects the radiative constant, thus a weak luminescence is observed (ϕ_{em} ≈ 1–2 %). The addition of a second group (*e.g.*, methyl), to make an asymmetric complex, reduces the distortions

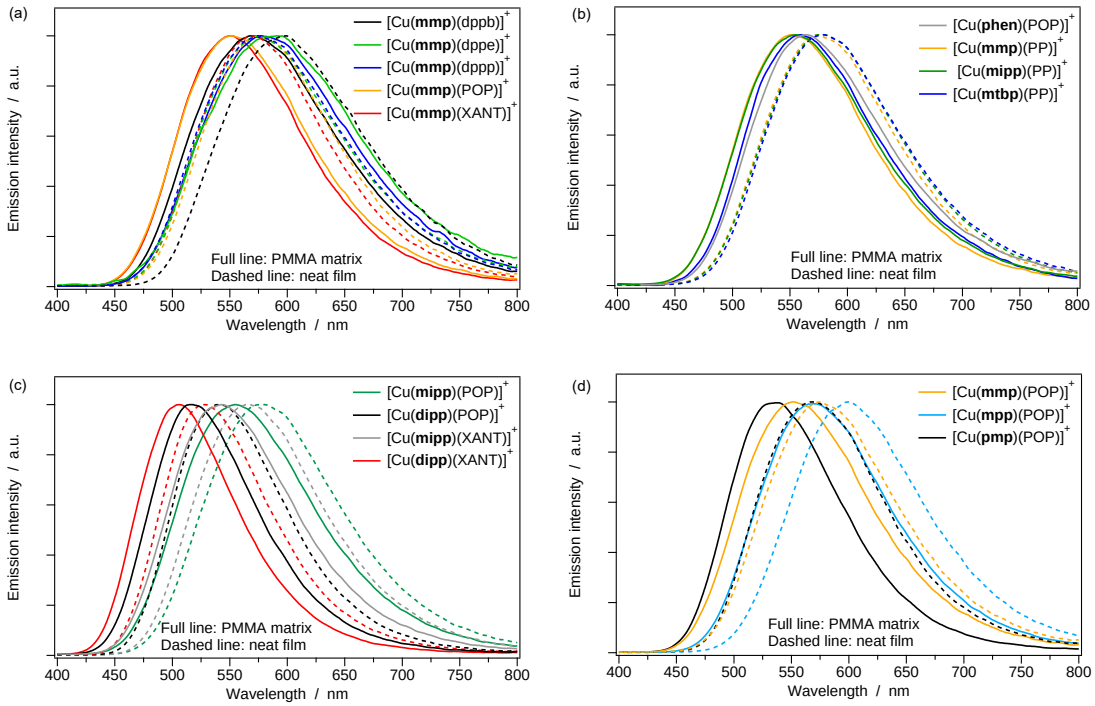

Figure 2.33. Normalized emission spectra in in PMMA (1 wt%) (full lines) and as neat film (dashed lines) at room temperature, (a) bite angle effect, (b) effect of the size of one single substituent on the **phen**, (c) effect of the symmetrical functionalization and (d) effect of the increase of the electronic conjugation; λ_{exc} = 360 nm.

and recover the emission efficiency, increasing the PLQY ($\phi_{em} \approx 25\,\%$), and blue-shifting the luminescence.

The photoluminescence of solid state samples (PMMA and neat film) is depicted in Figure 2.33 and the photophysical data are summarized in Table 2.12. The spectra are systematically shifted to higher energy with respect the liquid media, due to the rigidochromic effect. The PLQYs are considerably enhanced in solid, also for the complexes faintly-emitting in solution (see Section 2.1). Solid-state emission decays have been fitted with bi-exponential functions. The presence of multiple decay paths is most probably a consequence of the flexible pseudo-tetrahedral coordination geometry that, when complexes are embedded in rigid media, is frozen in several slightly different configurations.

Compared to CH_2Cl_2 solution, the excited-state lifetimes are increased in PMMA matrix ($\tau \approx 5$–$125\,\mu s$), while in neat film their variation is less systematic, probably due to stacking effects that promote deactivation processes that vary from complex to complex.

Trends of the luminescence efficiency and band position observed in solution are very similar in solid. In particular (i) the complexes with diphosphines displaying low bite angles exhibit weaker and red-shifted emissions compared to POP and XANTPHOS compounds, (ii) the size increase of the mono-substituted **phen** may enhance the PLQY, as long as no distortion are evidenced, then detrimental contributions are observed (as for [Cu(**mtbp**)(PP)]$^+$), (iii) doubling the substituents on the **phen**, the PLQY is increased by about a 2x factor and the emission is blue-shifted and also (iv) the asymmetrical **phen**-functionalization (**pmp** ligand) has the same effect, while (v) by extending the conjugation on the NN ligand, the emission is red-shifted and the PLQY virtually unaffected

Table 2.12. Photophysical data of the complexes in PMMA matrix (1 wt%) and as pure neat film at 298 K.

	PMMA matrix (1 wt%)				neat film		
	λ_{em} (nm)	ϕ_{em} [a] (%)	τ_1 [b] (µs)	τ_2 [b] (µs)	λ_{em} (nm)	ϕ_{em} [a] (%)	τ [b] (µs)
[Cu(**mmp**)(dppb)]$^+$	572	11.6	7.28	19.8[c]	595	5.0	3.17
[Cu(**mmp**)(dppe)]$^+$	588	3.0	5.27	19.5[c]	578	4.6	13.3
[Cu(**mmp**)(dppp)]$^+$	583	7.1	8.56	26.7[c]	578	8.7	18.9
[Cu(**mmp**)(POP)]$^+$	555	35.0	13.6[c]	31.3	577	17.4	9.16
[Cu(**mmp**)(XANT)]$^+$	552	38.8	14.2	28.9[c]	570	20.7	10.6
[Cu(**mipp**)(dppb)]$^+$	570	13.7	6.93	17.9[c]	593	4.7	2.92
[Cu(**mipp**)(dppp)]$^+$	582	8.5	9.89	27.9[c]	607	2.2	3.42
[Cu(**mipp**)(POP)]$^+$	555	43.2	18.4[c]	51.5	580	22.7	8.81
[Cu(**mipp**)(XANT)]$^+$	543	50.4	21.6[c]	45.1	568	31.7	12.3
[Cu(**mtbp**)(POP)]$^+$	560	17.9	8.59[c]	21.7	580	9.0	5.15[d]
[Cu(**mtbp**)(XANT)]$^+$	557	22.4	10.4[c]	29.7	580	13.2	5.86[d]
[Cu(**dmp**)(POP)]$^+$	520	50.0	25.3[c]	75.9	553	39.0	15.0[d]
[Cu(**dipp**)(POP)]$^+$	518	77.0	22.9[c]	53.3	542	68.7	15.0
[Cu(**bipp**)(XANT)]$^+$	505	69.3	31.9[c]	90.6	528	39.6	15.1
[Cu(**mpp**)(POP)]$^+$	571	31.9	12.9[c]	28.7	600	20.5	9.82
[Cu(**mpp**)(XANT)]$^+$	568	34.8	15.3[c]	33.9	600	6.5	6.91
[Cu(**pmp**)(POP)]$^+$	535	51.5	24.4[c]	67.7	570	10.0	9.47[d]
[Cu(**pmp**)(XANT)]$^+$	530	45.4	36.0[c]	124	555	21.6	19.4
[Cu(**phen**)(POP)]$^+$	565	11.3	14.08	-	-[e]		

[a] Determined using an integrating sphere [159], λ_{exc} = 360 nm. [b] λ_{exc} = 370 nm.
[c] predominant decay obtained from the biexponential fitting. [d] Decay reported as τ_{av}.
[e] Data not available. XANT = XANTPHOS

(respect **mmp**).

2.2.6 Conclusion

Among an overall number of thirty compounds, seventeen were not subject to significant ligand scrambling in solution and were selected for extensive characterization. We added to the study two established Cu(I) compounds for comparison purposes, [Cu(**dmp**)(POP)]$^+$ and [Cu(**phen**)(POP)]$^+$. We determined the structural, electrochemical and photophysical effects of various substituents on the **phen** ligand, together with the variation of the diphosphine bite angle. The correlation of the above properties has been systematically determined in the case of six different types of modification of the NN ligand: (i) mono-substitution (2-position) with alkyl moieties, (ii) size of this moiety, (iii) symmetrical functionalization (2,9-position), (iv) asymmetrical functionalization (on the same position), (v) expansion of the conjugation by introducing a phenyl moiety and (vi) P–Cu–P bite angle. We highlighted the presence of concomitant contributions, like the

electronic inductive effect, with the introduction of alkyl functionality, which may increase the HOMO-LUMO energy gap or the steric effect that can lock the geometry and protect the Cu(I) core from the oxidation, or even induce distortions when the group is too bulky.
The structure-property relationships highlighted that the most intense photoluminescence in solution is observed upon the addition of groups in both the 2,9-position of the phenanthroline. However, for solid state luminescence applications, also some monosubstituted **phen** systems are very promising. Finally, a fine tuning of the emission band also with the possibility to control the excited state lifetime, has been demonstrated feasible, opening the possibility to use these Cu(I) complexes in a wide range of applications.

2.3 Increasing the stability of $[Cu(NN)(PP)]^+$: *Topological constraints*

The thermal and photochemical instability of Copper(I) complexes, particularly in solution (Paragraph 2.0.4), is the main drawback that prevents the commercial exploitation of this class of coordination compounds for electroluminescent devices. For this reason, their luminescence properties are in most cases reported only in the solid state, as instability in solution may affect the reproducibility of experimental measurements.
The ligand exchange equilibria in solution can be partially controlled by a thorough selection of ligands that can minimize steric congestion, but further instability can occur due to the strong reducing character of Cu(I) complexes in the excited state.
As part of this research, a new class of heteroleptic copper(I) complexes has been studied, which is constructed from macrocyclic phenanthroline ligands and diphosphines. In this case, owing to the molecular design, the formation of the homoleptic macrocyclic complex is impossible, thus, when compared to analogous $[Cu(NN)(PP)]^+$ constructed from acyclic NN ligands, a higher stability is observed (see Figure 2.3).
The 2,9 position, as highlighted in Paragraph 2.0.3 is the best choice to minimize excited-state distortion, hence favor the radiative deactivation from this state. Preliminary investigations, made to evaluate the reaction feasibility and the validity of the idea, were performed using a macrocycle containing a 2,9-diphenyl-1,10-phenanthroline unit (**M30**, 30 atoms). However, the rigidity given by the phenyls in 2,9 position, together with the relative small size of the macrocycle, afforded a dinuclear trigonal complex in the presence of a dppp NN ligand, or even an almost totally unthreaded and highly rocked (angle *ca.* 37°) complex in presence of a chelating POP ligand (Figure 2.34) [64]. For both the coordination geometries, as confirmed by NMR (^{1}H and ^{31}P) and the X-ray crystal structures, the macrocycle is not adequate to prevent decomposition in solution and improve the luminescence properties. The signal broadening observed with NMR supports a fast dynamic interconversion between tri- and tetra-coordination in the case of $[Cu(\mathbf{M30})(POP)]^+$, due to the crowded and highly distorted structure. The *negative steric effect* is avoided in the presence of dppp which serves as chelating or bridging ligand, depending on the congestion of the Cu(I) core. The presence of the small and rigid **M30**

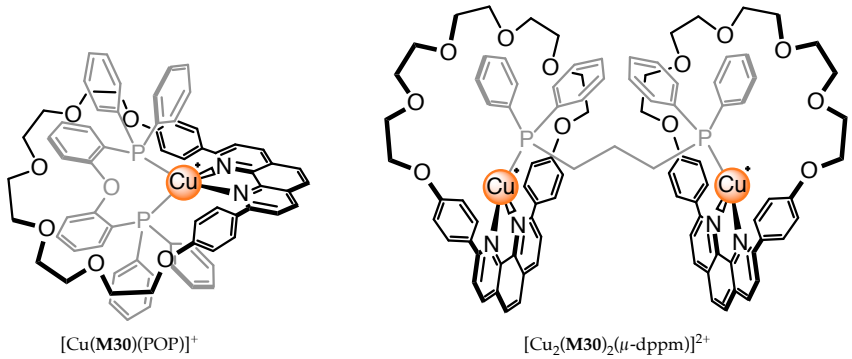

$[Cu(\mathbf{M30})(POP)]^+$ $[Cu_2(\mathbf{M30})_2(\mu\text{-dppm})]^{2+}$

Figure 2.34. Pseudoraxane $[Cu(\mathbf{M30})(POP)]^+$ and $[Cu_2(\mathbf{M30})_2(\mu\text{-dppp})]^{2+}$ complexes, as $[BF_4]^-$ salt, prepared for preliminary screening. Reproduced from [64].

macrocycle forces the bridged dinuclear form that shows better stability with respect to [Cu(**M30**)(POP)]$^+$. At any rate, the photophysical properties observed for this dinuclear complex are far from optimal. Therefore, despite the very interesting results in terms of coordination chemistry, the **M30** ligand does not seem to be appropriate to validate the *topological constraint* and increase the stability of heteroleptic Cu(I) complexes in solution.

2.3.1 The pseudo-rotaxane series

A new series of [Cu(NN)(PP)]$^+$incorporating macrocyclic phenanthroline ligands has been designed, exhibiting a larger ring size and a more flexible substituent in 2,9 positions of the phenanthroline.
A detailed study of the electronic, structural and topological properties of these three new complexes is reported herein. The copper(I) pseudorotaxanes are depicted in Figure 2.35. They differ for the size of the macrocycle, constituted by 30 (**m30**), 37 (**m37**) and 42 (**m42**) atoms. The smaller macrocycle has a flexible 2,9-dibutyl-1,10-phenanthroline chelator grafted to the crown ether moiety, while in the the larger ligands the alkyl functionality on the phenanthroline is replaced by a more rigid phenethyl group. The structural difference does not seem to affect the rigidity of the complexes, which, on the contrary, is correlated to the size of the macrocycle. The behavior of this series is also compared to that of the model complex **17** (*i.e.*, [Cu(**dmp**)(POP)]$^+$, Figure 2.5) previously reported. TADF is assessed for all of the compounds of the series, and a comparative study on OLED devices is reported. The results and discussion given in this section are essentially following the ones given in this reference [63].

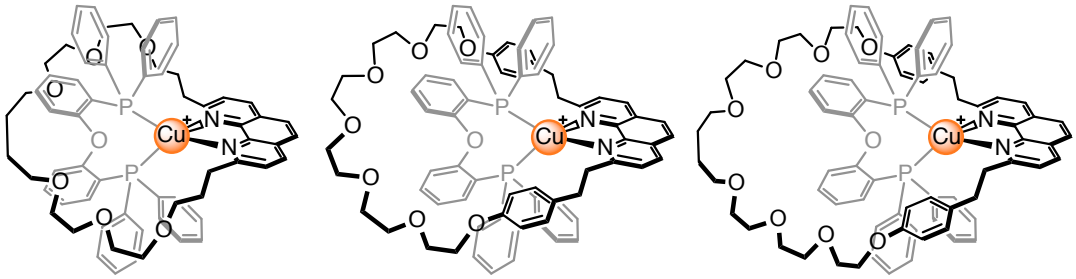

(**29**) [Cu(**m30**)(POP)]$^+$ (**30**) [Cu(**m37**)(POP)]$^+$ (**31**) [Cu(**m42**)(POP)]$^+$

Figure 2.35. Pseudorotaxane [Cu(NN)(PP)]$^+$complexes **29-31** as $[BF_4]^-$ salt.

2.3.2 X-ray single crystal structures

The coordination structure suggested by ^{1}H and ^{31}P NMR and electrospray mass spectrometry, has been confirmed for the [Cu(**m30**)(POP)]$^+$ and [Cu(**m37**)(POP)]$^+$ complexes by X-ray diffraction,[4] indeed single crystals for these compounds were obtained following the procedure reported in Appendix A. Both the structures show a moderate disorder in the ethylene glycol chain due to its flexibility, but the POP and the phenanthroline are well resolved, thus the pseudo-tetrahedral identity of the complexes is unambiguously

[4]X-ray measurement have been performed by the group of Jean-François Nierengarten, CNRS, Strasbourg, France.

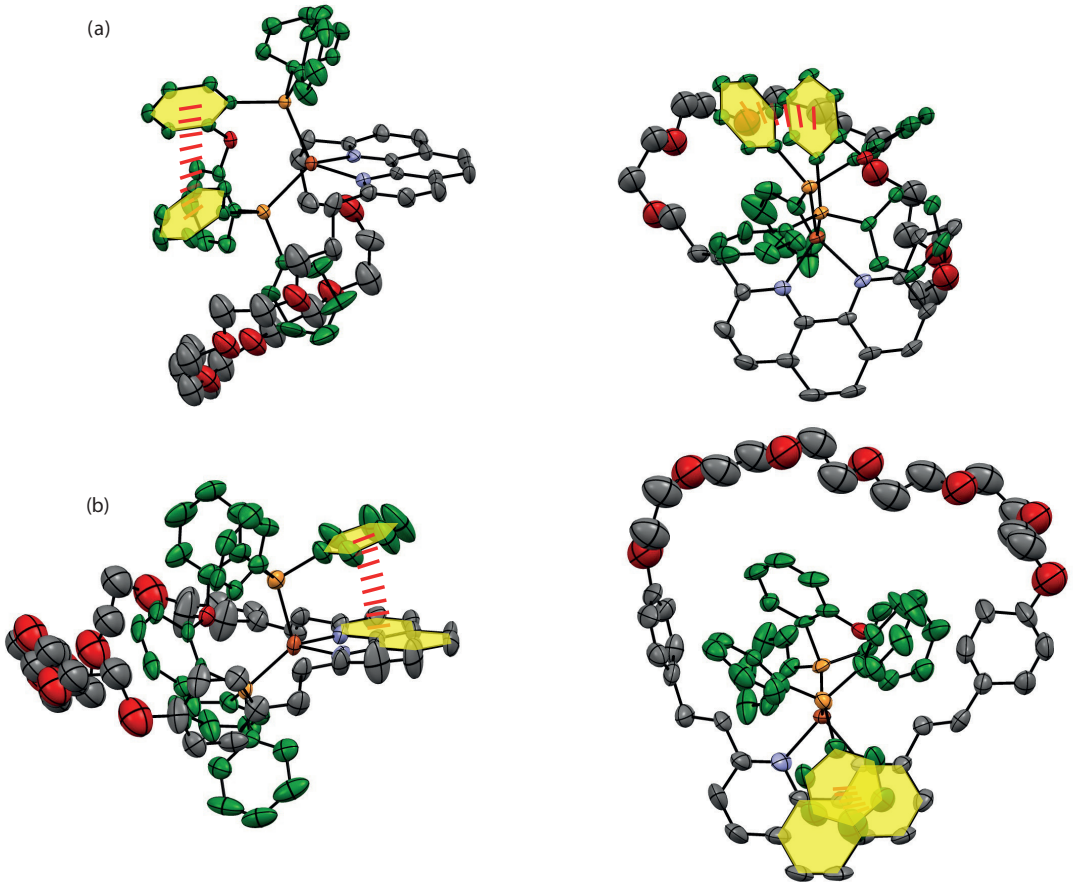

Figure 2.36. ORTEP representation of the structure of $[Cu(\mathbf{m30})(POP)]^+$ (a) and $[Cu(\mathbf{m37})(POP)]^+$ (b) complexes on two different views. Thermal ellipsoids are drawn at the 50% probability level, the POP phenyls are highlighted in green, yellow areas and red lines show the π-interactions. Thermal ellipsoids are plotted at the 50 % probability, using Mercury CSD 3.10 [165]. H atoms and $[BF_4]^-$ counterions are omitted.

confirmed [172, 173].

In $[Cu(\mathbf{m30})(POP)]^+$ the macrocycle only partially threads the POP ligand. The **m30** is completely folded and just one of the phenyl groups of the POP is nested inside the ring cavity, whereas the rest of the chelating diphosphine is located outside (Figure 2.36 (a)). However, this peculiar conformation of the macrocycle does not seem to affect the pseudo-tetrahedral coordination geometry of the Cu(I) core, that shows interatomic distances (Cu–P and Cu–N) and angles (P–Cu–P, P–Cu–N and N–Cu–N) comparable to the standard $[Cu(\mathbf{dmp})(POP)]^+$complex (Figure 2.37 (a) and Table 2.13) [48].

For the sake of comparison, the same macrocycle has been reported for another Cu(I) complex, in combination with the smaller dppe ligand [173]. In this case, the less bulky diphosphine is perfectly threaded by the ring and $[Cu(\mathbf{m30})(dppe)]^+$ crystallize in a symmetrical C_2v fashion. On the other side, the less crowded coordination compound (the dppe has four phenyl groups instead of the six of the POP) is more prone to distortion. Accordingly, also in the absence of evident intra- and intermolecular π-interaction, the complex adopts a slightly rocked configuration (angle $\approx 10°$) to maximize the space filling.

Table 2.13. Selected interatomic distance and angles of [Cu(**m30**)(POP)]$^+$ and [Cu(**m37**)(POP)]$^+$ and the equivalent macrocyclic-free [Cu(**dmp**)(POP)]$^+$ [48] and [Cu(**dpep**)(POP)]$^+$ [53] complexes, as obtained from X-ray single crystal structure.

	Cu–N	Cu–P	Cu–O	N–Cu–N	P–Cu–P	phen–PCuP	
	bond length (Å)			angle (°)		dihedral angle (°)	CCDC
[Cu(**m30**)(POP)]$^+$	2.095 2.140	2.287 2.288	3.157	79.77	111.99	81.02	975746
[Cu(**dmp**)(POP)]$^+$	2.084 2.104	2.269 2.273	3.151	80.88	116.44	81.02	177685
[Cu(**m37**)(POP)]$^+$	2.061 2.092	2.238 2.326	3.256	81.87	117.43	88.38	877890
[Cu(**dpep**)(POP)]$^+$	2.082 2.088	2.237 2.308	3.226	80.86	117.98	86.10	288414

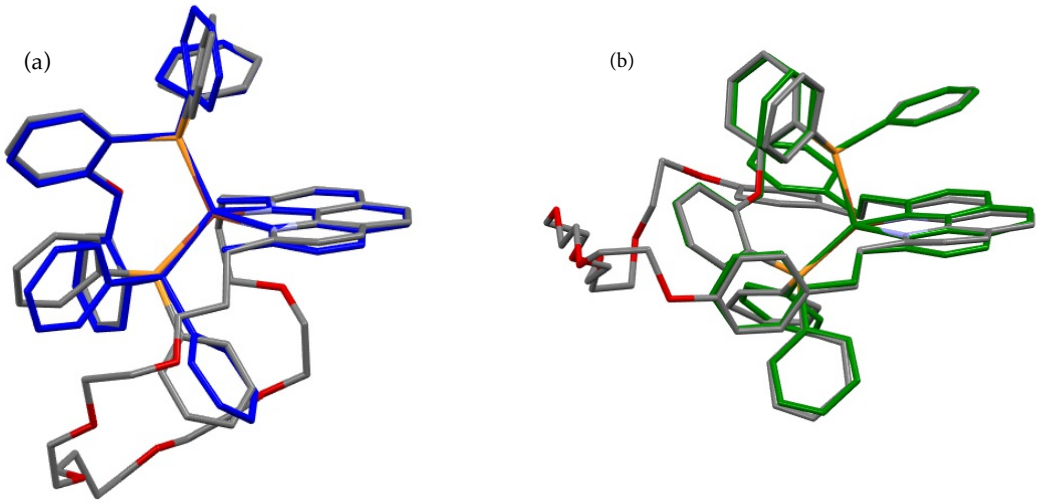

Figure 2.37. X-ray single crystal structure comparison between [Cu(**m30**)(POP)]$^+$ (a) or [Cu(**m37**)(POP)]$^+$ (b), reported with element-dependent colors, and [Cu(**dmp**)(POP)]$^+$ (blue, from [48]) or [Cu(**dpep**)(POP)]$^+$ (green, from [53]), respectively. The superimposition minimizes the RMSD on all the atoms; visualizations were performed by Mercury CSD 3.10 [165]. H atoms and counterions are omitted from the calculation and Figure.

The single crystal structure of the [Cu(**m37**)(POP)]$^+$ shows a complete threading of the POP ligand by the macrocyclic phenanthroline (Figure 2.36 (b)). The ring is large enough to avoid any constraint to the coordination structure and, as a matter of fact, one of the POP phenyls is free to form a π-interaction with the phenanthroline moiety, inducing a significant rocking of the PP ligand (ca. 17.5°), as also observed in the free macrocycle [Cu(**dpep**)(POP)]$^+$ (Figure 2.37 (b)) [53].
The PP bite angle for both of the complexes is in the range of 112–118°, in line with other complexes bearing this type of diphosphine. The smaller bite angle observed for **m30**

complex is due to a π-interaction between two POP phenyls that contract this ligand. Moreover, the difference in the phenanthroline NN bite angle, assuming a fixed geometry, is caused by the variation of the Cu–N bond length, that is strictly related to the change of the PP bite angle. Unlike what obsereved in Paragraph 2.1, the shorter Cu–N bond length observed for [Cu(**m37**)(POP)]$^+$, with respect to [Cu(**m30**)(POP)]$^+$, and the related increase of the N–Cu–N angle, is most probably due to the highly rocked PP ligand that, losing the C_{2v} symmetry shows a peculiar elongation of one of the Cu–P bonds. Therefore, despite the larger bite angle, there is less repulsion with the phenanthroline counterpart.

2.3.3 Pseudo-rotaxane conformers

The X-ray structures of [Cu(**m30**)(POP)]$^+$ and [Cu(**m37**)(POP)]$^+$ evidence the high flexibility of the ethylene glycol moiety. As a consequence, various conformers might occur in the absence of the crystal constraints, but the large POP ligand can hinder the movement of the ring and promote its locking in different position (*e.g.*, threaded and unthreaded).
Interesting results were reported by Mohankumar and coworkers for [Cu(**m30**)(POP)]$^+$: (i) at room temperature the ^{31}P NMR shows a single resonance peak suggesting the equivalence of the two P atoms of the diphosphine, while (ii) at low temperature, a nonequivalent chemical shift of the two phosphorous is observed, caused by the different shielding effect of the macrocycle on these atoms [172].
This signal splitting is not commonly observed in classic [Cu(NN)(PP)]$^+$ [75], neither in the pseudorotaxane [Cu(**m30**)(dppe)]$^+$ bearing a small diphosphine [172]: in both cases a single sharp resonance peak related to both the P atoms is obtained and the temperature does not affect the experiment. At room temperature, in the presence of the macrocycle and of a bulky diphosphine (*e.g.*, POP, having a smaller size, but comparable to that of the macrocycle) a fast dynamic exchange among conformers take place, as proved by a single resonance ^{31}P NMR peak. By cooling down the solution, the interconversion rate slows down and, at certain temperature, the exchange becomes slower than the timescale of an NMR experiment, thus it possible to observe the splitting of the signal in doublets and singlet, signalling the presence of different conformers.
We repeated the ^{1}H and ^{31}P NMR spectra for all the [Cu(**mXX**)(POP)]$^+$ (with **mXX**= **m30**, **m37** or **m42**) to quantify the effect of the ring size on its mobility. In CD_2Cl_2 at room temperature none of the three complexes reveals the presence of uncoordinated species (see Paragraph 2.0.4). The dynamic exchange between coordinated and uncoordinated species, is most probably faster than the NMR time scale and average spectra are obtained. Indeed, electrochemical studies suggest the presence of traces of [Cu(**mXX**)]$^+$, showing that a very minor amount of POP ligands is effectively non-coordinated in CH_2Cl_2 solution (see Paragraph 2.3.4).
The dynamic exchange between different conformers was effectively evidenced also for [Cu(**m37**)(POP)]$^+$ and [Cu(**m42**)(POP)]$^+$. As shown in Figure 2.38, the ^{31}P NMR spectra of these complexes, recorded at low temperature, show singlet signals attributed to the C_2v symmetrical conformer (B, top inset in Figure 2.38) and a more complicated set of signals for the partially threaded one (A and its enantiomer A'). In the latter case, the macrocyclic ligand adopts a folded conformation in which one or two phenyl groups of the POP moiety is located within the cavity of the macrocycle whereas the remaining

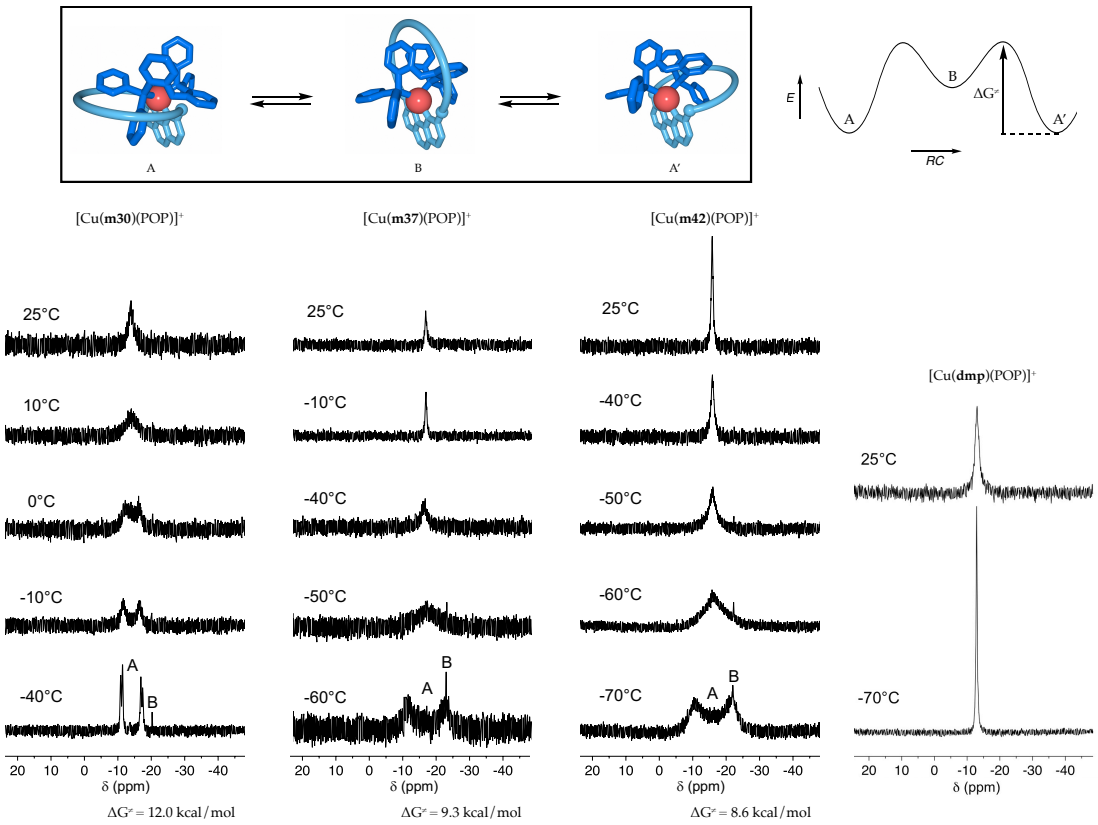

Figure 2.38. Schematic representation of conformers A, B, and A' (top insets, A and A' are enantiomers) and potential energy diagram of the dynamic exchange between A, B, and A' (right). ^{31}P NMR spectra (CD_2Cl_2, 202 MHz) of [Cu(**m30**)(POP)]$^+$, [Cu(**m37**)(POP)]$^+$, [Cu(**m42**)(POP)]$^+$ and [Cu(**dmp**)(POP)]$^+$ recorded at different temperatures.

others are located on one same side of the ring. As a result, the two P atoms of the POP ligand are no longer equivalent, and two sets of signals are observed in the ^{31}P NMR spectra. The bridging unit of the POP ligand is actually quite large and generates steric congestion, destabilizing conformer B, thus it is observed only at low temperature. Despite increased ring size, due the particular structure of the POP, the dynamic conformational equilibrium is still in favor of A for both [Cu(**m37**)(POP)]$^+$and [Cu(**m42**)(POP)]$^+$, as it was the case for the corresponding complex with the smallest macrocycle (**m30**). At higher temperatures, the dynamic exchange between conformers A and B is faster than the NMR time scale and a single resonance is obtained in the ^{31}P NMR spectra. By lowering the temperature, the dynamic exchange rate is reduced accordingly, until the coalescence point that corresponds to the signal changees from singlet to doublet. At this temperature a plateau is usually observed, and it is possible to calculate the rate constant of the dynamic process (k_{T_c}):

$$k_{T_c} = \pi \frac{\Delta \nu}{\sqrt{2}} \tag{2.2}$$

where $\Delta\nu$ is the difference between the chemical shifts of the doublet (in Hz). Applying the Eyring equation, then, it can be determined the free energy of activation ($\Delta G^{\neq}$, top

left in Figure 2.38) of the dynamic exchange among the conformers:

$$\Delta G^{\neq} = -RT \ln \frac{k_{T_c} h}{k_b T} \tag{2.3}$$

where R is the gas constant, T is the temperature (in K), h is the Planck constant and k_b correspond to the Boltzmann constant. The value of the energy barrier $\Delta G^{\neq}$ have been estimated [174] and however decreased by increasing the size of the macrocyclic ligands (**m30**: 12 kcal mol^{-1}, **m37**: 9.3 kcal mol^{-1}, and **m42**: 8.6 kcal mol^{-1}). Control experiments were also carried out with [Cu(**dmp**)(POP)]$^+$. At low temperature, the ^{31}P NMR spectrum of the **dmp** derivative shows a sharp singlet, thus confirming that the dynamic behavior observed for the pseudorotaxanes is specific to complexes incorporating a macrocyclic phenanthroline ligand and sterically demanding diphosphine (Figure 2.38).

2.3.4 Electrochemical Proporties

These compounds are stable for several hours in CH_2Cl_2 solutions under argon. In the particular case of [Cu(**m30**)(POP)]$^+$, oxidation of the POP ligand as well as the appearance of traces of Cu(II) species have been evidenced when the CH_2Cl_2 solutions are kept under air for several days (Figure 2.44). Similar observations were also done for CH_2Cl_2 solutions of the complexes incorporating larger macrocyclic ligands; however, the oxidation is far more limited for [Cu(**m37**)(POP)]$^+$ and [Cu(**m42**)(POP)]$^+$. These observations suggest a dynamic decoordination/coordination of the POP ligand. In this way, less stabilized Cu(I) species sensitive to oxygen are present in solution thus promoting the observed slow oxidations. The electrochemical properties of [Cu(**mXX**)(POP)]$^+$ were determined by CVs and OSWVs (see Appendix A).[5]

All the experiments were performed at room temperature in CH_2Cl_2 solutions containing [nBu$_4$N][BF$_4$] (0.10 M) as supporting electrolyte and ferrocene (Fc) as internal

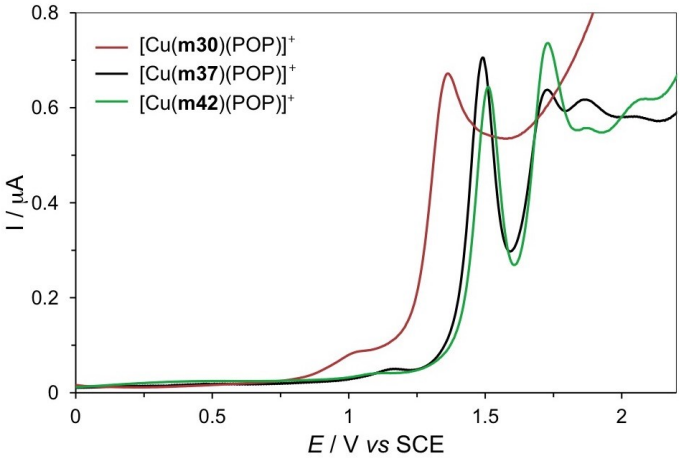

Figure 2.39. OSWVs (anodic scans) of the [Cu(**mXX**)(POP)]$^+$ series, on a Pt electrode in CH_2Cl_2 + 0.1 M [nBu$_4$N][BF$_4$] at room temperature (frequency 20 Hz, amplitude 20 mV, step potential 5 mV).

[5]Electrochemical measurement has been performed by Béatrice Delavaux-Nicot and coworkers, Laboratoire de Chimie de Coordination du CNRS in Toulouse, France.

Table 2.14. Electrochemical data of [Cu(**mXX**)(POP)]$^+$ series and [Cu(**dmp**)(POP)]$^+$ as reference, determined by OSWVs at room temperature. Potential values in volts vs SCE (Fc^+/Fc is observed at 0.55 ± 0.01 V vs SCE). Ferrocene has been used as internal reference.

	E_{Ox1} (V)	E_{Ox2} (V)	E_{Red} (V)	ΔE_{Redox} (V)
[Cu(**m30**)(POP)]$^+$	+1.35[a]		−1.66	3.01
[Cu(**m37**)(POP)]$^+$	+1.50[b]	+1.72	−1.65	3.15
[Cu(**m42**)(POP)]$^+$	+1.52[b]	+1.73	−1.63	3.15
[Cu(**dmp**)(POP)]$^+$[c]	+1.45[b]		−1.66	3.11

[a] Chemically irreversible process in CV.
[b] Electrochemically irreversible process in CV as the oxidation of the metal center is immediately followed by the oxidation of the phosphorus ligand.
[c] Data from ref. [175].

reference, with a Pt wire as the working electrode and a saturated calomel electrode (SCE) as a reference. Potential data for all of the compounds are collected in Table 2.14, and the anodic OSWV are reported in Figure 2.39, while complete voltammograms and OSWVs are shown in Figures 2.40 – 2.42. For comparison purposes, the redox potentials of model compound [Cu(**dmp**)(POP)]$^+$ obtained under identical experimental conditions are also included in Table 2.14 [175].

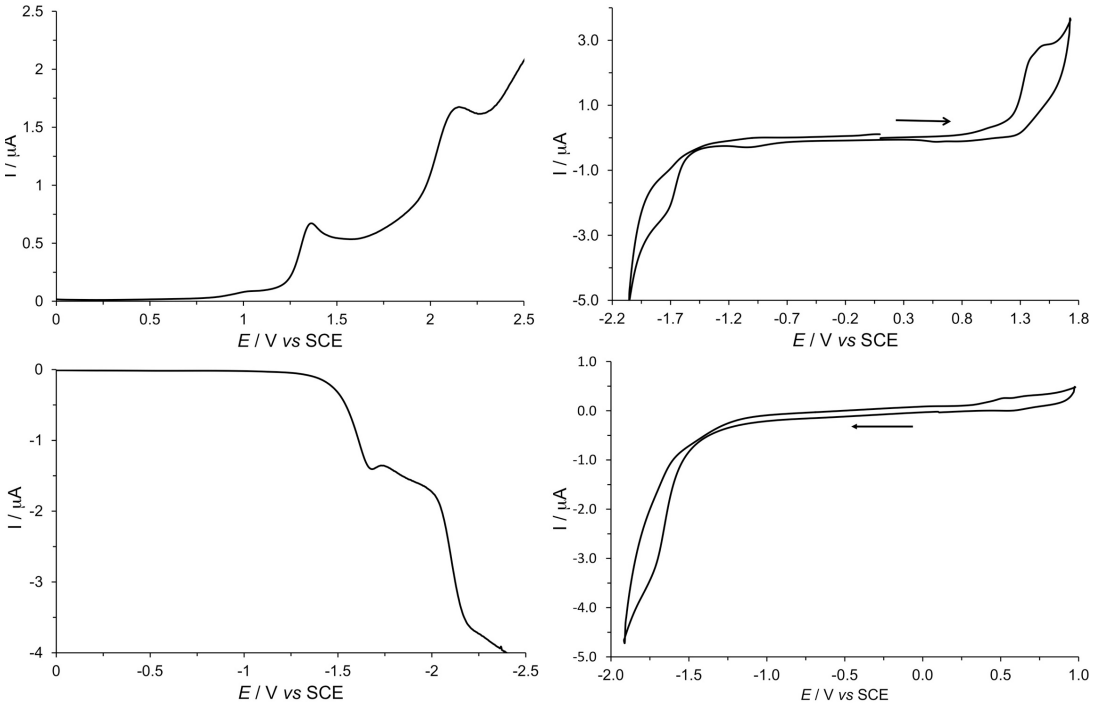

Figure 2.40. OSWVs (left column, anodic (top) and cathodic (bottom) scans), and representative cyclic voltammograms (right column) of [Cu(**m30**)(POP)]$^+$ on a Pt electrode in CH_2Cl_2 + 0.1 M [nBu$_4$N][BF$_4$] at room temperature (OSWVs: frequency 20 Hz, amplitude 20 mV, step potential 5 mV; CVs: scan rate 200 mV s^{-1}).

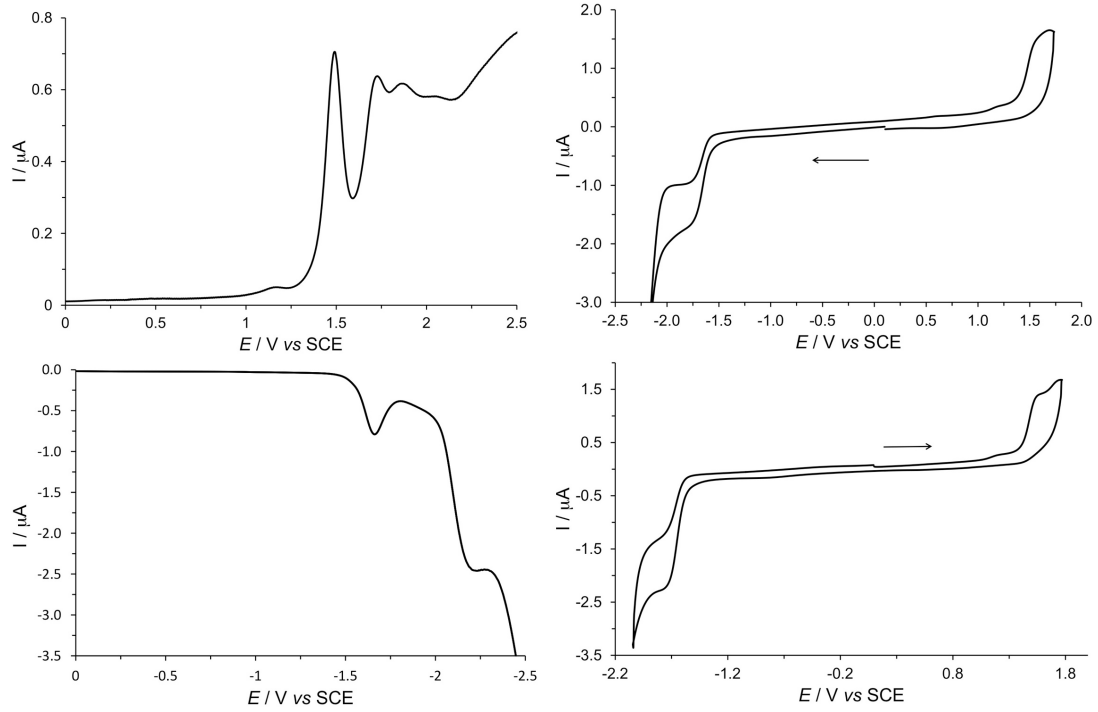

Figure 2.41. OSWVs (left column, anodic (top) and cathodic (bottom) scans), and representative cyclic voltammograms (right column) of $[Cu(\mathbf{m37})(POP)]^+$ on a Pt electrode in CH_2Cl_2 + 0.1 M $[n Bu_4N][BF_4]$ at room temperature (OSWVs: frequency 20 Hz, amplitude 20 mV, step potential 5 mV; CVs: scan rate 200 mV s^{-1}).

In the cathodic region, all the pseudorotaxanes revealed the typical electrochemical response of $[Cu(NN)(PP)]^+$derivatives [175], and the observed one-electron transfer process is centered on the phenanthroline moiety. In the anodic region, the one-electron transfer attributed to the Cu(II)/Cu(I) redox couple is observed at +1.35 V vs SCE for pseudorotaxane $[Cu(\mathbf{m30})(POP)]^+$. It can be noted that this oxidation is preceded by a wave of small intensity at +1.02 V vs SCE (Figure 2.39). The latter was tentatively ascribed to the presence of small amounts of $[Cu(\mathbf{m30})]^+$ in solution as already mentioned (vide supra). Moreover, CV revealed an electrochemical instability for $[Cu(\mathbf{m30})(POP)]^+$ and decomposition was evidenced upon oxidation. In contrast, the behavior of $[Cu(\mathbf{m37})(POP)]^+$ and $[Cu(\mathbf{m42})(POP)]^+$ is closer to that of the model compound $[Cu(\mathbf{dmp})(POP)]^+$. It can be noted that the oxidation of the Cu(I) center is slightly more difficult in the case of $[Cu(\mathbf{m37})(POP)]^+$ and $[Cu(\mathbf{m42})(POP)]^+$ when compared to $[Cu(\mathbf{dmp})(POP)]^+$ (ΔE = 50 and 70 mV, respectively). Indeed, the increased size of the 2,9-substituents on the phenanthroline ligand in $[Cu(\mathbf{m37})(POP)]^+$ and $[Cu(\mathbf{m42})(POP)]^+$ prevents the formation of a more flattened structure appropriate for the Cu(II) oxidation states [36, 37, 167, 168]. The potential shift results therefore from the destabilization of the Cu(II) complexes as typically observed in the case of homoleptic $[Cu(NN)_2]^+$ complexes.
For both $[Cu(\mathbf{m37})(POP)]^+$and $[Cu(\mathbf{m42})(POP)]^+$, the metal-centered oxidation is preceded by a wave of very small intensity as observed for the pseudorotaxane incorporating **m30**. The intensity of this wave is however significantly smaller for $[Cu(\mathbf{m37})(POP)]^+$ and virtually absent in the case of $[Cu(\mathbf{m42})(POP)]^+$. Indeed, the steric congestion resulting from the macrocyclic nature of the NN ligand is high for the Cu(I) pseudorotaxane with the smallest macrocycle (**m30**) thus generating some instability. By increasing the

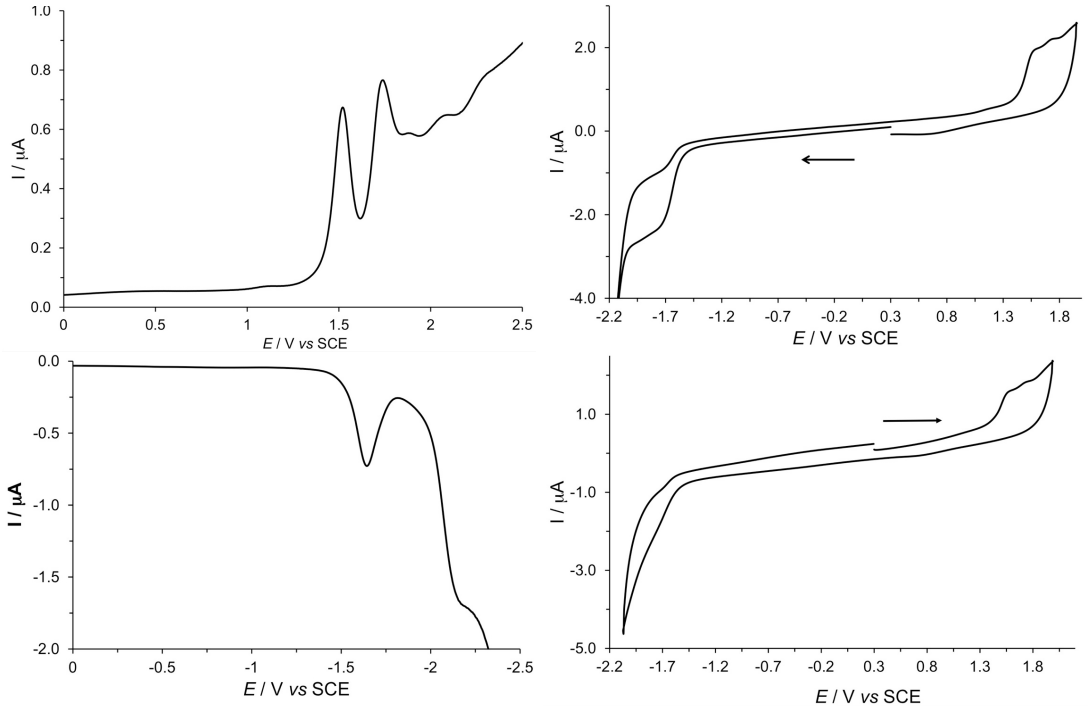

Figure 2.42. OSWVs (left column, anodic (top) and cathodic (bottom) scans), and representative cyclic voltammograms (right column) of $[Cu(\mathbf{m42})(POP)]^+$ on a Pt electrode in CH_2Cl_2 + 0.1 M $[n Bu_4N][BF_4]$ at room temperature (OSWVs: frequency 20 Hz, amplitude 20 mV, step potential 5 mV; CVs: scan rate 200 mV s^{-1}).

size of the macrocycle, this effect is progressively suppressed. This is also consistent with the differences observed along the series for the free energy of activation ($\Delta G^{\neq}$) estimated from the NMR data for the dynamic exchange between conformers.

2.3.5 Photophysical properties

The UV–Vis absorption spectra of $[Cu(\mathbf{mXX})(POP)]^+$ in CH_2Cl_2 are gathered in Figure 2.43, an example of excitation spectra is reported in Figure 2.44 (a). The experimental measurements were made on freshly prepared samples bubbled with argon for at least 20 min. All the pseudorotaxanes exhibit good stability at room temperature upon deaeration and under normal daily light for some hours in CH_2Cl_2, as shown in Figure 2.44 (b), by the absorption spectra recorded over time for $[Cu(\mathbf{m30})(POP)]^+$, the slightly less stable compound of the series. They are similar to previously reported spectra of heteroleptic cuprous complexes with phenanthroline and POP ligands, including $[Cu(\mathbf{dmp})(POP)]^+$ [48–50, 53, 54, 57, 169]. In particular, they show a relatively strong band in the UV, around 280 nm [170], mainly attributable to the phenanthroline ligand with some contribution from the POP moiety [126]. Additionally, a broader and weaker band at about 380 nm is observed, the MLCT transitions from the copper center to the phenanthroline ligand [48–50, 53, 54, 57, 169]. The spectra of the complexes with the largest macrocycles (**m37**, **m42**) are nearly superimposable, whereas the smaller analogue exhibits slightly broader features, suggesting a more distorted coordination environment.

The photoluminescence properties of the three pseudorotaxanes were investigated both

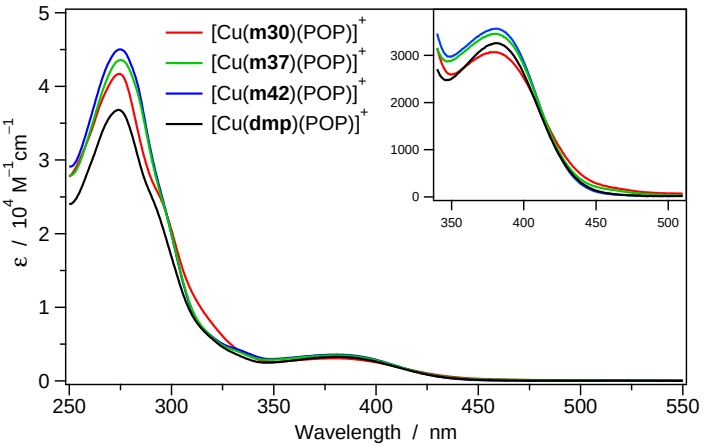

Figure 2.43. Absorption spectra of the complexes in CH_2Cl_2 at 298 K.

at 298 K (CH_2Cl_2 solution, PMMA matrix, pure powders, neat films) and at 77 K (CH_2Cl_2 rigid matrix). Luminescence spectra in CH_2Cl_2 at 298 K are nearly identical in shape and width and show extensive overlap also with $[Cu(\mathbf{dmp})(POP)]^+$; only a small blue-shift (8 nm) is found for the compound with the smallest ring (Figure 2.45 (a), Table 2.15).

Similarly to other heteroleptic $[Cu(NN)(PP)]^+$ complexes [48–50, 53, 54, 57, 169] the PLQY (ϕ_{em}, Table 2.15) is weak in aerated solution ($\phi_{em} \approx 0.7$–0.8 %), but gets remarkably enhanced upon oxygen removal ($\phi_{em} \approx 20$–30 %). In parallel, excited-state lifetimes are increased from 0.2–0.3 µs to 9–11 µs (Table 2.15). This trend supports a triplet character (^{3}MLCT) of the observed excited state [48–50, 53, 54, 57, 169].

In rigid CH_2Cl_2 at 77 K, the emission spectra are blue-shifted with respect to 298 K. The shift is less pronounced in the smallest system, again suggesting a more constrained environment, taking also into account that $[Cu(\mathbf{dmp})(POP)]^+$ shows the most pronounced blue-shift. Under these conditions a weak emission band on the high-energy side has been detected and is attributed to phosphorescence from some free phenanthroline ligand (Figure 2.45 (b)), by means of lifetime mapping and time-gated luminescence measurements.

By recording the emission spectra of the three pseudorotaxanes in a wide temperature range in CH_2Cl_2 (77–308 K), we observed that the spectral shift is not homogeneous. In

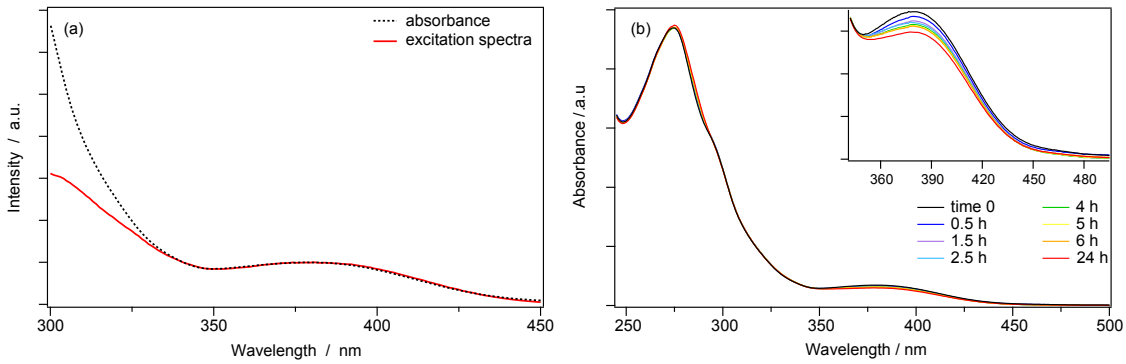

Figure 2.44. Absorption (dotted line) and excitation (full line) spectra (a) of $[Cu(\mathbf{m30})(POP)]^+$ (λ_{em} = 566 nm). Absorption spectra (b) of $[Cu(\mathbf{m30})(POP)]^+$ taken at several time intervals after sample solubilization. Spectra recorded in CH_2Cl_2 at 298 K.

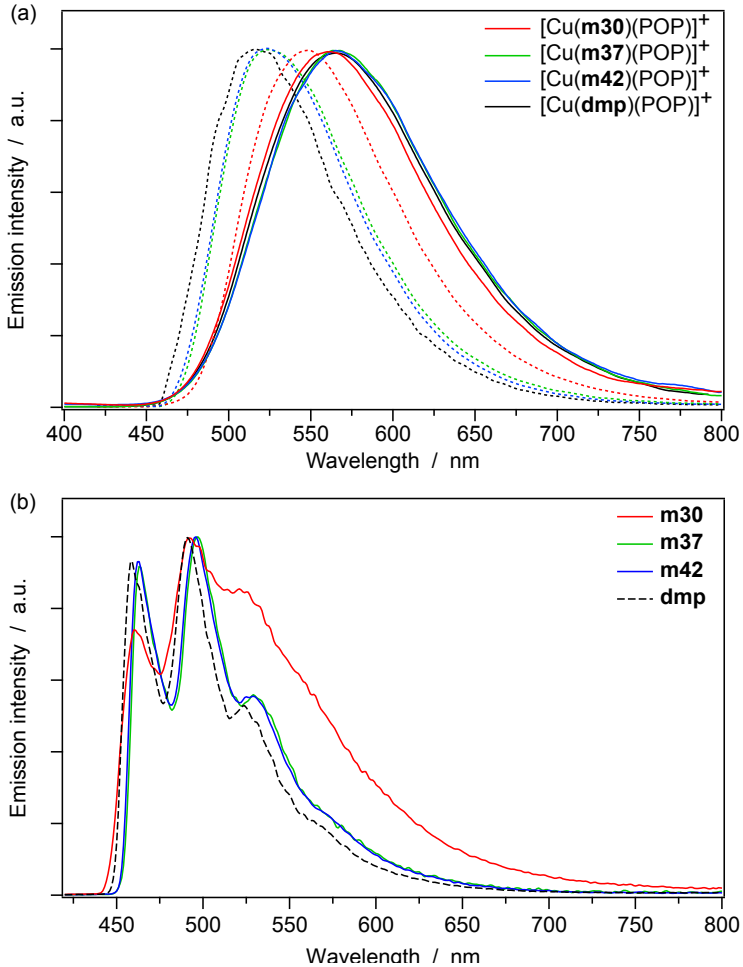

Figure 2.45. (a) Luminescence spectra in CH_2Cl_2 at 298 K (full line) and 77 K rigid matrix (dotted line). (b) Phosphorescence spectra of **m30**, **m37**, **m42** and **dmp** ligands in CH_2Cl_2 at 77 K. λ_{exc} = 380 nm.

the liquid CH_2Cl_2 domain, the temperature decrease (308–178 K) brings about a red shift (in line with the typical behavior of Cu(I) complexes in which the lowest singlet and triplet states are thermally equilibrated) [161], but when the matrix is solid, the temperature decrease (178–77 K) leads to a blue shift, because rigidochromic effects in the glass matrix prevail over electronic ones (Figure 2.46).
The luminescence properties were further investigated in PMMA rigid matrix (1 wt%), as powders or in neat films at 298 K; the spectra are reported in Figure 2.47 and the related photophysical data in Table 2.16. The spectra are blue-shifted compared to room temperature solution due to rigidochromic effects, and photoluminescence quantum yields are substantially higher particularly in PMMA, where they are all above 40 %. Emission decays in PMMA are best fitted with biexponential functions yielding lifetimes in the range of 20–80 µs, higher than in deaerated CH_2Cl_2 solution, but one order of magnitude shorter than at 77 K. The presence of various luminescence decays may be assigned to the plethora of slightly different coordination geometries locked by the rigid environment.

Table 2.15. Photophysical data in CH_2Cl_2 at 298 K and 77 K[a].

	CH_2Cl_2 at 298 K					CH_2Cl_2 at 77 K	
	λ_{em} (nm)	ϕ_{em}[a] (%)	τ (µs)	k_r (10^4 s^{-1})	k_{nr} (10^4 s^{-1})	λ_{em} (nm)	τ (µs)
$[Cu(\mathbf{m30})(POP)]^+$	560	28.5 0.84	10.9 0.26	2.61 3.23	6.56 381	546	321
$[Cu(\mathbf{m37})(POP)]^+$	568	20.3 0.68	9.0 0.26	2.26 2.62	8.86 382	525	173
$[Cu(\mathbf{m42})(POP)]^+$	568	23.0 0.73	10.0 0.22	2.30 3.32	7.70 451	525	178
$[Cu(\mathbf{dmp})(POP)]^+$	565	23.9	11.5	2.09	6.65	518	211

[a] Double entries for each complex refer to oxygen-free (top) and air–equilibrated samples (bottom).
[b] Measured with respect to quinine sulfate (1 N, H_2SO_4) as standard (ϕ_{em} = 0.546) [171], λ_{exc} = 380 nm.

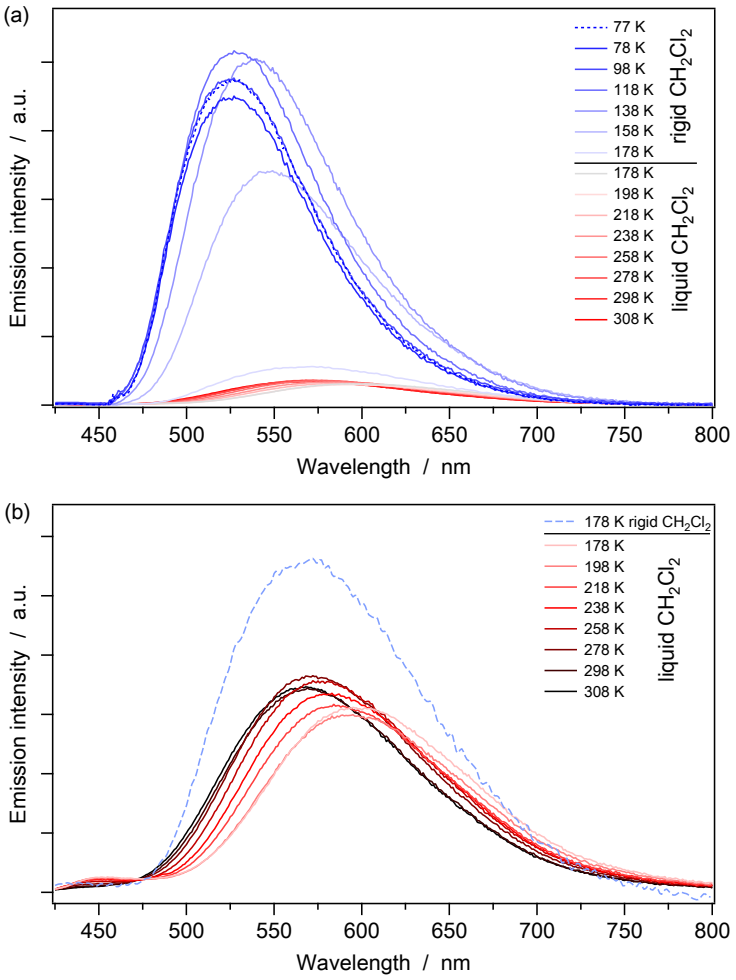

Figure 2.46. Luminescence spectra of $[Cu(\mathbf{m42})(POP)]^+$ in CH_2Cl_2 in the temperature range 77–308 K (a), with magnification of the spectra in the liquid domain (178–308 K, (b)). λ_{exc} = 380 nm.

Table 2.16. Photophysical Data in solid: in 1 wt% PMMA, as powders and in neat film at 298 K.

	PMMA (1 wt%)				powders			neat film			
	λ_{em} (nm)	ϕ_{em} [a] (%)	τ_1 (µs)	τ_2 (µs)	λ_{em} (nm)	ϕ_{em} [a] (%)	τ (µs)	λ_{em} (nm)	ϕ_{em} [a] (%)	τ_1 (µs)	τ_2 (µs)
[Cu(**m30**)(POP)]$^+$	532	44	18.0	36.5	553	32	16.3	547	24	6.5	14.5
[Cu(**m37**)(POP)]$^+$	520	39	22.8	57.9	548	11	14.9[b]	541	17	6.1	14.0
[Cu(**m42**)(POP)]$^+$	520	41	24.0	63.0	538	24	17.1	537	39	11.5	10.0
[Cu(**dmp**)(POP)]$^+$	520	50	25.3	75.1	527	28	27.5	553	39	9.0	16.2

[a] Determined using integrating sphere [159], λ_{exc} = 380 nm.
[b] This compound exhibits a biexponential decay with a short component of 7.29 µs.

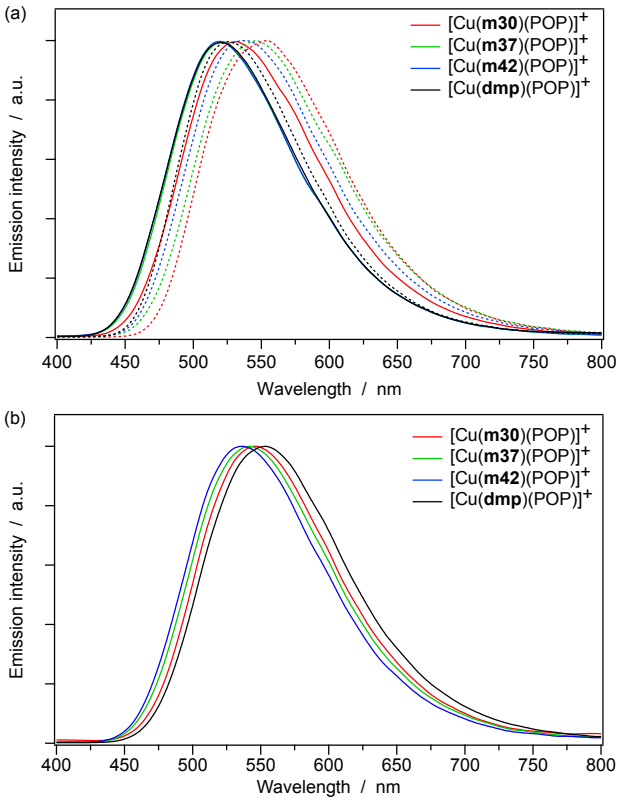

Figure 2.47. Luminescence spectra in PMMA 1 wt% (full line) and as powder samples (dotted line) (a) and as neat film (b) at 298 K. λ_{exc} = 380 nm.

2.3.6 Temperature dependent luminescence

The rather different excited-state lifetimes in various media at different temperatures prompted us to investigate the emission behavior of the three pseudorotaxanes and of the reference compound in solid as a function of temperature.
Emission spectra of the three pseudorotaxanes and of the [Cu(**dmp**)(POP)]$^+$ reference compound as powders in the range of 78–338 K are gathered in Figure 2.48. The ubiquitous red-shift as a function of temperature suggests the occurrence of TADF in solid samples. This hypothesis is corroborated by a marked elongation of the excited-state lifetime in passing from room temperature (≈15 µs) to 77 K (>100 µs), which is indicative

of triplet-to-singlet excited-state thermal equilibrium [13]. Interestingly, spectral red-shift at low temperatures is less pronounced in the pseudorotaxane systems, possibly as a function of a different, more constrained coordination environment, which impacts the singlet-triplet energy gap. Such gap has been evaluated by recording temperature-dependent emission spectra and excited-state lifetimes. The excited-state lifetimes as a function of temperature are fitted using eq. 2.1.
The parameters fitting the plots of Figure 2.49 are reported in Table 2.17 and show two interesting trends: (i) the energy gap of the pseudorotaxanes is constantly smaller than that of the reference compound; (ii) the pseudorotaxane with the smallest macrocycle has a remarkably longer triplet lifetime compared to all the other compounds, whereas the pseudorotaxane with the largest ring has a remarkably longer singlet lifetime. This confirms that the singlet and triplet parameters are extremely sensitive to relatively small structural differences.

The values of $\Delta E_{(S_1-T_1)}$ are relatively high when compared to a series of Cu(I) complexes with different ligands [13], but in line with compounds displaying phenanthroline and/or POP chelators [13, 161]. It has to be stressed again that a TADF behavior all across the examined temperature range is observed only in the powder samples and not in CH_2Cl_2 (see Paragraph 2.3.5 and Figure 2.46). This observation seems to be more general, as other investigators have often determined the singlet-triplet energy gap and the TADF behavior of luminescent Cu(I) complexes only as powder solid samples [13, 56, 69].

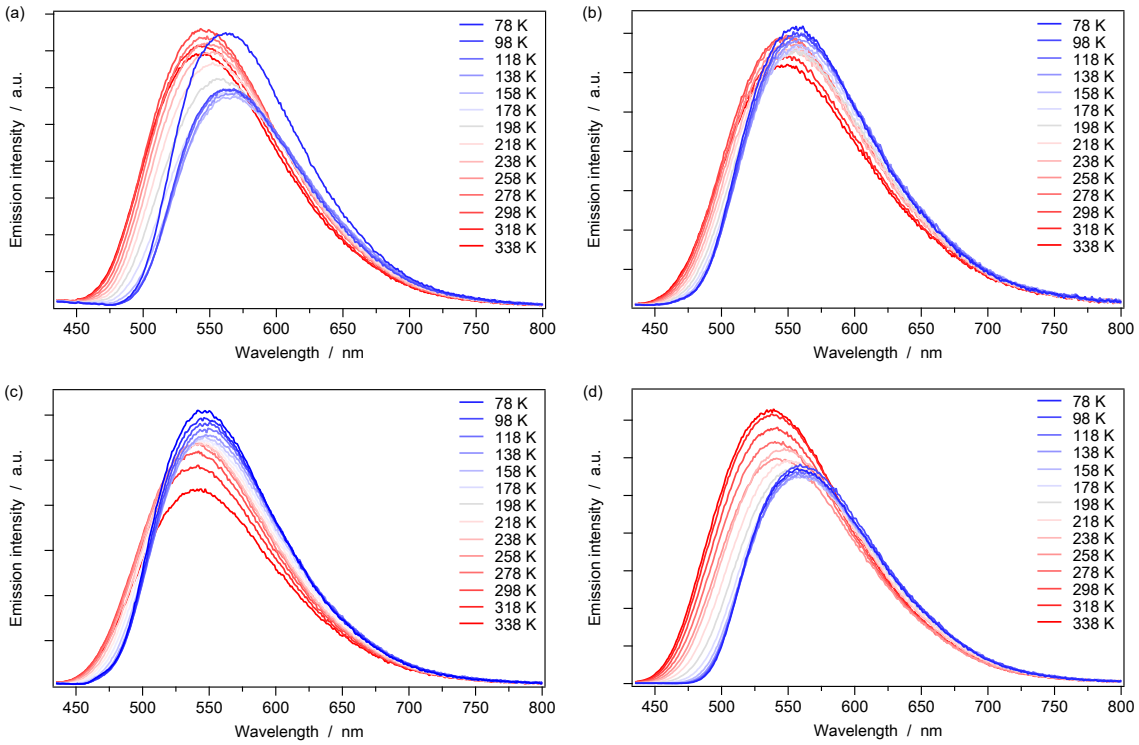

Figure 2.48. Luminescence spectra of $[Cu(\mathbf{m30})(POP)]^+$ (a), $[Cu(\mathbf{m37})(POP)]^+$ (b) $[Cu(\mathbf{m42})(POP)]^+$ (c) and $[Cu(\mathbf{dmp})(POP)]^+$(d) as powders in the temperature range 78–338 K. λ_{exc} = 380 nm.

Table 2.17. Energy Splitting $\Delta E_{(S_1-T_1)}$ between the First Excited Singlet and Triplet States (S_1, T_1) and Related Excited-State Lifetimes, Calculated According to eq. 2.1.

	$\Delta E_{(S_1-T_1)}$ (eV)	$\Delta E_{(S_1-T_1)}$ (cm^{-1})	$\tau_{(S_1)}$ (µs)	$\tau_{(T_1)}$ (ns)
[Cu(**m30**)(POP)]$^+$	0.121	970	55	261
[Cu(**m37**)(POP)]$^+$	0.109	880	66	122
[Cu(**m42**)(POP)]$^+$	0.111	900	100	167
[Cu(**dmp**)(POP)]$^+$	0.134	1080	58	169

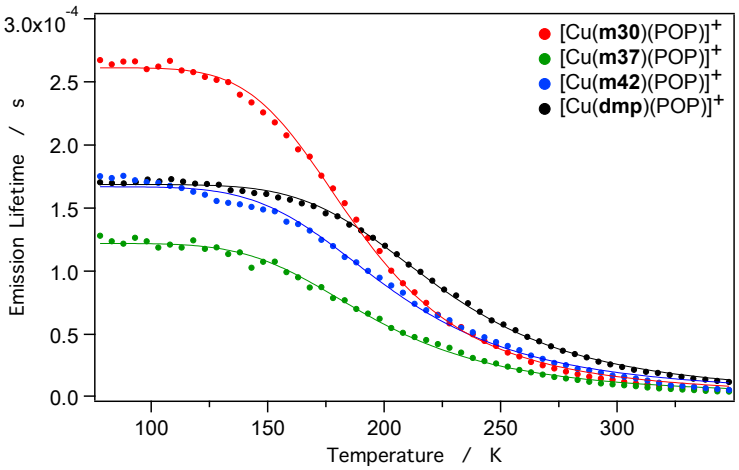

Figure 2.49. Excited-state lifetimes in the temperature range 78–338 K (powder samples). The lines connecting the experimental points are fitted using eq 2.1.

2.3.7 Device testing

The [Cu(**m42**)(POP)]$^+$ has been selected for the preparation of OLEDs owing to its electrochemical stability (Figure 2.39) associated with an easy synthesis; its high PLQY in PMMA ($\phi_{em} \approx 41\,\%$) makes it also an excellent candidate for the purpose. The Cu(I) complex has been incorporated as dopant in the emitting layer (EML) of an OLED device, affording intense green electroluminescence (EL), as shown in the inset of Figure 2.51. For comparison purposes, this device has been tested in parallel with an OLED exhibiting identical architecture but containing the reference complex [Cu(**dmp**)(POP)]$^+$ as emitter, which lacks the macrocyclic phenanthroline ligand.

In Figure 2.50 (a) and (b) is depicted the structure of the OLEDs and the energy levels of the materials studied. The devices were fabricated by a combination of wet and dry processes (spin coating and sublimation in high vacuum) onto a pre-cleaned indium tin oxide (ITO) glass substrate (see Appendix A). Holes were injected from the ITO anode and passed through a 40 nm thick transporting layer composed of poly(3,4-ethylenedioxythiophene):poly(styrenesulfonate) (PEDOT:PSS). Electrons were injected from an Al/LiF cathode and transported to the EML through a 25 nm thick layer of 2,2′,2′′-(1,3,5-benzinetriyl)-tris(1-phenyl-1H-benzimidazole) (TPBi). Charges recombined in the 50 nm thick EML made of a (bis-4-(N-carbazolyl)phenyl)phenylphosphine oxide (BCPO) bipolar matrix [176, 177], hosting the Cu complexes (15 wt%) as Cu-based emitters. EL

spectra of the OLEDs are shown in Figure 2.51. Both OLED emission bands are located in the green region; the CIE coordinates of $[Cu(\mathbf{m42})(POP)]^+$ and $[Cu(\mathbf{dmp})(POP)]^+$ are (0.32, 0.53) and (0.33, 0.54), respectively. The EL spectra are similar and closely match the photoluminescence spectra of the complexes in rigid media. No significant contribution to the EL emission bands from the TBPi electron-transporting (hole-blocking) or BCPO binder layers is observed, indicating good charge carrier confinement within the EML and complete energy transfer from the excited states of BCPO (generated by charge carrier recombination) to the Cu complexes. Indeed, the OLEDs show excellent optoelectronic performance as shown in the data of Table 2.18.

Luminance of $\approx 1000\,cd\,m^{-2}$ at about 10 V with $\eta_{ext} \approx 9\,\%$ and at about 11 V with $\eta_{ext} \approx 7\,\%$ were obtained for $[Cu(\mathbf{m42})(POP)]^+$ and $[Cu(\mathbf{dmp})(POP)]^+$, respectively. The luminance and external EL efficiency as a function of driving voltage and current density of both OLEDs are displayed in Figure 2.50. The excellent OLED performance and parameters observed with $[Cu(\mathbf{m42})(POP)]^+$ as emitter are also comparable and even better with respect to those previously reported for green OLEDs based on $[Cu(\mathbf{dnbp})(POP)]^+$ (**dnbp** = 2,9-di-n-butyl-phenanthroline) by Adachi and coworkers [178]. OLED performances were reproduced for five runs under argon atmosphere, excluding somehow short-term irreversible chemical and morphological changes in the OLEDs made of $[Cu(\mathbf{m42})(POP)]^+$, whereas the luminance falls by about 20 % for devices with the complex $[Cu(\mathbf{dmp})(POP)]^+$, indicating rapid degradation. The chemical stability under working condition is one of the big issues in the use of Cu complexes as active materials

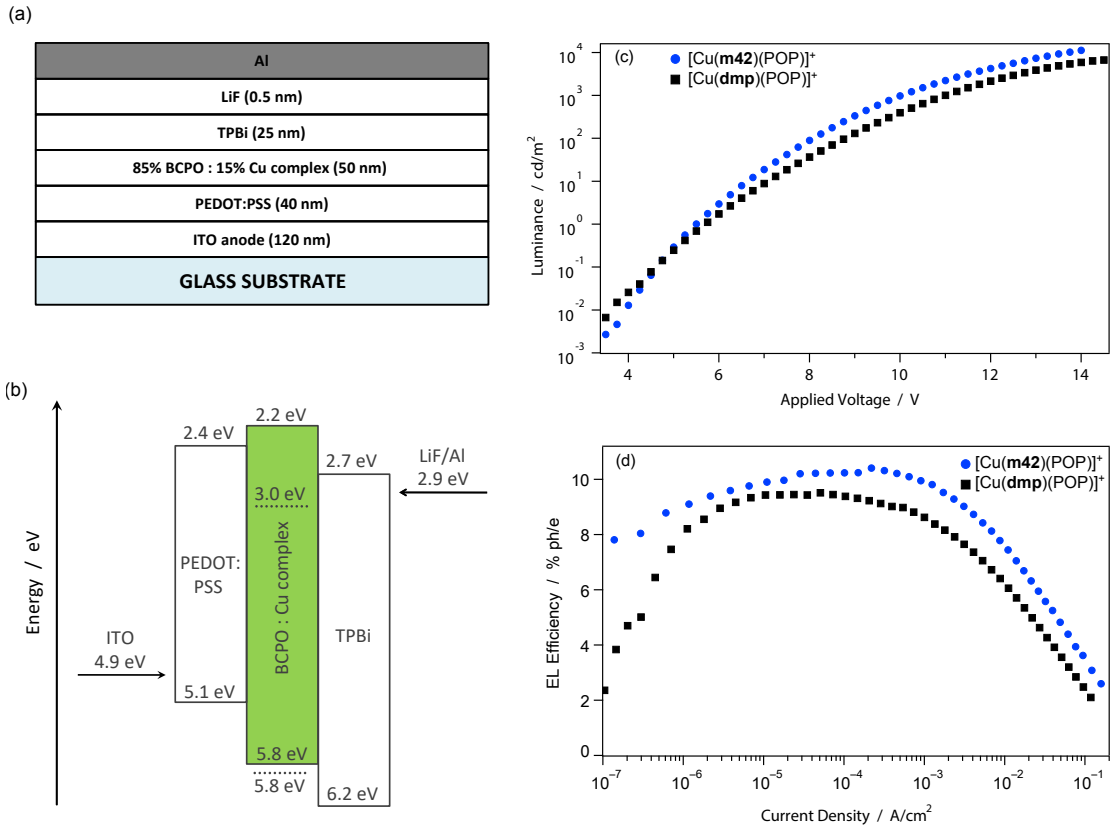

Figure 2.50. OLED configuration (a) and energy level diagram (b). HOMO and LUMO levels of $[Cu(\mathbf{m42})(POP)]^+$ were calculated from the redox potentials reported in Table 2.14. Luminance versus applied voltage (c) and external EL efficiency versus driving current (d) of the OLEDs.

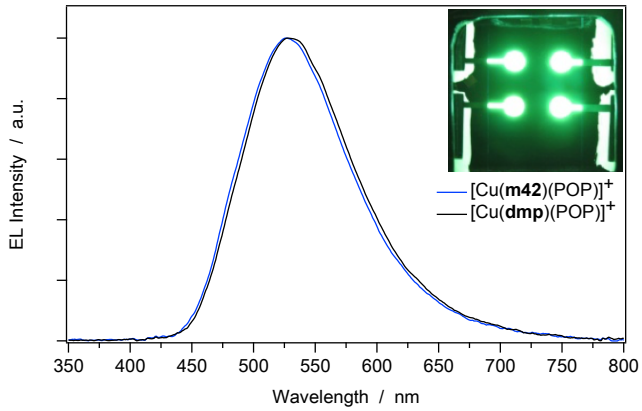

Figure 2.51. Electroluminescence spectra at 10 V of OLEDs. In the inset is reported a photograph of OLEDs based on [Cu(**m42**)(POP)]$^+$.

Table 2.18. Optoelectronic Performance of the OLEDs Tested.

		External EL efficiency		maximum luminance	
	turn-on-voltage (V)	η_{max} (%)	luminance (cd m^{-2})	L_{max} (cd m^{-2})	η (%)
[Cu(**m42**)(POP)]$^+$	4	10.5 (8 V)	100	12800 (14 V)	2.6
[Cu(**dmp**)(POP)]$^+$	4	9.5 (7.5 V)	20	7740 (14 V)	2.1

in OLEDs [67], and the enhanced device stability observed with [Cu(**m42**)(POP)]$^+$ can be attributed to the presence of the pseudorotaxane structure that may prevent chemical degradation.

2.3.8 Conclusion

A series of copper(I) pseudorotaxanes has been prepared from POP and macrocyclic phenanthroline derivatives with different ring sizes. Steric congestions resulting from the macrocyclic nature of the phenanthroline ligand is at the origin of a dynamic conformational equilibrium in all the pseudorotaxanes, which has been evidenced with ^{31}P NMR measurements over a wide temperature range. The macrocyclic component is forced to adopt a folded conformation. When the macrocycle is small (**m30**), steric congestion is important and concomitant distortion of the coordination sphere around the copper(I) led to electrochemical instability. By increasing the size of the macrocycle (**m37** and **m42**), the steric congestion is reduced and does not affect the electrochemical behavior of the pseudorotaxanes. Photophysical studies in a variety of media and across extensive temperature ranges show that the pseudorotaxane structure sizably impacts the excited-state properties of the complexes and, most importantly, enhances the stability of OLED devices. This finding may open a new route in the optimization of Cu(I) complexes for optoelectronics.

3 Iridium(III) photoactive complexes

The work presented in this Chapter was done in collaboration with Prof. Letizia Sambri (University of Bologna), and Henk Bolink (University of Valencia). Compounds where synthesized by Prof. Sambri and coworkers, while the device preparation and characterization was performed by the group of H. Bolink. It has been a honor to collaborate with them.

3.1 Iridium(III) complexes as lighting materials

In the second part of this thesis the focus is shifted towards Iridium-based ionic transition-metal complexes, one of the most widely used classes of emitters in solid-state electroluminescent devices, *i.e.*, OLEDs [14, 179] and LECs [19, 180], to be used for flat panel displays and lighting [19].
Iridium(III) complexes have drawn much attention thanks to their unique properties including short excited-state lifetimes (often <10 μs in organic solvents), high photoluminescence quantum yields, easy synthesis and purification, excellent stability, good solubility, high versatility in tuning the emission color by ligand variation (see Paragraph 1.1.2) and often reversible oxidation and reduction processes.
In particular, LECs devices, first reported by Pei et al. [82], have a simpler architecture compared to multilayer OLEDs analogues. They do not rely on air-sensitive layers or metals for charge injection and hence require less stringent packaging procedures [19]; practically, they can be easily fabricated from solution processes [181, 182]. Electrochemical reversibility is a key characteristic of the emitting material for such simple EL devices (see Paragraph 1.2.2) [19].

3.1.1 Purpose of the research activity

With the aim of exploring new luminescent Ir(III) coordination compounds to be applied in EL devices, we studied two series of complexes based on this transition-metal ion. One is characterized by an overall negative charge (a somewhat uncommon feature) [183], while the other is obtained by the coordination of new azaborine ancillary ligands [184]. The photophysical and electrochemical properties of eight $[Ir(C^{\wedge}N)_2(A^{\wedge}A)]^n$ complexes are reported in various matrices (solution, low temperature glass, PMMA, neat film), comparing the results, when necessary, with known complexes and supporting the observation with theoretical calculations.
In the first Section (3.2) is reported the characterization of three new phosphorescent red, blue, and green (RGB) anionic bis-cyclometalated iridium(III) complexes (**32**-**34**) with di(1H-tetrazol-5-yl)methane as the ancillary ligand [185]. The good emission properties and the electrochemical reversibility shown by these compounds prompted us to test them in LECs. Remarkably stable EL was observed for devices employing complex **33**, demonstrating the suitability of anionic compounds for such application.
In the last part of this chapter (Section 3.3) the heteroaromaticity has been exploited to obtain a novel class of bidentate ligands based on the azaborine functionality. The Ir(III) metal ion is coordinated by the two nitrogen atoms of this ancillary ligand, upon "activation" of the N–H on the boroazaronaphthalene moiety, forming the typical 5-membered cyclometallated ring. The negative charge located on such novel chelator leads to the formation of a series of neutral iridium(III) complexes, obtained by the coordination of different C^N ligands, which were designed to tune the emission band in the Vis range. The photophysical and electrochemical properties of these compounds were compared with the isoelectronic complexes containing a C=C equivalent on the ancillary ligand. Despite some instability observed for the complexes under certain conditions, the results are promising and a fine tuning of the ligand design may afford stable and highly luminescent compounds.

3.2 Shall we go negative? Unusual anionic Ir(III) complexes

While a very large number of phosphorescent cationic iridium(III) complexes with general molecular formula $[Ir(C^{\wedge}N)_2(A^{\wedge}A)]^n$ (where C^N are cyclometalated ligands and A^A a neutral ancillary ligand) has been investigated and tested in LECs [19, 180, 186], anionic luminescent analogues are still uncommon [186]. Even outside the field of luminescence, only some examples of negatively charged organometallic compounds have been reported, including hydrides [187], carbonyl clusters [188], or systems in which cyclopentadienyl [189], phosphine [190], alkyl and aryl [191] ligands are coordinated to the metal center. These complexes have been mainly used for their redox properties [192], which are particularly relevant in the area of catalysis [193].
Early examples of luminescent anionic iridium(III) complexes were reported by Nazeeruddin et al., with a series of highly phosphorescent anionic systems with general formula $[NBu_4]^+[Ir(ppy)_2(X)_2]^-$ (X = CN^-, NCS^-, and NCO^-) which were designed for OLEDs [194]. Eventually, other light-emitting anionic CN^- or NCS^- iridium complexes have been studied to clarify the effect of the modification of the ancillary or cyclometalated phenylpyridine ligands on the emission properties [195, 196]. Recently, anionic iridium complexes were paired with cationic iridium counterparts to create a new class of soft salts. In the former, the negatively charged cyanide or isothiocyanate ligands were replaced with bulkier 5-aryl tetrazolato derivatives [197].
Iridium(III) complexes with monodentate ligands exhibit low stability and may undergo easy degradation, particularly when incorporated in devices, owing to ligand exchange promoted by undesired coordination of small molecules (*e.g.*, water) [198]. Accordingly, most cationic cyclometalated iridium(III) complexes bear a neutral bidentate ancillary ligand.
In order to obtain negatively charged complexes, dianionic ligands are therefore preferable, but these are relatively uncommon in iridium(III) complexes. Some examples involve dianionic C^C [199] and N^N [200] chelators, in combination with bipyridine and/or phenylpyridine derivatives to form cationic or neutral iridium complexes. Bidentate dianionic ligands including tetrazolate N^N [201], catecholate O^O [202], and orotate acid O^N [203], as well as dithiolate and sulfinate S^S derivatives [204] were reported as ancillary ligands for anionic luminescent iridium(III) complexes.
Concerning LECs, cationic cyclometalated iridium(III) complexes are commonly used as active materials, typically with the hexafluorophosphate counterion, since it allows the fabrication of devices with optimized performances [26, 205–207]. Alkali cations have also been reported to improve the LEC performance, when used as ionic additives [208–210]. Moreover, recently, some anionic iridium complexes have been tested as single emitters for LECs [211, 212] or as co-emitters in soft salts for OLEDs [213, 214].
Herein, we report the characterization of three new phosphorescent red, blue, and green (RGB) anionic bis-cyclometalated iridium(III) complexes (**32**-**34**) with di(1H-tetrazol-5-yl)methane as the ancillary ligand. The latter has been recently used in combination with a mesoionic neutral carbene cyclometallating chelator to afford unconventional cationic iridium(III) complexes with the negative charges located on the ancillary ligand [215].

The electrochemical and photochemical properties of the complexes have been determined, moreover the compounds have been tested in LECs observing a remarkable stability for the devices.

3.2.1 The RGB series

A series of monoanionic Ir(III) complexes of general formula [Ir(C^N)$_2$(**b-trz**)][TBA] are presented, where C^N indicates three different cyclometallating ligands (**Hppy** = 2-phenylpyridine; **Hdfppy** = 2-(2,4-difluoro-phenyl)pyridine; **Hpqu** = 2-methyl-3-phenyl-quinoxaline), **b-trz** is a bis-tetrazolate anionic N^N chelator (**H$_2$b-trz** = di(1H-tetrazol-5-yl)methane), and TBA = tetrabutylammonium (Figure 3.1). The **32-34** coordiantion compounds are prepared in good yields by means of the reaction of the suitable **b-trz** bidentate ligand with the desired iridium(III) precursor. The chelating nature of the ancillary ligand, thanks to an optimized structure and geometry, improves the stability of the complexes, which have been characterized also by means of X-ray structure determination, that confirmed the binding mode of the **b-trz** ligand. The results and discussion given in this Section are based on the reference [183].

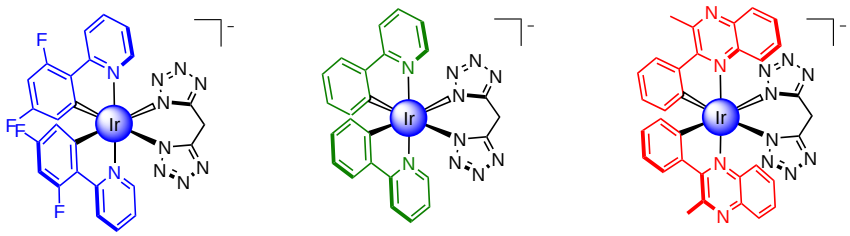

(**32**) Ir(dfppy)$_2$(**b-trz**) (**33**) Ir(ppy)$_2$(**b-trz**) (**34**) Ir(pqu)$_2$(**b-trz**)

Figure 3.1. Series of anionic ”RGB” Ir(III) complexes as TBA salt. In blue, green and red are highlighted the different cyclometallated ligand, while black color is used for the **b-trz** ancillary ligand.

3.2.2 X-ray structures and ground-state theoretical calculations

The molecular structure of **34** was also determined by single-crystal X-ray diffraction analysis (Figure 3.2 (a)). Crystals were grown by double layer diffusion of diethyl ether into CH$_3$CN. The compound crystallizes in the centrosymmetric P-1 triclinic space group, therefore accommodating both the enantiomers. The structure was deposited with the CCDC number 1555727.

The complex [Ir(pqu)$_2$(**b-trz**)]$^-$ displays a distorted octahedral geometry, with the two quinoxaline moieties of the C^N ligands in a trans relationship (N–Ir–N angle = 172.2°), as often observed for similar cyclometalated iridium(III) complexes [14, 179]. The two C^N bite angles are 79.0° and 79.5°, while the N–Ir–N bite angle of the ancillary ligand is 82.2°. The two Ir–N distances within the ancillary ligands are very similar (2.12 and 2.14 Å, respectively).

As it can be seen in Figure 3.2 (a), the ancillary ligand is not planar so that the complex lacks any symmetry element other than the identity, and, consequently, it belongs to the C_1 point group in the solid state. Anyway, the fast conformational rearrangement of the CH$_2$ bridge that takes place in solution implies a dynamic C_2 symmetry of the complex,

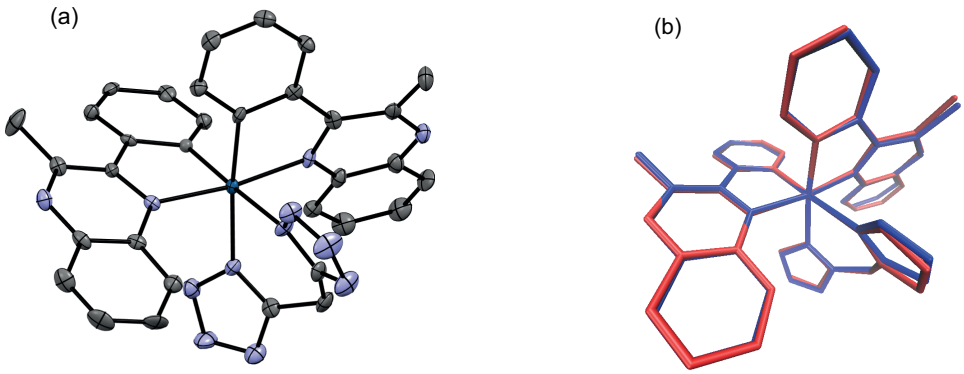

Figure 3.2. (a) Experimental X-ray structures of complex $[Ir(pqu)_2(\mathbf{b\text{-}trz})]^-$. Thermal ellipsoids are plotted at the 50 % probability, using Mercury CSD 3.10 [165]. The $[N(n\text{-}Bu)_4]^+$ countercation and hydrogen atoms are omitted for clarity. (b) Structural overlay (H atoms omitted) between the experimental X-ray structure of the **34** complex (blue) and the theoretically computed one (red). The structural overlay is calculated by minimizing the RMSD of all the atomic positions (RMSD = 0.176 Å).

making the two cyclometalating ligands NMR-equivalent [216].
The molecular geometries and the electronic properties of the complexes were investigated by DFT calculations and, in the case of **34**, compared to the corresponding X-ray crystallographic structure. The M06 hybrid meta exchange-correlation functional [153, 154] was used in combination with the 6- 31G(d,p) basis set for all the nonmetal atoms [217]. On the contrary, the Stuttgart/Cologne relativistic pseudopotential and its related correlation-consistent triple-ζ basis set were adopted for the iridium center (see Appendix A for further details) [218].
The ground-state (S_0) geometries of **32-34** were fully optimized without symmetry constraints in CH_3CN, using the polarizable continuum model (PCM) [219–221]. The accuracy of the computational method is validated by the comparison between the available X-ray structure of **34** and its theoretically calculated one. As shown in Figure 3.2 (b), the experimental and computed geometries of complex **34** are virtually superimposable; this is also corroborated by the low value of the minimized RMSD of all the atomic positions, except hydrogens (*i.e.*, RSMD = 0.176 Å). This value is substantially small, considering the highly distorted geometry of complex **34** due to the presence of the two bulky pqu ligands around the iridium(III) metal center.
The ground-state frontier molecular orbitals of the complexes are depicted in Figure 3.3. For this series of anionic complexes, the HOMO is mainly localized on the metal center and on both the cyclometalating rings of the two C^N ligands, as commonly found also in cationic bis-cyclometalated iridium(III) analogues. On the other hand, the LUMO and the LUMO+1 mainly reside on the nitrogen-containing moiety of each C^N ligands. Also this feature is common in cationic complexes having ancillary ligands with high-energy π^* orbitals, such as carbenes or isocyanides [222–225]. It is worth mentioning that the bis-tetrazolate ligand $(\mathbf{b\text{-}trz})^{2-}$ does not contribute to the frontier molecular orbitals of **32-34**, and the lowest unoccupied molecular orbitals partially centered on this bis-anionic ligand are the LUMO+6 and LUMO+7.

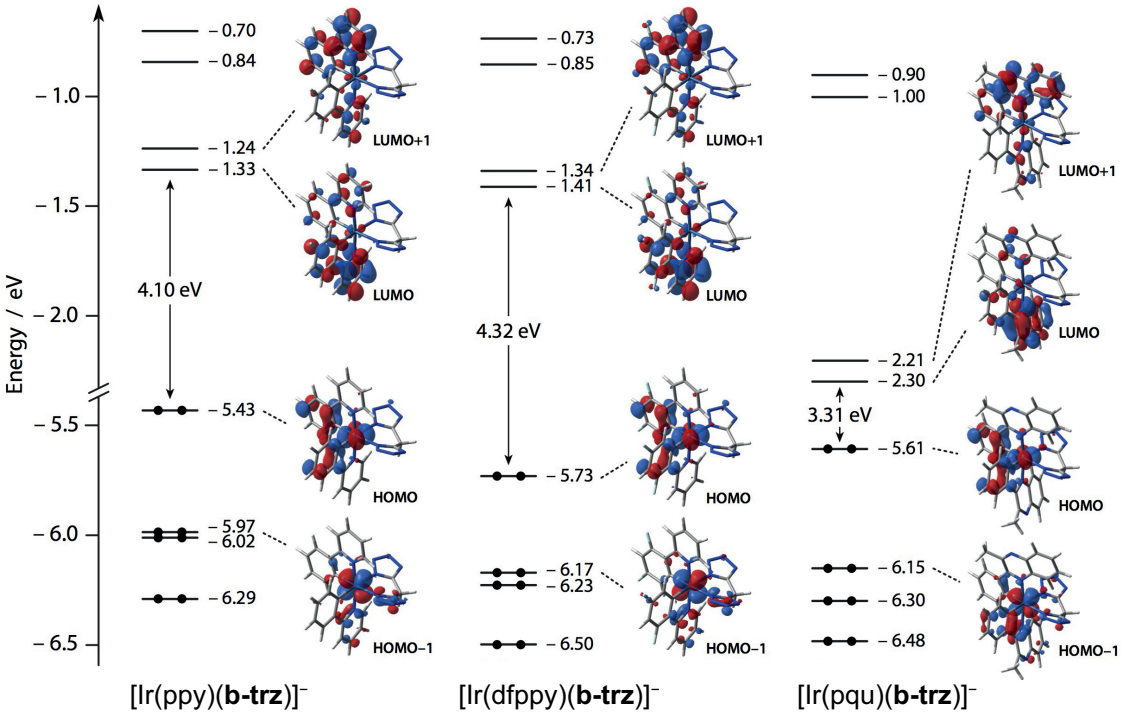

Figure 3.3. Energy diagram showing the energy values of the frontier Kohn-Sham molecular orbitals of **32-34** in CH_3CN. For some relevant orbitals, the corresponding isosurface is also displayed for the sake of clarity (isovalue = 0.04 $e^{1/2}$ $bohr^{-3/2}$).

As already widely observed in cationic iridium(III) complexes [19, 211], the fluorine substituents on the phenyl moiety of the cyclometalating ligands are able to induce a considerable stabilization of the HOMO with respect to pristine phenyl-pyridine C^N ligands (*i.e.*, HOMO is located at −5.73 eV in complex **32** vs −5.43 eV in **33**, see Figure 3.3). On the other hand, in the case of **34**, a pronounced LUMO (and LUMO+1) stabilization is observed due to the presence of the π-extended quinoxaline unit that replaces the pyridine moiety in the two C^N ligands. This finding is consistent with what has been observed for an analogous series of cationic complexes with the same cyclometalating ligand as in **32-34**, but having a neutral diisocyanide ancillary unit [216].
On the basis of the trends depicted in Figure 3.3, it seems that the anionic nature of these complexes does not strongly affect their electronic properties, when compared to those of their cationic counterparts. However, this is not true if the energy of the frontier molecular orbitals is considered, as it can be inferred by comparing the HOMO and LUMO energies of **33** (taken as a representative case of the present series) with those of the selected analogues reported in Figure 3.4 [214–216].

Even though all the complexes depicted in Figure 3.4 display the same HOMO and LUMO topologies (*i.e.*, HOMO centered on the iridium ion and on the cyclometalating ring of the C^N ligands, and LUMO on the pyridine moiety of the same C^N ligands), the energy associated with their frontier molecular orbitals is remarkably different (see Table 3.1).
First of all, it should be stressed that, despite the presence of an extremely high-field ligand like the bis-tetrazolate $(\mathbf{b\text{-}trz})^{2-}$, the HOMO energy of **33** is comparable to that of the archetypal complex $[Ir(ppy)_2(bpy)]^+$, equipped with a much lower-field ancillary

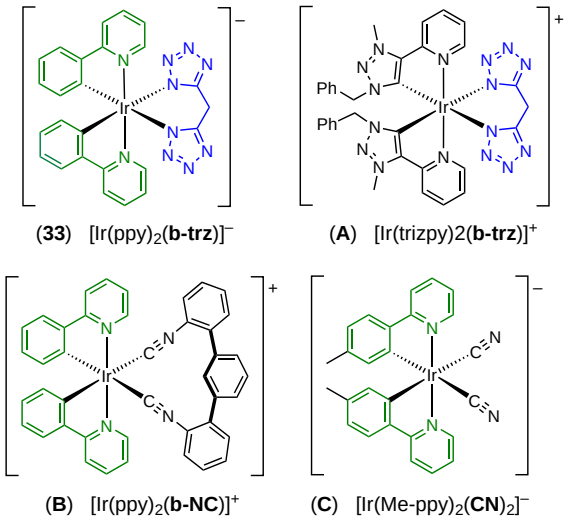

Figure 3.4. Selected ionic Iridium(III) complexes, as analogues of complex $[Ir(ppy)_2(\mathbf{b\text{-}trz})]^-$.

ligand (*i.e.*, the 2,2′-bipyridine).
This is surprising since a very large HOMO stabilization would be expected in **33** due to a larger *d*-*d* splitting of the iridium orbitals exerted by the high-field of ligand $(\mathbf{b\text{-}trz})^{2-}$. The high-field nature of the bis-tetrazolate ligand can be easily demonstrated by considering the higher HOMO stabilization that occurs in complex **A**, compared to **B** (*i.e.*, the ligand strength of $(\mathbf{b\text{-}trz})^{2-}$ is even greater than that exerted by the chelating diisocyanide ligand of complex **B**). Anyway, the HOMO of **33** is located around 1.5 eV above that of **A** (see Table 3.1). This peculiar feature can only be understood by taking into account the different charge of these two complexes: **A** is cationic, **33** is anionic. Accordingly, an oxidation process (*i.e.*, a formal removal of an electron from the HOMO) is more likely to occur in **33**, since it is more electron rich than the positively charged counterpart, resulting in a less stabilized HOMO. The same concept can also justify why the LUMO of complex **33** is more than 1 eV higher in energy with respect to that of **A** (see Table 3.1). In fact, the reduction of an anionic complex is disfavored compared to that of a positively charged analogue, resulting in a less stabilized LUMO.
Finally, it is also relevant to compare the energies of the frontier molecular orbitals of **33** with those of **C**, a cyanide-based anionic complex reported by Thompson and coworkers (see Figure 3.4) [214]. These complexes exhibit HOMOs and LUMOs with the same topology and also virtually identical energies ($\Delta E \approx 0.1$ eV, Table 3.1). This similarity can be rationalized by considering that both complexes have (i) the same negative net charge, (ii) nearly identical cyclometalating C^N ligands, and (iii) negatively charged ancillary ligands (*i.e.*, in **C**, the bis-anionic tetrazolate of **33** is replaced by two CN-ligands with identical point charges). Taken in concert, these features afford two complexes with virtually equivalent charge distributions, resulting in extremely similar frontier molecular orbital distribution and energies and, also, to an almost identical electrochemical behavior (see below).

3.2.3 Electrochemical properties

The electronic properties of the series were also experimentally investigated by CV and OSWV. All the experiments were carried out in room-temperature CH_3CN solutions and reported relative to the Fc^+/Fc redox couple (see Appendix A for further details). Cyclic voltammograms of all the complexes are shown in Figure 3.5 (a), while OSWV voltammograms are included in the Figure 3.5 (b). It has to be emphasized that the first oxidation and reduction processes of **32-34** are always reversible, which make them particularly attractive ionic emitters for LECs (see below). Their redox potentials are summarized in Table 3.1 and compared with those of the complexes reported in Figure 3.4.
The electrochemical experiments are in excellent agreement with DFT calculations (compare data in Table 3.1). In brief: (i) the oxidation potential in **32** is higher than that of **33** (*i.e.*, +0.85 vs +0.52 V, respectively) due to the HOMO stabilization promoted by the fluorine substituents; (ii) the reduction potentials of **33** and **32** are similar (*i.e.*, −2.64 vs −2.51 V, respectively), while complex **34** exhibits a more positive value due to LUMO stabilization (*i.e.*, −1.75 V, compare Table 3.1 and Figure 3.3); (iii) both oxidation and reduction potentials of **33** are shifted by about −0.9 V if compared to the cationic counterpart **A**, as already suggested by DFT (theoretically estimated shift: 1.3 ± 0.2 eV); (iv) the redox properties of **33** are virtually identical to those of **C**, a similar anionic cyanide-based complex with the same overall charge and a comparable electronic distribution. In addition to that, it should be mentioned that the experimental results found by both

Table 3.1. Electrochemical data[a] and DFT energies of the FMOs[b] of the **32-34** complexes and of the selected analogues **A-C**, together with the archetypal complex $[Ir(ppy)_2(\mathbf{bpy})]^+$.

	Electrochemical data[c] (V)				DFT calculated energies (eV)		
	E_{Ox}	E_{Red1}	E_{Red2}	ΔE_{Redox}[d]	E_{HOMO}	E_{LUMO}	ΔE_{DFT}[e]
$[Ir(fpppy)_2(\mathbf{b\text{-}trz})]^-$	+0.85 (+0.85)	−2.51 (−2.50)	$-2.80^{irr.}$ (−2.80)	3.36 (3.35)	−5.73	−1.41	4.32
$[Ir(ppy)_2(\mathbf{b\text{-}trz})]^-$	+0.52 (+0.52)	−2.64 (−2.64)		3.16 (3.16)	−5.43	−1.33	4.10
$[Ir(pqu)_2(\mathbf{b\text{-}trz})]^-$	+0.67 (+0.66)	−1.75 (−1.76)	−2.04 (−2.05)	2.42 (2.42)	−5.61	−2.30	3.31
$[Ir(ppy)_2(\mathbf{bpy})]^+$ [f]	+0.87	−1.78	−2.60	2.65	−5.88	−2.29	3.59
$[Ir(trizpy)_2(\mathbf{b\text{-}trz})]^+$ [g]	+1.42	−1.82	−1.98	3.24	−6.93	−2.46	4.47
$[Ir(ppy)_2(\mathbf{b\text{-}NC})]^+$ [h]	$(+1.20)^{irr.}$	$(-2.30)^{irr.}$	$(-2.50)^{irr.}$	(3.50)	−6.48	−1.79	4.69
$[Ir(Me-ppy)_2(\mathbf{CN})_2]^-$ [i]	+0.51	−2.62		3.13	−5.47	−1.19	4.28

[a] Data in brackets refer to OSWV experiments; ferrocene is used as internal reference. For the sake of comparison, electrochemical data of **A-C** and of the archetypal complex $[Ir(ppy)_2(bpy)]^+$ are reported. [b] Data refer to calculation performed in CH_3CN using the M06 functional (see Appendix A for further details). Calculations on complexes **A-C** and $[Ir(ppy)_2(bpy)]^+$ were repeated to be fully consistent with the theoretical method adopted in the present article for **32-34**. [c] All redox processes are reversible, unless otherwise stated (*irr.*). [d] $\Delta E_{Redox} = E_{Ox} - E_{Red}$. [e] Data refer to calculation performed in CH_3CN using a fully optimized structure in vacuum (Appendix A). $\Delta E_{DFT} = E_{LUMO} - E_{HOMO}$.
[f] Data from [226] and [19]. [g] Data from [215]. [h] Data from [216]. [i] Data from [214].

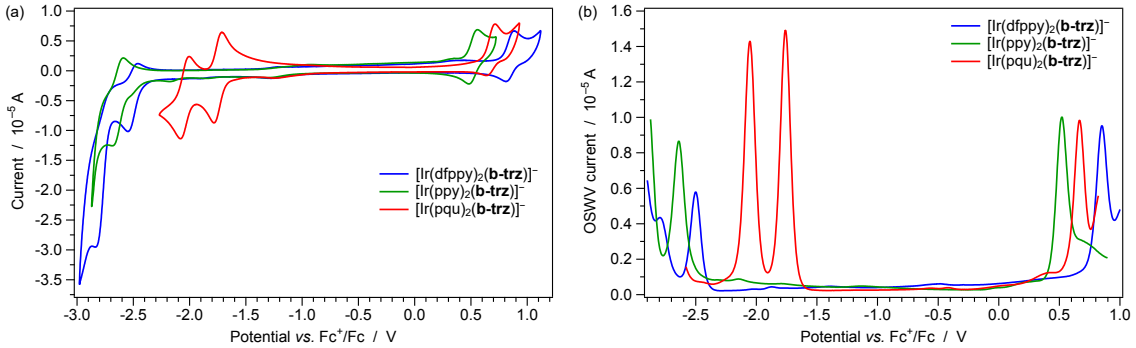

Figure 3.5. CVs (a) and OSWVs (b) of **32-34** recorded in CH_3CN solution. CVs: scan rate of 200 mV s^{-1}. OSWVs: scan rate of 25 mV s^{-1} with a square wave amplitude of ± 20 mV and a frequency of 25 Hz.

CV and OSWV experiments show a good correlation with those estimated by DFT, with the HOMO-LUMO energy gap systematically higher than the redox gap of 1.1 ± 0.1 eV for all the reported complexes,including those of Figure 3.4.

3.2.4 Photophysical properties and excited-state calculations

All the investigated complexes **32-34** are stable in CH_3CN solution for several months and do not show degradation under standard laboratory conditions. The room-temperature electronic absorption spectra of **32-34** are reported in Figure 3.6 and compared with the theoretically calculated ones in Figures 3.7.
The spectral window between 230 and 300 nm shows intense absorption bands ($\varepsilon \approx 2 \div 5 \times 10^4$ M^{-1} cm^{-1}) that are assigned to spin-allowed LC π-π^* transitions involving both the cyclometalating and the ancillary ligand $(\mathbf{b\text{-}trz})^{2-}$ with some likely contribution from ^{3}LC forbidden transitions, promoted by the heavy-atom effect of the iridium center (ζ_{Ir} = 3909 cm^{-1}). At longer wavelengths (λ > 300 nm; Figure 3.6, inset), several weaker and broader bands are present, but their attribution is less straightforward. Therefore, we compared the experimental spectra of **32-34** with (i) TD-DFT calculated ones and (ii) to the absorption profiles of a series of cationic complexes with identical cyclometallating ligands and a high field ancillary moiety, whose simplest representative is **B** [216].

As already observed for the above-mentioned diisocyanide-based series [216] and in line with theoretical predictions, the absorption spectrum of **34** is the most red-shifted of the group, showing broad absorption features spreading up to 650 nm. The main responsible for this behavior is the lowest singlet electronic transition, centered at 546 nm and involving an almost pure HOMO ⟶ LUMO excitation (Figure 3.3 and 3.7 (c)). In **34**, the presence of the quinoxaline moiety in the C^N ligands is able to strongly stabilize the LUMO and, as a consequence, lower the energy of the $S_0 \longrightarrow S_1$ electronic transition. On the other hand, the absorption profiles of **32** and **33** extend only up to 475 and 500 nm, respectively. The observed blue shift in the spectrum of the fluorinated system **32** is attributable to the remarkable HOMO stabilization exerted by the electron-withdrawing substituents on the phenyl moieties of the cyclometalating ligand, where the HOMO is centered. This photophysical behavior is commonly observed in fluorinated cationic iridium(III) complexes [19, 227], and is confirmed in the present anionic systems (Figures 3.3 and 3.6).

It is worth noting that the spin-forbidden $S_0 \longrightarrow T_1$ direct transition is clearly detectable in the spectra of **32** and **33** (*i.e.*, at 452 nm with $\epsilon = 3.8 \times 10^2$ M^{-1} cm^{-1} for **32** and at 474 nm with $\epsilon = 4.5 \times 10^2$ M^{-1} cm^{-1} for **33**; Figure 3.6, inset). In both cases, TD-DFT calculations indicate that this transition is a strongly multiconfigurational excitation that can be hardly visualized in terms of a compact and clear series of occupied/virtual Kohn-Sham molecular-orbital couples. For this reason, this $S_0 \longrightarrow T_1$ transition is reported in Figure 3.8 (a) and (b) in terms of two couples of natural transition orbitals (NTOs) [228] for both **32** and **33**. This compact representation allows one to understand that, in both complexes, the direct population of the lowest triplet can be essentially achieved by promotion of one electron from the iridium d orbitals and the π orbitals on both the cyclometalating ligands to the π^* orbitals of the C^N ligands themselves. As a consequence, the emission from these complexes is expected to arise from a ^{3}LC state (centered on the cyclometalating ligands) with a mixed ^{3}MLCT contribution. As expected, the bis-tetrazolate ligand $(\mathbf{b\text{-}trz})^{2-}$ is not directly involved in the transition, thus acting as a real ancillary ligand.

The emission spectra of **32**-**34** are collected in Figure 3.9 (a), in CH_3CN at 298 K (full lines) and 77 K (dashed lines); luminescence properties are summarized in Table 3.2. As expected, the spectra of complexes **32** and **33** are rather structured, suggesting an emission from a predominantly LC state. This scenario is corroborated by the small Stokes shift of 710 and 1020 cm^{-1} observed for **32** and **33**, respectively. In agreement with the absorption spectra, the emission of **32** is blue-shifted by about 0.17 eV compared to **33** (Figure 3.9 (a)).

Upon lowering the temperature to 77 K, the vibronic progression of the emission spectra of **32** and **33** becomes more pronounced and only a minor blue shift is observed (approximately 0.06 eV, Table 3.2), supporting the hypothesis of a LC state with some ^{3}MLCT contribution.

On the contrary, the room-temperature emission spectrum of **34** is broad and unstructured, which, at first sight might indicate emission from a pure ^{3}MLCT state. However, its radiative decay constant (k_r) is comparable to that of **32** and **33** (Table 3.2), and its k_r is rather low compared to other charged iridium(III) complexes emitting from ^{3}MLCT states [19]. Moreover, no spectral shift is observed between the room-temperature emission spectrum of **34** vs 77 K. All these experimental evidence indicate that the emission

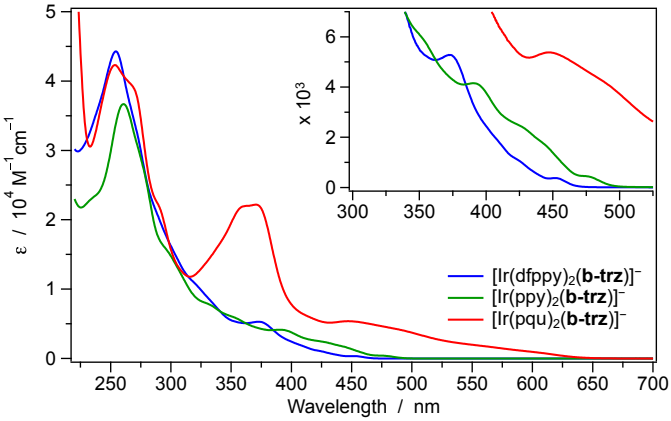

Figure 3.6. Absorption spectra of **32**-**34** at 298 K in CH_3CN solution. The lowest-energy transitions are magnified in the inset.

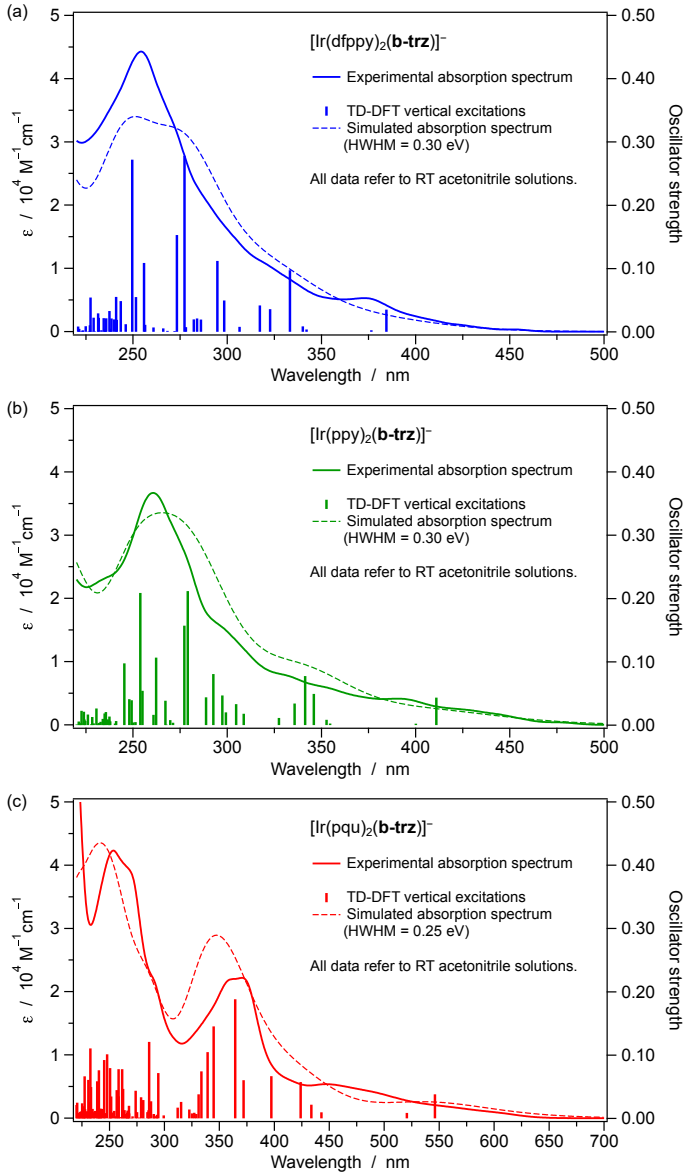

Figure 3.7. First 100 singlet vertical excitations (green bars) computed for **32-34** at the PCM-TD-M06/6-31G(d,p) level of theory in CH_3CN, using the ECP60MDF pseudopotential for the Ir center in combination with the associated cc-pVTZ-PP basis set. Theoretical data (dashed line) are compared with the room-temperature experimental absorption spectrum (full line) in the same solvent.

of **34** can also arise from a predominantly ^{3}LC state, likewise **32** and **33**.

In order to get a deeper insight on the emitting states of all the investigated complexes, spin-unrestricted DFT calculations were carried out to optimize the lowest triplet state (T_1) of **32-34**. Theoretical results indicate that, after relaxation from the Franck-Condon region, all the complexes emit from a predominantly ^{3}LC state with a ^{3}MLCT contribution from the iridium *d* orbitals. As clearly indicated by the T_1 spin-density distributions reported in Figure 3.10, in all the complexes the unpaired electrons are mainly located on the cyclometalating ligand facing the nonplanar bis-tetrazolate ancillary unit, whereas

the iridium metal center shares only 0.43 ± 0.03 e on its d_π orbitals. Therefore, the unstructured emission of **34** might arise from the highly distorted conformation adopted by the phenylquinoxaline ligand (pqu) that prevents the observation of any vibronic progression in the emission spectrum. A similar behavior has been reported for the corresponding cationic analogue of **34** [216].
The TD-DFT calculated emission energies are computed to be 2.47 eV (502 nm), 2.31 eV (536 nm) and 1.69 eV (733 nm) for **32**, **33** and **34**, respectively. These values are in excellent agreement with the mean-photon energy of the emission spectra recorded in room-temperature CH_3CN solution (*i.e.*, 2.50, 2.37, and 1.77 eV for **32**, **33** and **34**, respectively).
As far as PLQYs (ϕ_{em}) are concerned, the best emitter is **32**, with ϕ_{em} = 83 % in room-temperature CH_3CN solution; also the non-fluorinated analogue **33** shows a remarkable emission efficiency (ϕ_{em} = 75 %, Table 3.2). On the contrary, a lower value is measured for **33** (ϕ_{em} = 28 %), probably due to both the energy-gap law and the distorted excited state geometry of the quinoxaline ligands (see above). Anyway, all of these ϕ_{em} values are about twice as much those of a similar cationic series (whose archetype is **B**, Figure 3.4) [216] and are similar those of the already reported cyanide-based anionic iridium(III) complexes whose model compound is **C**, (Figure 3.4) [214].
The excited-state properties of **32** and **33** are also comparable in terms of emission energies, to similar anionic iridium(III) complexes based on differently substituted tetrazolate ligands [197, 201]. However, in the first case [197], such ligands are monodentate and lead to coordination compounds with lower emission quantum yields and, apparently, to relevant stability problems, as evidenced by the presence of degradation products and/or

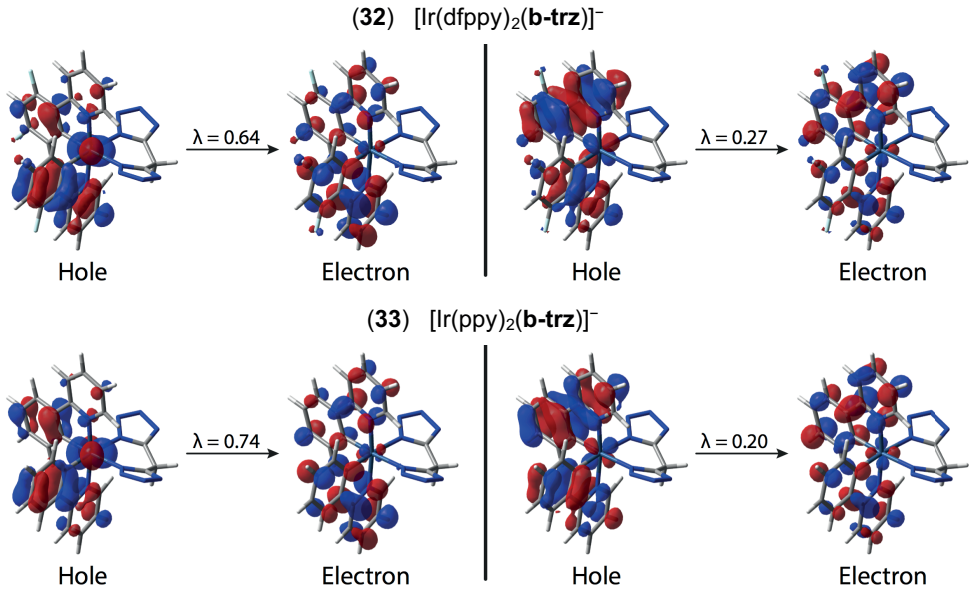

Figure 3.8. Calculated NTOs couples describing the first triplet vertical excitation (*i.e.*, $S_0 \longrightarrow T_1$) for complex **32** and **33** in CH_3CN at the PCM-TD-M06/6-31G(d,p) level of theory, using the ECP60MDF pseudopotential for the Ir center in combination with the associated cc-pVTZ-PP basis set. The reported λ value is the natural transition orbital eigenvalue associated with that particular NTOs couple. Excitation energy for **32** is computed at 436 nm (2.84 eV), to be compared with the experimental value of 452 nm (2.74 eV), while for **33** is computed at 463 nm (2.68 eV), to be compared with the experimental value of 474 nm (2.62 eV).

impurities in the NMR spectra. In the other case [201], probably to prevent the latter issue, a chelating bis-tetrazolate is used, but quantum yields remain around 50 %. Such limitations have been overcome with the present bis-tetrazolate chelator $(\mathbf{b\text{-}trz})^{2-}$.
Since the anionic iridium(III) complexes **32-34** have been ultimately created for their potential application as active materials in LECs, we also investigated their emission properties in solid state under different conditions: (i) in a PMMA matrix at a concentration of 1 wt% by weight or (ii) as neat films.
Figure 3.9 (b) shows the solid-state emission spectra of **32-34** in both experimental conditions and Table 3.2 summarizes the associated luminescence properties and photophysical parameters. The emission spectra in PMMA matrix are virtually superimposable to those recorded in CH_3CN (Figure 3.9 (b)), indicating that all complexes deactivate from the same triplet state responsible for the emission in diluted solution. Notably, in PMMA matrix, the emission quantum yields of **32** and **33** approach 100 %, with complex **32** being always the best emitter of the series (*i.e.*, ϕ_{em} = 95 %, Table 3.2).
On the other hand, in neat films, the distance between the iridium complexes is small and exciton diffusion becomes possible, in particular due to their long lifetimes. This very often leads to a reduction in the PLQY, as excited states can decay nonradiatively

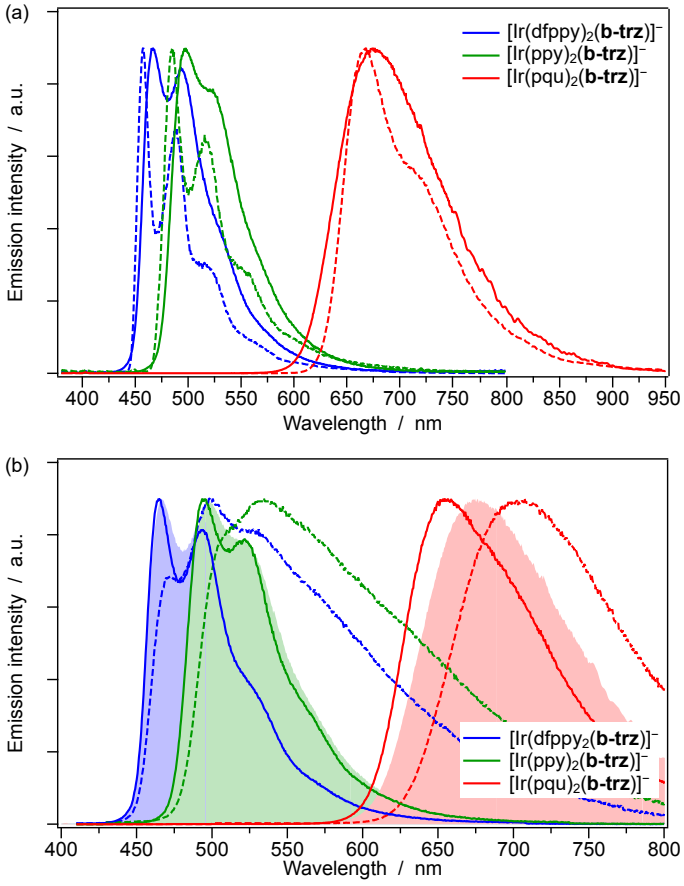

Figure 3.9. (a) Corrected and normalized emission spectra of **32-34** in CH_3CN at 298 K (full lines) and at 77 K (dashed lines). λ_{exc} = 360 nm. (b) Corrected and normalized emission spectra in solid state at 298 K. Full lines: samples in 1 % PMMA matrix; dashed lines: neat films. λ_{exc} = 370 nm. Solid-state spectra are also compared with data recorded in room-temperature CH_3CN solution (transparent filled curves).

Table 3.2. Luminescence properties and photophysical parameters of **32-34** in CH_3CN solution (298 K and 77 K) and in solid state (PMMA matrix and neat film).[a]

	media	λ_{em} (nm)	ϕ_{em} [b] (%)	τ [c] (µs)	k_r [d] (10^5 s^{-1})	k_{nr} [e] (10^5 s^{-1})
$[Ir(dfppy)_2(\mathbf{b\text{-}trz})]^-$	CH_3CN	467, 494	83	2.27	3.7	0.75
	PMMA[f]	465, 494	95	1.88	5.1	0.27
	neat film	472, 499, 525^{sh}	9.3	-[g]		
	77 K	457, 488	-	3.61 (74 %) 1.14 (26 %)		
$[Ir(ppy)_2(\mathbf{b\text{-}trz})]^-$	CH_3CN	498, 520^{sh}	75	2.09	3.6	1.2
	PMMA[f]	495, 521	83	1.76	4.7	0.97
	neat film	535	4.8	-[g]		
	77 K	485, 516	-	4.31 (93 %) 0.79 (7 %)		
$[Ir(pqu)_2(\mathbf{b\text{-}trz})]^-$	CH_3CN	676	28	1.37	2.0	5.3
	PMMA[f]	656	44	1.44	3.1	3.9
	neat film	704	4.3	-[g]		
	77 K	666, 710^{sh}	-	5.66 (77 %) 1.51 (23 %)		

[a] Temperature = 298 K if not specified. [b] In CH_3CN solution: measured with respect to quinine sulfate (1 N, H_2SO_4) as standard (ϕ_{em} = 0.546) [171]; λ_{exc} = 360 nm. In solid samples: determined using an integrating sphere [159]; λ_{exc} = 370–400 nm. [c] λ_{exc} = 373 nm. [d] $k_r = \phi_{em}/\tau$. [e] $k_r = 1 - \phi_{em}/\tau$. [f] 1 wt% of sample content. [g] Multi-exponential decay not reported. [sh] Shoulder.

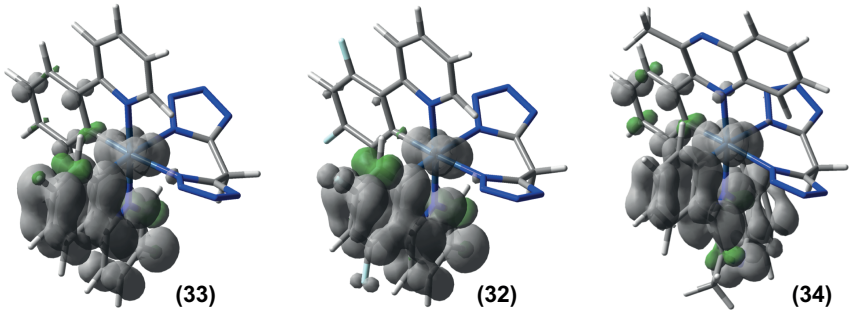

Figure 3.10. Spin-density distribution for the fully relaxed lowest triplet state (T_1) of complexes **32-34**, computed in CH_3CN (isovalue: 0.002 e $bohr^{-3}$).

when encountering trapping sites (both intrinsic and extrinsic). Additionally, it is possible that triplet-triplet annihilation processes play a role. Hence, ϕ_{em} are dramatically reduced and emission lifetimes are no longer monoexponential (Table 3.2). For all of the complexes, an emission red shift is observed with respect to solution, due to band broadening and change of the relative intensities of the luminescence peaks (Figure 3.9 (b)). This behavior is typically observed also in cationic iridium(III) complexes whose ligands are not equipped with bulky substituents, which limits aggregation-induced detrimental effects on luminescence [222].

3.2.5 LEC devices

LECs were prepared to evaluate the electroluminescence properties of complexes **32-34** in a sandwich architecture (Figure 3.11 (a)). The devices were fabricated on cleaned glass ITO-patterned substrate, where a 60 nm PEDOT:PSS layer was deposited by spin-coating. The LEC active layer (200 nm) was deposited from CH_2Cl_2 solution, which consisted of the emitter mixed with the ionic liquid (IL) 1-butyl-3-methylimidazolium hexafluorophosphate ([Bmim][PF_6]) in a 4:1 molar ratio (complex/IL). As top contact electrode, aluminum was thermally evaporated. For simplicity, the LECs containing complexes **32-34** are referred to as **L32-L34**.
LECs are typically characterized by applying a bias and monitoring the emitted light over time. Under a bias, the ions present in the active layer dissociate and migrate toward the electrodes. Once injection overcomes, the resistance of the active layer decreases due to formation of p- and n-doped regions. Yet, it was found that their performance strongly improves when driven by a pulsed current [229]. Under this driving, the pulsed current is applied and the voltage drops reaching a minimum. Therefore, the devices were characterized by applying an average pulsed current (1 kHz, 50 % duty cycle) 100 A m^{-2} in inert atmosphere. The LEC characteristics for **L32-L33** (luminance and electroluminescence) are depicted in Figure 3.11 (b-d) and summarized in Table 3.3.

The electroluminescence of **L34** was unnoticeable under the driving conditions selected, which could be attributed to the low photoluminescence quantum yield in neat film (4 %) and the low solubility of **34** in different solvents, leading to films with a poor

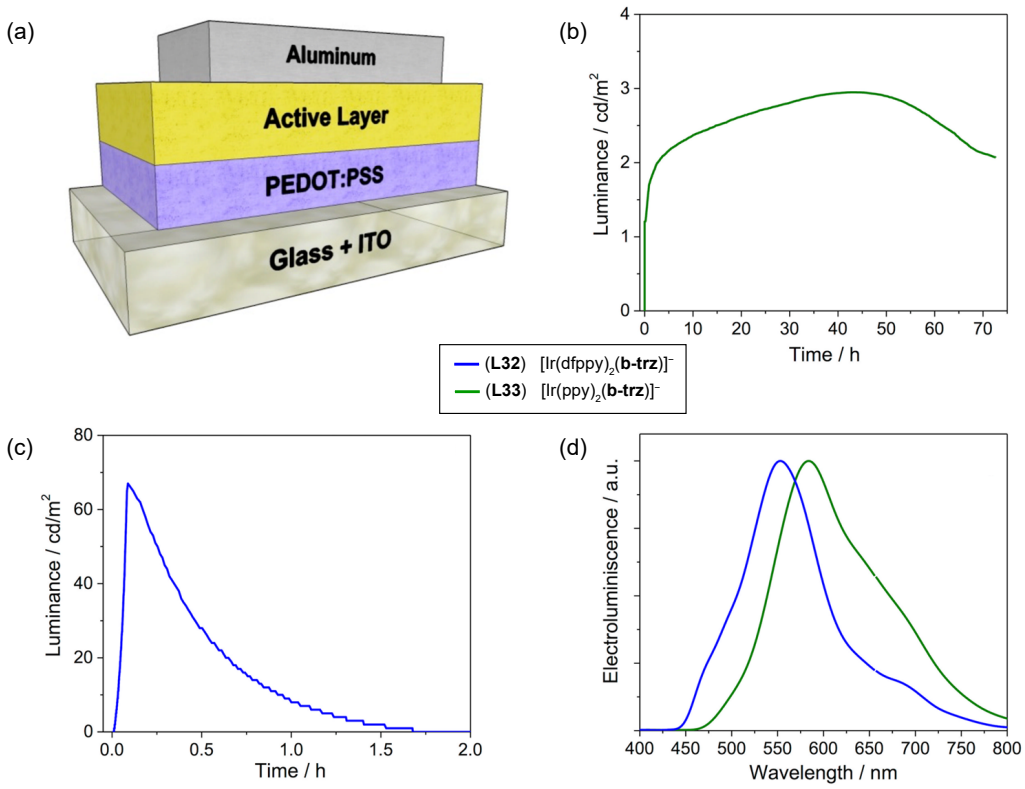

Figure 3.11. (a) LEC architecture. (b, c) Luminance vs time registered respectively for **L32** and **L33** (LEC operated with a pulsed current of 100 A m^{-2}, 1 kHz, 50 % duty cycle and block wave). (d) EL spectrum of **L32** and **L33**.

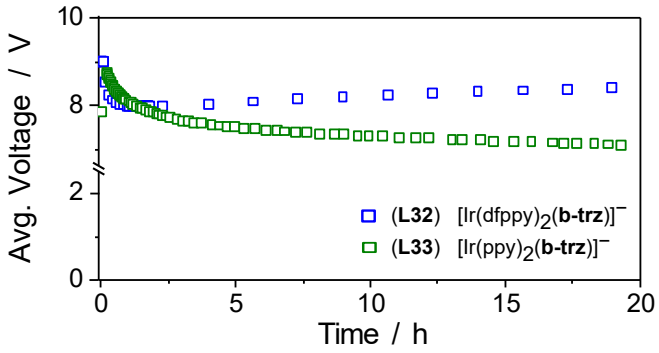

Figure 3.12. Avereage voltage vs. time registered when the LEC containing either **32** (blue) or **33** (green) is operated with a pulsed current of 100 A m^{-2} (1 kHz, 50 % duty cycle and block wave).

morphology. Only **L32** and **L33** exhibit electroluminescence under the tested conditions, displaying a broad and not well-defined band corresponding to green and yellow-orange light with a peak at 553 and 584 nm, respectively. However, the required voltages to sustain the low current densities applied are rather high (around 16 V during the pulse, close to the compliance of the setup) (Figure 3.12). A small but notable decrease in average driving voltage can be observed, indicating that the devices do operate as LECs; in fact, charge injection is improved as a function of driving time. It would appear, however, that the transport of carriers through the film is problematic as the voltage required is significantly higher than what is observed for state of the art LECs.
The luminance of **L32** and **L33** is low, which is not surprising considering the low PLQY observed in neat films. Additionally, the high driving voltage also indicates a nonideal transport of charge carriers, and therefore, it is likely that the mobility of electrons and holes are not balanced leading to a nonideal position of the emission zone. In agreement with the fast decrease in driving voltage, the luminance in **L33** increases in a few minutes, and then it remains almost constant for a long time until it reaches a maximum luminance after 43 h. In the case of **L32** the luminance rises during the first 5 min and then rapidly decreases. For this device, the driving voltage decreases slightly over the same initial time frame after which it starts to increase. The increase in driving voltage usually indicates a permanent degradation in the emitting film, which would explain the rapid decrease in luminance.

Similar trends in decreasing operation lifetimes have been observed in LECs using

Table 3.3. Device performance of the LEC: ITO/PEDOT:PSS/iTMC:[Bmim][PF_6]/Al operated with a pulsed current of 100 A m^{-2}.[a]

	L_{max}[b] (cd m^{-2})	t_{max}[c] (h)	$t_{1/2}$[d] (h)	efficacy[e] (cd A^{-1})	PE[f] (lm W^{-1})	η_{max}[g] (%)	λ_{EL} (nm)
L32	67	0.1	0.4	0.66	0.12	0.22	553
L33	3	43	> 70	0.06	0.01	0.03	584

[a] 1 kHz, 50 % duty cycle and block wave. [a] Maximum luminance.
[c] Time to reach maximum luminance. [d] Time to reach one-half of the maximum luminance.
[e] Maximum efficacy. [f] Maximum power efficiency. [g] Maximum external quantum efficiency.

cationic iridium complexes with an increasing number of F-substituents on the ppy [230]. However, the operation stability of **L33** is rather good, which demonstrates the robustness of the compound as corroborated by the reversible oxidation and reduction in solution.
In perspective, preparation of host-guest systems in which the exciton is confined to the lower bandgap material or ligand functionalization with bulky groups that avoid intermolecular interaction in solid state, should strongly improve the PLQY observed in neat films and, as a consequence, the LEC performance.

3.2.6 Conclusion

We have reported a series of anionic iridium(III) complexes equipped with the bistetrazolate ligand $(\mathbf{b\text{-}trz})^{2-}$. The chelating nature of such a ligand improves the stability of the complexes, thanks to an optimized structure and geometry, which allows a better coordination of the metal center, without causing distortions of bond angles and structural stress. This chelator is particularly simple, as it has only a methylene bridge between the two tetrazolate moieties. This severely limits the occurrence of undesired nonradiative processes promoted by rotational or vibrational motions, which may compromise the emission performance.
All the complexes emit from a predominantly ligand centered state in the red, green, and blue regions of the visible spectrum. Accordingly, DFT calculations show that the HOMO and LUMO are mainly localized on the metal center and on cyclometalating ligands, while the bis-tetrazolate unit does not contribute to the frontier orbitals. By comparison with selected classes of previously published cationic and anionic complexes with high ligand field and even identical cyclometallating moieties, it is shown that the HOMO-LUMO gap is similar. However, the absolute energy of HOMOs and LUMOs is remarkably higher for anionic vs cationic compounds, due to electrostatic effects.
Neat films of the complexes were easily prepared, and the films were sandwiched in between two electrodes allowing for the evaluation of the electroluminescence properties. Probably because of the small intersite distance, the photoluminescence of the complexes is strongly reduced in the films and this inevitably hampers electroluminescence. However, surprisingly stable electroluminescence was observed for devices employing complex **33**, demonstrating the robustness of the anionic compounds. These device results hold promise for further improvements in the area of luminescent anionic complexes for LECs.

3.3 We do want to experiment! Azaborine-ligand Ir(III) complexes

In many technological applications, new molecules and functionalities are continuously needed. A typical approach used in the presence of an aromatic compound is introducing heteroatoms in the ring. For instance, the borazaro unit (B–N) can be inserted in place of the isoelectronic C=C bond inside aromatic or conjugated systems.
Azaborines were discovered by Alfred Stock in 1926 and firstly reported for the synthesis of the borazine ($B_3H_6N_3$), the electronic equivalent of benzene [231, 232]. Among the different possible isomers, 1,2-azaborines are the most investigated, due to an easier synthetic procedure. Azaborine compounds, were proven to have aromatic character and stability similar to the related carbon-carbon analogues [233]. The most evident difference of these compounds from their isoelectronic equivalents is the polarization of the B–N bond with respect to C=C. This local dipole might affect intramolecular interactions and molecular orbitals [234].
Recently, the importance of the borazaro functionlality in biological systems has been reviewed [235]. The use of B–N is interesting for at least two research fields, *i.e.*, the pharmaceutical and the agrochemical one, because of their continuous need of new compounds, while the use of azaborine in material science is related to their good luminescence properties. Considering an application that needs light emission, two notable effects are played by the azaborines on the electronic properties of the molecule: (i) the donor/acceptor system given by the π orbitals of the borazaro system tends to reduce the energy of the HOMO-LUMO transition, while (ii) the aromatic character is slightly reduced by the polarization of the B–N bond and (iii) the planarity of the system is essentially maintained [233, 236].
With the aim of expanding the library of known bidentate ligands suitable for luminescent iridium complexes and widening research in EL devices [237], a novel 1-2 azaborine system (*i.e.*, 4-methyl-2-(pyridine-2-yl)-1,2-borazaronaphthalene, **Hpbzn**) has been used as ancillary ligand to prepare three Ir(III) complexes. The effect of the borazaro moiety on the free ligand and the properties of the complexes has been assessed by comparison with the isoelectronic C=C equivalent 2-(naphthalen-2-yl)pyridine (**Hnpy**), studied independently and used as ancillary ligand in Ir(III) coordination compounds.

3.3.1 The considered complexes

A series of cyclometallated ligands (**Hppy**, **Hdfppy** and **Hpqu**) has been combined with two different anionic ancillary ligands, the **Hpbzn** and its C=C analogue **Hnpy**, to obtain azaborine and isoelectronic C=C Ir(III) complexes (Figure 3.13). The general formula of the series is [Ir(C^N)$_2$(A^A)] (with C^N as a cyclometallating ligand and A^A as the ancillary ligand). In all of the compounds, the metal ion forms a cyclometallated-coordination bond with the three ligands, thus the complexes are neutral.
Two different complexes are reported, based on the same **Hnpy** ligand, due to the possibility to preferentially obtain one of the two isomers by tailoring the preparative strategy. It must be emphasized that, due to the less sterically hindered structure, Ir(ppy)$_2$(**3-npy**) is the most thermodynamically stable and Ir(ppy)$_2$(**1-npy**) slowly converts into the most

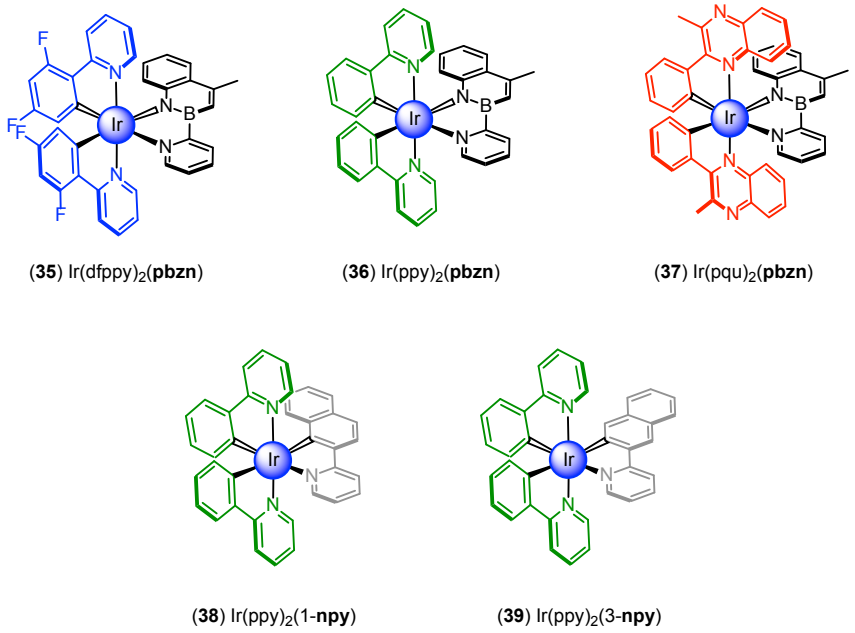

Figure 3.13. Azaborine and isoelectronic carbon-carbon Ir(III) neutral complexes. In blue, green and red are higlighted the different cyclometallated ligands, while black and grey colors are used, respectively, for ancillary azaborine and naphthalene-pyridine ligands.

stable structural isomer. The results and discussion given in this Section follow and update those reported in the reference [184].

3.3.2 X-ray single crystal structures

The coordination structure of **36** was determined by single-crystal X-ray diffraction. The crystal has the Pbcn orthorombic space group, the structure (not yet deposited) is depicted in Figure 3.14.

The distorted octahedral geometry of the complex is characterized by the two pyridine of the C^N ligands in trans positions (N–Ir–N angle = 174.2°), as commonly observed for

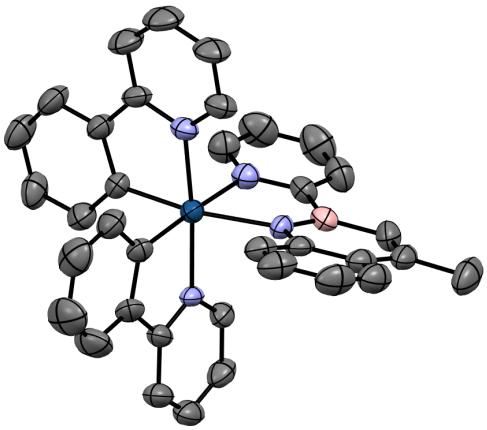

Figure 3.14. Experimental X-ray structures of complex Ir(ppy)$_2$(**pbzn**). Thermal ellipsoids are plotted at the 50 % probability, using Mercury CSD 3.10 [165]. The counterion and hydrogen atoms are omitted for clarity.

similar cyclometalated iridium(III) complexes [231, 232]. The two C^N ligands exhibit a similar bite angle (79.4° and 80.1°), comparable to that of the azaborine ligand (78.4°). The two Ir–N coordination bonds of the azaborine ligand are slightly elongated with respect to those of the cyclometallated ligands (2.16 and 2.19 Å vs. < 2.05 Å, respectively). As expected, the ancillary ligand is planar, corroborating the aromatic character of the borazaronaphthalene moiety [233].

3.3.3 Electrochemical properties

The **Hpbzn** ligand, as highlighted in Figure 3.16 (b), can be easily protonated on the pyridinic nitrogen atom, upon addition of acid to its solution. This observation is confirmed by the presence of both the forms when samples are dissolved in not stabilized CH_2Cl_2, which is known to contain traces of HCl. The observed proton affinity is probably the origin of the slight instability of the complexes with the azaborine ancillary ligand. To minimize protonation the solutions containing the complexes or the free ligand where treated with µM concentrations of Hunig's base (N,N-Diisopropylethylamine), whenever possible.

The two ligands in their neutral form and all the complexes have been investigated by CVs and OSWVs; selected electrochemical data are summarized in Table 3.4. The Fc^+/Fc redox couple has been used as internal reference, the experiments have been carried out in CH_3CN at ambient temperature with a cell made of a glassy carbon electrode, a platinum wire counter electrode, a SCE reference electrode and [TBA][PF_6] as supporting electrolyte (see Appendix A). The OSWVs are reported in Figure 3.15 (a-c), while the CVs

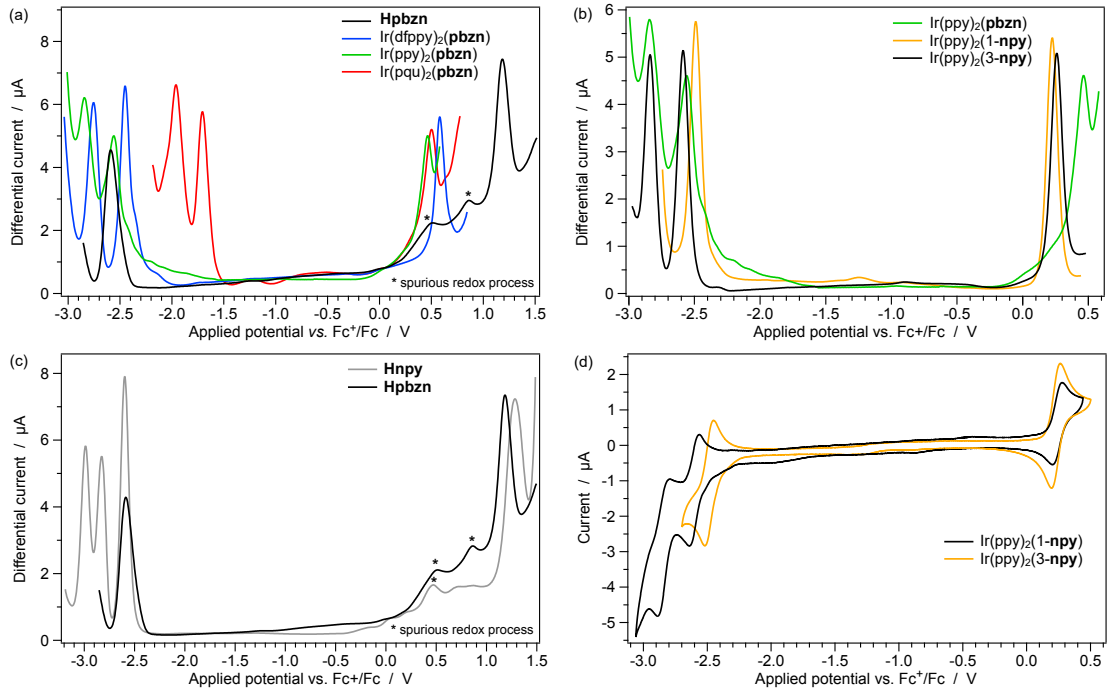

Figure 3.15. OSWVs of (a) azaborine ligand and related complexes, (b) Ir(ppy)$_2$(**pbzn**) and isoelectronic C=C complexes, (c) **Hpbzn** and **Hnpy** ligands and (d) CV of Ir(ppy)$_2$(**1-npy**) and Ir(ppy)$_2$(**3-npy**). Measurements are made with a glassy carbon electrode in CH_2Cl_2 + 0.1 M [nBu$_4$N][BF_4] at room temperature (OSWVs: frequency 20 Hz, amplitude 20 mV, step 5 mV).

Table 3.4. Electrochemical data and DFT energies of the FMOs for the ligands and the complexes containing the azaborines or their isoelectronic C=C analogues as ancillary ligands, in CH_2Cl_2.

	Electrochemical data[a] (V)			DFT calculated energies[b] (eV)		
	E_{Ox}	E_{Red}	ΔE_{Redox}	E_{HOMO}	E_{LUMO}	ΔE_{DFT}
$Ir(dfppy)_2$(**pbzn**)	+0.58	−2.45	3.03	−5.57	−1.48	4.09
$Ir(ppy)_2$(**pbzn**)	+0.46	−2.56	3.02	−5.47	−1.40	4.07
$Ir(pqu)_2$(**pbzn**)	+0.50	−1.71	2.21	−5.48	−2.36	3.12
Hpbzn	+1.18[c]	−2.59	3.77	−6.24	−1.28	4.96
Hnpy	$+1.28^{rev}$	-2.60^{rev}	3.88	−6.15	−1.36	4.79
$Ir(ppy)_2$(1-**npy**)	$+0.25^{rev}$	-2.59^{rev}	2.84	−5.31	−1.38	3.93
$Ir(ppy)_2$(3-**npy**)	$+0.23^{rev}$	-2.49^{rev}	2.72	−5.29	−1.49	3.80

[a] Data refer to OSWV experiments; ferrocene is used as internal reference. $\Delta E_{Redox} = E_{Ox} - E_{Red}$.
[b] Data refer to calculation performed in CH_2Cl_2 using the M06 functional (see Appendix A). $\Delta E_{DFT} = E_{LUMO} - E_{HOMO}$. [c] Two spurious oxidation processes occur at lower potentials.
^{rev} Reversible process.

of the two **npy** complexes are in Figure 3.15 (d).
None of the redox processes exhibited by the azaborine complexes or by the free **Hpbzn** ligand is reversible, as also found for other azaborine systems [236]. On the contrary, electrochemical reversibility is observed for all the first oxidations and reductions of **Hpny** and for the two complexes where this ligand is used.
The electrochemical results are corroborated by DFT calculations (Table 3.4). The three azaborine complexes have comparable oxidation potentials and HOMO energy. This is an expected result due to the match of the HOMO orbital, which is located in all of the complexes on the borazaronaphthalene moiety and the *d* orbitals of the Ir(III) (Figure 3.24). On the other hand, the reduction shows a clear trend: with the increase of the electronic delocalization on the cyclometallated ligands (passing from ppy to pqu), the process becomes energetically less demanding.
It is worth mentioning that the ΔE_{Redox} of the azaborine complex **36** is increased with respect to the two C=C equivalents, in line with the HOMO and LUMO energies determined by DFT calculations (see Table 3.4). Since the LUMO energies are equal (comparing **36** and **38**), this behavior is attributed to the HOMO stabilization induced by the electron-withdrawing effect of boron [231, 238].

3.3.4 Photophysical properties of the novel azaborine ligand

The photophysical properties of the azaborine ligands **Hpbzn** and $\mathbf{H_2pbzn^+}$ were studied in solution (CH_2Cl_2 and CH_3CN) at ambient conditions and in rigid matrix (77 K frozen solvent). The protonated form are obtained by the stoichiometric addition of acid in solution, exploiting the basicity of the pyridine nitrogen. The experimental results were supported by theoretical calculations to determine structural and electronic properties of the ground state as well as of the lowest singlet (S_1) and triplet states (T_1) (see Appendix A).

The absorption features of **Hpbzn** (Figure 3.16 (a)), are substantially independent from the solvent, confirming the absence of charge transfer (CT) excited states in the recorded region, while the spectra of the protonated form are significantly blue-shifted with a polar solvent. The titration of **Hpbzn** with trifluoroacetic acid (TFA) affords isosbestic points, suggesting that a single product is obtained, *i.e.*, $\mathbf{H_2pbzn^+}$. The basicity of the ligand is confirmed by the total conversion of **Hpbzn** in the protonated form upon addition of 1 eq. of acid (Figure 3.16 (b)).

TD-DFT vertical excitations suggest a high oscillator strength of the HOMO-LUMO transition for both molecules (Table 3.5). The HOMO in **Hpbzn** is mainly centered on the borazaronaphthalene moiety, but is extended to the whole molecule, while the LUMO has a similar character and the contribution is more uniform across the molecule (Figure 3.17). Upon protonation a stabilization of the LUMO and a reduction of the energy gap are expected. The CT character of $\mathbf{H_2pbzn^+}$ is also confirmed, since the HOMO mainly resides on the borazaronaphthalene moiety, whilst the LUMO is located predominantly on the pyridine and the boron atom (Figure 3.17).

As depicted in Figure 3.18, the simulated absorption spectra obtained with the two vertical transition $S_0 \longrightarrow S_1$ and $S_0 \longrightarrow S_4$ that exhibit the strongest oscillator strength, well

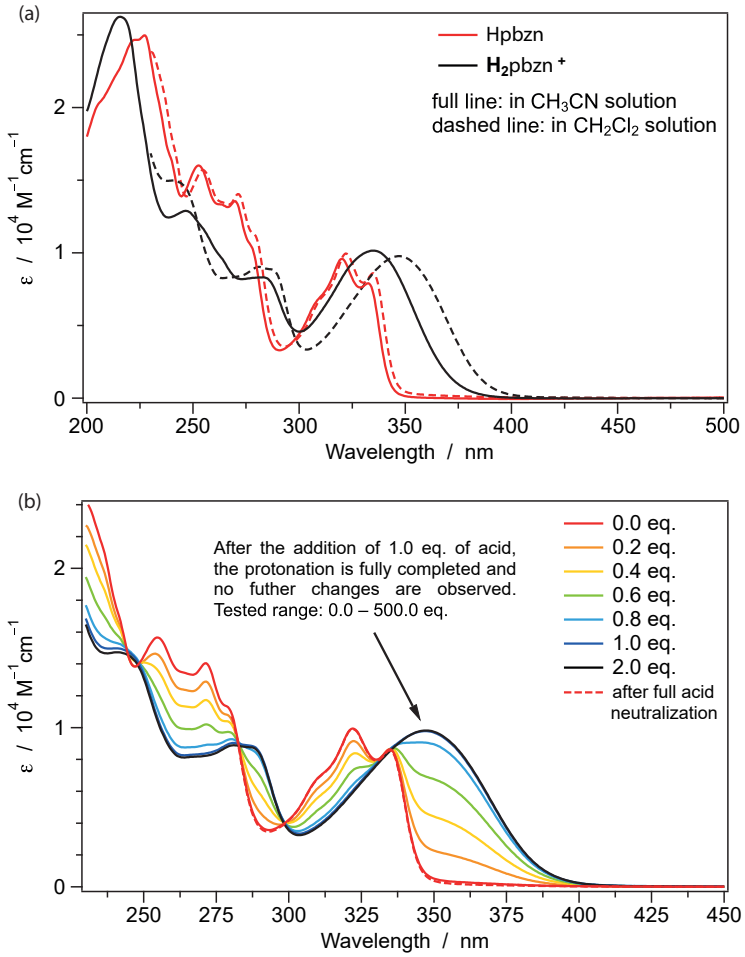

Figure 3.16. Absorption spectra of (a) **Hpbzn** (red) and $\mathbf{H_2pbzn^+}$ (black) in CH_3CN (full line) and CH_2Cl_2 (dashed line) solutions. (b) Changes of the absorption spectra of **Hpbzn** upon addition of TFA (0-2.0 equivalents) in CH_2Cl_2; [**Hpbzn**] = 40 μM.

Table 3.5. TD-DFT singlet excited-states calculated for **Hpbzn** and **H_2pbzn$^+$** in CH_3CN. The vertical excitation contribution to the dominant monoexcitation is reported in brackets. The nature of the electronic state is given in brackets for minor contributions. napht = borazaronaphthalene; py = pyridine.

	state	λ (nm)	f	dominant monoexcitation	nature
Hpbzn	S_1	311	0.616	HOMO⟶LUMO (94 %)	napht(py)⟶napth+py
	S_2	283	0.003	HOMO-2⟶LUMO (84 %)	py⟶napth+py
	S_3	282	0.068	HOMO-1⟶LUMO (88 %)	napht⟶napth+py
	S_4	261	0.463	HOMO⟶LUMO+1 (73 %)	napht(py)⟶napth+py
	S_5	247	0.062	HOMO⟶LUMO+2 (73 %)	napht(py)⟶py
H_2pbzn$^+$	S_1	363	0.452	HOMO⟶LUMO (89 %)	napht⟶py
	S_2	342	0.020	HOMO-1⟶LUMO (87 %)	napht⟶py
	S_3	296	0.124	HOMO⟶LUMO+1 (89 %)	napht⟶py
	S_4	281	0.134	HOMO-1⟶LUMO+1 (90 %)	napht⟶py
	S_5	263	0.212	HOMO⟶LUMO+2 (82 %)	napht⟶napht+py

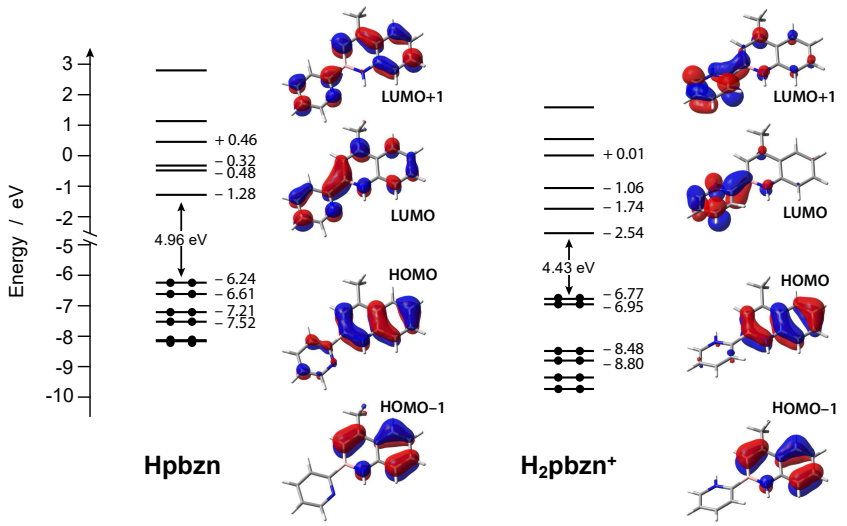

Figure 3.17. Frontier molecular orbitals of the neutral **Hpbzn** and protonated **H_2pbzn$^+$** forms, displayed at isovalue = 0.04 $e^{1/2}$ $bohr^{-3/2}$. Orbital energies are reported ineV.

overlap the experimental ones.

The emission features in CH_2Cl_2 solution of the neutral and protonated ligands are depicted in Figure 3.19 and Table 3.6. The fluorescence band of **Hpbzn** is vibrationally resolved with λ_{max} = 362 nm; on the other hand, **H_2pbzn$^+$** shows a broader and lower energy emission band, with an almost doubled Stokes' shift (0.98 vs. 0.42 eV). These characteristics of the fluorescence band are in line with the CT character of the transition, and the different structure adopted by the excited-state. The increase of PLQY upon protonation of **Hpbzn** is essentially due to a reduction of the k_{nr} constant with respect to the neutral form. A similar CT character of the excited state, which induces a red-shifted broad emission band, has been observed in other azaborine systems upon

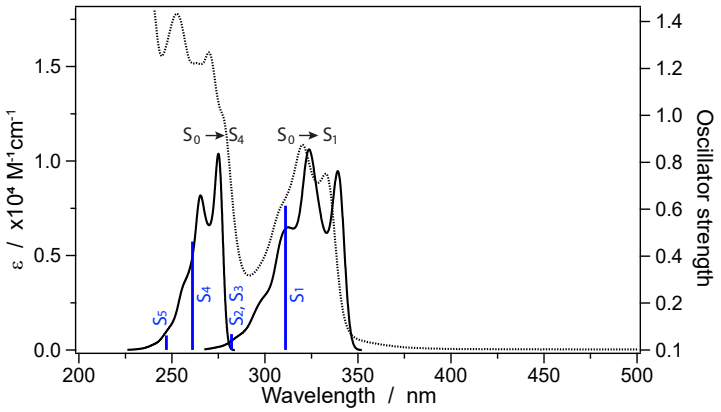

Figure 3.18. Experimental (dotted line) and calculated (full line) absorption spectra of **Hpbzn** in CH_3CN solution. Blue lines represent the oscillator strength of the vertical excitations.

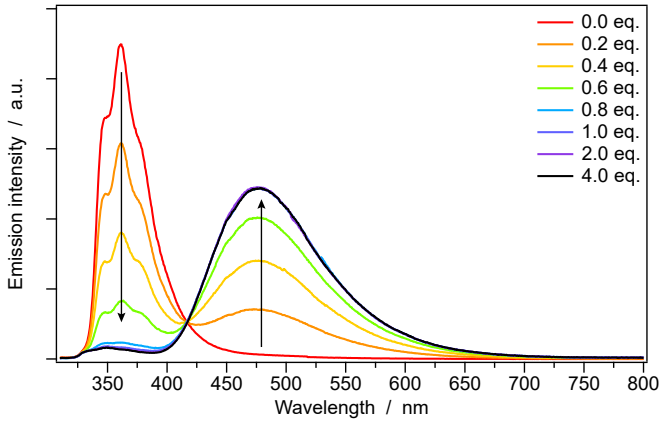

Figure 3.19. Emission-spectra variation of **Hpbzn** upon addition of TFA (0-4.0 equivalents) in CH_2Cl_2 solvent; [**Hpbzn**] = 30 μM.

the selective complexation of fluoride ions [238].
The structures of the ground and the first singlet excited states, determined by DFT calculations (Figure 3.20) essentially confirm the above observations. The S_0 and S_1 states of **Hpbzn** are both planar and characterized by the same N–H···N hydrogen bonding, while the C–B bond shortens in the excited state due to the bonding character of the LUMO located on that connection.
On the other hand, the ground state geometry of $\mathbf{H_2pbzn^+}$, has a dihedral angle between the two nitrogen atoms of ≈ 153° thus, upon proton addition, a flip of the pyridine is observed. Again, the bonding character of the C–B connection observed in the LUMO entails the molecule flattening with the two aromatic moieties on the same plane and a shortening of the C–B bond. Low temperature experiments in CH_2Cl_2 rigid matrix (Figure 3.21 and Table 3.6) show the presence of the fluorescence and the phosphorescence for both the ligand forms. In the case of **Hpbzn** the fluorescence band at 77 K exhibits a more structured shape, due to the increase of the vibrational resolution, with no net variation of the transition energy; moreover, a structured band, assigned to the phosphorescence, is observed at lower energy. This emission is characterized by an

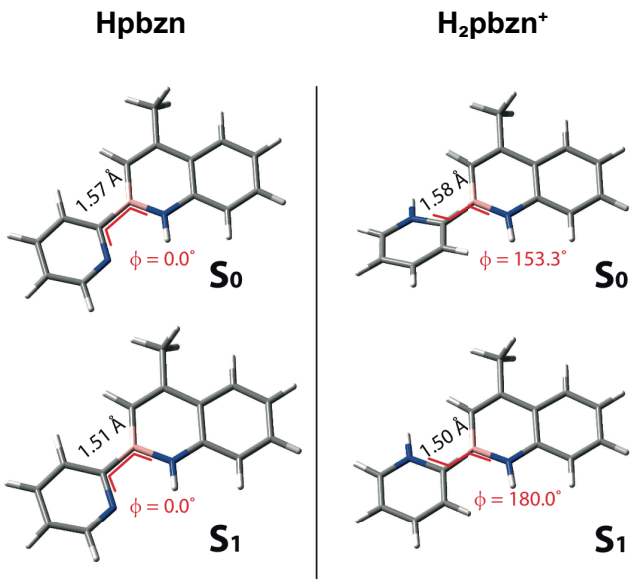

Figure 3.20. DFT-calculated S_0 and S_1 geometries of **Hpbzn** and **H_2pbzn$^+$**.

Table 3.6. Photophysical data of the neutral and protonated azaborine ligand in CH_3CN and CH_2Cl_2 at 298 K and 77 K.

	solvent	temp. (K)	em. state	λ_{em} (nm)	ϕ_{em} [a] (%)	τ [b] (ns)	k_r (10^8 s^{-1})	k_{nr} (10^8 s^{-1})
Hpbzn	CH_3CN	298	S_1	347^{sh}, 358, 372^{sh}	21.5	1.3	1.6	5.9
	CH_2Cl_2	298	S_1	348^{sh}, 362, 376^{sh}	27.8	1.4	2.0	5.1
		77	S_1	347^{sh}, 357, 374, 391^{sh}		2.3		
			T_1	418, 432, 447, 460, 478		$2.68 \cdot 10^9$		
H_2pbzn$^+$	CH_3CN	298	S_1	490	0.9	0.1	0.7	80
	CH_2Cl_2	298	S_1	480	41.3	3.9	1.1	1.5
		77	S_1	417		4.1		
			T_1	452^{sh}, 478, 502^{sh}		$1.52 \cdot 10^9$		

[a] Measured with respect to quinine sulfate (1 N, H_2SO_4) as standard (ϕ_{em} = 0.546) [171], λ_{exc} = 305 nm.
[b] λ_{exc} = 278 nm. ^{sh} Shoulder.

excited-state lifetime of 2.68 s, in line with other organic molecules displaying phosphorescence. On the other hand, the rigidocromic effect at 77 K, affects the CT character of the first excited state of **H_2pbzn$^+$**, blue-shifting the fluorescence. This emission band remains broad, while a slightly more structured phosphorescence band is observed at lower wavelength. The $T_1 \longrightarrow S_0$ transitions, estimated from DFT calculations, are in agreement with the experimental data. The lowest triplet of **Hpbzn** has been calculated to be 2.97 eV above the ground state (GS), which corresponds to an emission maximum of 417 nm, perfectly in accordance with experimental data at 77 K (0-0 transition at 418 nm). In the case of **H_2pbzn$^+$** the T_1 has been estimated at 2.97 eV above the GS, which corresponds to 471 nm, again confirmed by the experimental data (0-0 transition at 478 nm).

In Figure 3.22 are depicted the spin density distributions of the lowest triplet states.

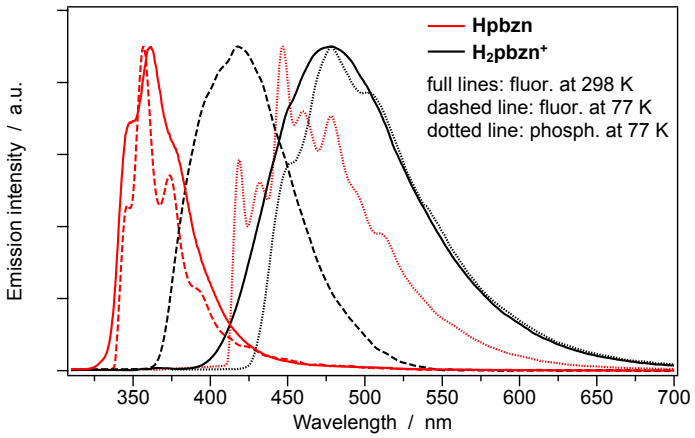

Figure 3.21. Fluorescence (full line: r.t.; dashed line: 77 K) and phosphorescence (dotted line: 77 K) spectra of the **Hpbzn** (red) and **H_2pbzn$^+$** (black) in CH_2Cl_2.

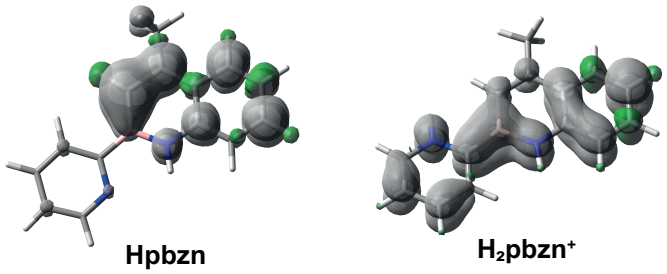

Figure 3.22. Spin density distribution (0.002 e bohr^{-3}) of the T_1 state of **Hpbzn** and **H_2pbzn$^+$**

The unrestricted DFT calculation of the T_1 state for **Hpbzn** highlights the substantial difference between the triplet spin density, centered on the borazaronaphthalene, with the HOMO $\longrightarrow$ LUMO excitation that is spread across the whole molecule. In the case of **H_2pbzn$^+$** the triplet spin density well matches the HOMO $\longrightarrow$ LUMO excitation.

3.3.5 Photophysical properties of the azaborine complexes

The Ir(III) complexes incorporating the azaborine ligands were studied in solution at room temperature (CH_2Cl_2 and CH_3CN), in butyrronitrile glass at 77 K (BuCN) and in PMMA matrix (1 wt% of sample content).

The absorption spectra of the complexes in solution are reported in Figure 3.23. The spectra of Ir(dfppy)$_2$(**pbzn**) and Ir(ppy)$_2$(**pbzn**) are similar, but the first is shifted by 0.13 eV to higher energy due to the electron withdrawing effect of the fluorine atoms on the C^N ligands. On the other hand, the Ir(pqu)$_2$(**pbzn**) shows a stronger transition around 350 nm and the tail of the lowest energy absorption band goes up to 650 nm, while the absorption of the two other complexes stops at about 500 nm.

The high energy absorption band around 250 nm, observed for all the complexes, corresponds to the $\pi \longrightarrow \pi^*$ LC transition ($\epsilon \approx 4 \times 10^4$ M^{-1} cm^{-1}), while the features observed at $\lambda > 300$ nm have been assigned with the support of the TD-DFT calculated transitions, which well reproduce the spectra (Figure 3.25).

The main transition observed at $\approx$ 360 nm occurs in all the azaborine compounds. In the

case of dfppy and ppy complexes, the band arises from a mixed contribution of the vertical excitations from GS to S_4, S_5 and S_6. The involved FMOs (Figure 3.24) are located on the borazaronaphthalene moiety (HOMO) or on the cyclometallated ligands (HOMO-1), in both cases the *d*-orbitals contribution of the metal ion is observed. On the contrary, the acceptor orbital, in all cases, is located on a pyridine ring, thus, as a rule of thumb, the absorption band has a MLCT character (which explains the low oscillator strength observed (0.04-0.07)) also with contribution from ILCT and LC transitions. In the pqu complex, at the same energy, the vertical excitation correspond to transition from the GS to the S_{16} and S_{19} excited states. In agreement with the larger ϵ, the higher oscillator strength (0.1) is explained by the stronger LC character of the transition, centered on the pqu ligands, with minor contribution from the orbitals of the metal center (Figure 3.25). Due to the strong SOC induced by the heavy atom, spin forbidden transition to the

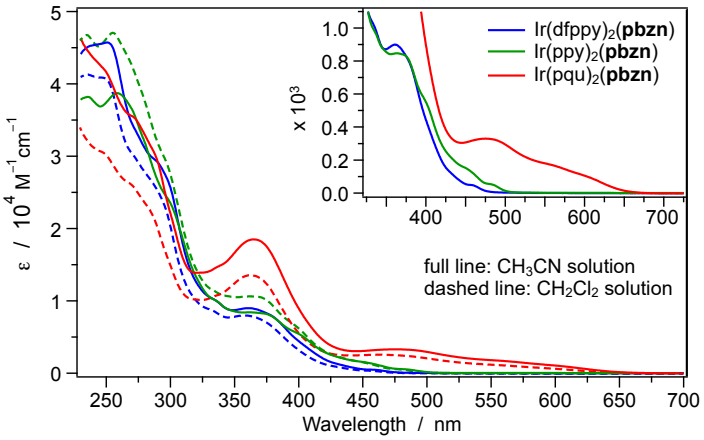

Figure 3.23. Absorption spectra of the complexes with the azaborine ligands in CH_3CN (full line) and CH_2Cl_2 (dashed line). The inset refers to CH_3CN solution.

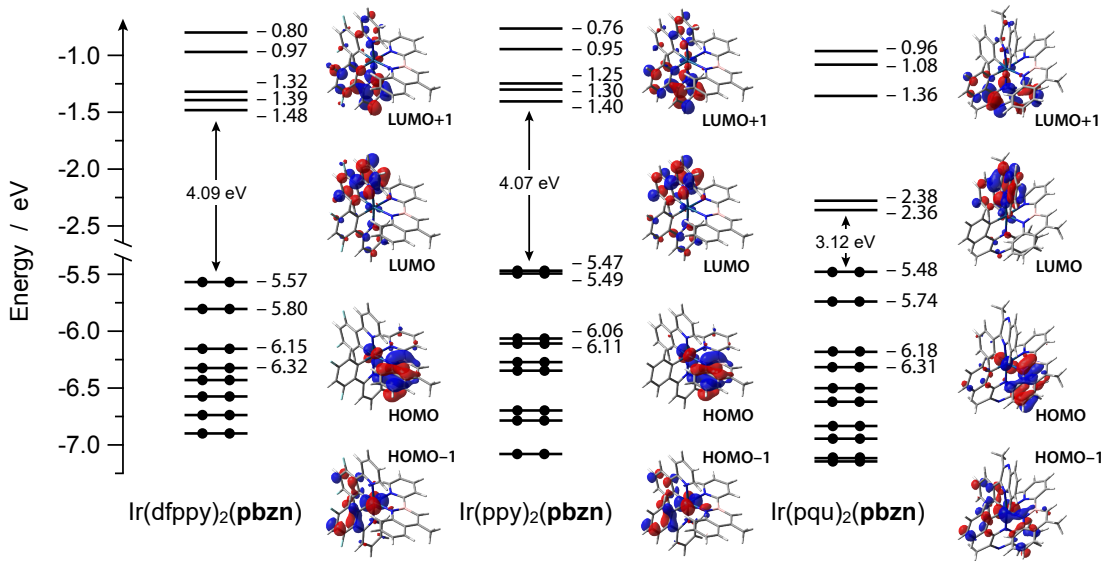

Figure 3.24. Frontier molecular orbitals of the neutral Ir(dfppy)$_2$(**pbzn**), Ir(ppy)$_2$(**pbzn**) andIr(pqu)$_2$(**pbzn**), displayed at isovalue = 0.04 $e^{1/2}\,bohr^{-3/2}$. Orbital energies are reported in eV.

triplets are observed at lower energies. In the case of dfppy and ppy complexes the S_0 and T_1 transitions are barely visible at 456 and 480 nm in CH_3CN, respectively (Figure 3.23, inset). The character of these transitions is extrapolated from TD-DFT natural transition orbitals (NTOs), so as to determine where the emitting triplet state is located. The S_0 and T_n (with n = 1, 2, 3) NTOs couples are depicted in Figure 3.27. For Ir(dfppy)$_2$(**pbzn**) the lowest triplet has a LC character involving the azaborine ancillary ligand. In the case of Ir(ppy)$_2$(**pbzn**) the calculated triplets exhibit minimal energy separation, with the lower being centered on one of the cyclometallating ligands. Further calculations assessing the geometry relaxation need to be considered. Possibly, the Ir(pqu)$_2$(**pbzn**) emission is expected to have a mixed character (MLCT/LLCT/LC).

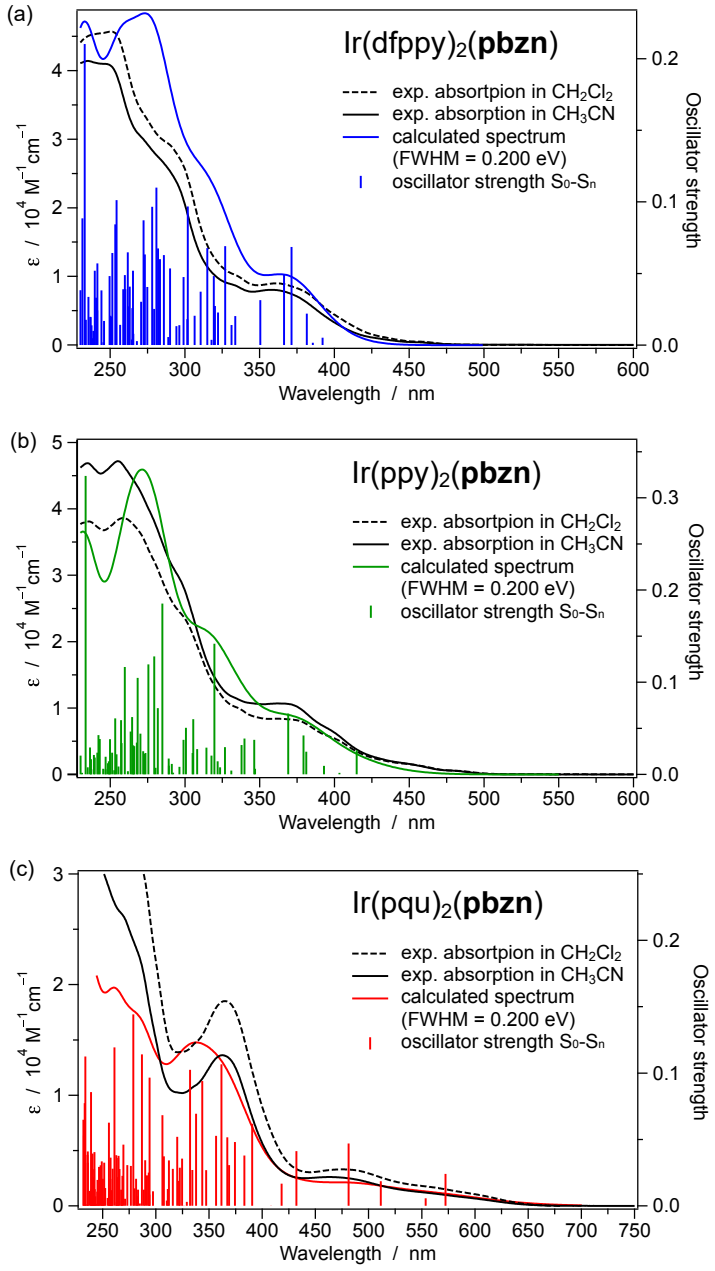

Figure 3.25. TD-DFT calculated absorption spectra of the complexes with the azaborine-ligands in CH_3CN, compared experimental absorption spectra in solution (black lines).

Table 3.7. Photophysical data of the azaborine complexes, in CH_3CN and CH_2Cl_2 at 298 K and 77 K and in PMMA matrix.[a]

	media	λ_{em} (nm)	ϕ_{em}[b] (%)	τ[c] (μs)	k_r (10^4 s^{-1})	k_{nr} (10^4 s^{-1})
Ir(dfppy)$_2$(**pbzn**)	CH_3CN	516	5.7	1.7	3.4	55.5
	CH_2Cl_2	545	5.7	1.9	3.0	50.0
	PMMA[d]	505	68.9	14.2	4.9	2.2
	77 K[e]	484, 516, 556, 598^{sh}		21.8		
Ir(ppy)$_2$(**pbzn**)	CH_3CN	516	15.9	1.6	9.9	52.6
	CH_2Cl_2	510, 530^{sh}	19.2	1.3	14.8	62.2
	PMMA[c]	513, 534	67.4	3.5	19.3	9.3
	77 K[d]	490, 526, 566		4.5		
Ir(pqu)$_2$(**pbzn**)	CH_3CN	692	6.5	1.4	4,6	66.8
	CH_2Cl_2	672	12.0	1.5	8.0	58.7
	PMMA[c]	673	22.3	1.3	17.2	59.8
	77 K[d]	643		10.7		

[a] Temperature = 298 K if not specified otherwise.
[b] In solution: measuredwith respect an air-equilibrated water solution of $[Ru(bpy)_3]Cl_2$ (ϕ_{PL} = 0.028) [239]; λ_{exc} = 450 nm. In solid samples: determined using an integrating sphere [159]; λ_{exc} = 450 nm.
[c] λ_{exc} = 373 nm. [d] 1 wt% of sample content. [e] in BuCN glass. ^{sh} Shoulder.

The emission spectra of the series, reported in Table 3.7 and Figure 3.26 show the effects of the solvent polarity (CH_2Cl_2 vs. CH_3CN). Due to oxygen quenching of the luminescence, the spectra were recorded after bubbling the solution at least 20 min in Ar.
The spectra of Ir(dfppy)$_2$(**pbzn**) and Ir(ppy)$_2$(**pbzn**) exhibit a weak vibronic structure and, in both cases, they are only slightly affected by the change of the solvent or by passing to the polymer matrix. Furthermore, the luminescence band of the two complexes arises from similar energies, with the maximum centered at ≈ 520 nm in CH_3CN. When the temperature is reduced to 77 K, the emission bands in BuCN solutions of the dfppy and ppy complexes show the same onset but become strongly structured, with a good resolution of the vibronic progressions. The above observations are in line with a triplet emission having a LC character, as suggested by the above reported NTOs.

In the case of Ir(pqu)$_2$(**pbzn**) the phosphorescence is red-shifted compared to the parent complexes and shows a broad and unstructured shape in any media (solid or liquid) at room temperature. The significant MLCT character of the transition is further evidenced by the rigidochromism observed for the emission band at low temperature and by the stabilization of the same emitting state in a more polar solvent (Figure 3.26 (b)).
As a general trend, a strong enhancement of the luminescence in PMMA matrix is observed for the entire series (ϕ_{em} = 22–69 % in the polymer), while for dfppy and ppy complexes the variation is due to a reduction of the k_{nr}, in the case of Ir(pqu)$_2$(**pbzn**) the lifetime is similar, so it is the increase of the k_r that rises the luminescence intensity (Table 3.7).
A deeper insight on the emitting state is obtained by TD-DFT optimization of the lowest triplet states (T_1-T_3), reported in Figures 3.28 (a-c). After a full geometry relaxation, the

energetic ordering of the triplets is confirmed for Ir(dfppy)$_2$(**pbzn**), with consistent energy separation (> 0.2 eV) for such triplets splitting. On the other hand, a state flipping is observed in the case of Ir(ppy)$_2$(**pbzn**) with a three-fold lower energy separation among the triplets. As a consequence, the emitting state in dfppy and ppy azaborine-complexes is the same, confirming the experimental observations; such state is essentially centered on the **pbzn** ancillary ligand, with just a minor contribution from the *d* orbitals of the metal ion.
The experimental emission bands are also supported by the adiabatic energy difference calculated between the lowest triplet and the GS: the energy gap has been estimated in 2.53 eV for the dfppy complex, and 2.51 eV for the ppy one (490 and 494 nm respectively), in good agreement with the low temperature spectra (Ir(dfppy)$_2$(**pbzn**): 484 nm and Ir(ppy)$_2$(**pbzn**): 484 nm).
The situation for Ir(pqu)$_2$(**pbzn**) is by far more complex: two of the three triplets are degenerate, while the third appears to be just 0.001 eV higher in energy. In this case, it is possible to take advantage of the evident ^{3}MLCT character of the emission shown by this compound to identify the lowest triplet state as T_1 and T_3 of Figure 3.28 (c). By comparing the spin densities, it is also possible to tentatively rationalize the different behaviour exhibited by the pqu complex in PMMA matrix. The large increase of the k_r observed in this medium might be the result of an energy flipping of the triplet states,

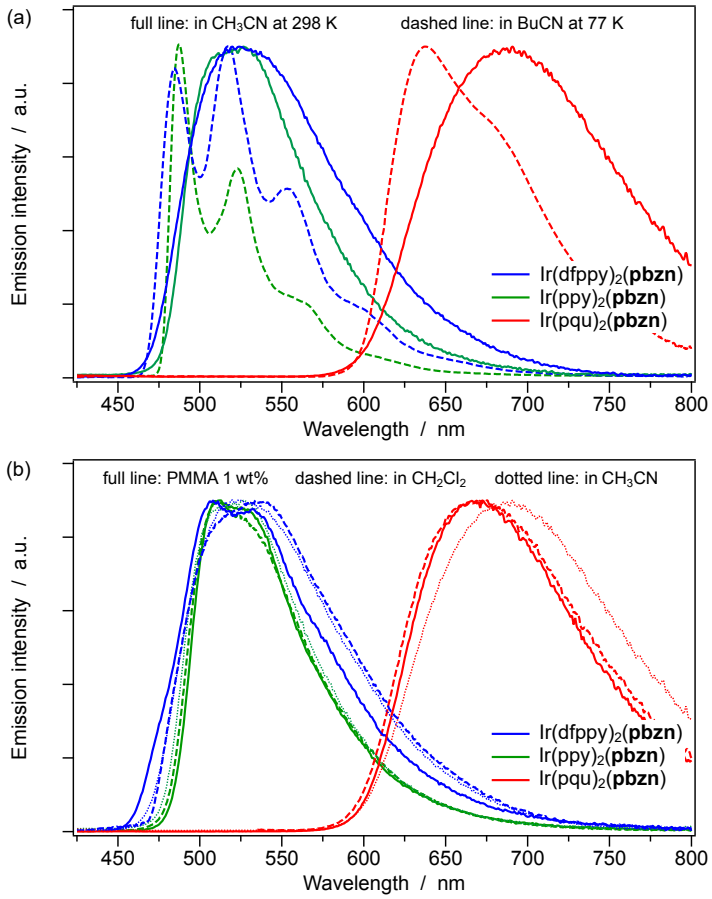

Figure 3.26. (a) Emission spectra in CH_3CN ant r.t. (full line) and in BuCN at 77 K (dashed line). (b) comparison of the effect of the media on the emission band (full line: PMMA matrix; dashed line: CH_3CN and dotted line: CH_2Cl_2).

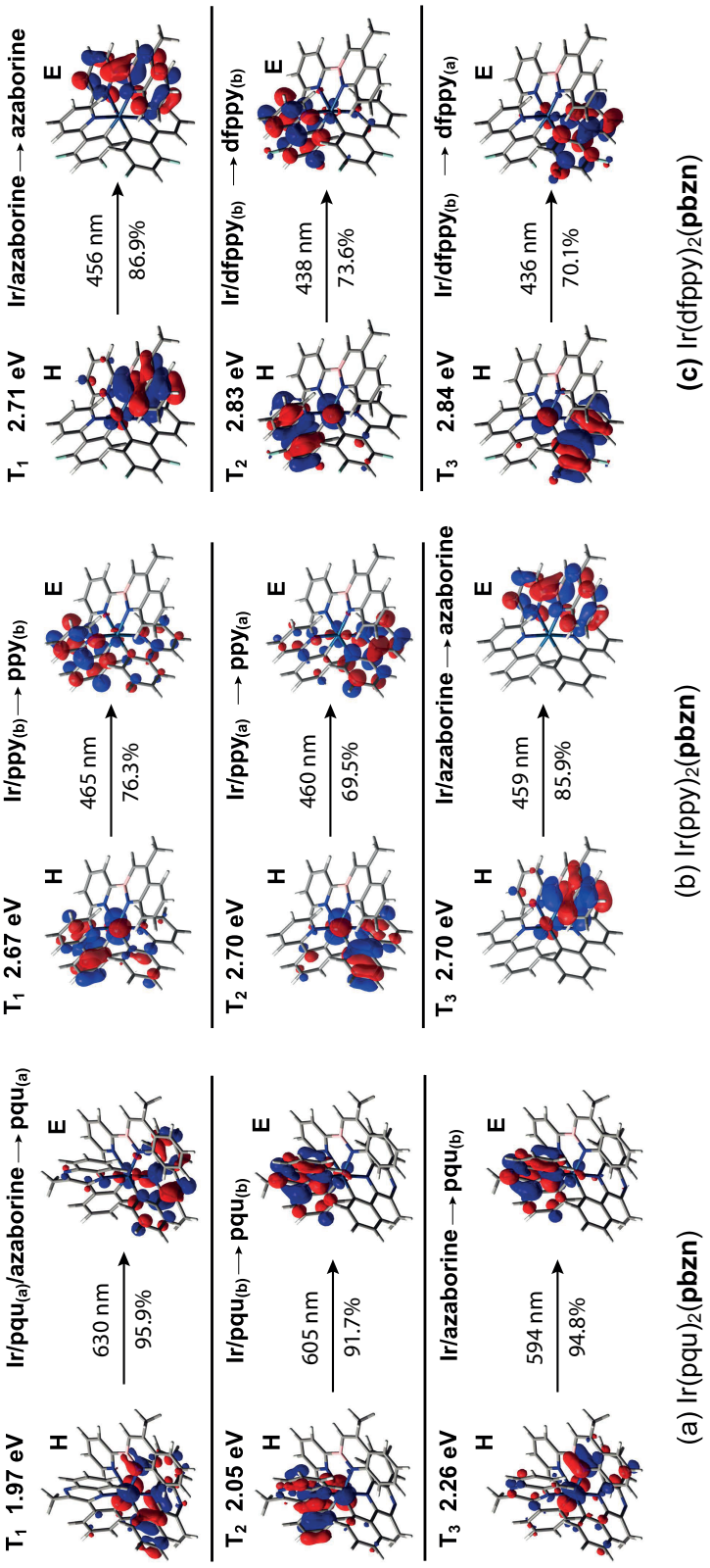

Figure 3.27. Natural transition orbitals associated with the $S_0 \longrightarrow T_n$ (n = 1, 2, 3) of the complexes with the azaborine-ligands. The contribution of the various electronic states to the transition is indicated by the percentage. H = hole; E = electron.

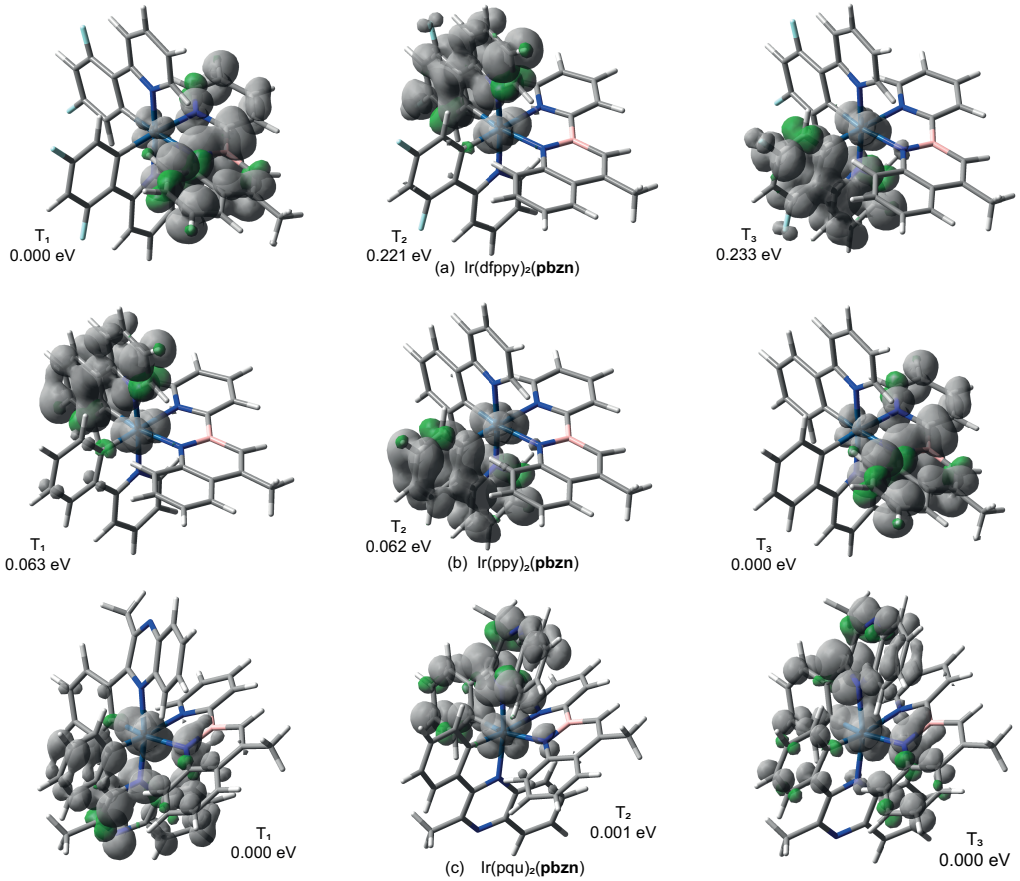

Figure 3.28. Spin density distribution (0.002 e bohr^{-3}) for the optimized T_1, T_2 and T_3 states of the azaborine series, in CH_3CN.

induced by the destabilization played by the solid matrix on the MLCT state characterized by a high-dipole-moment. The same matrix might stabilize the T_2 state that has a predominant LC character, which becomes the lowest in energy.

3.3.6 Comparison with isoelectronic C=C Ir(III) complexes

The similarities between the **Hnpy** and **Hpbzn** ligands are confirmed by the photopysics of the two molecules (see Figure 3.16, 3.21 and 3.29). Both the neutral forms exhibit an emission band centered at 367 nm, with a vibronic progression that is slightly affected by the different nodal planes of the HOMO orbitals on the naphthalene/borazaronaphthalene moieties.

The protonation of the pyridine nitrogen brings about a red-shift of the fluorescence band, which is more marked for the azaborine molecule (**Hnpy**: 445 nm vs. **Hpbzn**: 490 nm), probably due to the stronger CT character observed for the lowest excited singlet of such ligand.

As far as the the two ancillary ligands are concerned, we noticed a less pronounced basicity for the **Hnpy**, which requires a TFA solution two orders of magnitude more concentrated to accomplish complete protonation (compare Figure 3.19 and 3.30).

The absorption spectrum of Ir(ppy)$_2$(**pbzn**) shows just minor variations with respect to the Ir(ppy)$_2$(**1-npy**) C=C parent compound, while the thermodinamically more stable **39**

Table 3.8. Photophysical data of the neutral and protonated azaborine ligand in CH_3CN and CH_2Cl_2 at 298 K and 77 K.

	solvent	temp. (K)	em. state	λ_{em} (nm)	ϕ_{em} [a] (%)	τ [b] (ns)	k_r (10^8 s^{-1})	k_{nr} (10^8 s^{-1})
Hnpy	CH_2Cl_2	298	S_1	346, 363, 380, 403^{sh}	25.4	11.9	0.21	0.63
		77	S_1	344, 361, 380, 400^{sh}		12.1[c]		
			T_1	500, 539, 581, 634^{sh}		$0.90 \cdot 10^9$		
H_2npy$^+$	CH_2Cl_2	298	S_1	445	64.0	11.5	0.56	0.31
		77	S_1	415		9.31[c]		
			T_1	513, 551, 593, 650^{sh}		$0.78 \cdot 10^9$		

[a] Measured with respect to quinine sulfate (1 N, H_2SO_4) as standard (ϕ_{em} = 0.546) [171], λ_{exc} = 310 nm. [b] λ_{exc} = 278 nm. [c] Biexponential decay reported as average excited-state lifetime. [sh] Shoulder.

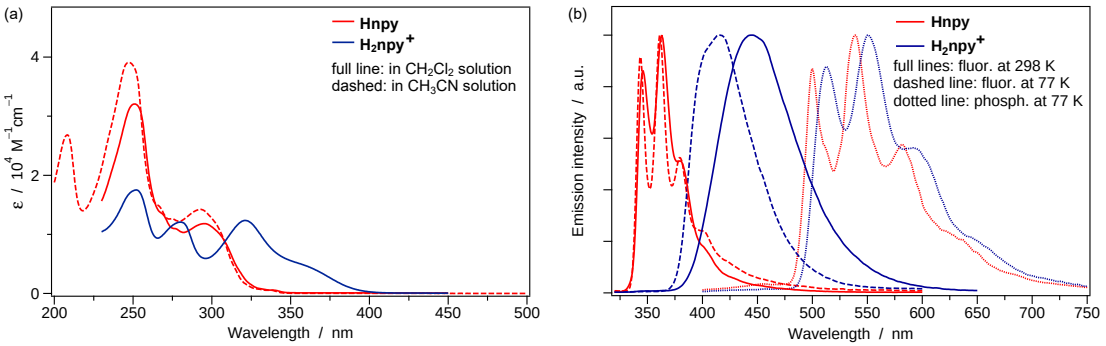

Figure 3.29. (a) Absorption spectra of **Hnpy** (red) and **H_2npy$^+$** (blue) in CH_2Cl_2 (full line) and CH_3CN (dashed line) solutions. (b) Fluorescence (full line: r.t.; dashed line: 77 K) and phosphorescence (dotted line: 77 K) spectra of the **Hnpy** (red) and **H_2npy$^+$** (blue) in CH_2Cl_2 solution.

exhibits a slightly more intense LC band at wavelength < 350 nm (see Figure 3.9 (a)).
On the other hand, the luminescence is clearly affected by the introduction of the B–N bond, whilst the vibronic structure of the emission band is generally preserved, with the complexes bearing **npy** – that show an emission red-shift of about 0.18 eV. This effect is consistent with electrochemical and DFT data, where an increase of the HOMO-LUMO energy gap occurs in the presence of the borazaro moiety (Table 3.4).
In **38** and **39**, as well as for the azaborine complex **36**, the ^{3}LC character of the emission seems to prevail, since (i) it does not undergo rigidochromic effect, (ii) the vibronic structure is enhanced by reducing the temperature, and (iii) the excited-state lifetime is kept in the µs time domain. Anyhow, a precise assignment of this transition for **38** and **39**, is difficult, due to the energy proximity of the three lowest triplets and the different stabilization effect observed upon geometrical relaxation (see Paragraph 3.3.5, for the azaborine complexes). The NTOs of the two **npy** complexes, reported in Figure 3.31, may indicate the emitting-state character.
The first evident aspect is that **38** and **39** – despite the orientation of the naphthalene moiety – have similar energy separations among the triplets, which also keep the same order.

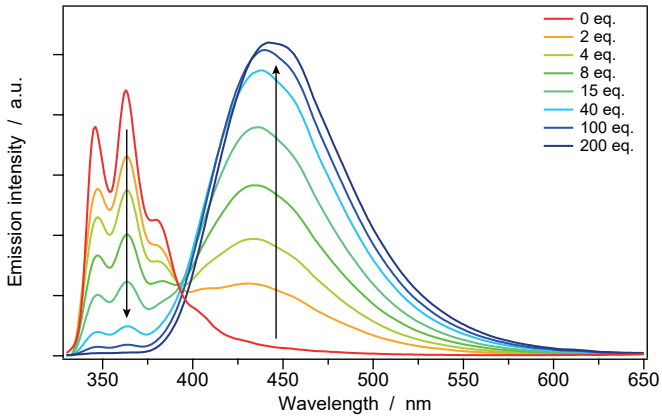

Figure 3.30. Emission-spectra variation of **Hnpy** upon addition of TFA (0-200 equivalents) in CH_2Cl_2; [**Hnpy**] = 15 µM.

Following the observations made for azaborine complexes, it is possible to expect a larger stabilization of the triplet transition centered on the ancillary ligand (Ir/npy⟶npy), upon geometry relaxation. As a consequence, this excited state may become the lowest in energy, *i.e.*, the emitting one, as observed for the ppy azaborine-complex **34**. In the case of **38** and **39**, where the transition centered on the ancillary ligand is already the lowest one, we can expect that, upon geometrical relaxation, such transition remains the main contributor to the emitting state. The experimental results confirm this hypothesis, the phosphorescence of the two C=C complexes being almost superimposable both in solution at room temperature and at 77 K.
The influence of the B–N moiety on the PLQY is again ambiguous, in solution $Ir(ppy)_2$-(**1-npy**) is a better emitter, while in PMMA the situation is inverted, with the azaborine

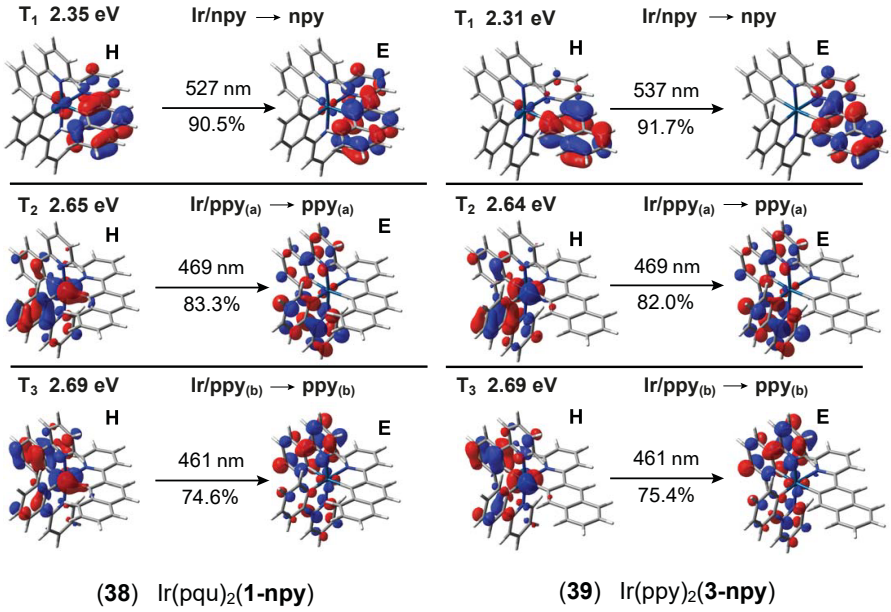

Figure 3.31. Natural transition orbitals associated to the $S_0 \longrightarrow T_n$ (n = 1, 2, 3) of the **npy** complexes (**38** and **39**). The contribution to the transition of the specific states is represented as percentage. H = hole; E = electron.

Table 3.9. Luminescence properties and photophysical parameters of the **npy** and Ir(ppy)$_2$(**pbzn**) complexes in CH_2Cl_2 (298 K and 77 K) and in solid state (PMMA matrix).[a]

	media	λ_{em} (nm)	ϕ_{em} [b] (%)	τ [c] (µs)	k_r [d] (10^4 s^{-1})	k_{nr} [e] (10^4 s^{-1})
Ir(ppy)$_2$(**1-npy**)	CH_2Cl_2	549, 578	38.8	6.7	5.8	9.13
	PMMA[c]	541, 576, 620^{sh}	49.6	8.27	6.0	6.1
	77 K[d]	527, 570, 617, 669^{sh}		14.9		
Ir(ppy)$_2$(**3-npy**)	CH_2Cl_2	552^{sh}, 583	8.4	2.6	3.2	35
	PMMA[c]	539, 575, 620^{sh}	27.1	16.7[g]	-[h]	-[h]
	77 K[d]	526, 570, 619, 670^{sh}		132.4		
Ir(ppy)$_2$(**pbzn**)	CH_2Cl_2	510, 530^{sh}	19.2	1.3	14.8	62.2
	PMMA[c]	513, 534	67.4	3.5	19.3	9.3
	77 K[d]	490, 526, 566		4.5		

[a] Temperature = 298 K if not specified otherwwise. [b] In CH_2Cl_2 solution: measured with respect an air-equilibrated water solution of $[Ru(bpy)_3]Cl_2$ (ϕ_{PL} = 0.028) [239], λ_{exc} = 450 nm. In solid samples: determined using an integrating sphere [159], λ_{exc} = 450 nm. [c] λ_{exc} = 373 nm.
[d] $k_r = \phi_{em}/\tau$. [e] $k_r = 1 - \phi_{em}/\tau$. [sh] Shoulder. [f] 1 wt% of sample content. [g] Biexponential decay reported as average excited-state lifetime. [h] Not calculated since the biexponential decay.

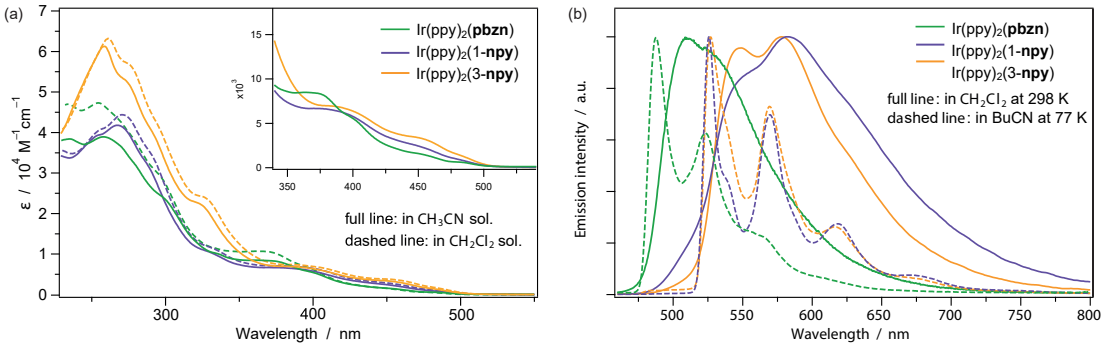

Figure 3.32. (a) Absorption spectra of Ir(ppy)$_2$(**1-npy**) (violet), Ir(ppy)$_2$(**3-npy**) (yellow) and Ir(ppy)$_2$(**pbzn**) (green) in CH_3CN (full line) and CH_2Cl_2 (dashed line) at r.t.. (b) Emission spectra at r.t. in CH_2Cl_2 (full line) and at 77 K in BuCN (dashed line) of Ir(ppy)$_2$(**1-npy**) (violet), Ir(ppy)$_2$(**3-npy**) (yellow) and Ir(ppy)$_2$(**pbzn**) (green).

complex (**36**) showing the highest PLQY.

3.3.7 Conclusion

We reported a novel 1,2-azaborine as anionic ancillary ligand (**Hpbzn**) to get a series of neutral Ir(III) complexes. The aromatic character of the ligand is maintained despite the B–N bond and its rigidity seems to effectively limit distortions and non-radiative deactivation processes of the excited state.
The novel ligand displays interesting luminescence properties in solution (ϕ_{em} = 22 %) and good basicity of the pyridine moiety, as demonstrated by protonation studies. The

protonated form $\mathbf{H_2pbzn^+}$ is also luminescent, with an even greater PLQY (41 %) in solution. The emission nature of the two forms is quite different. While **Hpbzn** exhibits a structured emission band, its protonated form is characterized by a red-shifted broad luminescence with strong CT character.
The neutral azaborine-complexes display good luminescence properties in solution (ϕ_{em} = 19 % for **36**), which are further enhanced in PMMA matrix (ϕ_{em} = 22–69 %). The nature of the luminescent excited states has been determined with the support of DFT calculations. It mainly arises from ^{3}LC states in **35** and **36**, while in the presence of larger conjugation on the C^N ligands (**37**), the specific medium affects the emitting states. The MLCT state appears to be the lowest lying in solution, while in polymer matrix the lowest level is LC.
The comparison with two complexes bearing the isoelectronic **npy** ligand showed the effectiveness of this particular approach: the use of the borazaro chelator bring about complexes with photophysical properties comparable with the classic isoelectronic C=C ligands. In particular, the emitting state has a similar character, but the presence of the B–N polarized bond induces a larger band gap, thus blue-shifted emission.
The stability of the azaborine complexes is still an issue, since slight decomposition in solution is observed together with irreversible redox processes. However, the thorough design of modified azaborine systems could overcome these hurdles, making such compounds fully suitable for optoelectronic applications.

4 Conclusion

4.1 Final remarks on heteroleptic Cu(I) complexes

Three series of $[Cu(NN)(PP)]^+$ complexes (thirty one in total) have been studied to improve the design of Cu(I) coordination compounds in view of the required properties, with particular attention to obtain highly stable and highly emissive systems suitable for optoelectronic applications.
The compounds have been systematically investigated with the fundamental support of theoretical modelling to determine stability, structural and electronic properties, and the direct correlation of these properties with the ligands applied. The key findings are summarized herein.

- $[Cu(NN)(PP)]^+$ complexes possess a labile and flexible pseudo-tetrahedral structure, which can easily undergo distortion and ligand scrumbling equilibrium in solution. The best balance in the size of sterically demanding NN and PP ligands affords solutions for limiting the processes that frustrate the emission performance along several directions.

- The stability of a heteroleptic complex in solution is controlled by the relative association constant of the related homoleptic complexes, thus also a thermodynamically stable $[Cu(NN)(PP)]^+$ compound might undergo ligand exchange when placed in solution. Acting on the stability of the homoleptic complexes to disfavor their formation is an effective strategy. The *negative steric effect* and high P–Cu–P bite angles rely on this principle, both suggesting the use of large ligands which hinder their homo-coupling in a Cu(I) complex. Another possibility consists in the application of *topological constraint*, such as a macrocyclic diimine chelator that, working like a key and lock, can be coupled with the right ligand to form a heteroleptic complex.

- The photoluminescence efficiency in solution is dictated by various parameters. Among them, the above mentioned excited-state distortion plays a central role in the decrease of the radiative constant.

  - The higher the number of intramolecular π-interactions the more intense is the luminescence, underpinning a locking effect that limits the flattening of the excited state.
  - The mono- and di-functionalization on the phenanthroline, in the same way, enhance the PLQY as long as no distortion are induced by these bulky groups.
  - The diphosphines with larger bite angle stabilize more effectively the tetrahedral coordination, thus increasing the luminescence.

- The HOMO-LUMO transition energy is strongly dependent on the type of the ligand used, small variation in the molecular structure visibly affect the energy of the absorption and emission bands.
  - The energy of the MLCT absorption bands linearly increases with increasing the P–Cu–P bite angle.
  - The energy of the emission spectra are not controlled by this parameter, but are red-shifted for the weaker luminophores (*e.g.*, low bite angle PP ligands).
  - The addition of two symmetric substituents on the phenantroline brings about an increase of the average photon energy.
  - A red shift is observed if the electronic delocalization of the diimine is increased.

- The TADF emission is affected by structural parameters, such as the flexibility of the coordination compound or the number of soft intramolecular interactions inside the complex. Sizable differences in the singlet-triplet energy gap is obtained by varying the number and type of functional groups on the phenantroline or by changing the type of PP ligand.

- The steric congestion observed for the macrocyclic phenanthroline ligand reported in the last series of compounds affords a dynamic conformational equilibrium in the pseudorotaxane complex, which is evidenced with a systematic variable-temperature NMR study. The macrocyclic component is indeed forced to adopt a preferential folded conformation, and the activation constant for the macrocycle movement is highly dependent on the steric crowding of the complex.

Furthermore, one of the most promising complexes here reported (compound **31**) has been tested as electroluminescent material in an OLED. Good device stability is found for the OLED based on the pseudorotaxane complex, outperforming the luminescence efficiency of a reference established material (compound **17**).
The amount of data obtained from the complexes reported here has been used to connect our starting point – the structure – to the observed phenomena – luminescence, electrochemistry – and increase the capability to predict the electronic properties during the design phase. Finally, this optimization-by-design approach can be also exported in other relevant areas beyond luminescence, such as photocatalysis, material science and photochemistry.

4.2 Final remarks on luminescent Ir(III) complexes

The design engineering, through the use of heteroaromatic ligands, has been applied to two series of Ir(III) coordination compounds. New luminescent materials suitable for electroluminescent devices are presented. The eight complexes have been compared to similar and already reported analogues, showing excellent photophysical properties.
The structural and photophysical stability of the anionic series of Ir(III) complexes corroborated the strong chelating character of the bis-anionic (**b-trz**)$^{2-}$ ligand. The negative net charge of the complexes, with respect to much more common neutral or positive systems, promotes the oxidation and destabilizes the LUMO, substantially preserving the HOMO-LUMO energy gap.
By a judicious choice of the cyclometallating ligands, distinct luminescence of the three additive primary colors – red, green and blue – can be obtained. Outstanding PLQY, close to unity, is observed for the two compounds emitting at higher energies (**32** and **33**), both in solution and in polymeric media. The electrochemical reversibility of the oxidation and reduction processes proves the robustness of these compounds, prompting their testing in LEC devices. Unfortunately, the quenching of the luminescence observed in neat films hampers electroluminescence, particularly in the case of the **34**. However, a good device stability has been observed for the LEC containing the complex **33**, suggesting the suitability of anionic Ir(III) complexes for LECs. These three Ir-based materials widen the still limited number of anionic complexes available for luminescent soft salts, which are made of emissive cations and anions.

An aromatic azaborine molecule, **Hpbzn**, has been prepared and used as ligand in Ir(III) complexes for the first time. Due to the electron-withdrawing effect of the boron the B–N bond was elongated, with respect the C=C bond in equivalent compounds, and the HOMO-LUMO energy gap was increased due to HOMO stabilization. The novel azaborine is characterized by interesting photophysical properties and a good basicity of the pyridine nitrogen site, which can be exploited to obtain the stable protonated form. This cation has a red-shifted fluorescence, attributable to charge transfer emission and even greater PLQY (41 % in solution). For both forms the phosphorescence is observed in rigid matrix (77 K).
The neutral complexes are characterized by good luminescence in solution (PLQY ≤ 19 %), further enhanced in polymer matrix (22–69 %), which arises from ^{3}LC states in **35** and **36** complexes and strongly depends on the specific medium for **37**. The isoelectronic complex containing the C=C parent ligand confirms that the ancillary azaborine chelator does not affect the character of the emissive electronic state. The stability of the **pbzn** is still not comparable to isoelectronic C=C compounds. At the moment, the irreversible electrochemical processes of its complexes prevent the application in optoelectronic devices. However, further improvements of the molecular structure may increase the stability, opening up a wider use of this new class of ligands in transition-metal complexes.

A Experimental Techniques

A.1 Structural determination and NMR

Crystals suitable for X-ray crystal structure analysis were obtained by slow diffusion of Et_2O into a CH_2Cl_2 solution of the complex as $[BF_4]^-$ salt. Data were collected at 173 K on a Nonius Kappa-CCD diffractometer (Mo Kα radiation, λ = 0.710 73 Å). The structure was solved by direct methods (SHELXS-97) and refined against F^2 using the SHELXL-97 software. Non-hydrogen atoms were refined anisotropically using weighted full-matrix least-squares on F^2. H atoms were included in calculated positions and treated as riding atoms using SHELXL default parameters.
When necessary moiety constrains were applied, as well as a semiempirical absorption correction using the MULscanABS routine in PLATON [240]; transmission factors, Tmin/Tmax = 0.69776/0.84015. The SQUEEZE instruction in PLATON [240] was applied if needed.
NMR spectra were recorded on a Bruker AC 300 or AC 400 with solvent peaks as reference. Variable-temperature NMR spectra were recorded with an Agilent DD2 500 MHz equipped with the OneNMR probe.

A.2 Photophysical measurements

Spectrofluorimetric grade dichloromethane and acetonitrile (Sigma-Aldrich) were used as solvent for spectroscopic investigations. The absorption spectra were recorded with a PerkinElmer Lambda 950 spectrophotometer. For the photoluminescence experiments, the samples were placed in fluorimetric Suprasil quartz cuvettes (1 cm) and deaerated by bubbling argon for at least 20 min. The uncorrected emission spectra were obtained with an Edinburgh Instruments FLS920 spectrometer equipped with a Peltier-cooled Hamamatsu R928 photomultiplier tube (PMT) (185–850 nm). An Edinburgh Xe 900 with 450 W xenon arc lamp was used as the excitation light source. The corrected spectra were obtained via a calibration curve, determined using an Ocean Optics Deuterium-Halogen calibrated lamp (DH-3plus-CAL-EXT). The luminescence quantum yields (ϕ_{em}, PLQY) in solution were obtained from the corrected spectra on a wavelength scale (nm) and measured according to the approach described by Demas and Crosby [241], using an

air-equilibrated water solution of $[Ru(bpy)_3]Cl_2$ (ϕ_{em} = 0.028) [239] and air-equilibrated water solution of quinine sulfate in 1 N H_2SO_4 (ϕ_{em} = 0.546) [171] as reference.
The emission lifetimes (τ) in the sub-microsecond time range were measured through the time-correlated single-photon counting (TCSPC) technique using an HORIBA Jobin Yvon IBH FluoroHub controlling a spectrometer equipped with a pulsed NanoLED (λ_{exc} = 373 nm; $fwhm$ = 1.2 ns) as the excitation source and a red-sensitive Hamamatsu R-3237-01 PMT (185–850 nm) as the detector. The analysis of the luminescence decay profiles, taken on the emission maximum, was accomplished with the DAS6 Decay Analysis Software provided by the manufacturer, and the quality of the fit was assessed with the χ^2 value close to unity and with the residuals randomly scattered along the time axis. To record the 77 K luminescence spectra, sample solutions were put in quartz tubes (2 mm inner diameter) and inserted into a special quartz Dewar flask filled with liquid nitrogen, and SpectraLED (λ_{exc} = 370 nm; $fwhm$ = 11 ns) was used as excitation source for the excitedstate lifetime determination.
Solid state measure were carried out on (i) PMMA films containing 1 wt% of the complex drop-cast from dichloromethane solutions and (ii) powders, as obtained after the crystallization, placed in quartz tubes. The thickness of the films was not determined. Solid-state ϕ_{em} values were calculated by corrected emission spectra obtained from an Edinburgh FLS920 spectrometer equipped with a barium sulfate-coated integrating sphere (diameter of 3 in) following the procedure described by Würth et al. [159].
For temperature-dependent measurements, the samples (PMMA films or powders) were placed inside an Oxford Optistat DN variable-temperature liquid-nitrogen cryostat (operating range: 77–500 K) equipped with an ITC5035 temperature controller and interfaced with the aforementioned Edinburgh FLS920 spectrometer. The temperature-dependent emission lifetimes were measured through the multichannel scaling single-photon counting (MCS-SPC) technique with the use of the same luminescence spectrometer described above and equipped with a 60 W xenon flashlamp (Edinburgh μF920H) as the excitation source (100 Hz; 2 µs pulse width) and the aforementioned PMT as detector (minimum response 600 ps). The analysis of the luminescence decay profiles upon deconvolution of the instrumental response function (IRF) was accomplished with the software provided by the manufacturer, and the quality of the fit was assessed following abovementioned conditions. The decays were fitted as mono-exponential if possible. In case of biexponential fitting the shorter lifetime contributes below 20 % and is attributed to scattering, whereas the longer lifetime is taken as the experimental value. Experimental uncertainties are estimated to be ± 8 % for τ determinations, ± 20 % for ϕ_{em}, and ± 2 nm and ± 5 nm for absorption and emission peaks, respectively.

A.3 Electrochemistry

Voltammetric experiments were performed using a Metrohm AutoLab PGSTAT 302N electrochemical workstation in combination with the NOVA 2.0 software package. All the measurements were carried out at room temperature in CH_2Cl_2 or CH_3CN solutions with a sample concentration of ≈ 1 mM and using 0.1 M tetrabutylammonium hexafluorophosphate (electrochemical grade, $[TBA][PF_6]$) as the supporting electrolyte. Oxygen was removed from the solutions by bubbling argon for 20 min. All the experiments were carried out using a three-electrode setup (BioLogic VC-4 cell, volume range: 1–3 ml) using a platinum or a glassy carbon working electrode (both having an active

surface disk of 1.6 mm in diameter), the $Ag/AgNO_3$ redox couple (0.01 M in acetonitrile, with 0.1 M [TBA][ClO_4] supporting electrolyte) as the reference electrode and a platinum wire as the counter electrode. At the end of each measurement, ferrocene was added as the internal reference. Cyclic voltammograms (CV) were recorded at different scan rates, from 100–5000 mV s^{-1}. Osteryoung square-wave voltammograms (OSWV) were recorded with scan rate of 125–200 mV s^{-1}, a SW amplitude of ± 5–20 mV, and a frequency of 20–25 Hz.

A.4 Computational details

Density functional calculations were carried out with the D.01 revision of the Gaussian 09 program package [242]. Both the PBE0 hybrid functional [243, 244] and the M06 hybrid meta exchange-correlation functional [153, 154] were used to carry out the calculations. The ECP10MDF fully relativistic Stuttgart/Cologne energy-consistent pseudopotential with multi-electron fit was used to replace the first 10 inner-core electrons of the copper metal center [245] and it was combined with the associated cc-pVTZ-PP triple-ζ basis set[246]. On the other hand, Pople basis sets were adopted for non-metal atoms: the 6-31G(d) basis set was used for C, H, N, O atoms [247, 248], while the more flexible 6-311G(2d) basis for P [249]. The geometry of all complexes was optimized in vacuum (if not differently stated), starting from the X-ray molecular structure as initial guess. The same level of theory was used to perform the calculation of Kohn-Sham energy levels. A frequency job always confirmed that the stationary point found by the geometry optimization was actually corresponding to a minimum on the potential energy surface (no imaginary frequencies). TD-DFT calculations [250–252], at the same level of theory used for geometrical optimization, were employed to calculate the first 24 singlet vertical excitations and the lowest 9 triplet vertical excitations were calculated within the linear-response formalism. For these calculations, the polarizable continuum model (PCM) [219–221] was employed to take in to account solvation effects. For having an estimation of both the geometry distortions and the energy of the first excited state, the lowest triplet excited state (T_1) was optimized at the spin-unrestricted level of theory with a spin multiplicity of 3, using the above mentioned density functionals. All the pictures showing molecular orbitals and spin-density surfaces were created using GaussView 5 [253].

A.5 OLED Fabrication and assessment

OLEDs were fabricated on glass substrates pre-coated with a 120 nm thick layer of indium tin oxide (ITO) with a sheet resistance of 20 Ω per square. The substrates were cleaned by ultrasonication in acetone and 2-propanol baths and then placed in a UV cleaner for 25 min. After the treatment of the substrates, a 40 nm thick layer of poly(3,4-ethylenedioxythiophene):poly-styrenesulfonate (PEDOT:PSS CLE-VIOS P VP AI 4083) was spincoated (4000 rpm), and then the substrates were placed in an oven at 140 °C for 10 min. After the ITO/PEDOT:PSS substrates were cooled down, a 50 nm thick film of emitting layer composed of 15 wt% of Cu(I) complex and 85 wt% of bis-4-(N-carbazolyl)-phenyl)phenylphosphine oxide) (BCPO, Lumtec) host was spin-coated (2000 rpm) in

clean room environment from a 8 mg ml^{-1} CH_2Cl_2 solution, which had the above indicated weight percent concentrations of Cu(I) complex and BCPO. The layers of the OLED devices were deposited in clean room environment by thermal evaporation under high vacuum of ≈ 10 × 10^{-6} hPa without vacuum interruption. First, a 25 nm thick electron transporting layer of 2,2′,2′′-(1,3,5-benzinetriyl)-tris(1-phenyl-1H-benzimidazole) (TPBi, Jilin OLED Material Tech Co., Ltd.) was evaporated and then the cathode layer consisting of 0.5 nmthick LiF (Sigma-Aldrich, ≥ 99.98 %) and 100 nm thick Al cap. All solvents employed in substrates cleaning and device preparation were purchased from Sigma-Aldrich and were of analytical grade.
The current-voltage characteristics were measured with a Keithley Source-Measure unit, model 236, under continuous operation mode, while the light output power was measured with an EG& G power meter, and electroluminescence spectra recorded with a StellarNet spectroradiometer. All measurements were carried out at room temperature under argon atmosphere. The OLED devices had a lighting area of 7.1 mm.

A.6 LEC Fabrication and characterization

All materials were used as received. PEDOT:PSS (CLE-VIOS P VP AI 4083) was purchased from Heraeus. The ionic liquid (IL) 1-butyl-3-methylimidazolium hexafluorophosphate ([Bmim][PF_6]) and the dichloromethane were purchased from Sigma-Aldrich. The photolithography-patterned ITO glass substrates were purchased from Naranjo Substrates (www.naranjosubstrates.com).
The substrates were cleaned with sonication and soap, then deionized water, isopropanol, and UV-O_3 lamp for 20 min. The thickness of the films was determined with an Ambios XP-1 profilometer. The 80 nm PEDOT:PSS layer was coated at 1000 rpm for 60 s and then was dried at 150 ˚C for 15 min. The emitting layer (200 nm) was prepared by spin-coating of a CH_2Cl_2 solution consisting of the **32-34** with the addition of the ionic liquid ([Bmim][PF_6]) in a 4:1 molar ratio. The devices were then transferred to an inert atmosphere glovebox (< 0.1 ppm of O_2 and H_2O, MBraun) and annealed during 1 h at 100 ˚C. Finally, a layer (70 nm) of aluminum (the top electrode) was thermally evaporated onto the devices using an Edwards Auto500 evaporator integrated in the inert atmosphere glovebox. The area of the device was 6.5 mm^2. The devices were not encapsulated and were characterized inside the glovebox at room temperature.
The device lifetime was measured by applying a pulsed current and monitoring the voltage and the luminance versus time by a True Color Sensor MAZeT (MTCSiCT Sensor) with a Botest OLT OLED Lifetime-Test System. The average current density was determined by multiplying the peak current density by the time-on time and dividing by the total cycle time. The average luminance is directly obtained by taking the average of the obtained photodiode results and correlating it to the value of a luminance meter. The current efficiency is obtained by dividing the average luminance by the average current density. The electroluminescent spectra were measured using an Avantes AvaSpec-2048 Fiber Optic Spectrometer during device lifetime measurement.

B

Permissions

Title: Heteroleptic Copper(I) Complexes Prepared from Phenanthroline and Bis-Phosphine Ligands: Rationalization of the Photophysical and Electrochemical Properties

Author: Enrico Leoni, John Mohanraj, Michel Holler, et al

Publication: Inorganic Chemistry

Publisher: American Chemical Society

Date: Dec 1, 2018

LOGIN

If you're a copyright.com user, you can login to RightsLink using your copyright.com credentials.

Already **a RightsLink user** or want to learn more?

PERMISSION/LICENSE IS GRANTED FOR YOUR ORDER AT NO CHARGE

This type of permission/license, instead of the standard Terms & Conditions, is sent to you because no fee is being charged for your order. Please note the following:

- Permission is granted for your request in both print and electronic formats, and translations.
- If figures and/or tables were requested, they may be adapted or used in part.
- Please print this page for your records and send a copy of it to your publisher/graduate school.
- Appropriate credit for the requested material should be given as follows: "Reprinted (adapted) with permission from (COMPLETE REFERENCE CITATION). Copyright (YEAR) American Chemical Society." Insert appropriate information in place of the capitalized words.
- One-time permission is granted only for the use specified in your request. No additional uses are granted (such as derivative works or other editions). For any other uses, please submit a new request.

BACK CLOSE WINDOW

Bibliography

[1] N. G. Connelly, T. Damhus, R. M. Hartshorn, A. T. Hutton, *Nomenclature of Inorganic Chemistry, IUPAC Recommendations 2005*, The Royal Society of Chemistry, **2005**.

[2] V. W.-W. Yam, K. M.-C. Wong, *Chemical Communications* **2011**, *47*, 11579–11592.

[3] A. W. Adamson, J. N. Demas, *Journal of the American Chemical Society* **1971**, *93*, 1800–1801.

[4] A. Juris, V. Balzani, F. Barigelletti, S. Campagna, P. Belser, A. von Zelewsky, *Coordination Chemistry Reviews* **1988**, *84*, 85–277.

[5] J. V. Caspar, T. J. Meyer, *Inorganic Chemistry* **1983**, *22*, 2444–2453.

[6] D. Kumaresan, K. Shankar, S. Vaidya, R. H. Schmehl, *Topics in Current Chemistry* **2007**, *281*, 101–142.

[7] K. A. King, P. J. Spellane, R. J. Watts, *Journal of the American Chemical Society* **1985**, *107*, 1431–1432.

[8] M. Wrighton, D. L. Morse, *Journal of the American Chemical Society* **1974**, *96*, 998–1003.

[9] M. A. Baldo, D. F. O'Brien, Y. You, A. Shoustikov, S. Sibley, M. E. Thompson, S. R. Forrest, *Nature* **1998**, *395*, 151–154.

[10] M. Maestri, D. Sandrini, V. Balzani, L. Chassot, P. Jolliet, A. von Zelewsky, *Chemical Physics Letters* **1985**, *122*, 375–379.

[11] D. R. McMillin, M. T. Buckner, B. T. Ahn, *Inorganic Chemistry* **1977**, *16*, 943–945.

[12] M. T. Buckner, T. G. Matthews, F. E. Lytle, D. R. McMillin, *Journal of the American Chemical Society* **1979**, *101*, 5846–5848.

[13] R. Czerwieniec, M. J. Leitl, H. H. H. Homeier, H. Yersin, *Coordination Chemistry Reviews* **2016**, *325*, 2–28.

[14] L. Flamigni, A. Barbieri, C. Sabatini, B. Ventura, F. Barigelletti, *Topics in Current Chemistry* **2007**, *281*, 143–203.

[15] R. J. Watts, *Comments on Inorganic Chemistry* **1991**, *11*, 301–337.

[16] K. Dedeian, P. I. Djurovich, F. O. Garces, G. Carlson, R. J. Watts, *Inorganic Chemistry* **1991**, *30*, 1685–1687.

[17] A. B. Tamayo, B. D. Alleyne, P. I. Djurovich, S. Lamansky, I. Tsyba, N. N. Ho, R. Bau, M. E. Thompson, *Journal of the American Chemical Society* **2003**, *125*, 7377–7387.

[18] D. Roundhill, *Photochemistry and Photophysics of Metal Complexes*, Plenum Press, New York, **1994**.

[19] R. D. Costa, E. Orti, H. J. Bolink, F. Monti, G. Accorsi, N. Armaroli, *Angewandte Chemie International Edition* **2012**, *51*, 8178–8211.

[20] H. Yersin in *Transition Metal and Rare Earth Compounds: Excited States, Transitions, Interactions III*, Springer Berlin Heidelberg, Berlin, Heidelberg, **2004**, pp. 1–26.

[21] J. D. Slinker, J. Rivnay, J. S. Moskowitz, J. B. Parker, S. Bernhard, H. D. Abruña, G. G. Malliaras, *Journal of Materials Chemistry* **2007**, *17*, 2976–2988.

[22] M. S. Lowry, S. Bernhard, *Chemistry – A European Journal* **2006**, *12*, 7970–7977.

[23] C. Ulbricht, B. Beyer, C. Friebe, A. Winter, U. S. Schubert, *Advanced Materials* **2009**, *21*, 4418–4441.

[24] P.-T. Chou, Y. Chi, *Chemistry – A European Journal* **2006**, *13*, 380–395.

[25] R. D. Costa, D. Tordera, E. Ortí, H. J. Bolink, J. Schönle, S. Graber, C. E. Housecroft, E. C. Constable, J. A. Zampese, *Journal of Materials Chemistry* **2011**, *21*, 16108–16118.

[26] C. D. Ertl, C. Momblona, A. Pertegas, J. M. Junquera-Hernandez, M. G. La-Placa, A. Prescimone, E. Orti, C. E. Housecroft, E. C. Constable, H. J. Bolink, *Journal of the American Chemical Society* **2017**, *139*, 3237–3248.

[27] N. Armaroli, H. J. Bolink, *Photoluminescent Materials and Electroluminescent Devices*, Springer, **2017**.

[28] A. C. Hernandez-Perez, S. K. Collins, *Accounts of Chemical Research* **2016**, *49*, 1557–1565.

[29] O. Reiser, *Accounts of Chemical Research* **2016**, *49*, 1990–1996.

[30] E. Mejía, S. Luo, M. Karnahl, A. Friedrich, S. Tschierlei, A. Surkus, H. Junge, S. Gladiali, S. Lochbrunner, M. Beller, *Chemistry – A European Journal* **2013**, *19*, 15972–15978.

[31] R. S. Khnayzer, C. E. McCusker, B. S. Olaiya, F. N. Castellano, *Journal of the American Chemical Society* **2013**, *135*, 14068–14070.

[32] H. Takeda, K. Ohashi, A. Sekine, O. Ishitani, *Journal of the American Chemical Society* **2016**, *138*, 4354–4357.

[33] M. Sandroni, Y. Pellegrin, F. Odobel, *Comptes Rendus Chimie* **2016**, *19*, 79–93.

[34] C. S. Smith, K. R. Mann, *Journal of the American Chemical Society* **2012**, *134*, 8786–8789.

[35] A. O. Razgoniaev, C. E. McCusker, F. N. Castellano, A. D. Ostrowski, *ACS Macro Letters* **2017**, *6*, 920–924.

[36] N. Armaroli, G. Accorsi, F. Cardinali, A. Listorti, *Topics in Current Chemistry* **2007**, *280*, 69–115.

[37] N. Armaroli, *Chemical Society Reviews* **2001**, *30*, 113–124.

[38] M. Iwamura, S. Takeuchi, T. Tahara, *Accounts of Chemical Research* **2015**, *48*, 782–791.

[39] G. B. Shaw, C. D. Grant, H. Shirota, E. W. Castner, G. J. Meyer, L. X. Chen, *Journal of the American Chemical Society* **2007**, *129*, 2147–2160.

[40] L. X. Chen, X. Zhang, M. L. Shelby, *Chemical Science* **2014**, *5*, 4136–4152.

[41] J. Huang, M. W. Mara, A. B. Stickrath, O. Kokhan, M. R. Harpham, K. Haldrup, M. L. Shelby, X. Zhang, R. Ruppert, J. P. Sauvage, L. X. Chen, *Dalton Transactions* **2014**, *43*, 17615–17623.

[42] D. Hayes, L. Kohler, R. G. Hadt, X. Zhang, C. Liu, K. L. Mulfort, L. X. Chen, *Chem. Sci.* **2018**, *9*, 860–875.

[43] C. E. McCusker, F. N. Castellano, *Inorganic Chemistry* **2013**, *52*, 8114–8120.

[44] S. Garakyaraghi, P. D. Crapps, C. E. McCusker, F. N. Castellano, *Inorganic Chemistry* **2016**, *55*, 10628–10636.

[45] S. Garakyaraghi, C. E. McCusker, S. Khan, P. Koutnik, A. T. Bui, F. N. Castellano, *Inorganic Chemistry* **2018**, *57*, 2296–2307.

[46] G. Blasse, D. R. McMillin, *Chemical Physics Letters* **1980**, *70*, 1–3.

[47] Y. Onoue, K. Hiraki, Y. Nishikawa, *Analytical Sciences* **1987**, *3*, 509–513.

[48] D. G. Cuttell, S. M. Kuang, P. E. Fanwick, D. R. McMillin, R. A. Walton, *Journal of the American Chemical Society* **2002**, *124*, 6–7.

[49] S. M. Kuang, D. G. Cuttell, D. R. McMillin, P. E. Fanwick, R. A. Walton, *Inorganic Chemistry* **2002**, *41*, 3313–3322.

[50] L. Yang, J. K. Feng, A. M. Ren, M. Zhang, Y. G. Ma, X. D. Liu, *European Journal of Inorganic Chemistry* **2005**, *10*, 1867–1879.

[51] K. Saito, T. Arai, N. Takahashi, T. Tsukuda, T. Tsubomura, *Dalton Transactions* **2006**, *0*, 4444–4448.

[52] L. M. Zhang, B. Li, Z. M. Su, *Langmuir* **2009**, *25*, 2068–2074.

[53] N. Armaroli, G. Accorsi, M. Holler, O. Moudam, J. F. Nierengarten, Z. Zhou, R. T. Wegh, R. Welter, *Advanced Materials* **2006**, *18*, 1313–1316.

[54] A. Listorti, G. Accorsi, Y. Rio, N. Armaroli, O. Moudam, A. Gegout, B. Delavaux-Nicot, M. Holler, J. F. Nierengarten, *Inorganic Chemistry* **2008**, *47*, 6254–6261.

[55] S. Tschierlei, M. Karnahl, N. Rockstroh, H. Junge, M. Beller, S. Lochbrunner, *ChemPhysChem* **2014**, *15*, 3709–3713.

[56] C. L. Linfoot, M. J. Leitl, P. Richardson, A. F. Rausch, O. Chepelin, F. J. White, H. Yersin, N. Robertson, *Inorganic Chemistry* **2014**, *53*, 10854–10861.

[57] T. Tsubomura, K. Kimura, M. Nishikawa, T. Tsukuda, *Dalton Transactions* **2015**, *44*, 7554–7562.

[58] Y. H. Sun, V. Lemaur, J. I. Beltran, J. Cornil, J. W. Huang, J. T. Zhu, Y. Wang, R. Frohlich, H. B. Wang, L. Jiang, G. F. Zou, *Inorganic Chemistry* **2016**, *55*, 5845–5852.

[59] K. Kubicek, S. T. Veedu, D. Storozhuk, R. Kia, S. Techert, *Polyhedron* **2017**, *124*, 166–176.

[60] F. L. Zhang, Y. Q. Guan, X. L. Chen, S. S. Wang, D. Liang, Y. F. Feng, S. F. Chen, S. Z. Li, Z. Y. Li, F. Q. Zhang, C. Z. Lu, G. X. Cao, B. Zhai, *Inorganic Chemistry* **2017**, *56*, 3742–3753.

[61] F. Brunner, S. Graber, Y. Baumgartner, D. Haussinger, A. Prescimone, E. C. Constable, C. E. Housecroft, *Dalton Transactions* **2017**, *46*, 6379–6391.

[62] G. K. M. So, G. Cheng, J. Wang, X. Y. Chang, C. C. Kwok, H. X. Zhang, C. M. Che, *Chemistry - An Asian Journal* **2017**, *12*, 1490–1498.

[63] M. Mohankumar, M. Holler, E. Meichsner, J. F. Nierengarten, F. Niess, J. P. Sauvage, B. Delavaux-Nicot, E. Leoni, F. Monti, J. M. Malicka, M. Cocchi, E. Bandini, N. Armaroli, *Journal of the American Chemical Society* **2018**, *140*, 2336–2347.

[64] M. Mohankumar, F. Monti, M. Holler, F. Niess, B. Delavaux-Nicot, N. Armaroli, J. P. Sauvage, J. F. Nierengarten, *Chemistry - A European Journal* **2014**, *20*, 12083–12090.

[65] M. Osawa, *Chemical Communications* **2014**, *50*, 1801–1803.

[66] S. Y. Shi, L. R. Collins, M. F. Mahon, P. I. Djurovich, M. E. Thompson, M. K. Whittlesey, *Dalton Transactions* **2017**, *46*, 745–752.

[67] K. J. Lotito, J. C. Peters, *Chemical Communications* **2010**, *46*, 3690–3692.

[68] M. G. Crestani, G. F. Manbeck, W. W. Brennessel, T. M. McCormick, R. Eisenberg, *Inorganic Chemistry* **2011**, *50*, 7172–7188.

[69] M. J. Leitl, V. A. Krylova, P. I. Djurovich, M. E. Thompson, H. Yersin, *Journal of the American Chemical Society* **2014**, *136*, 16032–16038.

[70] R. Molteni, K. Edkins, M. Haehnel, A. Steffen, *Organometallics* **2016**, *35*, 629–640.

[71] W. Liu, Y. Fang, G. Z. Wei, S. J. Teat, K. C. Xiong, Z. C. Hu, W. P. Lustig, J. Li, *Journal of the American Chemical Society* **2015**, *137*, 9400–9408.

[72] X. Zhang, W. Liu, G. Z. Wei, D. Banerjee, Z. C. Hu, J. Li, *Journal of the American Chemical Society* **2014**, *136*, 14230–14236.

[73] K. M. Miller, S. M. McCullough, E. A. Lepekhina, I. J. Thibau, R. D. Pike, X. B. Li, J. P. Killarney, H. H. Patterson, *Inorganic Chemistry* **2011**, *50*, 7239–7249.

[74] Y. Zhang, M. Schulz, M. Wächtler, M. Karnahl, B. Dietzek, *Coordination Chemistry Reviews* **2018**, *356*, 127–146.

[75] A. Kaeser, M. Mohankumar, J. Mohanraj, F. Monti, M. Holler, J. J. Cid, O. Moudam, I. Nierengarten, L. Karmazin-Brelot, C. Duhayon, B. Delavaux-Nicot, N. Armaroli, J. F. Nierengarten, *Inorganic Chemistry* **2013**, *52*, 12140–12151.

[76] M. J. Leitl, D. M. Zink, A. Schinabeck, T. Baumann, D. Volz, H. Yersin, *Topics in Current Chemistry* **2016**, *374*, 25.

[77] Bernanose, André, Comte, Marcel, Vouaux, Paul, *Journal de Chimie Physique* **1953**, *50*, 64–68.

[78] Bernanose, André, Vouaux, Paul, *Journal de Chimie Physique* **1953**, *50*, 261–263.

[79] M. Pope, H. P. Kallmann, P. Magnante, *Journal of Chemical Physics* **1963**, *38*, 2042–2043.

[80] P. S. Vincett, W. A. Barlow, R. A. Hann, G. G. Roberts, *Thin Solid Films* **1982**, *94*, 171–183.

[81] C. W. Tang, S. A. VanSlyke, *Applied Physics Letters* **1987**, *51*, 913–915.

[82] Q. Pei, G. Yu, C. Zhang, Y. Yang, A. J. Heeger, *Science* **1995**, *269*, 1086–8.

[83] K. M. Maness, R. H. Terrill, T. J. Meyer, R. W. Murray, R. M. Wightman, *Journal of the American Chemical Society* **1996**, *118*, 10609–10616.

[84] R. D. Costa, E. Ortí, H. J. Bolink, S. Graber, S. Schaffner, M. Neuburger, C. E. Housecroft, E. C. Constable, *Advanced Functional Materials* **2009**, *19*, 3456–3463.

[85] A. F. Rausch, H. H. H. Homeier, H. Yersin in *Photophysics of Organometallics*, Springer Berlin Heidelberg, Berlin, Heidelberg, **2010**, pp. 193–235.

[86] C. T. Cunningham, J. J. Moore, K. L. H. Cunningham, P. E. Fanwick, D. R. McMillin, *Inorganic Chemistry* **2000**, *39*, 3638–3644.

[87] H. Yersin, R. Czerwieniec, M. Z. Shafikov, A. F. Suleymanova, *ChemPhysChem* **2017**, *18*, 3508–3535.

[88] B. X. Yang, C. Yao, G. Zhou, *Platinum Metals Review* **2013**, *57*, 2–16.

[89] G. Cheng, P.-K. Chow, S. C. F. Kui, C.-C. Kwok, C.-M. Che, *Advanced Materials* **2013**, *25*, 6765–6770.

[90] Q. Wang, I. W. H. Oswald, M. R. Perez, H. Jia, A. A. Shahub, Q. Qiao, B. E. Gnade, M. A. Omary, *Advanced Functional Materials* **2014**, *24*, 4746–4752.

[91] H. Uoyama, K. Goushi, K. Shizu, H. Nomura, C. Adachi, *Nature* **2012**, *492*, 234–238.

[92] Q. Zhang, B. Li, S. Huang, H. Nomura, H. Tanaka, C. Adachi, *Nature Photonics* **2014**, *8*, 326–332.

[93] H. Kaji, H. Suzuki, T. Fukushima, K. Shizu, K. Suzuki, S. Kubo, T. Komino, H. Oiwa, F. Suzuki, A. Wakamiya, Y. Murata, C. Adachi, *Nature Communications* **2015**, *6*, 8476.

[94] L.-S. Cui, H. Nomura, Y. Geng, J. U. Kim, H. Nakanotani, C. Adachi, *Angewandte Chemie* **2017**, *129*, 1593–1597.

[95] A. Al Mousawi, D. M. Lara, G. Noirbent, F. Dumur, J. Toufaily, T. Hamieh, T.-T. Bui, F. Goubard, B. Graff, D. Gigmes, J. P. Fouassier, J. Lalevée, *Macromolecules* **2017**, *50*, 4913–4926.

[96] E. Fresta, R. D. Costa, *Journal of Materials Chemistry C* **2017**, *5*, 5643–5675.

[97] J. C. deMello, N. Tessler, S. C. Graham, R. H. Friend, *Physical Review B* **1998**, *57*, 12951–12963.

[98] J. C. deMello, *Physical Review B* **2002**, *66*, 235210.

[99] G. G. Malliaras, J. D. Slinker, J. A. DeFranco, M. J. Jaquith, W. R. Silveira, Y.-W. Zhong, J. M. Moran-Mirabal, H. G. Craighead, H. D. Abruña, J. A. Marohn, *Nature Materials* **2008**, *7*, 167–168.

[100] Q. Pei, Y. Yang, G. Yu, C. Zhang, A. J. Heeger, *Journal of the American Chemical Society* **1996**, *118*, 3922–3929.

[101] D. L. Smith, *Journal of Applied Physics* **1997**, *81*, 2869–2880.

[102] D. B. Rodovsky, O. G. Reid, L. S. C. Pingree, D. S. Ginger, *ACS Nano* **2010**, *4*, 2673–2680.

[103] S. De, K. Mahata, M. Schmittel, *Chemical Society Reviews* **2010**, *39*, 1555–1575.

[104] S. Durot, F. Reviriego, J. P. Sauvage, *Dalton Transactions* **2010**, *39*, 10557–10570.

[105] M. W. Mara, K. A. Fransted, L. X. Chen, *Coordination Chemistry Reviews* **2015**, *282*, 2–18.

[106] C. E. Housecroft, E. C. Constable, *Chemical Society Reviews* **2015**, *44*, 8386–8398.

[107] D. Volz, M. Wallesch, C. Flechon, M. Danz, A. Verma, J. M. Navarro, D. M. Zink, S. Brase, T. Baumann, *Green Chemistry* **2015**, *17*, 1988–2011.

[108] A. F. Henwood, E. Zysman-Colman, *Chemical Communications* **2017**, *53*, 807–826.

[109] D. X. Ma, T. Tsuboi, Y. Qiu, L. Duan, *Advanced Materials* **2017**, *29*, 1603253.

[110] E. A. Medlycott, G. S. Hanan, *Coordination Chemistry Reviews* **2006**, *250*, 1763–1782.

[111] M. C. Tang, A. K. W. Chan, M. Y. Chan, V. W. W. Yam, *Topics in Current Chemistry* **2016**, *374*, 46.

[112] S. Keller, A. Pertegas, G. Longo, L. Martinez, J. Cerda, J. M. Junquera-Hernandez, A. Prescimone, E. C. Constable, C. E. Housecroft, E. Orti, H. J. Bolink, *Journal of Materials Chemistry C* **2016**, *4*, 3857–3871.

[113] O. Moudam, A. Kaeser, B. Delavaux-Nicot, C. Duhayon, M. Holler, G. Accorsi, N. Armaroli, I. Seguy, J. Navarro, P. Destruel, J. F. Nierengarten, *Chemical Communications* **2007**, *0*, 3077–3079.

[114] J. Yuasa, M. Dan, T. Kawai, *Dalton Transactions* **2013**, *42*, 16096–16101.

[115] Z. Q. Wang, C. J. Zheng, W. Z. Wang, C. Xu, B. M. Ji, X. H. Zhang, *Inorganic Chemistry* **2016**, *55*, 2157–2164.

[116] N. Y. Chen, L. M. Xia, A. J. J. Lennox, Y. Y. Sun, H. Chen, H. M. Jin, H. Junge, Q. A. Wu, J. H. Jia, M. Beller, S. P. Luo, *Chemistry - A European Journal* **2017**, *23*, 3631–3636.

[117] D. R. McMillin, J. R. Kirchhoff, K. V. Goodwin, *Coordination Chemistry Reviews* **1985**, *64*, 83–92.

[118] M. W. Mara, N. E. Jackson, J. Huang, A. B. Stickrath, X. Zhang, N. A. Gothard, M. A. Ratner, L. X. Chen, *The Journal of Physical Chemistry B* **2013**, *117*, 1921–1931.

[119] S. Garakyaraghi, E. O. Danilov, C. E. McCusker, F. N. Castellano, *The Journal of Physical Chemistry A* **2015**, *119*, 3181–3193.

[120] R. Englman, J. Jortner, *Molecular Physics* **1970**, *18*, 145–164.

[121] Z. A. Siddique, Y. Yamamoto, T. Ohno, K. Nozaki, *Inorganic Chemistry* **2003**, *42*, 6366–6378.

[122] A. J. J. Lennox, S. Fischer, M. Jurrat, S.-P. Luo, N. Rockstroh, H. Junge, R. Ludwig, M. Beller, *Chemistry – A European Journal* **2016**, *22*, 1233–1238.

[123] B. R. James, R. J. P. Williams, *Journal of the Chemical Society* **1961**, 2007–2019.

[124] F. Arnaud-Neu, E. Marques, M.-J. Schwing-Weill, C. O. Dietrich-Buchecker, J.-P. Sauvage, J. Weiss, *New Journal of Chemistry* **1988**, *12*, 15–20.

[125] M. Schmittel, A. Ganz, *Chemical Communications* **1997**, 999–1000.

[126] A. Kaeser, O. Moudam, G. Accorsi, I. Seguy, J. Navarro, A. Belbakra, C. Duhayon, N. Armaroli, B. Delavaux-Nicot, J. F. Nierengarten, *European Journal of Inorganic Chemistry* **2014**, 1345–1355.

[127] S. B. Harkins, J. C. Peters, *Journal of the American Chemical Society* **2005**, *127*, 2030–2031.

[128] A. J. M. Miller, J. L. Dempsey, J. C. Peters, *Inorganic Chemistry* **2007**, *46*, 7244–7246.

[129] J.-J. Cid, J. Mohanraj, M. Mohankumar, M. Holler, G. Accorsi, L. Brelot, I. Nierengarten, O. Moudam, A. Kaeser, B. Delavaux-Nicot, N. Armaroli, J.-F. Nierengarten, *Chemical Communications* **2013**, *49*, 859–861.

[130] C. Dietrich-Buchecker, J. Sauvage, J. Kintzinger, *Tetrahedron Letters* **1983**, *24*, 5095–5098.

[131] C. Dietrich-Buchecker, J. Sauvage, *Tetrahedron Letters* **1983**, *24*, 5091–5094.

[132] C. O. Dietrich-Buchecker, J. P. Sauvage, J. M. Kern, *Journal of the American Chemical Society* **1984**, *106*, 3043–3045.

[133] C. Dietrich-Buchecker, J.-P. Sauvage, *Tetrahedron* **1990**, *46*, 503–512.

[134] J.-P. Sauvage, *Angewandte Chemie International Edition* **2017**, *56*, 11080–11093.

[135] J. F. Stoddart, *Angewandte Chemie International Edition* **2017**, *56*, 11094–11125.

[136] D. Donges, J. K. Nagle, H. Yersin, *Inorganic Chemistry* **1997**, *36*, 3040–3048.

[137] H. Yersin, D. Donges, *Topics in Current Chemistry*, Topics in Current Chemistry **2001**, *214*, 81–186.

[138] G. J. Hedley, A. Ruseckas, I. D. Samuel, *Chemical Physics Letters* **2008**, *450*, 292–296.

[139] C.-W. Hsu, C.-C. Lin, M.-W. Chung, Y. Chi, G.-H. Lee, P.-T. Chou, C.-H. Chang, P.-Y. Chen, *Journal of the American Chemical Society* **2011**, *133*, 12085–12099.

[140] T. Sajoto, P. I. Djurovich, A. B. Tamayo, J. Oxgaard, W. A. Goddard, M. E. Thompson, *Journal of the American Chemical Society* **2009**, *131*, 9813–9822.

[141] E. Leoni, J. Mohanraj, M. Holler, M. Mohankumar, I. Nierengarten, F. Monti, A. Sournia-Saquet, J.-F. Nierengarten, N. Armaroli, *Inorganic Chemistry* **2018**, *57*, 15537–15549.

[142] W.-W. Fan, Z.-F. Li, J.-B. Li, Y.-P. Yang, Y. Yuan, H.-Q. Tang, L.-X. Gao, Q.-H. Jin, Z.-W. Zhang, C.-L. Zhang, *Journal of Molecular Structure* **2015**, *1099*, 351–358.

[143] Y. Sun, S. Zhang, G. Li, Y. Xie, D. Zhao, *Transition Metal Chemistry* **2003**, *28*, 772–776.

[144] R. N. Yang, D. M. Wang, Y. F. Liu, D. M. Jin, *Russian Journal of Inorganic Chemistry* **2001**, *46*, 993–998.

[145] E. C. Constable, C. E. Housecroft, P. Kopecky, E. Schonhofer, J. A. Zampese, *CrystEngComm* **2011**, *13*, 2742–2752.

[146] D. Saravanabharathi, A. Samuelson, *Indian Journal of Chemistry* **2003**, *42A*, 2300–2306.

[147] X.-L. Li, Y.-B. Ai, B. Yang, J. Chen, M. Tan, X.-L. Xin, Y.-H. Shi, *Polyhedron* **2012**, *35*, 47–54.

[148] Y.-R. Zhang, X. Yu, S. Lin, Q.-H. Jin, Y.-P. Yang, M. Liu, Z.-F. Li, C.-L. Zhang, X.-L. Xin, *Polyhedron* **2017**, *138*, 46–56.

[149] Z. G. Kong, W. L. Li, G. B. Che, B. Chu, D. F. Bi, L. L. Han, L. L. Chen, Z. Z. Hu, Z. Q. Zhang, *Applied Physics Letters* **2006**, *89*, 161112.

[150] S. P. Luo, E. Mejia, A. Friedrich, A. Pazidis, H. Junge, A. E. Surkus, R. Jackstell, S. Denurra, S. Gladiali, S. Lochbrunner, M. Beller, *Angewandte Chemie International Edition* **2013**, *52*, 419–423.

[151] B. Su, C. Liu, G. Che, M. Liu, S. Zhang, Z. Xu, Q. Wang, *Optoelectronics and Advanced Materials Rapid Communications* **2011**, *5*, 999–1002.

[152] W. Humphrey, A. Dalke, K. Schulten, *Journal of Molecular Graphics & Modelling* **1996**, *14*, 33–38.

[153] Y. Zhao, D. G. Truhlar, *Accounts of Chemical Research* **2008**, *41*, 157–167.

[154] Y. Zhao, D. G. Truhlar, *Theoretical Chemistry Accounts* **2008**, *120*, 215–241.

[155] G. Accorsi, N. Armaroli, B. Delavaux-Nicot, A. Kaeser, M. Holler, J.-F. Nierengarten, A. Degli Esposti, *Journal of Molecular Structure: THEOCHEM* **2010**, *962*, 7–14.

[156] Y. Pellegrin, M. Sandroni, E. Blart, A. Planchat, M. Evain, N. C. Bera, M. Kayanuma, M. Sliwa, M. Rebarz, O. Poizat, C. Daniel, F. Odobel, *Inorganic Chemistry* **2011**, *50*, 11309–11322.

[157] J. J. Cid, J. Mohanraj, M. Mohankumar, M. Holler, F. Monti, G. Accorsi, L. Karmazin-Brelot, I. Nierengarten, J. M. Malicka, M. Cocchi, B. Delavaux-Nicot, N. Armaroli, J. F. Nierengarten, *Polyhedron* **2014**, *82*, 158–172.

[158] G. D. Hager, G. A. Crosby, *Journal of the American Chemical Society* **1975**, *97*, 7031–7037.

[159] C. Würth, M. Grabolle, J. Pauli, M. Spieles, U. Resch-Genger, *Nature Protocols* **2013**, *8*, 1535–1550.

[160] K. F. Freed, J. Jortner, *The Journal of Chemical Physics* **1970**, *52*, 6272–6291.

[161] D. Felder, J. F. Nierengarten, F. Barigelletti, B. Ventura, N. Armaroli, *Journal of the American Chemical Society* **2001**, *123*, 6291–6299.

[162] I. Vorontsov, T. Graber, A. Y. Kovalevsky, I. V. Novozhilova, M. Gembicky, Y. S. Chen, P. Coppens, *Journal of the American Chemical Society* **2009**, *131*, 6566–6573.

[163] C. T. Cunningham, K. L. H. Cunningham, J. F. Michalec, D. R. McMillin, *Inorganic Chemistry* **1999**, *38*, 4388–4392.

[164] C. S. Smith, C. W. Branham, B. J. Marquardt, K. R. Mann, *Journal of the American Chemical Society* **2010**, *132*, 14079–14085.

[165] C. F. Macrae, P. R. Edgington, P. McCabe, E. Pidcock, G. P. Shields, R. Taylor, M. Towler, J. van de Streek, *Journal of Applied Crystallography* **2006**, *39*, 453–457.

[166] M. Brookhart, M. L. H. Green, G. Parkin, *Proceedings of the National Academy of Sciences* **2007**, *104*, 6908–6914.

[167] D. V. Scaltrito, D. W. Thompson, J. A. O'Callaghan, G. J. Meyer, *Coordination Chemistry Reviews* **2000**, *208*, 243–266.

[168] A. Lavie-Cambot, M. Cantuel, Y. Leydet, G. Jonusauskas, D. M. Bassani, N. D. McClenaghan, *Coordination Chemistry Reviews* **2008**, *252*, 2572–2584.

[169] C. Bizzarri, C. Strabler, J. Prock, B. Trettenbrein, M. Ruggenthaler, C. H. Yang, F. Polo, A. Iordache, P. Bruggeler, L. De Cola, *Inorganic Chemistry* **2014**, *53*, 10944–10951.

[170] N. Armaroli, L. De Cola, V. Balzani, J. P. Sauvage, C. O. Dietrich-Buchecker, J. M. Kern, A. Bailal, *Journal of the Chemical Society Dalton Transactions* **1993**, 3241–3247.

[171] S. R. Meech, D. Phillips, *Journal of Photochemistry* **1983**, *23*, 193–217.

[172] M. Mohankumar, M. Holler, J.-F. Nierengarten, J.-P. Sauvage, *Chemistry - A European Journal* **2012**, *18*, 12192–12195.

[173] M. Mohankumar, M. Holler, M. Schmitt, J.-P. Sauvage, J.-F. Nierengarten, *Chemical Communications* **2013**, *49*, 1261–1263.

[174] H. Friebolin, *Basic One- and Two-Dimensional NMR Spectroscopy*, 5th, Wiley-VCH, Weinheim, **2010**, pp. 316–319.

[175] N. Armaroli, G. Accorsi, G. Bergamini, P. Ceroni, M. Holler, O. Moudam, C. Duhayon, B. Delavaux-Nicot, J.-F. Nierengarten, *Inorganica Chimica Acta* **2007**, *360*, 1032–1042.

[176] H. H. Chou, C. H. Cheng, *Advanced Materials* **2010**, *22*, 2468–2471.

[177] B. Umamahesh, N. S. Karthikeyan, K. I. Sathiyanarayanan, J. M. Malicka, M. Cocchi, *Journal of Materials Chemistry C* **2016**, *4*, 10053–10060.

[178] Q. Zhang, T. Komino, S. Huang, S. Matsunami, K. Goushi, C. Adachi, *Advanced Functional Materials* **2012**, *22*, 2327–2336.

[179] R. C. Evans, P. Douglas, C. J. Winscom, *Coordination Chemistry Reviews* **2006**, *250*, 2093–2126.

[180] T. Hu, L. He, L. Duan, Y. Qiu, *Journal of Materials Chemistry* **2012**, *22*, 4206–4215.

[181] Q. Zeng, F. Li, T. Guo, G. Shan, Z. Su, *Science Reports* **2016**, *6*, 27613.

[182] J. Slinker, D. Bernards, P. L. Houston, H. D. Abruna, S. Bernhard, G. G. Malliaras, *Chemical Communications* **2003**, 2392–2399.

[183] E. Matteucci, A. Baschieri, A. Mazzanti, L. Sambri, J. Ávila, A. Pertegás, H. J. Bolink, F. Monti, E. Leoni, N. Armaroli, *Inorganic Chemistry* **2017**, *56*, 10584–10595.

[184] F. Aleotti, Master Thesis, Università di Bologna, **2017**.

[185] V. Y. Zubarev, R. E. Trifonov, V. V. Poborchii, V. A. Ostrovskii, *Chemistry of Heterocyclic Compounds* **2006**, *42*, 469–474.

[186] E. Zysman-Colman, *Iridium(III) in Optoelectronic and Photonics Applications, Vol. 1*, John Wiley & Sons, Hoboken, New Jersey, **2017**.

[187] R. D. Simpson, W. J. Marshall, A. A. Farischon, D. C. Roe, V. V. Grushin, *Inorganic Chemistry* **1999**, *38*, 4171–4173.

[188] N. D. Triantafillou, B. C. Gates, *Langmuir* **1999**, *15*, 2595–2598.

[189] S. M. Whittemore, J. Gallucci, J. P. Stambuli, *Organometallics* **2011**, *30*, 5273–5277.

[190] A. A. Del Paggio, R. A. Andersen, E. L. Muetterties, *Organometallics* **1987**, *6*, 1260–1267.

[191] M. P. Garcia, M. V. Jimenez, L. A. Oro, F. J. Lahoz, M. C. Tiripicchio, A. Tiripicchio, *Organometallics* **1993**, *12*, 4660–4663.

[192] M. Kinauer, M. G. Scheibel, J. Abbenseth, F. W. Heinemann, P. Stollberg, C. Wurtele, S. Schneider, *Dalton Transactions* **2014**, *43*, 4506–4513.

[193] K. Fujita, R. Kawahara, T. Aikawa, R. Yamaguchi, *Angewandte Chemie International Edition* **2015**, *54*, 9057–9060.

[194] M. K. Nazeeruddin, R. Humphry-Baker, D. Berner, S. Rivier, L. Zuppiroli, M. Graetzel, *Journal of the American Chemical Society* **2003**, *125*, 8790–8797.

[195] J. Li, P. I. Djurovich, B. D. Alleyne, M. Yousufuddin, N. N. Ho, J. C. Thomas, J. C. Peters, R. Bau, M. E. Thompson, *Inorganic Chemistry* **2005**, *44*, 1713–1727.

[196] D. Di Censo, S. Fantacci, F. De Angelis, C. Klein, N. Evans, K. Kalyanasundaram, H. J. Bolink, M. Grätzel, M. K. Nazeeruddin, *Inorganic Chemistry* **2008**, *47*, 980–989.

[197] V. Fiorini, A. D'Ignazio, K. D. Magee, M. I. Ogden, M. Massi, S. Stagni, *Dalton Transactions* **2016**, *45*, 3256–3259.

[198] Q. Zhang, Q. Zhou, Y. Cheng, L. Wang, D. Ma, X. Jing, F. Wang, *Advanced Functional Materials* **2006**, *16*, 1203–1208.

[199] K. R. Lee, M. S. Eum, C. S. Chin, S. C. Lee, I. J. Kim, Y. S. Kim, Y. Kim, S. J. Kim, N. H. Hur, *Dalton Transactions* **2009**, 3650–3652.

[200] J. L. Liao, Y. Chi, Z. T. Sie, C. H. Ku, C. H. Chang, M. A. Fox, P. J. Low, M. R. Tseng, G. H. Lee, *Inorganic Chemistry* **2015**, *54*, 10811–10821.

[201] V. Fiorini, S. Zacchini, P. Raiteri, R. Mazzoni, V. Zanotti, M. Massi, S. Stagni, *Dalton Transactions* **2016**, *45*, 12884–12896.

[202] E. I. Szerb, A. Ionescu, N. Godbert, Y. J. Yadav, A. M. Talarico, M. Ghedini, *Inorganic Chemistry Communications* **2013**, *37*, 80–83.

[203] A. Ionescu, E. I. Szerb, Y. J. Yadav, A. M. Talarico, M. Ghedini, N. Godbert, *Dalton Transactions* **2014**, *43*, 784–789.

[204] V. H. Nguyen, H. Q. Chew, B. Su, J. H. Yip, *Inorganic Chemistry* **2014**, *53*, 9739–9750.

[205] J. E. Namanga, N. Gerlitzki, A.-V. Mudring, *Advanced Functional Materials* **2017**, *27*, 1605588.

[206] J. E. Namanga, N. Gerlitzki, B. Mallick, A.-V. Mudring, *Journal of Materials Chemistry C* **2017**, *5*, 3049–3055.

[207] A. F. Henwood, E. Zysman-Colman, *Topics in Current Chemistry* **2016**, *374*, 36.

[208] K. J. Suhr, L. D. Bastatas, Y. Shen, L. A. Mitchell, B. J. Holliday, J. D. Slinker, *ACS Appl Mater Interfaces* **2016**, *8*, 8888–8892.

[209] Y. Shen, D. D. Kuddes, C. A. Naquin, T. W. Hesterberg, C. Kusmierz, B. J. Holliday, J. D. Slinker, *Applied Physics Letters* **2013**, *102*, 203305.

[210] T.-H. Kwon, Y. H. Oh, I.-S. Shin, J.-I. Hong, *Advanced Functional Materials* **2009**, *19*, 711–717.

[211] H. F. Chen, C. Wu, M. C. Kuo, M. E. Thompson, K. T. Wong, *Journal of Materials Chemistry* **2012**, *22*, 9556–9561.

[212] F. Dumur, Y. Yuskevitch, G. Wantz, C. R. Mayer, D. Bertin, D. Gigmes, *Synthetic Metals* **2013**, *177*, 100–104.

[213] S. Guo, T. C. Huang, S. J. Liu, K. Y. Zhang, H. R. Yang, J. M. Han, Q. Zhao, W. Huang, *Chemical Science* **2017**, *8*, 348–360.

[214] C. Wu, H. F. Chen, K. T. Wong, M. E. Thompson, *Journal of the American Chemical Society* **2010**, *132*, 3133–3139.

[215] A. Baschieri, F. Monti, E. Matteucci, A. Mazzanti, A. Barbieri, N. Armaroli, L. Sambri, *Inorganic Chemistry* **2016**, *55*, 7912–7919.

[216] F. Monti, A. Baschieri, E. Matteucci, A. Mazzanti, L. Sambri, A. Barbieri, N. Armaroli, *Faraday Discuss* **2015**, *185*, 233–248.

[217] M. M. Francl, W. J. Pietro, W. J. Hehre, J. S. Binkley, M. S. Gordon, D. J. Defrees, J. A. Pople, *Journal of Chemical Physics* **1982**, *77*, 3654–3665.

[218] D. Figgen, K. A. Peterson, M. Dolg, H. Stoll, *Journal of Chemical Physics* **2009**, *130*, 164108.

[219] J. Tomasi, M. Persico, *Chemical Reviews* **1994**, *94*, 2027–2094.

[220] J. Tomasi, B. Mennucci, R. Cammi, *Chemical Reviews* **2005**, *105*, 2999–3093.

[221] C. J. Cramer, D. G. Truhlar in *Solvent Effects and Chemical Reactivity*, (Eds.: O. Tapia, J. Bertrán), Understanding Chemical Reactivity, Springer Netherlands, **2002**, Chapter 1, pp. 1–80.

[222] F. Monti, F. Kessler, M. Delgado, J. Frey, F. Bazzanini, G. Accorsi, N. Armaroli, H. J. Bolink, E. Orti, R. Scopelliti, M. K. Nazeeruddin, E. Baranoff, *Inorganic Chemistry* **2013**, *52*, 10292–10305.

[223] N. M. Shavaleev, F. Monti, R. D. Costa, R. Scopelliti, H. J. Bolink, E. Orti, G. Accorsi, N. Armaroli, E. Baranoff, M. Grätzel, M. K. Nazeeruddin, *Inorganic Chemistry* **2012**, *51*, 2263–2271.

[224] N. M. Shavaleev, F. Monti, R. Scopelliti, N. Armaroli, M. Grätzel, M. K. Nazeeruddin, *Organometallics* **2012**, *31*, 6288–6296.

[225] N. M. Shavaleev, F. Monti, R. Scopelliti, A. Baschieri, L. Sambri, N. Armaroli, M. Grätzel, M. K. Nazeeruddin, *Organometallics* **2013**, *32*, 460–467.

[226] S. Ladouceur, D. Fortin, E. Zysman-Colman, *Inorganic Chemistry* **2011**, *50*, 11514–11526.

[227] E. C. Constable, M. Neuburger, P. Rosel, G. E. Schneider, J. A. Zampese, C. E. Housecroft, F. Monti, N. Armaroli, R. D. Costa, E. Orti, *Inorganic Chemistry* **2013**, *52*, 885–897.

[228] R. L. Martin, *Journal of Chemical Physics* **2003**, *118*, 4775–4777.

[229] D. Tordera, S. Meier, M. Lenes, R. D. Costa, E. Orti, W. Sarfert, H. J. Bolink, *Advanced Materials* **2012**, *24*, 897–900.

[230] D. Tordera, J. J. Serrano-Perez, A. Pertegas, E. Orti, H. J. Bolink, E. Baranoff, M. K. Nazeeruddin, J. Frey, *Chemistry of Materials* **2013**, *25*, 3391–3397.

[231] P. G. Campbell, A. J. V. Marwitz, S.-Y. Liu, *Angewandte Chemie International Edition* **2012**, *51*, 6074–6092.

[232] A. Stock, E. Pohland, *Berichte der Deutschen Chemischen Gesellschaft (A and B Series)* **1926**, *59*, 2215–2223.

[233] S. R. Wisniewski, C. L. Guenther, O. A. Argintaru, G. A. Molander, *The Journal of Organic Chemistry* **2014**, *79*, 365–378.

[234] A. Mazzanti, E. Mercanti, M. Mancinelli, *Organic Letters* **2016**, *18*, 2692–2695.

[235] D. B. Diaz, A. K. Yudin, *Nature Chemistry* **2017**, *9*, 731.

[236] T. Taniguchi, S. Yamaguchi, *Organometallics* **2010**, *29*, 5732–5735.

[237] R. Kwong, B. Ma, J.-Y. Tsai, S. Beers, E. Barron, G. Kottas, A. B. Dyatkin, *US Pat.*, US8586203 B2, **2010**.

[238] M. Lepeltier, O. Lukoyanova, A. Jacobson, S. Jeeva, D. F. Perepichka, *Chemical Communications* **2010**, *46*, 7007–7009.

[239] K. Nakamaru, *Bulletin of the Chemical Society of Japan* **1982**, *55*, 2697–2705.

[240] A. L. Spek, *Journal of Applied Crystallography* **2003**, *36*, 7–13.

[241] J. N. Demas, G. A. Crosby, *Journal of Physical Chemistry* **1971**, *75*, 991–1024.

[242] M. J. Frisch, G. W. Trucks, H. B. Schlegel, G. E. Scuseria, M. A. Robb, J. R. Cheeseman, G. Scalmani, V. Barone, B. Mennucci, G. A. Petersson, H. Nakatsuji, M. Caricato, X. Li, H. P. Hratchian, A. F. Izmaylov, J. Bloino, G. Zheng, J. L. Sonnenberg, M. Hada, M. Ehara, K. Toyota, R. Fukuda, J. Hasegawa, M. Ishida, T. Nakajima, Y. Honda, O. Kitao, H. Nakai, T. Vreven, J. Montgomery, J. A., J. E. Peralta, F. Ogliaro, M. Bearpark, J. J. Heyd, E. Brothers, K. N. Kudin, V. N. Staroverov, T. Keith, R. Kobayashi, J. Normand, K. Raghavachari, A. Rendell, J. C. Burant, S. S. Iyengar, J. Tomasi, M. Cossi, N. Rega, J. M. Millam, M. Klene, J. E. Knox, J. B. Cross, V. Bakken, C. Adamo, J. Jaramillo, R. Gomperts, R. E. Stratmann, O. Yazyev, A. J. Austin, R. Cammi, C. Pomelli, J. W. Ochterski, R. L. Martin, K. Morokuma, V. G. Zakrzewski, G. A. Voth, P. Salvador, J. J. Dannenberg, S. Dapprich, A. D. Daniels,

O. Farkas, J. B. Foresman, J. V. Ortiz, J. Cioslowski, D. J. Fox, *Gaussian 09, Revision D.01*, Gaussian, Inc.: Wallingford, CT, **2013**.

[243] C. Adamo, V. Barone, *Journal of Chemical Physics* **1999**, *110*, 6158–6170.

[244] C. Adamo, G. E. Scuseria, V. Barone, *Journal of Chemical Physics* **1999**, *111*, 2889–2899.

[245] D. Figgen, G. Rauhut, M. Dolg, H. Stoll, *Chemical Physics* **2005**, *311*, 227–244.

[246] K. A. Peterson, C. Puzzarini, *Theoretical Chemistry Accounts* **2005**, *114*, 283–296.

[247] A. D. McLean, G. S. Chandler, *The Journal of Chemical Physics* **1980**, *72*, 5639–5648.

[248] R. Krishnan, J. S. Binkley, R. Seeger, J. A. Pople, *Journal of Chemical Physics* **1980**, *72*, 650–654.

[249] P. J. Hay, W. R. Wadt, *Journal of Chemical Physics* **1985**, *82*, 299–310.

[250] R. E. Stratmann, G. E. Scuseria, M. J. Frisch, *Journal of Chemical Physics* **1998**, *109*, 8218–8224.

[251] M. E. Casida, C. Jamorski, K. C. Casida, D. R. Salahub, *Journal of Chemical Physics* **1998**, *108*, 4439–4449.

[252] R. Bauernschmitt, R. Ahlrichs, *Chemical Physics Letters* **1996**, *256*, 454–464.

[253] R. Dennington, T. Keith, J. Millam, *Gaussview, Version 5*, Semichem Inc.: Shawnee Mission, KS, USA, **2009**.

Ringrazio il personale dell'Istituto per la Sintesi Organica e la Fotoreattività del Consiglio Nazionale delle Ricerche, del Laboratorio Tecnologie dei Materiali dell'ENEA di Faenza e del Dipartimento di Chimica "Giacomo Ciamician" dell'Università di Bologna, che ha collaborato nella realizzazione di questo progetto.